NATIONAL TECHNICAL
UNIVERSITY OF ATHENS
School of Applied Mathematical and
Physical Sciences

Study of the Planetary Boundary Layer and its influence on cloud properties

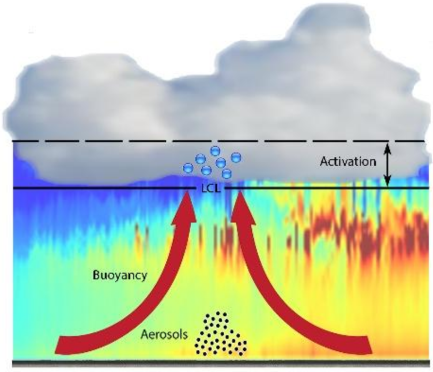

Ph.D. Thesis

Athina A. Argyrouli

Graduated from:

School of Applied Mathematical & Physical Sciences,
National Technical University of Athens

Electrical Engineering, Telecommunications, Delft
University of Technology

Ph.D. Thesis Supervisor:

Prof. Alexandros Papayannis

September 2016

NATIONAL TECHNICAL
UNIVERSITY OF ATHENS
School of Applied Mathematical and
Physical Sciences

MARIE CURIE ACTIONS

ITaRS
Initial Training for
atmospheric Remote Sensing

Study of the Planetary Boundary Layer and its influence on cloud properties

Ph.D. Thesis

Athina A. Argyrouli

3-member Ph.D. committee:

1. Prof. Alexandros Papayannis
2. Dr. Vasilis Amiridis
3. Prof. Ioannis Ziomas

7-member Ph.D. committee:

1. Prof. Alexandros Papayannis
2. Dr. Vassilis Amiridis
3. Prof. Ioannis Ziomas
4. Prof. Herman Russchenberg
5. Dr. Ulla Wandinger
6. Prof. Athanasios Nenes
7. Dr. Konstantinos Eleftheriadis

September 2016

The research leading to these results has received funding from the People Programme (ITN Marie Curie Actions) of the European Union's Seventh Framework Programme (FP7/2007-2013) under REA grant agreement n° 289923 (ITARS project)

“Είναι δύσκολο να φτιάξει κανείς ένα έργο χωρίς να κάνει κανένα λάθος, αλλά δύσκολο είναι κι αν ακόμα φτιάξει κάτι αλάθητο να μην πέσει σε άδικο κριτή.”

Σωκράτης

Acknowledgements

I would like to thank my daily supervisor Prof. Dr. Alexandros Papayannis for giving me the opportunity to develop this Thesis in the Laser Remote Sensing Unit of the National Technical University of Athens. From the day one, he gave me a exhaustive list of references and he taught me how to work and behave in a lab with optics. During my stay at the lab, I had plenty of support and freedom to find my research interests. Moreover, I should admit that this Thesis would have been poorer without his detailed comments. Sorry for making you spend your vacation days correcting this Thesis!

I am specially grateful to my Ph.D. advisor Dr. Vassilis Amiridis researcher in the National Observatory of Athens. I was feeling always welcome in his group. At the beginning of this Thesis, he spent hours, discussing with me about the challenges in the field of lidar remote sensing and he gave me his notes from the time of his Ph.D. Thesis. He has always been encouraging when I was lacking motivation, he has been an advisor and he has been a friend. I apologize for the arguments we had so far; often I am high-tempered and cannot hide my feelings.

Furthermore, I would like to thank from the depths of my heart the Ph.D. committee members Prof. Dr. Herman Russchenberg and Dr. Ulla Wandinger. They were keeping track of my progress so as everything goes smoothly until the day of my defense. Many times during these years of the Ph.D. they supported me in many different ways, both scientifically and personally.

I have to say a big thank you to Prof. Dr. Athanasios Nenes. He is a very inspiring scientist and he knows A LOT! His guidance and feedback on my work during the final year of my Ph.D. was critical and I owe him a significant part of my scientific achievements. The cloud droplet number retrieval was one of the main pillars of this Ph.D.

Special thanks to Prof. Dr. Detlef Müller. He hosted me twice at his group and he introduced me to the *magic* of the so-called lidar inversion. The retrievals I have gotten from the HygrA-CD dataset look good because he showed me how to be critical on the inversion results.

Last but not least, I would like to thank the Ph.D. committee members Dr. Kostas Eleftheriadis and Prof. Dr. Ioannis Ziomas. Dr. Kostas Eleftheriadis hosted me at DEM station during the HygrA-CD campaign. He gave me an office and he made me feel comfortable there. During the month the campaign lasted, we had the chance to discuss about science. Prof. dr. Ioannis Ziomas gave me some final boost to my Thesis when he shot me with numerous questions on atmospheric physics and chemistry topics.

I personally thank my colleagues Dr. Ioannis Binietoglou, Dr. Katerina Bougiatioti, Dr. Spyros Bezantakos, Dr. Panos Kokkalis, Dr. George Tsaknakis, Dr. Stavros Solomos, Dr. Prodromos Fetfatzis, Stergios Vratolis, Eleni Marinou and Dr. Alexandra Tsekeri. They have all contributed to this Thesis in a way. They devoted time on helping me find solutions on my problems (both scientific and psychological problems) when I was stuck and could not move forwards.

In addition, I want to thank people from ITaRS consortium, the coordinator Prof. Dr. Susanne Crewell, and Dr. Doina Nicolae who secured the operation of the Microwave

Radiometer during the HygrA-CD campaign and the quality of the retrievals after the campaign. Many thanks to the ITaRS fellows, my colleagues Dr. Lev Labzovsky and Maria Barrera Verdejo who came to Athens during the campaign. Finally, I want to thank the project manager of ITaRS, Sarah Henkel for everything she did for us during the ITaRS project. I am happy that I met all these people and I am proud I was part of this lovely network.

I should never forget my parents, my brother and our dog. All the members of my family help me on keep on trying in life. They are patient with me and they always show how much they love me.

Finally, the credit of this Ph.D. Thesis goes to my beloved partner. During the Ph.D. he was always there for me when I was disappointed when the lidar measurement was not good or my code was not working. During the final month of the Ph.D. when I was finalizing this Thesis, he has done everything he could for me: from cooking and cleaning the house to finding the latex commands in making a proper glossary for this Ph.D.

Abstract

The main objective of this Ph.D. Thesis was to study the impact of aerosols on cloud properties under the effect of turbulence in the Planetary Boundary Layer (PBL). The current work has been triggered by the uncertainties of cloud adjustments due to their interaction with aerosols within the PBL. The impact of turbulence and aerosols' properties on cloud development was studied in the urban environment of Athens from the database of the Hygroscopic Aerosols to Cloud Droplets (HygrA-CD) campaign which took place in May-June 2014.

This Thesis is structured in eight chapters. In Chapter 1, we present the structure and the diurnal variation of the PBL. Its turbulent characteristics are certainly important for the cloud development and are identified from the energy spectrum. The kinetic energy dissipation rate, defined from the turbulent kinetic energy budget is a variable which we can retrieve from a Doppler lidar in the PBL. Moreover, methods for tracking the PBL height with the use of lidar remote sensing techniques are discussed in the same chapter.

In Chapter 2, we introduce the concept of the aerosol-cloud interactions and their impact to climate change. More specifically, the relations between aerosol properties and cloud droplet activation are briefly explained and, finally, the growth mechanisms of cloud droplets' radius in warm clouds are presented.

Chapter 3 deals with the remote sensing of the atmosphere and especially of aerosols. The detailed description of the National Technical University of Athens (NTUA) lidar instrumentation (EOLE and AIAS lidars) is part of this chapter. We provide, in an analytic method, the technical characteristics of the NTUA lidar systems. Furthermore, we describe the Klett and Raman methods for deriving aerosol characteristics regarding their optical properties, based on the received lidar signals. Calibration techniques and signal processing of raw lidar data, are also provided here.

In Chapter 4, aiming to describe the interaction of light with matter, we make an introduction to the electromagnetic scattering theory and how we determine aerosols' optical properties from the scattering field. In the same chapter we also present the inversion techniques based on the aerosols optical properties, to extract information for aerosols' microphysical properties.

One of these inversion algorithms has been used within this Ph.D. Thesis and it is presented in Chapter 5. The LIdar Radiometer Inversion Code (LIRIC) algorithm combines active and passive remote sensing data and gives as output the profile of the aerosol volume concentrations for fine and coarse-mode particles. LIRIC was applied on several case studies over Athens. The results and sensitivity tests are included in Chapter 5.

The subject of Chapter 6 is the description of the research objectives of the international experimental campaign HygrA-CD. The instrumentation network involved six participants (academic institutes and research centers). The prevailing meteorological conditions over the Athens basin were studied using a cluster analysis of the air mass backtrajectories arriving over Athens. The major findings of the campaign are included in this chapter. In particular, the vertical profiles of the aerosols' optical properties (retrieved from NTUA multi-wavelength Raman lidar data) are presented and an aerosol typing scheme has been performed. The thermodynamic state of the atmosphere was explored from radio soundings and the PBL

dynamics from the wind lidar data.

Moreover, in Chapter 7, two methodologies which were developed during this Ph.D. Thesis are presented. First, a methodology aimed to link the aerosol number concentrations to cloud droplet number was developed. The algorithm uses synergistic data obtained from a multi-wavelength Raman lidar and a Doppler lidar and provides estimation of the Cloud Condensation Nuclei (CCN) spectra and the cloud droplet number. Second, a methodology aimed to quantify the vertical aerosol flux in the cloud-topped PBL, was developed. The collocated measurements from a Doppler lidar and the NTUA elastic aerosol lidar were used to estimate the aerosol turbulent flux through the eddy correlation technique. Both methodologies were applied to cases from the HygrA-CD campaign and the results are presented in Chapter 7. Finally, the conclusions and perspectives for future studies are provided in Chapter 8.

Greek Abstract

Ο βασικός στόχος της διατριβής είναι η μελέτη των επιπτώσεων των αιωρούμενων σωματιδίων στις ιδιότητες των νεφών υπό την επίδραση της τύρβης στο Ατμοσφαιρικό Οριακό Στρώμα (ΑΟΣ). Η συγκεκριμένη μελέτη κρίθηκε σημαντική καθώς υπάρχουν μεγάλες αβεβαιότητες στις προσαρμογές των νεφών λόγω της αλληλεπίδρασής τους με τα αιωρούμενα σωματίδια μέσα στο ΑΟΣ. Η επίδραση της τύρβης και των φυσικο-χημικών ιδιοτήτων των σωματιδίων στην ανάπτυξη των νεφών μελετήθηκε στο αστικό περιβάλλον της Αθήνας με χρήση των μετρήσεων που συλλέχθηκαν στην Αθήνα την περίοδο Μαΐος-Ιούνιος 2014.

Η διατριβή είναι δομημένη σε οκτώ κεφάλαια. Στο Κεφάλαιο 1 παρουσιάζονται τα χαρακτηριστικά του ΑΟΣ. Μάλιστα, τα χαρακτηριστικά της τυρβώδους κατάστασης είναι ιδιαίτερα σημαντικά για την ανάπτυξη νέφωσης και αναγνωρίζονται από το ενεργειακό φάσμα. Ο ρυθμός κατανάλωσης της τυρβώδους κινητικής ενέργειας είναι μία παράμετρος που μπορούμε να ανακτήσουμε μέσα στο ΑΟΣ με ένα Doppler lidar. Επιπλέον, σε αυτό το κεφάλαιο παρουσιάζονται διάφορες μέθοδοι για την ανίχνευση του ύψους ανάμειξης του ΑΟΣ με χρήση τηλεπισκόπησης lidar.

Στο Κεφάλαιο 2, εισάγουμε στον αναγνώστη την έννοια της αλληλεπίδρασης σωματιδίων-νεφών και την επιδρασή τους στην κλιματική αλλαγή. Συγκεκριμένα, αναφερόμαστε στις οπτικές ιδιότητες των αιωρούμενων σηματιδίων και την ενεργοποίηση αυτών σε νεφοσταγονίδια καθώς επίσης παρουσιάζουμε τους μηχανισμούς ανάπτυξης των νεφοσταγονιδίων στα θερμά νέφη.

Στο Κεφάλαιο 3 ασχολούμαστε με μεθόδους τηλεπισκόπησης της ατμόσφαιρας και ιδιαίτερα των αιωρούμενων σωματιδίων. Αναλυτικά περιγράφεται το σύστημα lidar του ΕΜΠ με τα διάφορα τεχνικά χαρακτηριστικά της διάταξής του. Επιπρόσθετα, περιγράφουμε τις μεθόδους (Klett και Raman) για την ανάκτηση των οπτικών ιδιοτήτων των αιωρούμενων σωματιδίων από σήματα lidar. Οι μέθοδοι βαθμονόμησης και επεξεργασίας σήματος lidar παρουσιάζονται, επίσης, σε αυτό το κεφάλαιο.

Με στόχο την περιγραφή της αλληλεπίδρασης ακτινοβολίας–ύλης, στο Κεφάλαιο 4 εισάγουμε τον αναγνώστη στην κλασσική θεωρία σκέδασης και στον τρόπο ανάκτησης των οπτικών ιδιοτήτων των αιωρούμενων σωματιδίων από το πεδίο σκέδασης. Στο ίδιο κεφάλαιο παρουσιάζονται μαθηματικές μέθοδοι αντιστροφής των οπτικών ιδιοτήτων των σωματιδίων με σκοπό τον προσδιορισμό των μικροφυσικών τους ιδιοτήτων. Αλγόριθμοι αντιστροφής έχουν χρησιμοποιηθεί ευρύτατα σε αυτή την διδακτορική διατριβή.

Ένας από τους αλγορίθμους αντιστροφής που χρησιμοποιήθηκε σε αυτή τη διατριβή είναι ο αλγόριθμος LIRIC που παρουσιάζεται στο Κεφάλαιο 5. Συνδυάζει όργανα ενεργητικής και παθητικής τηλεπισκόπησης προκειμένου να εξάγει πληροφορία για την καθ' ύψος ογκομετρική συγκέντρωση λεπτόκοκκων και χονδρόκοκκων σωματιδίων. Ο αλγόριθμος LIRIC εφαρμόστηκε σε διάφορα επεισόδια σωματιδιακής ρύπανσης στην Αθήνα. Τα αποτελέσματα αυτά μαζί με μελέτες ευαισθησίας συμπεριλαμβάνονται στο Κεφάλαιο 5.

Το αντικείμενο του Κεφαλαίου 6 είναι η περιγραφή των επιστημονικών στόχων του διεθνούς πειράματος HygrA-CD. Στο πείραμα συμμετείχαν έξι ελληνικοί φορείς (ακαδημαϊκά ιδρύματα και ερευνητικά κέντρα) συμβάλλοντας με τον εξοπλισμό των εργαστηρίων τους. Οι μετεωρολογικές συνθήκες που επικράτησαν στο λεκανοπέδιο των Αθηνών διερευνήθηκαν με ανάλυση κατά συστάδες των οπισθοτροχιών των αερίων μαζών. Τα πιο σημαντικά ευρύματα από το πείραμα

παρουσιάζονται σε αυτό το κεφάλαιο. Συγκεκριμένα, οι οπτικές ιδιότητες των αιωρούμενων σωματιδίων καθ' ύψος όπως ανακτήθηκαν από το σύστημα Raman lidar παρατίθενται σε αυτό το κεφάλαιο καθώς επίσης και ο χαρακτηρισμός του είδους των ανιχνευθέντων αιωρούμενων σωματιδίων. Η θερμοδυναμική κατάσταση της ατμόσφαιρας διερευνήθηκε με χρήση ραδιοβολίσεων. Τέλος, η δυναμική του ΑΟΣ μελετήθηκε με τη βοήθεια ενός συστήματος Doppler lidar, όργανο ενεργητικής τηλεπισκόπησης για την ανάκτηση των συνιστωσών της ταχύτητας του ανέμου.

Στο Κεφάλαιο 7 παρουσιάζονται οι δύο μεθοδολογίες που αναπτύχθηκαν στο πλαίσιο της παρούσας διδακτορικής διατριβής. Η πρώτη μεθοδολογία έχει στόχο να συσχετίσει τις συγκεντρώσεις των αιωρούμενων σωματιδίων με τις συγκεντρώσεις νεφοσταγονιδίων. Ο αλγόριθμος που αναπτύχθηκε χρησιμοποιεί συνεργιστικές μετρήσεις από ένα πολυκαναλικό σύστημα Raman lidar και ένα Doppler lidar με στόχο να παρέχει εκτιμήσεις του φάσματος Πυρήνων Συμπύκνωσης Νέφωσης (ΠΣΝ) και του αριθμού των νεφοσταγονιδίων. Η δεύτερη μεθοδολογία έχει ως στόχο να παρέχει την ποσοτικοποίηση της καθ' ύψος μεταφοράς μάζας αιωρούμενων σωματιδίων μέσα στο ΑΟΣ με χρήση μεθόδων τηλεπισκόπησης. Οι ταυτόχρονες μετρήσεις από το σύστημα Doppler lidar και το ελαστικό lidar σωματιδίων είναι απαραίτητες για την εκτίμηση της κατακόρυφης μεταφοράς αερολύματων μέσω της τεχνικής συσχέτισης στροβιλισμών. Και οι δύο μεθοδολογίες εφαρμόσθηκαν σε πραγματικές ατμοσφαιρικές συνθήκες κάνοντας χρήση της βάσης δεδομένων από το πείραμα HygrA-CD και παρουσιάζονται στο Κεφάλαιο 7. Τέλος, στο Κεφάλαιο 8 συνοψίζονται τα συμπεράσματα της παρούσας διδακτορικής διατριβής και διερευνώνται οι προοπτικές για μελλοντικές εργασίες.

Ακολούθως, θα εστιάσουμε στην περιληπτική παρουσίαση των βασικών Κεφαλαίων της παρούσας διδακτορικής εργασίας: τα Κεφάλαια 6, 7 και 8.

Κεφάλαιο 6: Το Πείραμα HygrA-CD

Το διεθνές πείραμα Hygroscopic Aerosols to Cloud Droplets (HygrA-CD) διεξήχθη στην Ευρύτερη Περιοχή της Αθήνας (ΕΠΑ) την περίοδο 15 Μαΐου - 22 Ιουνίου 2014. Το συγκεκριμένο πείραμα αποσκοπούσε στη μελέτη των συσχετισμών μεταξύ των αερολυμάτων και των νεφών στο ΑΟΣ και αποτέλεσε ένα από τα βασικά πειράματα που πραγματοποιήθηκαν στο πλαίσιο του προγράμματος ITaRS. Ένα αξιοσημείωτο επίτευγμα του συγκεκριμένου πειράματος ήταν η συντονισμένη προσπάθεια να ενδυναμώσει τη συνεργασία μεταξύ δύο επιστημονικών κοινοτήτων, αυτή των τηλεπισκοπικών μετρήσεων και αυτή των επιτόπιων μετρήσεων, που μελετούν την ατμόσφαιρα και τα συστατικά της. Ένα απλοποιημένο σχέδιο των βασικών φυσικών μηχανισμών που λαμβάνουν χώρα μέσα στο ΑΟΣ και συντελούν στην ανάπτυξη νέφωσης στην κορυφή του ΑΟΣ παρουσιάζεται στο Σχήμα 6.1. Τα αιωρούμενα σωματίδια μεταφέρονται κατακόρυφα μέσα στο ΑΟΣ λόγω θερμών ροών αέρα από το έδαφος προς τα ανώτερα στρώματα αέρα και ορισμένα από αυτά έχουν την ιδιότητα να λειτουργούν σαν ΠΣΝ. Σε ύψη πάνω από το σημείο του κόρου ξεκινά ο σχηματισμός νέφωσης δηλαδή η συμπύκνωση των υδρατμών πάνω στους ΠΣΝ. Στο Σχήμα 6.2 παρουσιάζονται τα όργανα και τα προγνωστικά μοντέλα που χρησιμοποιήθηκαν κατά την υλοποίηση του πειράματος.

6.1 Πειραματικοί στόχοι

Οι κυριότεροι επιστημονικοί στόχοι του πειράματος HygrA-CD ήταν οι παρακάτω: α) ο χαρακτηρισμός των αερολυμάτων ως προς τις ιδιότητές τους στο έδαφος και σε μεγαλύτερα ύψη στην κατώτερη τροπόσφαιρα, β) η ανάκτηση της αριθμητικής συγκέντρωσης αιωρούμενων σωματιδίων και η δυνατότητά τους να ενεργοποιούνται ως ΠΣΝ σε επίπεδα κορεσμού των υδρατών αντίστοιχα με αυτά των πραγματικών εξωτερικών συνθηκών για την παρουσία νέφωσης, γ) η διακύμανση των υδρατμών στην τροπόσφαιρα, δ) η μελέτη της δυναμικής στα νέφη και το περιεχόμενο υδρατμών σε σχέση με την ανάπτυξη χαμηλής νέφωσης, στ) η ανάκτηση των ιδιοτήτων νεφών που

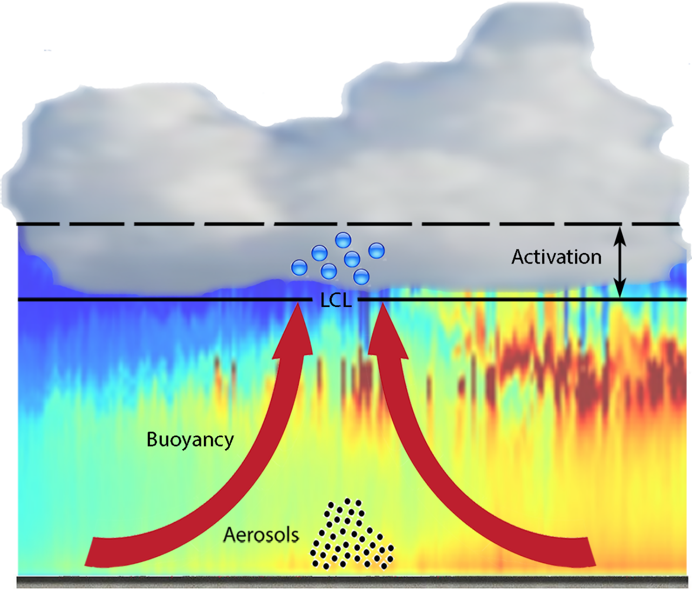

Σχήμα 6.1: *HygrA-CD: Σχηματική αναπαράσταση των φυσικών διεργασιών που εμφανίζονται στο νεφελώδες ΑΟΣ [94].*

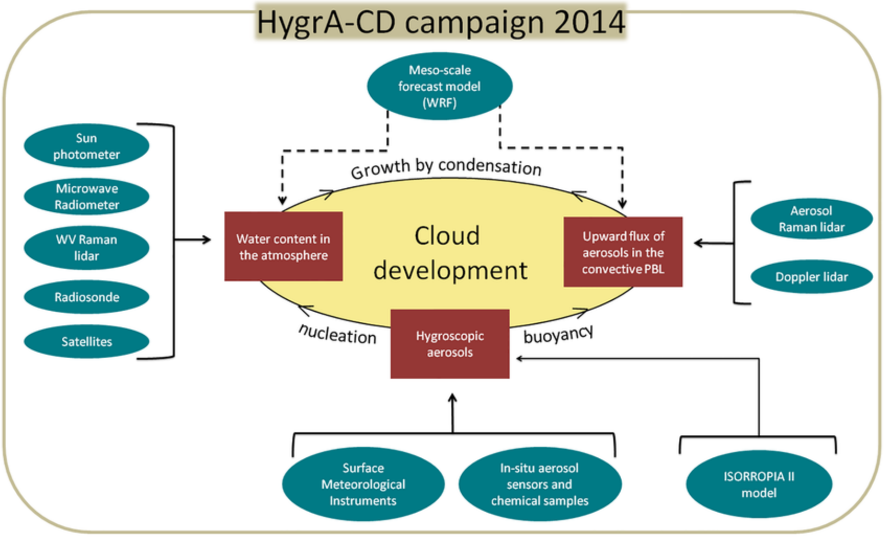

Σχήμα 6.2: *Φυσικοί μηχανισμοί που μελετήθηκαν κατά τη διάρκεια του πειράματος HygrA-CD. Η συνέργεια ανάμεσα στις επιτόπιες μετρήσεις εδάφους και τα όργανα τηλεπισκόπησης εξετάστηκε με στόχο την καλύτερη κατανόηση των φυσικών διεργασιών στο νεφελώδες ΑΟΣ. Ένα προγνωστικό μοντέλο καιρού και ένα μοντέλο αιωρούμενων σωματιδίων χρησιμοποιήθηκαν για την πρόγνωση εκείνων των ατμοσφαιρικών παραμέτρων που δεν ήταν άμεσα μετρήσιμες από τον διαθέσιμο εξοπλισμό [94].*

δεν οδηγούν σε υετό.

Γενικά, η ανάλυση των δεδομένων που συλλέχθηκαν κατά τη διάρκεια του πειράματος αυτού μας επέτρεψε να κατανοήσουμε καλύτερα το ρόλο των αιωρούμενων σωματιδίων και των μετεωρολογικών συνθηκών υπό τις οποίες σχηματίζονται νέφη κοντά στην κορυφή και πάνω από το ΑΟΣ στο αστικό περιβάλλον της Αθήνας. Συγκεκριμένα, στο πλαίσιο αυτής της διατριβής, τα θέματα τα οποία μελετήθηκαν εκτενέστερα σε βάθος είναι: α) Συνέργεια μεταξύ των επιτόπιων οργάνων στο έδαφος και των οργάνων τηλεπισκόπησης μέσα στο καλά αναμεμειγμένο ΑΟΣ [92], β) Μελέτη της δυναμικής του ΑΟΣ κάνοντας χρήση μετρήσεων από ένα σύστημα Doppler lidar και ένα Raman lidar [93, 94, 95], γ) Διερεύνηση της συσχέτισης ανάμεσα στις ιδιότητες των αιωρούμενων σωματιδίων και της ανάπτυξης νεφοσταγονιδίων σε συνάρτηση με τις επικρατούσες θερμοδυναμικές συνθήκες στην ατμόσφαιρα.

6.2 Η Ευρύτερη Περιοχή της Αθήνας

Η Ευρύτερη Περιοχή της Αθήνας (ΕΠΑ) βρίσκεται στη χερσόνησο της Αττικής (περίπου 37°58′ Β και 23°43′ Α) και φιλοξενεί 3.8 εκατομμύρια κατοίκους μέσα σε 415 km^2. Η ΕΠΑ χαρακτηρίζεται από μία πολύ πολύπλοκη τοπογραφία, όντας ανάμεσα σε τέσσερα μεγάλα βουνά: το Αιγάλεω (468 m) και την Πάρνηθα (1413 m) στα Βορειοδυτικά, την Πεντέλη (1109 m) στα Βόρεια και τον Υμηττό (1026 m) στα Ανατολικά, καθώς και με ένα μεγάλο άνοιγμα προς τη θάλασσα στο Νοτιοδυτικό κομμάτι (Σαρωνικός Κόλπος). Αυτά τα τέσσερα βουνά λειτουργούν σαν φυσικά εμπόδια, δίνοντας ένα μικρό άνοιγμα στα ΒΑ στην ξηρά προς τη θάλασσα. Αυτό το άνοιγμα είναι πολύ σημαντικό γιατί επιτρέπει στους εποχικούς κυρίως ΒΑ καλοκαιρινούς ανέμους (Μαΐος-Αύγουστος), τις ετησίες ή μελτέμια, να εισέρχονται στο Λεκανοπέδιο των Αθηνών. Μία συνοπτική περιγραφή των επικρατέστερων αέριων ροών στην ΕΠΑ δίνεται στο [96].

Το πείραμα HygrA-CD πραγματοποιήθηκε σε διάφορα σημεία στην ΕΠΑ. Συνολικά έξι ερευνητικά κέντρα και ακαδημαϊκά ιδρύματα έλαβαν μέρος στο πείραμα και φιλοξένησαν εκτός από το δικό τους εξοπλισμό όργανα από συνεργαζόμενα ερευνητικά ινστιτούτα του εξωτερικού. Το Σχήμα 6.3 παρουσιάζει τα σημεία όπου γίνονταν οι μετρήσεις. Το υψόμετρο του κάθε μετρητικού σταθμού σε σχέση με την επιφάνεια της θάλασσας δίνεται στην παρένθεση.

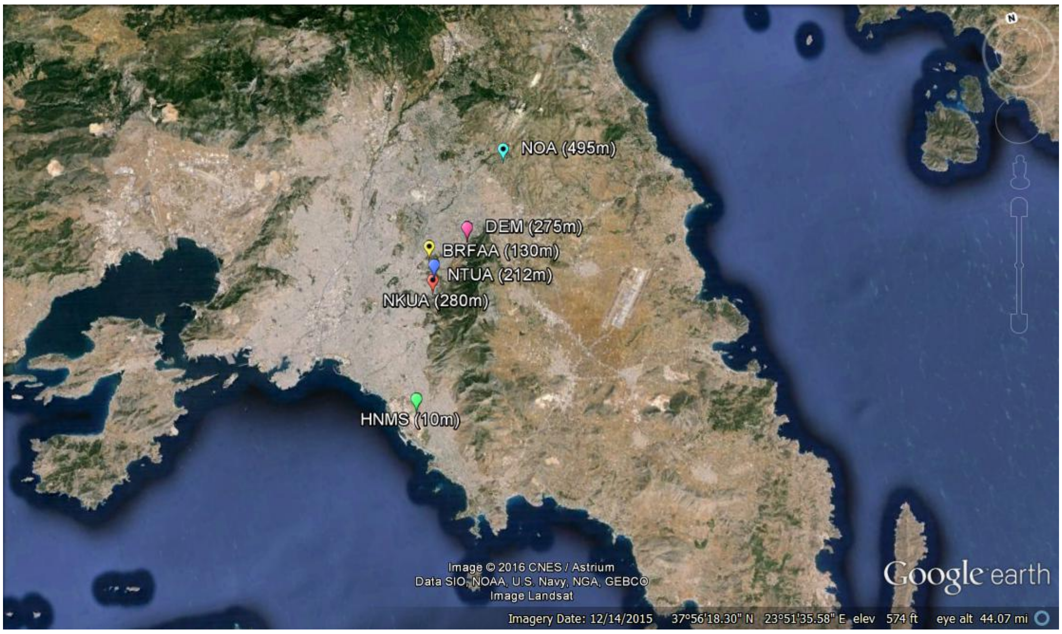

Σχήμα 6.3: *Το δίκτυο των οργάνων στο λεκανοπέδιο των Αθηνών. Οι έξι συμμετέχονται στο πείραμα φαίνονται με: (1) μπλέ σύμβολο το ΕΜΠ, (2) ροζ σύμβολο ο 'Δημόκριτος', (3) κίτρινο σύμβολο το ΙΙΒΕΑΑ, (4) κυανό σύμβολο το αστεροσκοπείο Αθηνών, (5) κόκκινο σύμβολο το ΕΚΠΑ και (6) πράσινο σύμβολο η ΕΜΥ. Οι αποστάσεις ανάμεσα στο ΕΜΠ και τα άλλα ερευνητικά ιδρύματα είναι τα ακόλουθα: ΕΜΠ από το 'ΔΗΜΟΚΡΙΤΟΣ' 4 km, ΕΜΠ από το ΙΙΒΕΑΑ 2 km, ΕΜΠ από το Αστεροσκοπείο 10 km, ΕΜΠ από το ΕΚΠΑ 1 km και ΕΜΠ από ΕΜΥ 12 km.*

6.3 Όργανα και Συνέργειες

Για να υλοποιηθούν οι επιστημονικοί στόχοι του πειράματος HygrA-CD, μία πληθώρα οργάνων (βλ. Σχήμα 6.2) λειτούργησαν στην ΕΠΑ με σκοπό να χαρακτηρισθεί ο ρόλος των αιωρούμενων σωματιδίων στην ανάπτυξη νεφοσταγονιδίων, ειδικά κοντά στην κορυφή του ΑΟΣ. Στους Πίνακες 6.1 και 6.2 παρουσιάζονται αντίστοιχα τα όργανα επιτόπιων μετρήσεων και μετρήσεων με τηλεπισκοπική μέθοδο που χρησιμοποιήθηκαν κατά τη διάρκεια του HygrA-CD. Σε αυτούς τους πίνακες, περιέχονται πληροφορίες ως προς το όνομα του οργάνου, την τοποθεσία και το χρονικό διάστημα λειτουργίας του. Για τα όργανα τηλεπισκόπησης, παρέχονται οι χρονικές και χωρικές τους διακριτικές ικανότητες ενώ για τα όργανα επιτόπιων μετρήσεων αναφέρεται μόνο η χρονική τους διακριτική ικανότητα. Τέλος, τα φυσικά μεγέθη που μπορούν να μετρηθούν από τα συγκεκριμένα όργανα εμπεριέχονται στους πίνακες.

6.4 Επικρατούσες μετεωρολογικές συνθήκες πάνω από το Λεκανοπέδιο των Αθηνών

Για να αποκτήσουμε μία γενική ιδέα ως προς την πηγή προέλευσης των αερίων μαζών που έφθασαν στην ΕΠΑ κατά τη διάρκεια του πειράματος HygrA-CD, εκτελέσαμε μία ανάλυση κατά συστάδες για τις οπισθοτροχιές των αερίων μαζών που ανιχνεύτηκαν κάνοντας χρήση του μοντέλου HYSPLIT [113]. Η μελέτη αυτή πραγματοποιήθηκε για ένα συνολικό χρόνο ζωής 96 ωρών ξεκινώντας από τις 12:00 UTC για κάθε μέρα διεξαγωγής του πειράματος. Τα ύψη άφιξης των αερίων μαζών πάνω από την Αθήνα είναι 0.5, 1, 2, 3, και 4 km. Η ανάλυση κατά συστάδες όλων των οπισθοτροχιών (στο συνολό τους 195) για όλα τα ύψη άφιξης δείχνουν την επικράτηση τριών συνοπτικών καταστάσεων, κατά 72.3% ροή από ηπειρωτικές περιοχές, κατά 14.4% ροή λόγω των Ετησίων και ροή από την έρημο Σαχάρα κατά 13.3%. Αναλυτικές πληροφορίες σχετικά με τις επικρατούσες μετεωρολογικές συνθήκες πάνω από την ΕΠΑ παρουσιάζονται στο [91].

6.5 Παρουσίαση των γενικών συμπερασμάτων

Δεδομένου ότι τα γενικά αποτελέσματα από το πείραμα HygrA-CD συνοψίζονται στο [91], στο παρόν κείμενο παρουσιάζουμε μόνο τα αποτελέσματα του πειράματος που σχετίζονται με την συγκεκριμένη εργασία. Αρχικά, ο χαρακτηρισμός των αιωρούμενων σωματιδίων ως προς τις οπτικές τους ιδιότητες επιτεύχθηκε με τη χρήση τεχνικών ενεργητικής και παθητικής τηλεπισκόπησης, δηλαδή συστήματα lidar και ηλιακά φωτόμετρα, αντίστοιχα. Η πηγή προέλευσης των ανιχνευόμενων αερολυμάτων ανιχνεύθηκε μέσω του μοντέλου HYSPLIT [114]. Επιπλέον, η θερμοδυναμική κατάσταση της ατμόσφαιρας ορίστηκε μέσω των διαγραμμάτων Skew-T LogP τα οποία παρήχθησαν βάσει των δεδομένων ραδιόλισης. Τελος, το πεδίο ανέμου (ένταση και διεύθυνση ανέμου) μέσα στο ΑΟΣ ανακτήθηκε από τις μετρήσεις με το σύστημα Doppler lidar [91].

6.6 Χαρακτηρισμός των αερολυμάτων καθ' ύψος

Το πολυκαναλικό σύστημα Raman lidar (EOLE) και το ελαστικό lidar αποπόλωσης (AIAS) χρησιμοποιήθηκαν για την ανάκτηση των οπτικών ιδιοτήτων των αιωρούμενων σωματιδίων. Ο συντελεστής οπισθοσκέδασης και εξασθένησης στα 355 nm και 532 nm ανακτήθηκε με την μέθοδο Raman [53] και ο συντελεστής οπισθοσκέδασης στο μήκος κύματος 1064 nm ανακτήθηκε με την μέθοδο Klett [51, 115]. Αυτές οι οπτικές ιδιότητες εξαρτώνται από το είδος του αερολύματος καθώς και από την συγκέντρωσή τους στα διάφορα ύψη της ατμόσφαιρας. Συχνά χαρακτηρίζουμε τα αερολύματα μέσω δύο επιπρόσθετων παραμέτρων, το λόγο lidar και τον εκθέτη Ångström οι οποίες είναι ανεξάρτητες της συγκέντρωσης των σωματιδίων στην ατμόσφαιρα. Ο λόγος lidar S_λ ορίζεται ως ο λόγος του συντελεστή εξασθένησης προς το συντελεστή οπισθοσκέδασης και αποτελεί μία ένδειξη για τη χημική σύσταση των αερολυμάτων και το μεγεθός τους. Ο εκθέτης Ångström AE εκφράζει την φασματική εξάρτηση του συντελεστή εξασθένησης και χρησιμοποιείται ως ενδεικτική παράμετρος του μεγέθους των σωματιδίων (συγκεκριμένα μικρά σωματίδια έχουν μία μεγαλύτερη εξάρτηση στο μήκος κύματος της δέσμης με την οποία αλληλεπιδρούν και συνεπώς έναν μεγαλύτερο εκθέτη Ångström).

Για 20 ημέρες κατά τη διάρκεια του πειράματος μπορέσαμε να ανακτήσουμε τις οπτικές τους ιδιότητες και τις παρουσιάζουμε στα Σχήματα 6.4-6.23. Επιπλέον, στον Πίνακα 6.3 παρουσιάζουμε συνοπτικά όλα τα ανιχνευθέντα στρώματα σωματιδίων για αυτές τις 20 ημέρες. Ο λόγος lidar στα μήκη κύματος 355 και 532 nm καθώς και ο εκθέτης Ångström ανακτήθηκαν από τις μετρήσεις με το σύστημα EOLE Raman lidar. Επιπλέον, ο συντελεστής αποπόλωσης δ_p είναι μία παράμετρος που ανακτήθηκε από μετρήσεις με το σύστημα AIAS lidar. Έγινε αναγνώριση του είδους του αερολύματος λαμβάνοντας υπόψη την πηγή προέλευσης των σωματιδίων καθως και τις παραπάνω αναφερθείσες παραμέτρους (δηλαδή S_λ, AE και δ_p) σε σύγκριση με εκείνες που αναφέρονται στην βιβλιογραφία [116, 117, 118, 119, 120, 121, 122]. Όπως φαίνεται και στα Σχήματα 6.24 και 6.25, τα παρατηρούμενα σωματίδια ταξινομήθηκαν στις κατηγορίες α) αναμεμειγμένη ερημική σκόνη Σαχάρας, β) ηπειρωτικά σωματίδια, γ) αναμεμειγμένα σωματίδια από καύση βιομάζας, δ) αναμεμειγμένα σωματίδια της Αρκτικής, ηπειρωτικά σωματίδια με σωματίδια από καύση βιομάζας, στ) αναμεμειγμένα ηπειρωτικά με θαλάσσια σωματίδια και ε) αναμεμειγμένα ηπειρωτικά σωματίδια, σωματίδια από καύση βιομάζας και ερημική σκόνη από την Ασία. Για κάθε ένα από τα τροποσφαιρικά στρώματα αιωρούμενων σωματιδίων (έως τα 5 km) που ανιχνεύθηκαν από το σύστημα lidar κατά την διάρκεια του πειράματος, εκτελέσαμε μία ανάλυση με οπισθοτροχιές 9-ημερών για την βάση, το κέντρο και την κορυφή του στρώματος προκειμένου να ορίσουμε την πηγή προέλευσης της μάζας (βλέπε Παράρτημα B). Στις περιπτώσεις ανίχνευσης σωματιδίων καπνού από το σύστημα lidar, επιβεβαιώσαμε αυτή την πληροφορία από δεδομένα του δορυφόρου MODIS [123, 124]. Τα μοντέλα DREAM [125] και WRF-Flexpart χρησιμοποιήθηκαν για να αναγνωρισθούν οι περιπτώσεις παρουσίας σκόνης από την έρημο Σαχάρα στην ΕΠΑ.

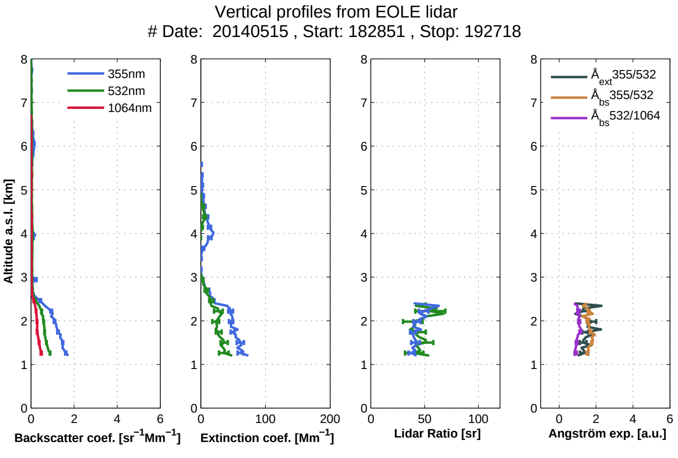

Σχήμα 6.4: *Οι οπτικές ιδιότητες των αιωρούμενων σωματιδίων καθ' ύψος (15 Μαΐου). Από αριστερά προς τα δεξιά, το πρώτο γράφημα δείχνει το συντελεστή οπισθοσκέδασης, το δεύτερο το συντελεστή εξασθένησης, το τρίτο το λόγο lidar S_λ και το τέταρτο γράφημα δείχνει τον εκθέτη Ångström AE.*

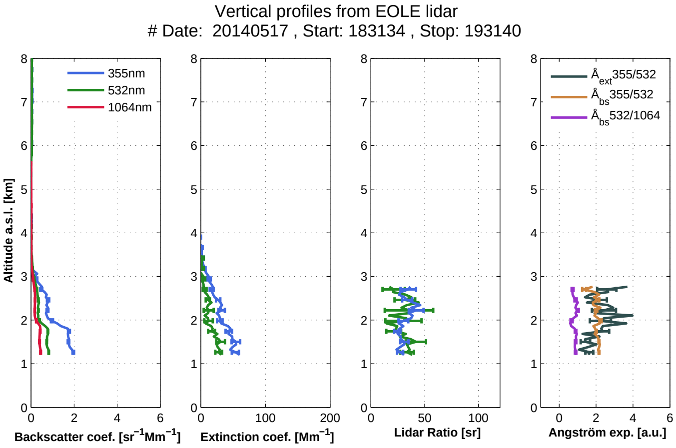

Σχήμα 6.5: *Οι οπτικές ιδιότητες των αιωρούμενων σωματιδίων καθ' ύψος (17 Μαΐου). Από αριστερά προς τα δεξιά, το πρώτο γράφημα δείχνει το συντελεστή οπισθοσκέδασης, το δεύτερο το συντελεστή εξασθένησης, το τρίτο το λόγο lidar S_λ και το τέταρτο γράφημα δείχνει τον εκθέτη Ångström AE.*

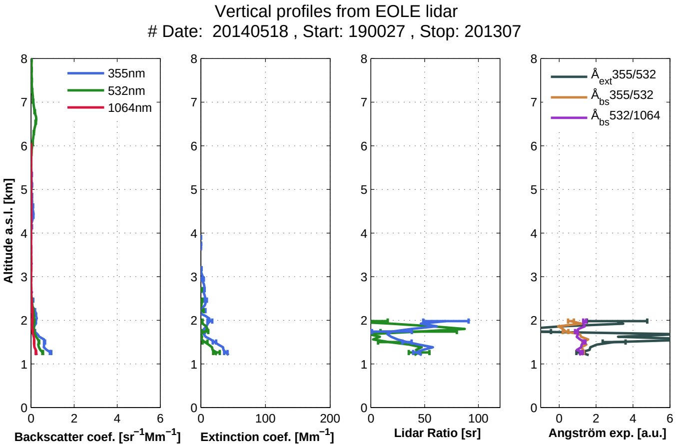

Σχήμα 6.6: *Οι οπτικές ιδιότητες των αιωρούμενων σωματιδίων καθ' ύψος (18 Μαΐου). Από αριστερά προς τα δεξιά, το πρώτο γράφημα δείχνει το συντελεστή οπισθοσκέδασης, το δεύτερο το συντελεστή εξασθένησης, το τρίτο το λόγο lidar S_λ και το τέταρτο γράφημα δείχνει τον εκθέτη Ångström AE.*

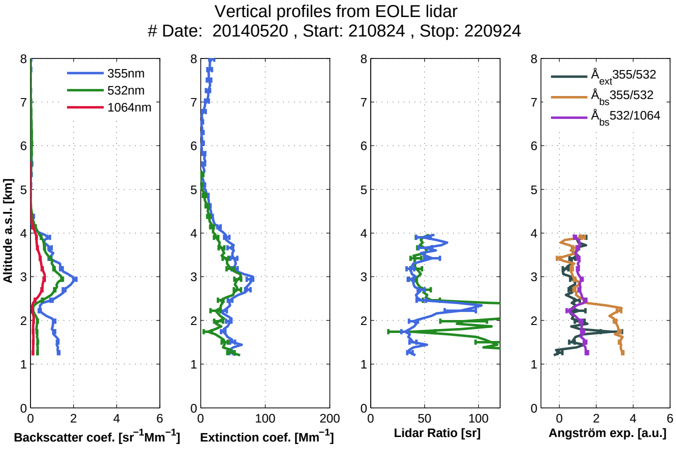

Σχήμα 6.7: *Οι οπτικές ιδιότητες των αιωρούμενων σωματιδίων καθ' ύψος (20 Μαΐου). Από αριστερά προς τα δεξιά, το πρώτο γράφημα δείχνει το συντελεστή οπισθοσκέδασης, το δεύτερο το συντελεστή εξασθένησης, το τρίτο το λόγο lidar S_λ και το τέταρτο γράφημα δείχνει τον εκθέτη Ångström AE.*

Πίνακας 6.1: *Όργανα τηλεπισκόπησης που λειτούργησαν κατά τη διάρκεια του πειράματος HygrA-CD*

Όργανο	**Ανακτούμενη παράμετρος**	**Διακριτική ικανότητα**	**Τόπος**	**Περίοδος**	**Αναφ.**
Ελαστικό lidar αποπόλωσης (AIAS)	Συντελεστής οπισθοσκέδασης, Λόγος αποπόλωσης	Χωρική: 7.5 m, Χρονική: 100 s	DEM	15.05-22.06	[1]
Raman lidar (EOLE)	Συντελεστής οπισθοσκέδασης και εξασθένησης	Χωρική: 7.5 m, Χρονική: 100 s	NTUA	15.05-22.06	[2]
Ηλιακό φωτόμετρο	Οπτικό Βάθος Αερολύματος, Ångström exponent, κατανομή σωματιδίων, ενεργός ακτίνα, ανακλαστικότητα μεμονωμένης σκέδασης	Χρονική: 15 min	BRFAA	15.05-17.06	[3], AERONET
Doppler lidar	Ένταση και διεύθυνση ανέμου, ταχύτητα Doppler, τυρβώδεις κινητική ενέργεια	Χωρική: 30 m, Χρονική: 24 s	DEM	15.05-17.06	[4]
Ραδιόμετρο μικροκυμάτων	Θερμοκρασία και Υγρασία καθ' ύψος, συνολική ποσότητα υδρατμών και νερού στη ατμοσφαιρική στήλη	Χωρική: 200 m (0-2 km), 400 m (2-5 km), 800 m (5-10 km), Χρονική: 1 s	NTUA	15.05-20.06	[5], [6], [7]
Ceilometer	Συντελεστής οπισθοσκέδασης, ύψος στρώματος ανάμειξης, βάση νέφους	Χωρική: 5 m, Χρονική: 30 s	DEM	15.05-22.06	[8]
Ραντάρ καιρού	ταχύτητα Doppler (ακτινική) και φασματικό εύρος, οριζόντια και διαφορική ανακλαστικότητα, διαφορική μετατόπιση φάσης, ρυθμός βροχόπτωσης και κατανομή μεγέθους σταγονιδίων (για σταγόνες $>$ 0.3 mm)	Χωρική οριζόντια: 120 m (24 km range), Χωρική κατακόρυφα: 12-25 m (from 0.5-12.5 km), Χρονική: 1 min	NOA	23.05-17.06	[9], [10]
Ραδιοβόλιση	Θερμοκρασία, πίεση, σχετική υγρασία, ένταση και διεύθυνση ανέμου, ύψος	Χωρική: 20 m, Χρονική: 0.4-20 s	HNMS	15.05-22.06	[11], Vaisala

Πίνακας 6.2: *Όργανα επιτόπιων μετρήσεων που λειτούργησαν κατά τη διάρκεια του πειράματος HygrA-CD*

Όργανο	**Ανακτούμενη παράμετρος**	**Χρόνος δείγματος**	**Τόπος**	**Περίοδος**	**Αναφ.**
PM_1	PM_1 συγκέντρωση μάζας	1 min	NTUA	15.05-22.06	N/A
PM_{10}	PM_{10} συγκέντρωση μάζας	1 min	NTUA	15.05-22.06	N/A
SMPS-OPC	Κατανομή μεγέθους σωματιδίων	5 min	DEM, NTUA	15.05-22.06	[12], [13]
CCN counter	αριθμητική συγκέντρωση CCN, κ-παράμετρος υπό υπερκορεσμό	10 min	DEM	18.06-22.06	[14]
Νεφελόμετρο	Συντελεστής ολικής σκέδασης και οπισθοσκέδασης σωματιδίων	1 min	DEM	15.05-22.06	[15]
Αιθαλόμετρο	Ισοδύναμη συγκέντρωση μαύρου άνθρακα	5 min	DEM	15.05-22.06	[16]
EC/OC	Συγκέντρωση στοιχειώδη και οργανικού άνθρακα	3 hours	DEM	15.05-22.06	[17], [18]
Ιοντική χρωματογραφία	Υδατοδιαλυτά ιόντα σε δείγματα αερολύματος	3-5 hours	NTUA	21.05-07.06	[19]
Μετεωρολογικός σταθμός	Θερμοκρασία, πίεση, σχετική υγρασία, ένταση και διεύθυνση ανέμου	10 min	NTUA, NOA, HNMS	15.05-22.06	N/A

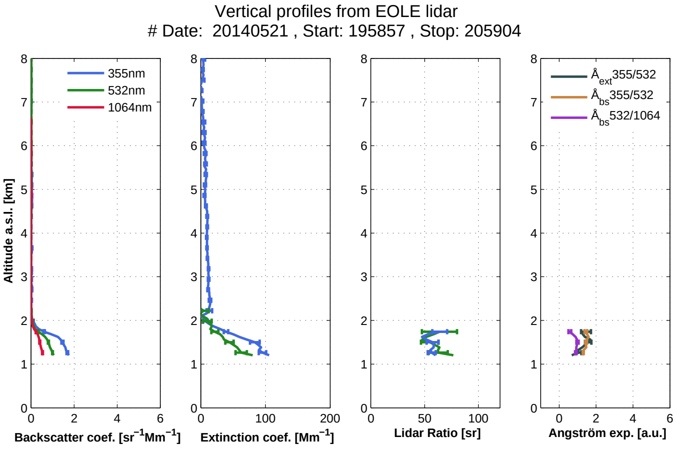

Σχήμα 6.8: *Οι οπτικές ιδιότητες των αιωρούμενων σωματιδίων καθ' ύψος (21 Μαΐου). Από αριστερά προς τα δεξιά, το πρώτο γράφημα δείχνει το συντελεστή οπισθοσκέδασης, το δεύτερο το συντελεστή εξασθένησης, το τρίτο το λόγο lidar* S_λ *και το τέταρτο γράφημα δείχνει τον εκθέτη Ångström AE.*

Πίνακας 6.3: *Οπτικές ιδιότητες των σωματιδίων από την βάση δεδομένων του HygrA-CD. Η πρώτη στήλη αναφέρεται στις ημερομηνίες εκείνες όπου επεξεργάστηκαν τα νυχτερινά σήματα lidar με τη μέθοδο Raman. Το OBA στα μήκη κύματος 355 και 532 nm δίνονται στην δεύτερη στήλη. Η τρίτη στήλη περιέχει τη βάση και την κορυφή των ατμοσφαιρικών στρωμάτων που ανιχνεύθηκαν. Η τέταρτη και πέμπτη στήλη αναφέρεται στον λόγο lidar* S_λ *και AE των σωματιδίων αντίστοιχα. Τέλος, η έκτη στήλη παρέχει πληροφορίες σχετικά με τον λόγο αποπόλωσης σωματιδίων από το AIAS lidar. Το AIAS λειτουργούσε μόνο κατά τη διάρκεια της μέρας και επομένως τα ανιχνευθέντα στρώματα σωματιδίων τη νύχτα ίσως διαφέρουν κυρίως μέσα στο ΑΟΣ.*

Ημ/νία [ηη/μμ]	**OBA**		**Στρώμα [km]**	S_λ [sr]		**Ångström Exponent (AE)**	δ_p [%]
	355nm	**532nm**		**355nm**	**532nm**		
15/05	0.06	0.04	1.2-2.0	41±2	44±5	1.5±0.3	1.1±0.9
			2.0-2.4	50±8	54±9	1.3±0.5	-
17/05	0.09	0.08	1.2-1.8	28±3	34±6	1.7±0.4	1.4±0.2
			2.0-2.5	37±5	33±7	2.4±0.7	1.2±0.3
18/05	0.03	0.02	1.2-1.5	46±8	38±11	1.9±0.6	2.3±0.1
20/05	0.20	0.16	2.5-3.2	41±3	47±5	0.6±0.2	28.4±2.6
			3.4-4.0	61±8	48±4	1.0±0.2	-
21/05	0.05	0.03	1.2-1.7	56±5	60±8	1.3±0.3	2.3±0.2
22/05	0.10	0.07	1.2-1.5	40±8	46±3	0.8±0.6	4.7±0.2
			1.6-2.0	40±3	38±6	1.3±0.3	6.9±0.6
23/05	0.28	0.24	1.3-2.8	35±3	43±5	1.5±0.4	14.0±2.5
26/05	0.28	0.24	3.0-4.0	53±9	44±5	0.5±0.3	-
27/05	0.13	0.08	1.2-2.0	35±3	40±6	1.3±0.3	25.1±3.7
			2.0-2.5	44±9	51±16	1.1±0.4	28.1±3.1
01/06	0.1	0.08	1.2-2.5	40±5	46±10	2.0±0.6	6.3±0.1
07/06	0.27	0.19	1.2-1.7	39±3	45±7	1.6±0.3	4.8±1.2
			2.5-3.2	51±5	47±5	2.0±0.3	2.9±0.5
10/06	0.19	0.11	1.2-2.1	59±4	58±8	1.3±0.4	6.4±0.7
11/06	0.22	0.12	1.2-2.1	59±4	55±9	1.2±0.4	2.0±0.1
			2.1-3.0	62±3	54±5	1.4±0.2	0.9±0.4
12/06	0.13	0.08	1.2-2.0	56±4	55±14	2.0±0.5	8.9±0.4
			2.1-2.8	73±8	76±7	1.4±0.1	11.3±1.7
14/06	0.34	0.19	1.3-1.7	37±3	41±7	2.2±0.4	5.7±0.1
			2.3-2.9	55±9	60±8	1.9±0.2	6.8±0.8
15/06	0.22	0.16	1.7-3.2	70±12	67±11	1.9±0.2	-
16/06	0.26	0.19	1.3-2.7	46±8	40±8	2.3±0.4	7.1±1.4
17/06	0.38	0.33	4.0-4.8	40±4	42±8	0.1±0.3	24.9±6.0
18/06	0.42	0.41	2.5-3.5	44±4	46±5	0.1±0.1	19.0±2.0
22/06	0.33	0.21	1.2-2.5	40±5	44±8	2.0±0.4	1.8±0.5

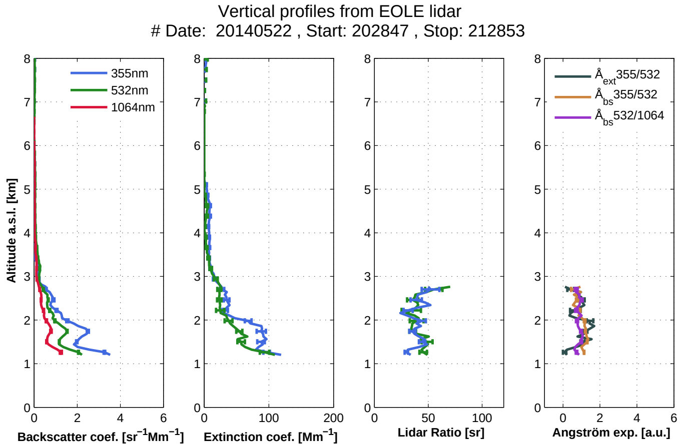

Σχήμα 6.9: *Οι οπτικές ιδιότητες των αιωρούμενων σωματιδίων καθ' ύψος (22 Μαΐου). Από αριστερά προς τα δεξιά, το πρώτο γράφημα δείχνει το συντελεστή οπισθοσκέδασης, το δεύτερο το συντελεστή εξασθένησης, το τρίτο το λόγο lidar* S_λ *και το τέταρτο γράφημα δείχνει τον εκθέτη Ångström AE.*

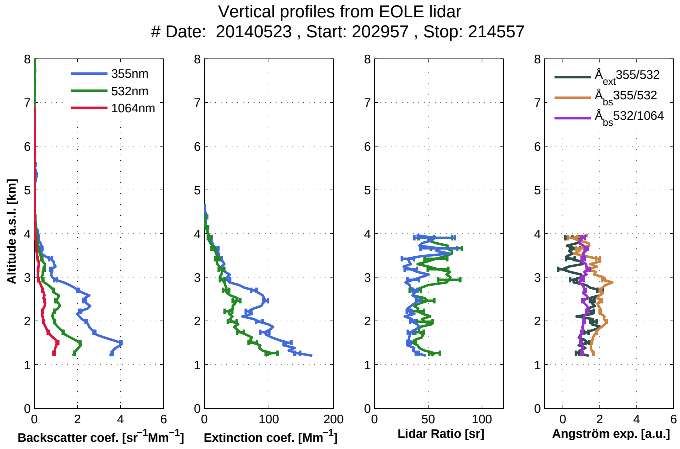

Σχήμα 6.10: *Οι οπτικές ιδιότητες των αιωρούμενων σωματιδίων καθ' ύψος (23 Μαΐου). Από αριστερά προς τα δεξιά, το πρώτο γράφημα δείχνει το συντελεστή οπισθοσκέδασης, το δεύτερο το συντελεστή εξασθένησης, το τρίτο το λόγο lidar* S_λ *και το τέταρτο γράφημα δείχνει τον εκθέτη Ångström AE.*

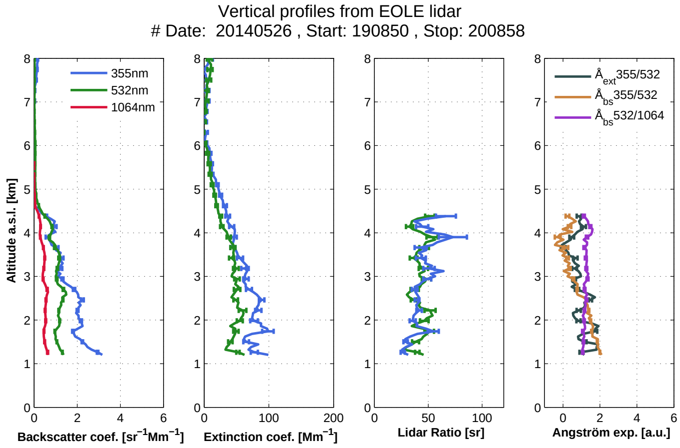

Σχήμα 6.11: *Οι οπτικές ιδιότητες των αιωρούμενων σωματιδίων καθ' ύψος (26 Μαΐου). Από αριστερά προς τα δεξιά, το πρώτο γράφημα δείχνει το συντελεστή οπισθοσκέδασης, το δεύτερο το συντελεστή εξασθένησης, το τρίτο το λόγο lidar* S_λ *και το τέταρτο γράφημα δείχνει τον εκθέτη Ångström AE.*

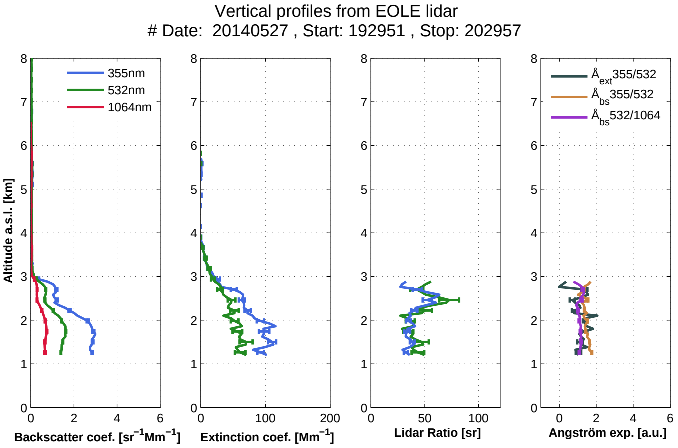

Σχήμα 6.12: *Οι οπτικές ιδιότητες των αιωρούμενων σωματιδίων καθ' ύψος (27 Μαΐου). Από αριστερά προς τα δεξιά, το πρώτο γράφημα δείχνει το συντελεστή οπισθοσκέδασης, το δεύτερο το συντελεστή εξασθένησης, το τρίτο το λόγο lidar S_λ και το τέταρτο γράφημα δείχνει τον εκθέτη Ångström AE.*

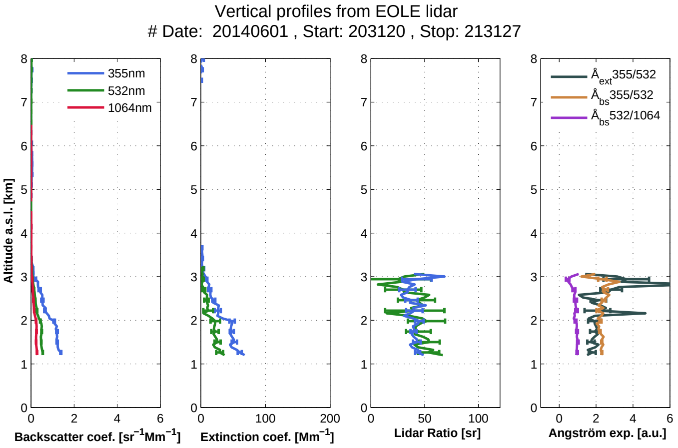

Σχήμα 6.13: *Οι οπτικές ιδιότητες των αιωρούμενων σωματιδίων καθ' ύψος (1 Ιουνίου). Από αριστερά προς τα δεξιά, το πρώτο γράφημα δείχνει το συντελεστή οπισθοσκέδασης, το δεύτερο το συντελεστή εξασθένησης, το τρίτο το λόγο lidar S_λ και το τέταρτο γράφημα δείχνει τον εκθέτη Ångström AE.*

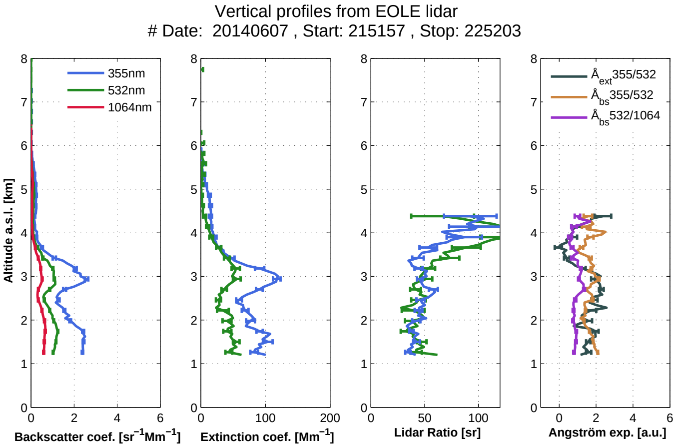

Σχήμα 6.14: *Οι οπτικές ιδιότητες των αιωρούμενων σωματιδίων καθ'ύψος (7 Ιουνίου). Από αριστερά προς τα δεξιά, το πρώτο γράφημα δείχνει το συντελεστή οπισθοσκέδασης, το δεύτερο το συντελεστή εξασθένησης, το τρίτο το λόγο lidar S_λ και το τέταρτο γράφημα δείχνει τον εκθέτη Ångström AE.*

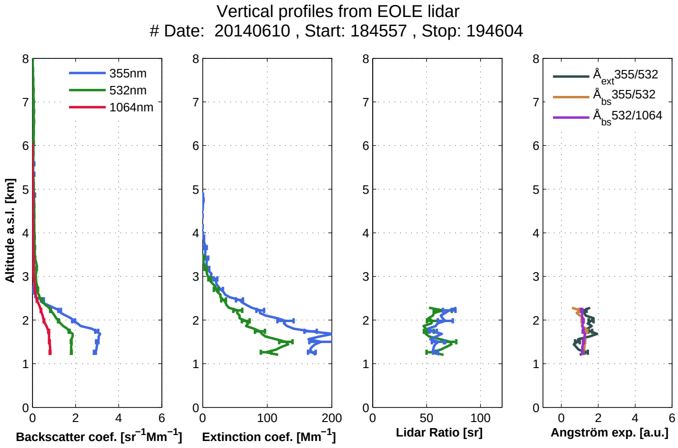

Σχήμα 6.15: *Οι οπτικές ιδιότητες των αιωρούμενων σωματιδίων καθ' ύψος (10 Ιουνίου). Από αριστερά προς τα δεξιά, το πρώτο γράφημα δείχνει το συντελεστή οπισθοσκέδασης, το δεύτερο το συντελεστή εξασθένησης, το τρίτο το λόγο lidar S_λ και το τέταρτο γράφημα δείχνει τον εκθέτη Ångström AE.*

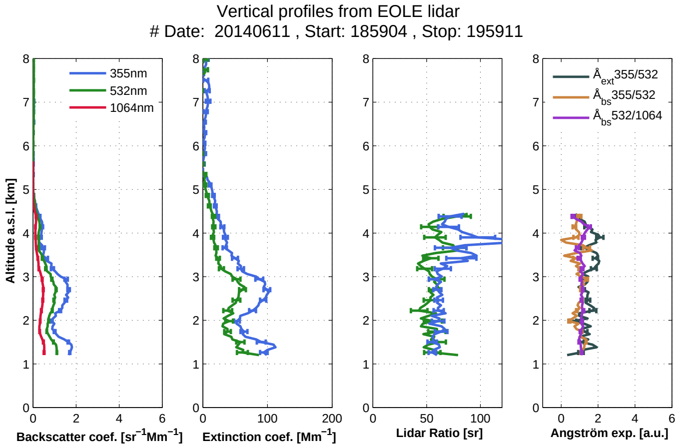

Σχήμα 6.16: *Οι οπτικές ιδιότητες των αιωρούμενων σωματιδίων καθ' ύψος (11 Ιουνίου). Από αριστερά προς τα δεξιά, το πρώτο γράφημα δείχνει το συντελεστή οπισθοσκέδασης, το δεύτερο το συντελεστή εξασθένησης, το τρίτο το λόγο lidar S_λ και το τέταρτο γράφημα δείχνει τον εκθέτη Ångström AE.*

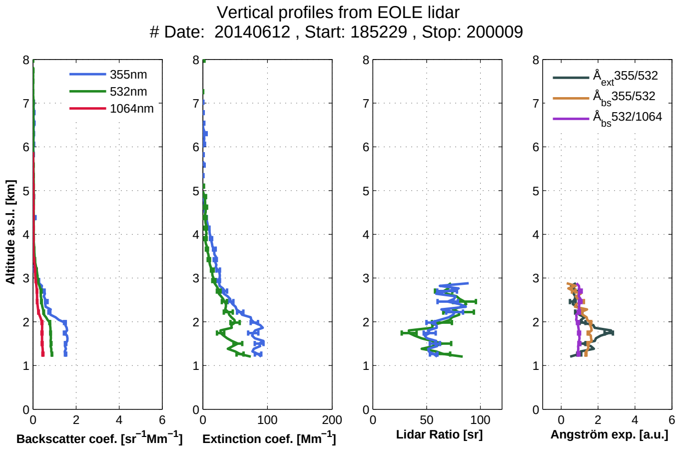

Σχήμα 6.17: *Οι οπτικές ιδιότητες των αιωρούμενων σωματιδίων καθ' ύψος (12 Ιουνίου). Από αριστερά προς τα δεξιά, το πρώτο γράφημα δείχνει το συντελεστή οπισθοσκέδασης, το δεύτερο το συντελεστή εξασθένησης, το τρίτο το λόγο lidar S_λ και το τέταρτο γράφημα δείχνει τον εκθέτη Ångström AE.*

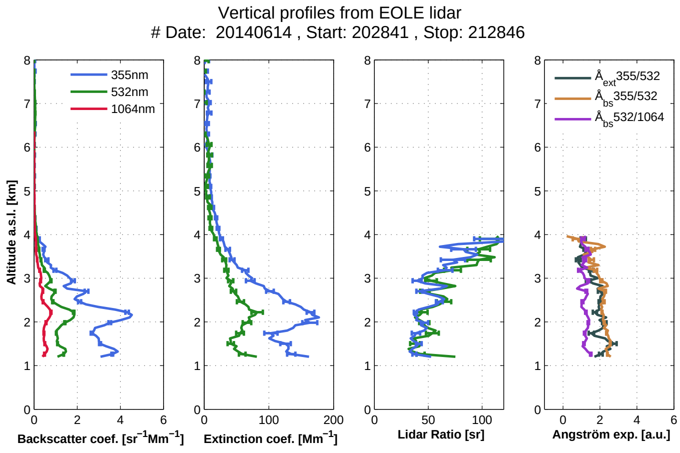

Σχήμα 6.18: *Οι οπτικές ιδιότητες των αιωρούμενων σωματιδίων καθ' ύψος (14 Ιουνίου). Από αριστερά προς τα δεξιά, το πρώτο γράφημα δείχνει το συντελεστή οπισθοσκέδασης, το δεύτερο το συντελεστή εξασθένησης, το τρίτο το λόγο lidar S_λ και το τέταρτο γράφημα δείχνει τον εκθέτη Ångström AE.*

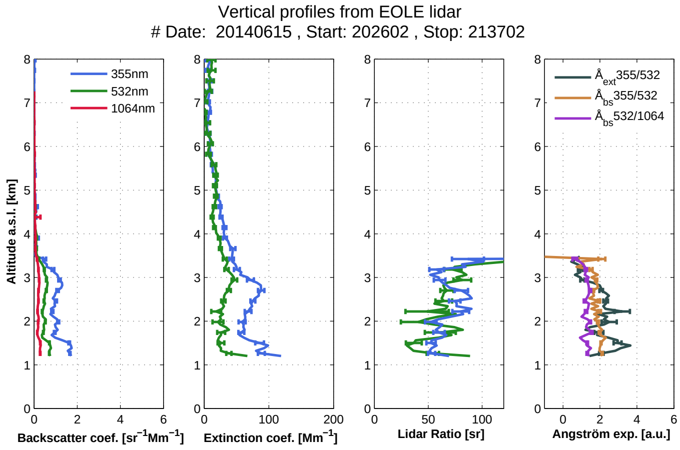

Σχήμα 6.19: *Οι οπτικές ιδιότητες των αιωρούμενων σωματιδίων καθ' ύψος (15 Ιουνίου). Από αριστερά προς τα δεξιά, το πρώτο γράφημα δείχνει το συντελεστή οπισθοσκέδασης, το δεύτερο το συντελεστή εξασθένησης, το τρίτο το λόγο lidar S_λ και το τέταρτο γράφημα δείχνει τον εκθέτη Ångström AE.*

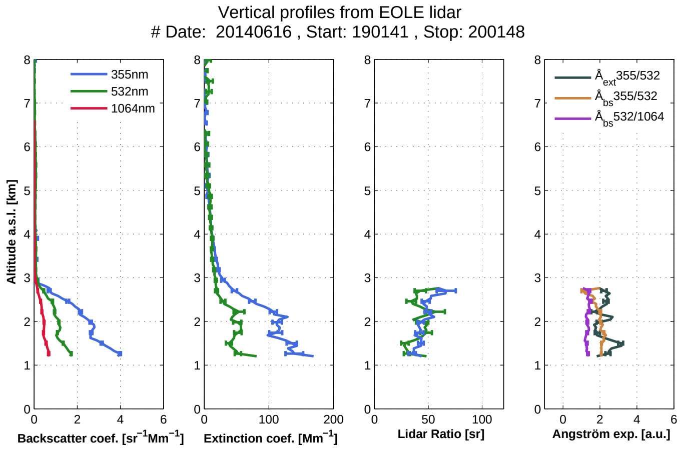

Σχήμα 6.20: *Οι οπτικές ιδιότητες των αιωρούμενων σωματιδίων καθ' ύψος (16 Ιουνίου). Από αριστερά προς τα δεξιά, το πρώτο γράφημα δείχνει το συντελεστή οπισθοσκέδασης, το δεύτερο το συντελεστή εξασθένησης, το τρίτο το λόγο lidar S_λ και το τέταρτο γράφημα δείχνει τον εκθέτη Ångström AE.*

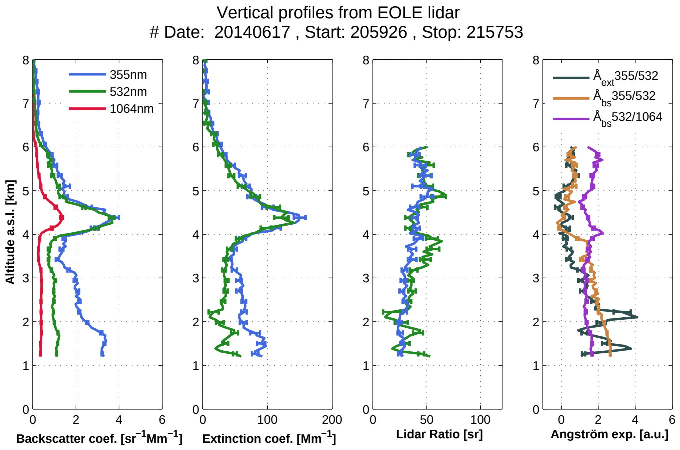

Σχήμα 6.21: *Οι οπτικές ιδιότητες των αιωρούμενων σωματιδίων καθ΄ ύψος (17 Ιουνίου). Από αριστερά προς τα δεξιά, το πρώτο γράφημα δείχνει το συντελεστή οπισθοσκέδασης, το δεύτερο το συντελεστή εξασθένησης, το τρίτο το λόγο lidar S_λ και το τέταρτο γράφημα δείχνει τον εκθέτη Ångström AE.*

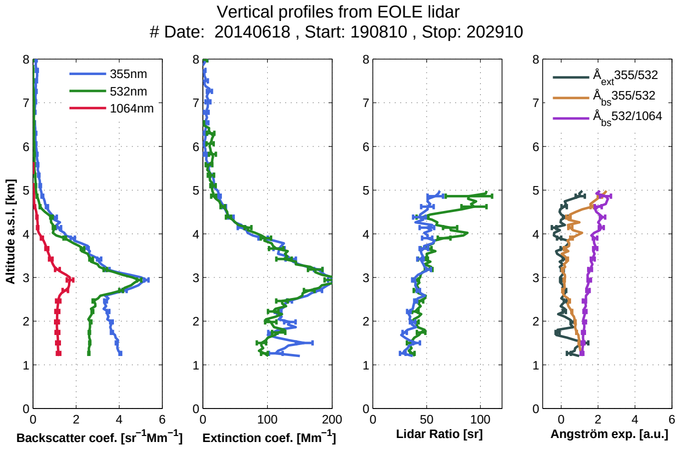

Σχήμα 6.22: *Οι οπτικές ιδιότητες των αιωρούμενων σωματιδίων καθ΄ύψος (18 Ιουνίου). Από αριστερά προς τα δεξιά, το πρώτο γράφημα δείχνει το συντελεστή οπισθοσκέδασης, το δεύτερο το συντελεστή εξασθένησης, το τρίτο το λόγο lidar S_λ και το τέταρτο γράφημα δείχνει τον εκθέτη Ångström AE.*

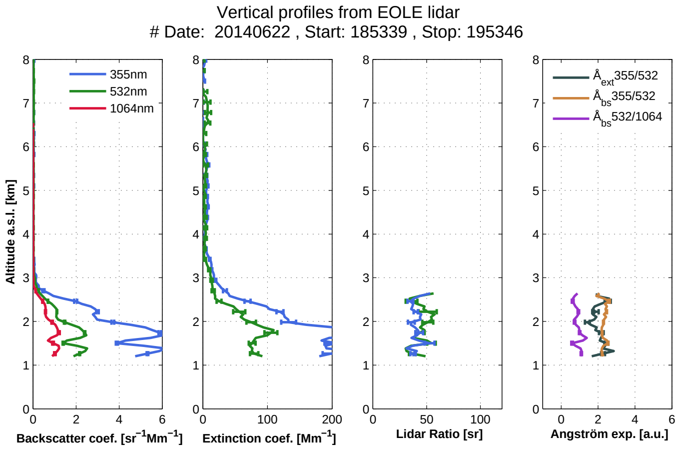

Σχήμα 6.23: *Οι οπτικές ιδιότητες των αιωρούμενων σωματιδίων καθ΄ ύψος (22 Ιουνίου). Από αριστερά προς τα δεξιά, το πρώτο γράφημα δείχνει το συντελεστή οπισθοσκέδασης, το δεύτερο το συντελεστή εξασθένησης, το τρίτο το λόγο lidar S_λ και το τέταρτο γράφημα δείχνει τον εκθέτη Ångström AE.*

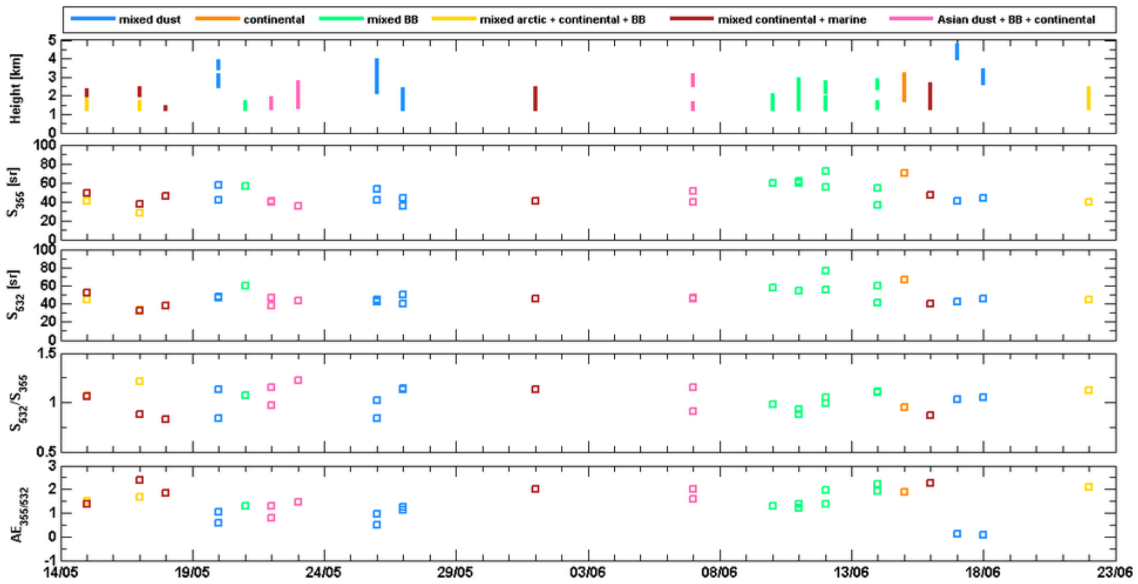

Σχήμα 6.24: *Οι οπτικές ιδιότητες* S_λ *και AE των ανιχνευθέντων σωματιδίων για όλη την διάρκεια του πειράματος από το EOLE Raman lidar.*

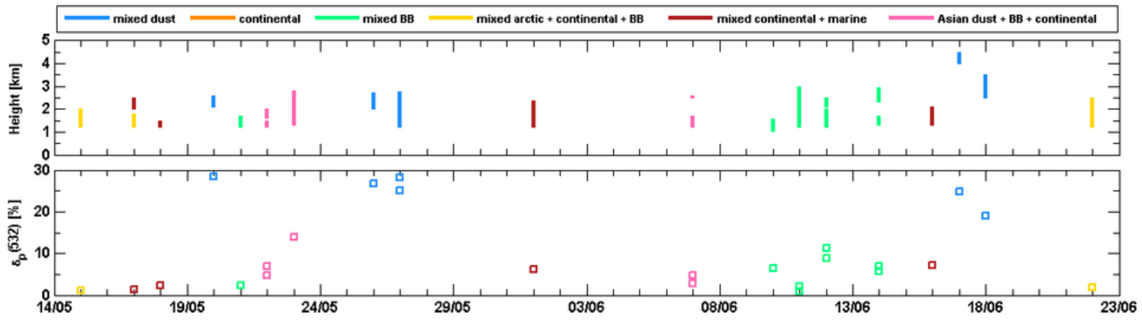

Σχήμα 6.25: *Ο λόγος αποπόλωσης σωματιδίων στα 532 nm παρουσιάζεται για όλα να ανιχνευθέντα σωματίδια κατά τη διάρκεια του πειράματος από το AIAS lidar.*

Επιπλέον, ειδικά η παράμετρος του λόγου lidar είναι πολύ σημαντική στην κατηγοριοποίηση της αέριας μάζας. Τα Σχήματα 6.26 και 6.27 παρουσιάζουν τα ιστογράμματα των παρατηρούμενων τιμών του λόγου lidar μέσα στο ΑΟΣ και στην Ελεύθερη Τροπόσφαιρα (ΕΤ) στα μήκη κύματος 355 και 532 nm, αντίστοιχα. Η πιο συχνά παρατηρούμενη τιμή για το λόγο lidar είναι 40-45 sr που είναι τυπική για μίξη ηπειρωτικών σωματιδίων με θαλάσσια σωματίδια. Αντίστοιχες τιμές του λόγου lidar παρατηρούνται όταν σκόνη μεταφέρεται από την Αφρική, όμως συνήθως ανιχνεύεται σε μεγαλύτερα ύψη στην ΕΤ και όχι μέσα στο ΑΟΣ. Το συμπέρασμα ότι ανιχνεύθηκε μίξη ηπειρωτικών με θαλάσσια σωματίδια ενισχύεται από τα ιστογράμματα του εκθέτη Ångström και του λόγου αποπόλωσης στα Σχήματα 6.28 και 6.29, όπου διαπιστώνεται η ύπαρξη μικρών και σφαιρικών σωματιδίων μέσα στο ΑΟΣ τα οποία χαρακτηρίζονται από έναν εκθέτη Ångström μεγαλύτερο από 1.2 και ένα δ_p μικρότερο από 5%.

Από την ολοκλήρωση του συντελεστή εξασθένησης σε ολόκληρη την ατμοσφαιρική στήλη μπορούμε να ανακτήσουμε το Οπτικό Βάθος των Αερολυμάτων (ΟΒΑ). Τα ΟΒΑ στα μήκη κύματος 355 και 532 nm του Σχήματος 6.30 είναι χαρακτηριστικά του ατμοσφαιρικού φορτίου στην ατμόσφαιρα κατά τη διάρκεια της νύχτας. Η σύγκριση ανάμεσα στα ΟΒΑ όπως ανακτήθηκαν από το σύστημα lidar και τα ΟΒΑ κατά τη διάρκεια της ημέρας που μετρήθηκαν από το ηλιακό φωτόμετρο CIMEL παρατίθενται στο Σχήμα 6.31. Οι μετρήσεις καταδεικνύουν ένα αυξημένο ΟΒΑ όταν υπάρχει παρουσία ερημικής σκόνης. Τις ημέρες όπου υπάρχει παρουσία σκόνης και συνεπώς υψηλό ΟΒΑ δεν παρατηρήθηκε η ανάπτυξη νέφωσης, επομένως το ΟΒΑ δεν μπορεί να χρησιμοποιηθεί σαν αντιπροσωπευτική παράμετρος για τη μελέτη της ενεργοποίησης των νεφοσταγονιδίων. Το ερώτημα που τίθεται είναι κατα πόσο η μη ενεργοποίηση των ΠΣΝ συνδέεται με τα αιωρούμενα σωματίδια (δηλαδή την ερημική σκόνη) και όχι με την θερμοδυναμική κατάσταση της ατμόσφαιρας. Η απάντηση δίνεται εάν χαρακτηρίσουμε θερμοδυναμικά την ατμόσφαιρα σε περιπτώσεις όπου οι αέριες μάζες που φθάνουν στην ΕΠΑ είναι από Δ-ΝΔ διευθύνσεις.

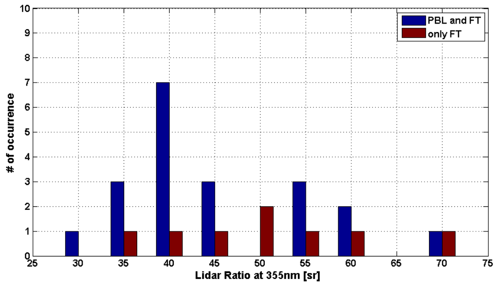

Σχήμα 6.26: *Ιστόγραμμα για το λόγο lidar στα 355 nm.*

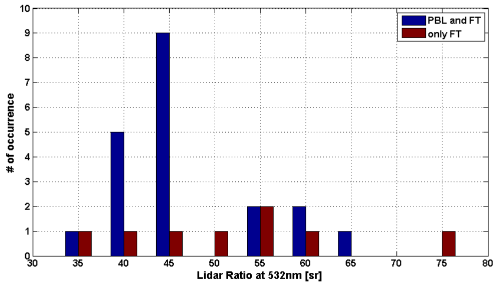

Σχήμα 6.27: *Ιστόγραμμα για το λόγο lidar στα 532 nm.*

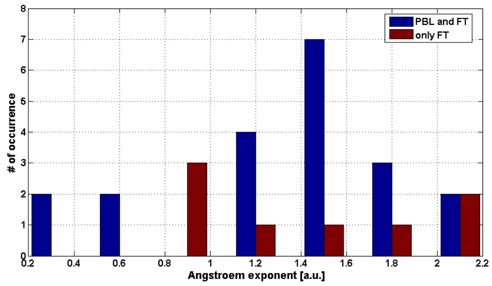

Σχήμα 6.28: *Ιστόγραμμα για το εκθέτη Ångström* $AE_{355/532}$.

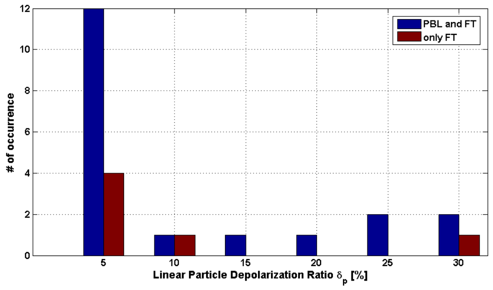

Σχήμα 6.29: *Ιστόγραμμα για το λόγο αποπόλωσης στα 532 nm.*

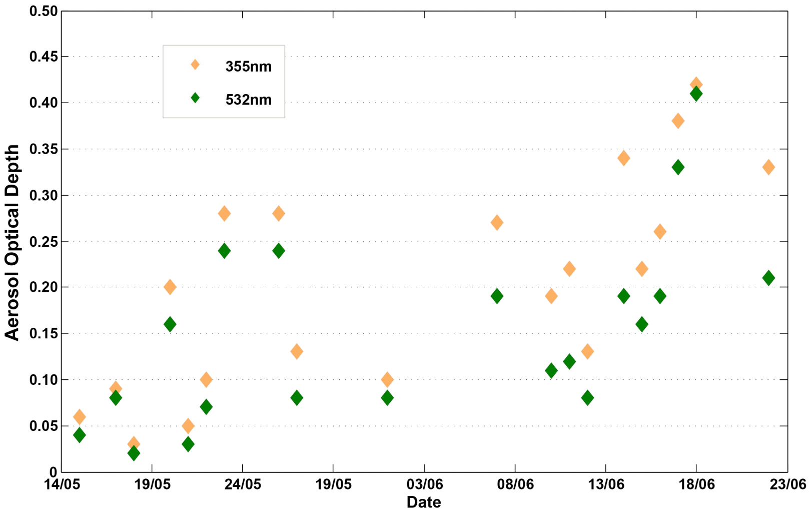

Σχήμα 6.30: *Μέσο ημερήσιο ΟΒΑ στα 355 και 532 nm, όπως μετρήθηκε από το σύστημα EOLE.*

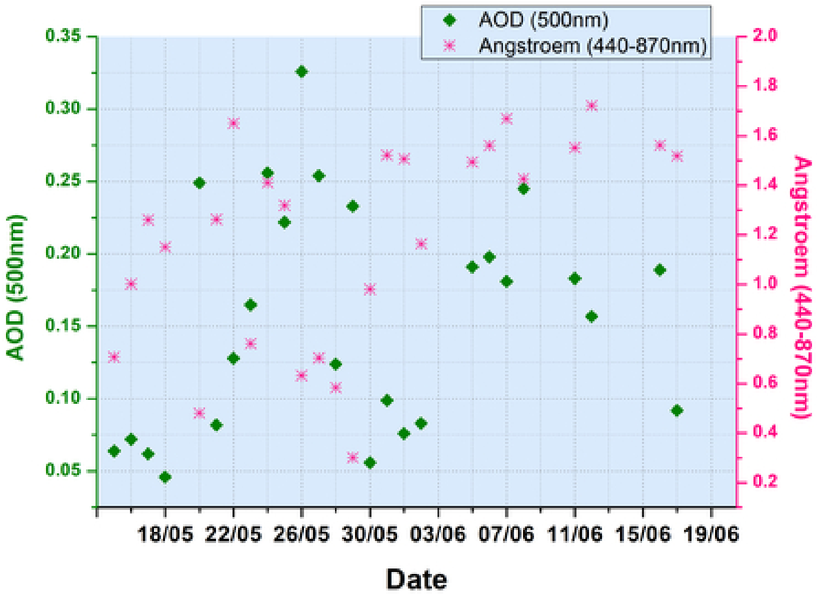

Σχήμα 6.31: *Μέσο ημερήσιο ΟΒΑ στα 500 nm και ο συντελεστής Ångström* $AE_{440/870}$*, όπως μετρήθηκε από το ηλιακό φωτόμετρο.*

6.7 Η θερμοδυναμική κατάσταση της ατμόσφαιρα

Η ατμόσφαιρα μπορεί να χαρακτηριστεί θερμοδυναμικά όταν υπάρχουν διαθέσιμες ραδιοβολίσεις στην περιοχή που μελετάται. Ο χαρακτηρισμός της γίνεται μέσω των διαγραμμάτων Skew-T Log-P και την κατακόρυφη πληροφορία ως προς τη θερμοκρασία δρόσου, το λόγο αναλογίας υδρατμών και την ενθαλπία [126]. Η βασική πληροφορία που χρειαζόμαστε είναι ο καθορισμός του ύψους όπου μπορεί να ξεκινήσει η συμπύκνωση υδρατμών. Οποιαδήποτε ανοδική κίνηση αέρα πάνω από το ύψος αυτό, θα οδηγήσει σε αλλαγή φάσης του νερού (από την αέρια φάση στην υγρή) και η ανερχόμενη αέρια μάζα θα συμπεριφέρεται σαν ψευδο-αδιαβατικό σύστημα που απελευθερώνει λανθάνουσα θερμότητα στο περιβάλλον. Επομένως, όταν η νέφωση ξεκινά να σχηματίζεται, σε εκείνο το ύψος παρατηρούμε μία απότομη αρνητική βαθμίδα στο λόγο αναλογίας των υδρατμών και στην ενθαλπία του συστήματος. Δεδομένου ότι οι ραδιοβολίσεις δεν ήταν διαθέσιμες κάθε μέρα, ο σχολιασμός αφορά μόνο τις διαθέσιμες ημερομηνίες που εμπεριέχονται στον Πίνακα 6.4. Η περίπτωση της 22 Μαΐου αποτελεί ένα τυπικό παράδειγμα ανάπτυξης νέφωσης. Το ύψος συμπύκνωσης των υδρατμών εντοπίστηκε στα 1660 m (∼ 840 hPa) (βλέπε Σχήμα 6.32) και η νέφωση δημιουργήθηκε στο ύψος των 1900 m όπως φαίνεται στο Σχήμα 6.33. Εκείνη την ημέρα, το οριακό στρώμα ήταν πλούσιο σε υδρατμούς σε ένα σχεδόν ομογενώς αναμεμειγμένο ΑΟΣ με λόγο ανάμειξης υδρατμών προς ξηρό αέρα ίσο με 8 g/kg. Παρόμοιες θερμοδυναμικές συνθήκες εμφανίζονται στην περίπτωση της 11ης Ιουνίου όπου ο μέσος λόγος ανάμειξης υδρατμών προς ξηρό αέρα (∼ 9 g/kg) ήταν σταθερός από το έδαφος έως το ύψος συμπύκνωσης υδρατμών στα 2000 m (βλέπε Σχήμα 6.34). Και τις δύο αυτές ημέρες, οι αέριες μάζες που έφθασαν πάνω από την ΕΠΑ προέρχονταν από Β-ΒΑ διευθύνσεις ανέμου και χαρακτηρίζονταν από ένα ΟΒΑ στα 500 nm μεγαλύτερο από 0.1 και εκθέτη Ångström μεγαλύτερο από 1.6-1.7 (Σχήμα 6.31). Επομένως, αυτές οι αέριες μάζες περιλάμβαναν μέτριο προς υψηλό σωματιδιακό φόρτο με μικρά σωματίδια. Μία άλλη ενδιαφέρουσα περίπτωση ανάπτυξης νέφωσης παρατηρήθηκε στις 30 Μαΐου με χαμηλό σωματιδιακό φόρτο και μεγάλα σωματίδια (ΟΒΑ(500 nm)∼0.05 και AE<1). Σε αυτή την περίπτωση, η ανερχόμενη αέρια μάζα φθάνει στο σημείο κόρου σε ένα χαμηλό ύψος στα 1050 m. Σε κάθε περίπτωση, η σημαντική παράμετρος για την δημιουργία νέφωσης κρίνεται ο δείκτης CAPE όπου εκείνη την ημέρα ήταν πολύ υψηλός (∼2300 J/kg).

Πίνακας 6.4: *Θερμοδυναμικές παράμετροι από ραδιοβολίσεις*

Ημ/νία [ηη/μμ]	**Ύψος συμπύκνωσης υδρατμών [m]**	**Θερμοκρασία [C]**	**CAPE [J/kg]**
21/05	2000	7	4
22/05	1660	11	668
23/05	1390	12	0
27/05	1410	14	0
30/05	1050	15	2295
02/06	1500	9	0
05/06	1090	15	0
08/06	1990	9	863
11/06	1360	15	863

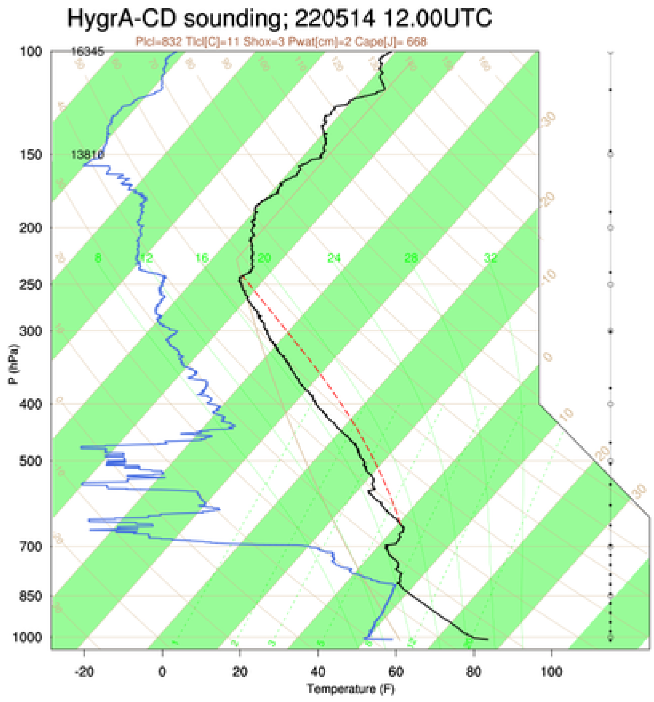

Σχήμα 6.32: *SkewT-logP διάγραμμα (22 Μαΐου 2014, 12:00 UTC)*

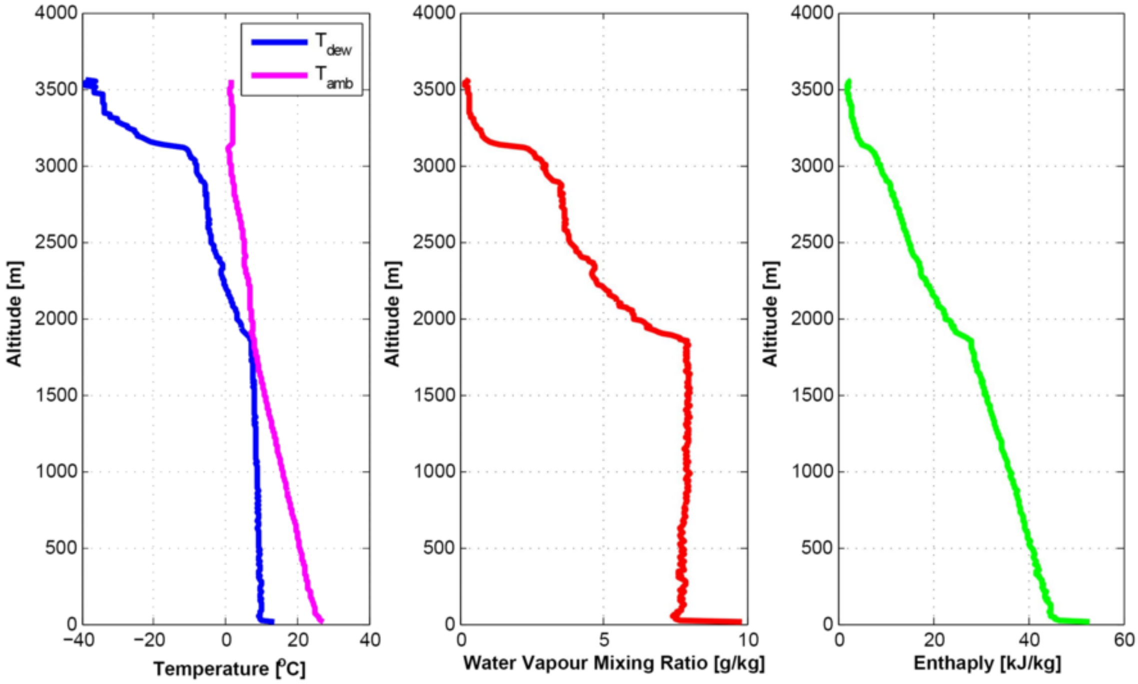

Σχήμα 6.33: *Ραδιοβόλιση στις 22 Μαΐου 2014, 12:00 UTC. Το αριστερό γράφημα δείχνει εξωτερική θερμοκρασία και θερμοκρασία δρόσου, το μεσαίο γράφημα δείχνει τον λόγο ανάμειξης υδρατμών και το δεξιό γράφημα δείχνει την ενθαλπία του ανερχόμενου αέρα.*

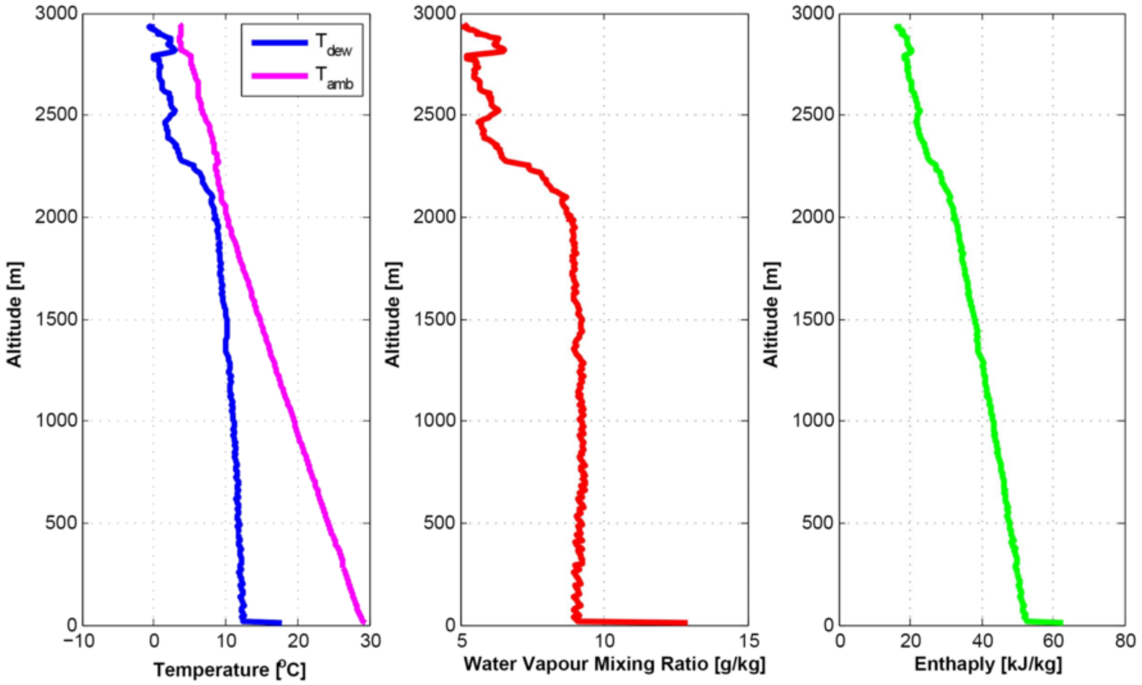

Σχήμα 6.34: *Ραδιοβόλιση στις 11 Ιουνίου 2014, 12:00 UTC. Το αριστερό γράφημα δείχνει εξωτερική θερμοκρασία και θερμοκρασία δρόσου, το μεσαίο γράφημα δείχνει τον λόγο ανάμειξης υδρατμών και το δεξιό γράφημα δείχνει την ενθαλπία του ανερχόμενου αέρα.*

6.8 Το πεδίο ανέμου μέσα στο ΑΟΣ

Εκτός από την ικανότητα των αιωρούμενων σωματιδίων να λειτουργούν σαν ΠΣΝ σύμφωνα με τις ιδιότητες τους, το πεδίο ανέμου παίζει έναν καθοριστικό ρόλο στην ανάπτυξη νέφωσης με διάφορους τρόπους: (1) η διεύθυνση του ανέμου (καθώς και η ένταση) καθορίζουν το είδος της αέριας μάζας η οποία μεταφέρεται πάνω από την τοποθεσία που μελετάται. Η πηγή προέλευσης και η διαδρομή που ακολούθησαν οι μάζες πριν την άφιξή τους στο σημείο ενδιαφέροντος είναι ιδιαίτερα σημαντικές καθώς καθορίζουν την χημική σύσταση των σωματιδίων και τις φυσικές τους ιδιότητες. Για παράδειγμα, όταν οι αέριες μάζες προέρχονται από Ν-ΝΔ διευθύνσεις ανέμου, το πιο πιθανό ανιχνεύσιμο αιωρούμενο σωματίδιο πάνω από την Αθήνα είναι η ερημική σκόνη. Επιπλέον, η διεύθυνση του ανέμου παίζει κρίσιμο ρόλο στον καθορισμό της θερμοκρασίας των αερίων μαζών και την περιεκτικότητά τους σε υδρατμούς. Ανεξάρτητα από την ικανότητα των σωματιδίων σκόνης να σχηματίζουν νεφοσταγονίδια, όταν η ποσότητα των υδρατμών στην ατμόσφαιρα είναι χαμηλή, η ενεργοποίηση των ΠΣΝ δεν μπορεί να συμβεί επειδή η θερμοδυναμική κατάσταση της ατμόσφαιρας δεν ευνοεί συνθήκες υπερκορεσμού και ετερογενούς πυρηνοποίησης. (2) η ένταση ανέμου είναι επίσης πολύ σημαντικός παράγοντας στην διαμόρφωση του σωματιδιακού φόρτου: π.χ., η χαμηλή ένταση ανέμου οδηγεί σε στασιμότητα των αερίων μαζών, η οποία ευνοεί την συσσώρευση ατμοσφαιρικών ρύπων μέσα στο ΑΟΣ σε περιοχές κοντά στις πηγές ρύπανσης.

Κατά τη διάρκεια του πειράματος HygrA-CD, το διάνυσμα της ταχύτητας (ένταση και διεύθυνση) αποκτήθηκε χρησιμοποιώντας δεδομένα από το σύστημα Doppler lidar. Στα Σχήματα 6.35 και 6.36, παρουσιάζουμε συνοπτικά την μέση ένταση και διεύθυνση ανέμου μέσα στο ΑΟΣ για όλη την περίοδο του πειράματος. Αυτή η πληροφορία είναι ιδιαίτερα χρήσιμη για να αποκτήσουμε μία γρήγορη αντίληψη των χαρακτηριστικών του ανέμου μέσα στο ΑΟΣ. Ας κάνουμε μία διάκριση της έντασης του ανέμου στο ΑΟΣ εισάγοντας τις παρακάτω κατηγορίες: (1) χαμηλή ένταση $w<8$ ms^{-1}, (2) μέτρια ένταση $8<w<16$ ms^{-1} και (3) υψηλή ένταση $w>16$ ms^{-1}. Στις περισσότερες περιπτώσεις, ισχυροί και ασθενείς άνεμοι εμφανίζονται όταν η διεύθυνση του ανέμου ήταν Δ-ΝΔ. Νεφώσεις εμφανίσθηκαν στο ΑΟΣ όταν οι αέριες μάζες που έφθαναν πάνω από την Αθήνα δεν περιείχαν ερημική σκόνη και ο άνεμος ήταν πολύ ισχυρός, όπως στις περιπτώσεις των 15, 30 και 31 Μαΐου (βλέπε Σχήμα 6.35 και Πίνακα 6.5). Όταν σωματίδια σκόνης φθάνουν πάνω από την Αθήνα από Δ-ΒΔ διευθύνσεις (π.χ. περιπτώσεις στις 24 και 25 Μαΐου), η ένταση του ανέμου ήταν ασθενής και δεν σχηματίστηκαν νέφη. Πολύ συχνά, μέτριας έντασης άνεμοι μετρήθηκαν από το σύστημα Doppler lidar όταν η διεύθυνση του ανέμου ήταν Β-ΒΑ (βλέπε Σχήματα 6.35 και 6.36). Για παράδειγμα, σε πολλές περιπτώσεις (π.χ. 21-22 Μαΐου και 09-11 Ιουνίου) παρουσίας νέφωσης στην κορυφή του ΑΟΣ, οι αέριες μάζες προέρχονταν από Β-ΒΑ διευθύνσεις και η μετρούμενη ένταση ανέμου ήταν μέτρια. Τα χαρακτηριστικά του ανέμου και της τύρβης στο ΑΟΣ αποδείχθηκαν να είναι πολύ σημαντικά για την ενεργοποίηση νεφοσταγονιδίων, ακόμα και πιο σημαντικά από τον αριθμό των σωματιδίων και της χημικής σύστασης.

6.9 Γενικά συμπεράσματα από τα ευρύματα του πειράματος HygrA-CD

Βάσει των συνοψισμένων πληροφοριών που παρουσιάζονται στον Πίνακα 6.5, μπορούμε να συμπεράνουμε ότι τα νέφη δεν εμφανίζονται κοντά στο ΑΟΣ όταν οι αέριες μάζες φθάνουν από Ν-ΝΔ διευθύνσεις και περιέχουν σωματίδια σκόνης. Ο βασικός λόγος για αυτό είναι ότι το σημείο δρόσου εντοπίζεται σε πολύ μεγάλα ύψη, πολύ μεγαλύτερα από την κορυφή του ΑΟΣ, και συνεπώς, τα ανερχόμενες δεμάτια αέρα μέσα στο ΑΟΣ δεν φθάνουν ποτέ στον υπερκορεσμό.

Αντιθέτως, η νέφωση στην κορυφή του ΑΟΣ συνήθως εμφανίζεται όταν οι αέριες μάζες φθάνουν από Β-ΒΑ διευθύνσεις και μεταφέρουν ανθρωπογενοί σωματίδια και σωματίδια από καύση βιομάζας και πιο σπάνια σωματίδια σκόνης. Όπως παρατηρούμε στον Πίνακα 6.5 οι υψηλές τιμές ΟΒΑ (ΟΒΑ(500 nm)>0.1) δεν αντιστοιχούν σε ημέρες με εμφάνιση νέφωσης στο ΑΟΣ.

Πίνακας 6.5: *Παρουσία αιωρούμενων σωματιδίων και νεφών στο ΑΟΣ σε σχέση με την διεύθυνση του ανέμου. Το ΟΒΑ στα 500 nm (τρίτη στήλη) ανακτήθηκε από ημερήσιες μετρήσεις του ηλιακού φωτομέτρου CIMEL όπως παρουσιάζεται στο Σχήμα 6.31.*

Ημ/νία [ηη/μμ]	**Νέφος**	**ΟΒΑ** > 0.1	**Δ - ΒΔ**		**Β - ΒΑ**		**Ν - ΝΔ**	**Ύψος ΑΟΣ [m]**
			Σκόνη	Άλλο	Σκόνη	Άλλο	Σκόνη	
15/05	x			x				0.85±0.15
16/05	x			x				1.68±0.07
17/05	x			x				1.13±0.07
18/05	x			x				1.69±0.20
19/05								N/A
20/05		x					x	2.01±0.10
21/05	x					x		1.71±0.10
22/05	x	x				x		2.52±0.20
23/05		x			x			2.59±0.20
24/05		x	x					0.79±0.15
25/05		x	x					1.82±0.10
26/05		x	x					1.57±0.07
27/05		x	x					1.94±0.15
28/05		x					x	0.79±0.10
29/05		x					x	N/A
30/05	x	x		x				1.52±0.20
31/05	x			x				1.71±0.25
01/06	x			x				2.31±0.15
02/06	x			x				2.32±0.15
03/06								N/A
04/06								N/A
05/06	x	x		x				0.68±0.10
06/06	x	x				x		0.65±0.05
07/06	x	x				x		0.72±0.05
08/06	x	x				x		1.88±0.16
09/06	x	N/A				x		2.23±0.25
10/06	x	N/A				x		1.45±0.18
11/06	x	x				x		2.47±0.20
12/06	x	x				x		2.31±0.20
13/06	x	N/A				x		2.57±0.07
14/06	x	N/A				x		2.13±0.18
15/06	x	N/A				x		2.33±0.20
16/06		x		x				1.86±0.30
17/06			x					0.86±0.15
18/06		N/A	x					N/A
19/06		N/A	x					2.11±0.20
20/06	x	N/A		x				1.98±0.15
21/06		N/A				x		1.18±0.16
22/06		N/A				x		1.88±0.15

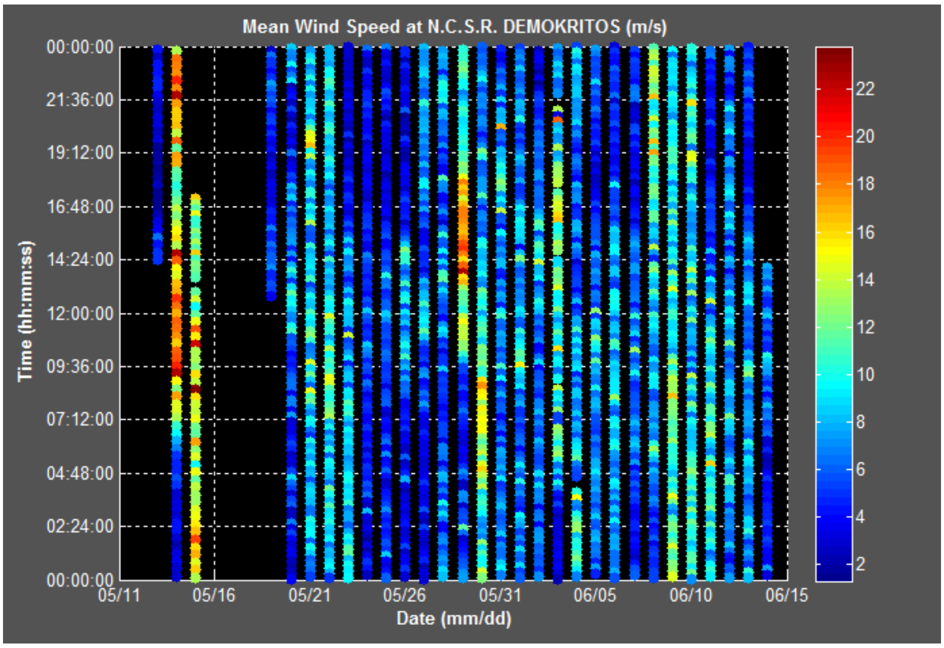

Σχήμα 6.35: *Μέση ταχύτητα ανέμου μέσα στο ΑΟΣ όπως ανακτήθηκε από το HALO lidar*

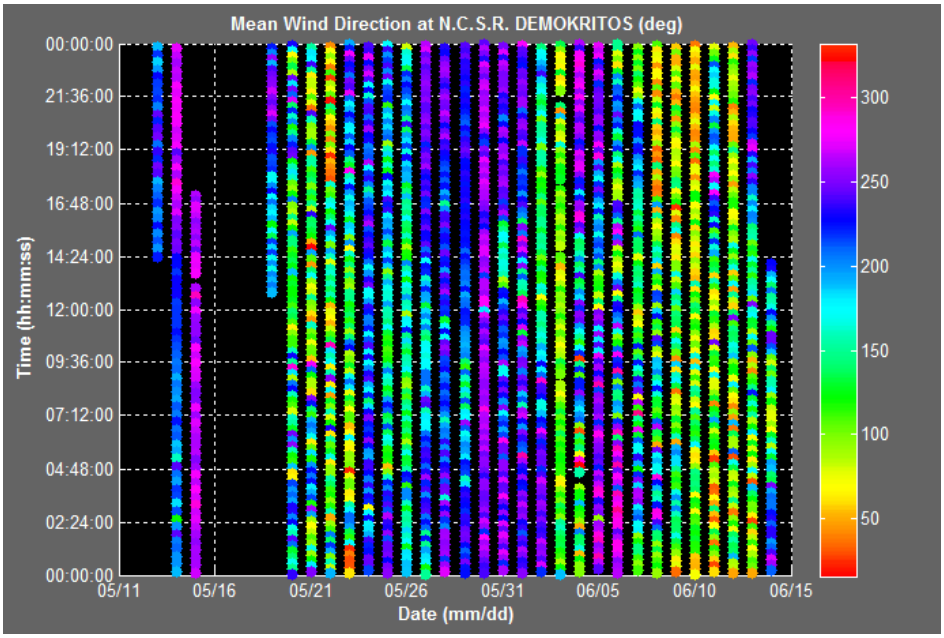

Σχήμα 6.36: *Μέση διεύθυνση ανέμου μέσα στο ΑΟΣ όπως ανακτήθηκε από το HALO lidar*

Επομένως, είναι ξεκάθαρο από την χρονοσειρά του HygrA-CD ότι η ενεργοποίηση νεφοσταγονιδίων, πάνω από την Αθήνα δεν μπορεί να συσχετιθεί μόνο με μία παράμετρο όπως το ΟΒΑ. Στην πράξη, η δημιουργία νέφωσης συμβαίνει ακόμα και με χαμηλό σωματιδιακό φόρτο, όταν υπάρξει θερμοδυναμική αστάθεια που οδηγεί σε θετική άνωση και κατακόρυφη μεταφορά των σωματιδίων μέσα στο ΑΟΣ μέχρι το ύψος του σημείου δρόσου. Από την βάση δεδομένων του πειράματος, μπορούμε να συμπεράνουμε ότι τα νέφοσταγονίδια δημιουργούνται όταν τα αιωρούμενα σωματίδια έχουν το μέγεθος εκείνο που οδηγεί σε ενεργοποίηση ακόμα και σε χαμηλούς υπερκορεσμούς ($s<0.1\%$). Η υγροσκοπικότητα των σωματιδίων παίζει επίσης έναν βασικό ρόλο στην ενεργοποίηση του σαν ΠΣΝ, όμως ακόμη και λογότερο υγροσκοπικά σωματίδια (όπως τα σωματίδια σκόνης) ενεργοποιούνται όταν φτάσουν στην κρίσιμη διάμετρο κατά την διάρκεια της κατακόρυφης μεταφοράς τους μέσα στο ΑΟΣ.

Τέλος, σαν ένα γενικό συμπέρασμα, το πείραμα HygrA-CD ανέδειξε την σημασία των συνδιακυμάνσεων και συσχετισμών ανάμεσα στη δυναμική του ΑΟΣ και τα αιωρούμενα σωματίδια προκειμένου να ερμηνεύσουμε τη δημιουργία νέφωσης κοντά στην κορυφή του ΑΟΣ πάνω από μία περιοχή όπως η Αθήνα με εξαιρετικά πολύπλοκη τοπογραφία. Επιπρόσθετα, κατανοήσαμε ότι η μεγαλύτερη συνεισφορά στην διακύμανση του αριθμού των ενεργοποιημένων νεφοσταγονιδίων οφείλεται στην μεταβλητότητα της κατακόρυφης συνιστώσας της ταχύτητας, κατά δεύτερον στην συνολική αριθμητική συγκέντρωση των σωματιδίων και τέλος, στην χημική σύσταση και κατανομή μεγέθους των σωματιδίων.

Κεφάλαιο 7: Μεθοδολογίες για ανακτούμενες παραμέτρους με χρήση lidar

Κάνοντας χρήση των δεδομένων από το πείραμα HygrA-CD, η διατριβή επικεντρώθηκε στην ανάπτυξη δύο μεθόδων με σκοπό την ποσοτικοποίηση 1) του φάσματος ΠΣΝ και την αριθμητική συγκέντρωση των νεφοσταγονιδίων σε ένα συγκεκριμένο ατμοσφαιρικό στρώμα και 2) κατακόρυφη ροή σωματιδίων μέσα στο ΑΟΣ.

7.1 Πρώτη μέθοδος: Υπολογισμός του φάσματος ΠΣΝ και των νεφοσταγονιδίων από δεδομένα lidar

Η πρώτη μέθοδος εκμεταλλεύεται τις επίγειες μετρήσεις τηλεπισκόπησης από το σύστημα EOLE lidar για να ανακτήσουμε τον αριθμό των ΠΣΝ σαν συνάρτηση του υπερκορεσμού. Η πληροφορία αυτή συνδυαζόμενη με την κατακόρυφη συνιστώσα της ταχύτητας μας επιτρέπει να υπολογίσουμε και την συγκέντρωση των νεφοσταγονιδίων. Τα Raman lidar παρέχουν τις οπτικές ιδιότητες των αιωρούμενων σωματιδίων οι οποίες είναι οι συντελεστές οπισθοσκέδασης και εξασθένησης. Η βασική ιδέα και δομή της προσέγγισής αυτής της μεθόδου παρουσιάζεται στο Σχήμα 7.37. Οι οπτικές ιδιότητες των αιωρούμενων σωματιδίων χρησιμοποιούνται για την ανεύρεση των μικροφυσικών ιδιοτήτων μέσα στο ανιχνευόμενο ομογενές ατμοσφαιρικό στρώμα. Συγκεκριμένα, η ανακτούμενη ιδιότητα αφορά την κατανομή μεγέθους των σωματιδίων σε διάφορα ύψη πάνω από το σύστημα lidar. Τα αιωρούμενα σωματίδια ανάλογα με την χημική τους σύσταση και επομένως την υγροσκοπικότητα τους, δημιουργούν ΠΣΝ τους οποίους και ανακτούμε από την κατανομή μεγέθους. Τέλος, με την χρήση παραμετροποίησης και με γνωστή την κατακόρυφη ταχύτητα, ο αλγόριθμος επιτρέπει τον υπολογισμό συγκέντρωσης νεφοσταγονιδίων και άλλων λοιπών παραμέτρων.

Στην παρούσα εφαρμογή επικεντρωνόμαστε στο χαμηλότερο τμήμα της ατμόσφαιρας για ύψη <2000 m στο εναπομένον στρώμα του ΑΟΣ. Συγκεκριμένα, επιλέξαμε στρώματα αερίων μαζών που πληρούν τα εξής κριτήρια: (α) τα σωματίδια είναι προσεγγιστικά σφαιρικά ώστε η θεωρία Mie να είναι εφαρμόσιμη, (β) τα σωματίδια έχουν εσωτερική ανάμειξη και (γ) η μάζα είναι ομοιόμορφα κατανεμημένη. Η εγκυρότητα της σφαιρικότητας των σωματιδίων εξασφαλίζεται από

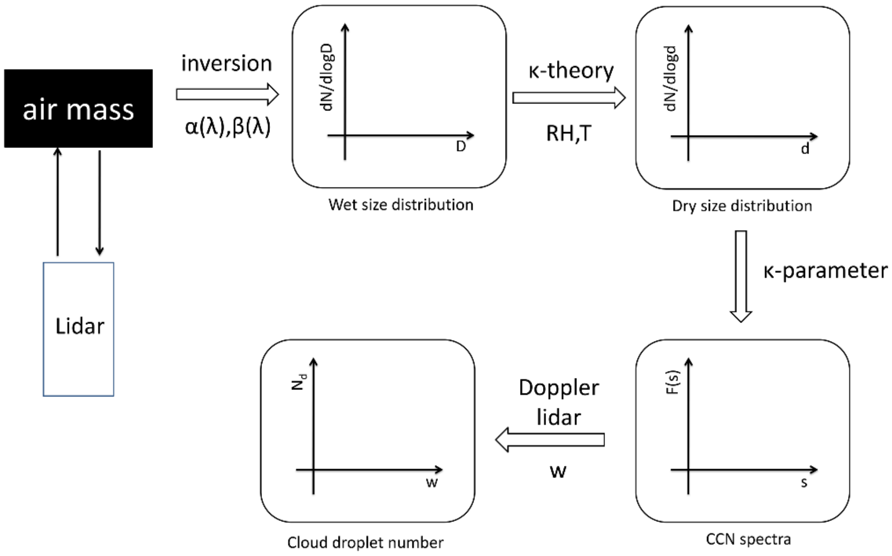

Σχήμα 7.37: *Παρουσίαση του αλγορίθμου: ανακτούμενες ποσότητες και ανάλυση*

τον ανακτούμενο συντελεστή αποπόλωσης των σωματιδίων που μετράται από το σύστημα AIAS lidar. Τα σωματίδια με συντελεστή αποπόλωσης μικρότερο από 5% θεωρούνται προσεγγιστικά σφαιρικά [133]. Η αντιστροφή των οπτικών δεδομένων εφαρμόζεται μόνο σε περιπτώσεις που παρατηρούνται σφαιρικά σωματίδια και περιορίζεται στις διαμέτρους [0.1 μm, 20 μm] λόγω του μήκους κύματος της δέσμης laser που αλληλεπιδρά λιγότερο με μικρότερα ή μεγαλύτερα σε μέγεθος σωματίδια. Η κοινή πηγή προέλευσης ελέγχθηκε με τις οπισθοτροχιές αερίων μαζών από το μοντέλο HYSPLIT. Ετσι, εξασφαλίζεται και η ομοιομορφία των αερίων μαζών αυτών που μελετήθηκαν.

Ο αλγόριθμος που απαπτύχθηκε, εφαρμόσθηκε σε τέσσερα ατμοσφαιρικά στρώματα από την περίοδο του πειράματος: 21 Μαΐου, 22 Μαΐου, 10 Ιουνίου και 11 Ιουνίου. Η οπτική σφραγίδα των ανιχευθέντων σωματιδίων παρουσιάζεται στον Πίνακα 7.6. Η αντιστροφή των δεδομένων lidar οδήγησε στις κατανομές του Σχήματος 7.38 που δείχνουν ότι η πιο φορτωμένη σωματιδιακά μέρα είναι αυτή της 10ης Ιουνίου. Παρόλ΄ αυτά, η ημέρα με τα μεγαλύτερα σωματίδια είναι αυτή της 22ας Μαΐου. Μέσω της θεώρησης μίας χαρακτηριστικής για την περιοχή κ-παραμέτρο υγροσκοπικότητας μπορέσαμε να ανακτήσουμε από τις αρχικές κατανομές σε εξωτερικές συνθήκες σε κατανομές υπό ξηρές συνθήκες. Από αυτές τις κατανομές βρήκαμε την κρίσιμη διάμετρο για κάθε υπερκορεσμό και κατασκευάσαμε τα φάσματα των ΠΣΝ που παρουσιάζονται στο Σχήμα 7.39. Τα λιγότερο υγροσκοπικά σωματίδια θεωρήθηκαν με κ=0.1, ενώ τα πιο υγροσκοπικά θεωρήθηκαν με κ=0.3. Για τα πρώτα παρατηρούμε ότι για έναν κρίσιμο υπερκορεσμό s=0.2% όλα τα διαθέσιμα σωματίδια ενεργοποιούνται ως ΠΣΝ. Για τα πιο υγροσκοπικά, ένας υπερκορεσμός της τάξης του s=0.1% είναι ακρετός για να ενεργοποιήσει όλα τα αιωρούμενα σωματίδια. Συγκρίνοντας μεταξύ των διαφορετικών περιπτώσεων, παρατηρούμε ότι ο μεγαλύτερος αριθμός ΠΣΝ εμφανίζεται για την περίπτωση της 10ης Ιουνίου καθώς είναι και η μέρα με το μεγαλύτερο σωματιδιακό φόρτο. Ο μέγιστος αριθμός των ΠΣΝ είναι 770 ανά cm^{-3}. Αυτό ευρίσκεται σε συνέπεια με το υψηλό ΟΒΑ στα 355 nm που εκείνη την ημέρα βρέθηκε ίσο με 0.069. Αντιθέτως, η λιγότερο ρυπασμένη μέρα φαίνεται αυτή της 22 Μαΐου με συνολικό αριθμό ΠΣΝ 330 cm^{-3} σε ένα ατμοσφαιρικό στρώμα με ΟΒΑ στα 355 nm ίσο με 0.037.

Όλα τα σωματίδια ενεργοποιούνται ως ΠΣΝ εάν έχουν την κατάλληλη κρίσιμη διάμετρο. Το φάσμα ΠΣΝ σαν συνάρτηση του υπερκορεσμού που ανακτούμε από την κατανομή σωματιδίων είναι εξαιρετικά σημαντικό για την ταξινόμηση των ανιχνευόμενων στρωμάτων σε σχέση με την αποδοτικότητά τους να λειτουργούν ως ΠΣΝ. Στο Σχήμα 7.40 φαίνεται η ικανότητά των

Πίνακας 7.6: *Οπτικές ιδιότητες αιωρούμενων σωματίδιων στα ατμοσφαιρικά στρώματα που ανιχνεύθηκαν*

Ημ/νία	**Ύψος στρώματος** $[m]$	S_λ $[sr]$		**AE**
		355nm	**532nm**	
21 Μαΐου	1200-1700	56 (5)	60 (8)	1.3 (0.3)
22 Μαΐου	1200-1600	40 (8)	46 (3)	0.8 (0.6)
10 Ιουνίου	1200-1600	59 (4)	58 (8)	1.3 (0.4)
11 Ιουνίου	1200-1800	59 (4)	55 (9)	1.2 (0.4)

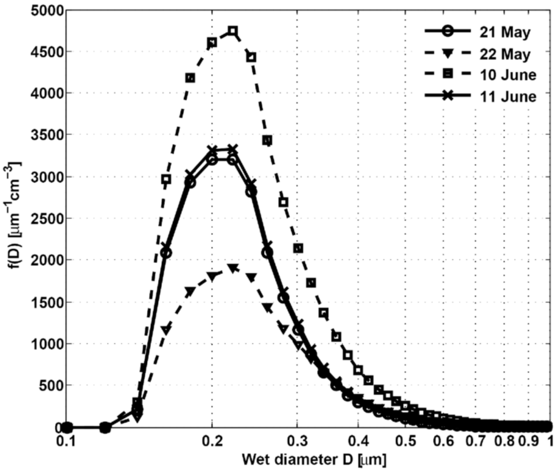

Σχήμα 7.38: *Κατανομή σωματιδίων σε εξωτερικές ατμοσφαιρικές συνθήκες για τις τέσσερις μέρες όπως ανακτήθηκε από τα οπτικά δεδομένα του lidar.*

σωματιδίων να γίνονται νεφοσταγονίδια για τις διάφορες περιπτώσεις. Τα πιο αποδοτικά σωματίδια είναι αυτά της 22 Μαΐου. Για έναν εξωτερικό υπερκορεσμό 0.05%, ο λόγος ενεργοποίησης στην περίπτωση της 22 Μαΐου είναι μεγαλύτερος από 40% ενώ στην περίπτωση της 11ης Ιουνίου λιγότερα από το 30% των σωματιδίων μπορούν να ενεργοποιηθούν σαν ΠΣΝ. Η προηγούμενη παρατήρηση εξηγεί γιατί ολόκληρο το φάσμα ΠΣΝ είναι μία σημαντική ιδιότητα που πρέπει να μπορεί να ανακτηθεί από δεδομένα lidar και όχι μόνο ο συνολικός αριθμός ΠΣΝ.

Η απόκριση του αλγορίθμου ανάκτησης σε σχέση με την σταθερότητα των λύσεων αντιστροφής είναι πολύ κρίσιμη για τις κατανομές μεγέθους. Η σημασία ως προς τους λόγους ενεργοποίησης των ΠΣΝ είναι εμφανής στο Σχήμα 7.41. Η επίδραση των μη σταθερών λύσεων είναι πιο σημαντική για υπερκορεσμούς μικρότερους από 0.1%. Η μεγαλύτερη διαφορά κατά 30-35% εμφανίζεται για τις περιπτώσεις 10 και 11 Ιουνίου στον υπερκορεσμό 0.06%. Αυτό σημαίνει ότι μία υποεκτίμηση κατά περίπου 30% μπορεί να εισαχθεί στον αριθμό των ΠΣΝ. Όπως φαίνεται και το Σχήμα 7.41, αυτή η υποεκτίμηση μπορεί να μειωθεί από 30% σε 10% εάν χρησιμοποιηθεί μία εκτιμήτρια μέγιστης πιθανοφάνειας στις κατανομές μεγέθους των σωματιδίων πριν ανακτηθεί ο αριθμός των ΠΣΝ.

Μετά από τα φάσματα των ΠΣΝ, ο υπολογισμός των νεφοσταγονιδίων μπορεί να επιτευχθεί εάν γνωρίζουμε την κατακόρυφη συνιστώσα της ταχύτητας από την χρονοσειρά του συστήματος Doppler lidar. Από τις συναρτήσεις πυκνότητας πιθανότητας που δημιουργήσαμε, ανακτήσαμε την μέση τιμή και τη διασπορά των κατανομών των μετρήσεων και τις παρουσιάζουμε για τις τέσσερις ημέρες στο Σχήμα 7.42. Παρατηρούμε ότι τα ανοδικά και καθοδικά ρεύματα επικρατούν σε διαφορετικές στιγμές της ημέρας. Η μέση ημερίσια χαρακτηριστική ταχύτητα σε όλες τις περιπτώσεις βρέθηκε ίση με 0.6 ms^{-1} που είναι τυπική για το ΑΟΣ κατακόρυφης μεταφοράς [146]. Γενικά, για τον υπολογισμό του μέγιστου υπερκορεσμού και τον αριθμό των νεφοσταγονιδίων,

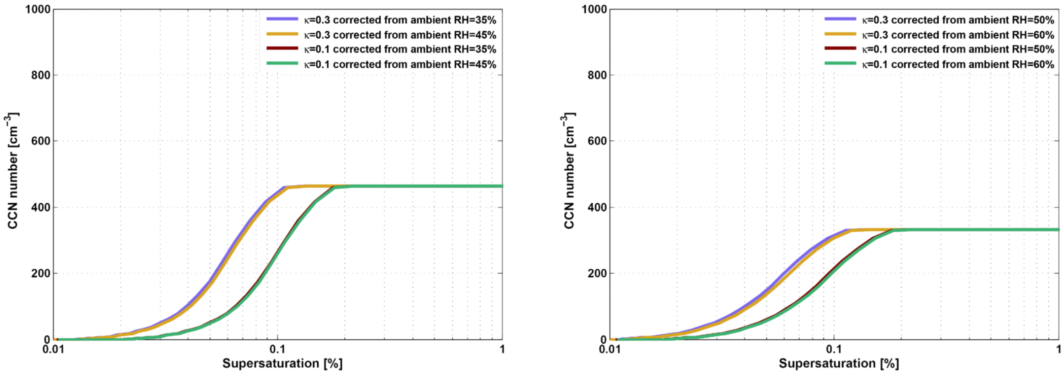

(a) **21 May:** $CCN_{max} = 460cm^{-3}$ (b) **22 May:** $CCN_{max} = 330cm^{-3}$

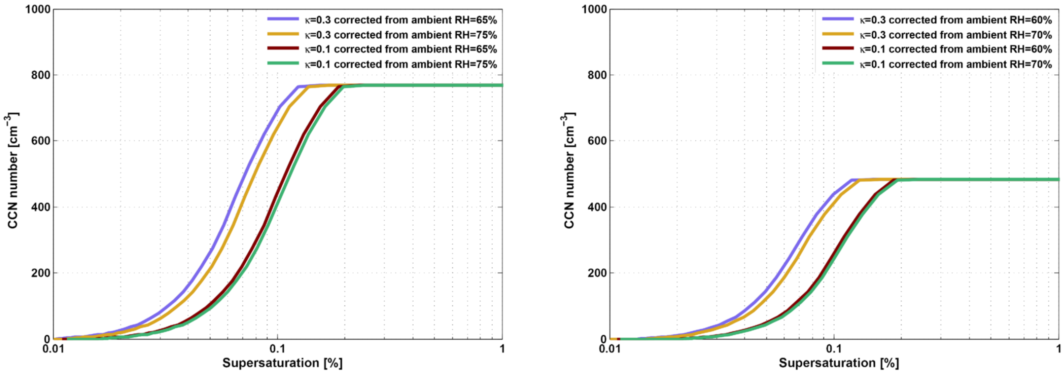

(c) **10 June:** $CCN_{max} = 770cm^{-3}$ (d) **11 June:** $CCN_{max} = 480cm^{-3}$

Σχήμα 7.39: *Φάσμα ΠΣΝ για τις τέσσερις ημέρες, όπου παρουσιάζεται ο συνολικός αριθμός ενεργοποιημένων ΠΣΝ σαν συνάρτησει του υπερκορεσμού. Σε όλες τις περιπτώσεις, τα ανιχνευθέντα αιωρούμενα σωματίδια ενεργοποιούνται ως ΠΣΝ ανεξάρτητα από τις φυσικοχημικές ιδιότητες τους στους υπερκορεσμούς* $s > 0.2\%$.

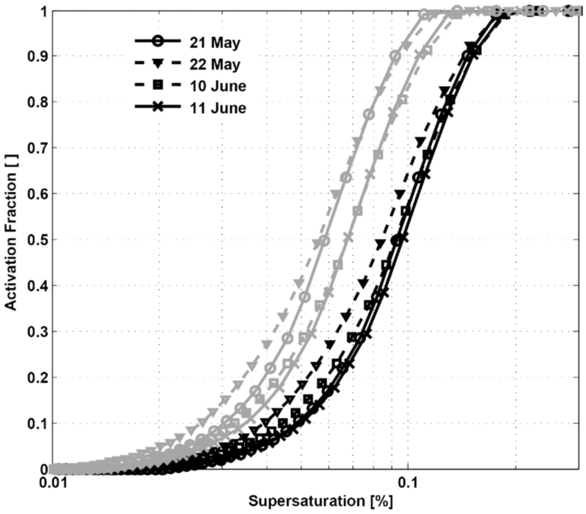

Σχήμα 7.40: *Οι λόγοι ενεργοποίησης προέκυψαν από τον αριθμό των ΠΣΝ προς το συνολικό αριθμό των σωματιδίων. Οι λόγοι ενεργοποίησης σημειώνονται με γκρί χρώμα για* $\kappa = 0.3$ *και με μαύρο χρώμα για* $\kappa = 0.1$.

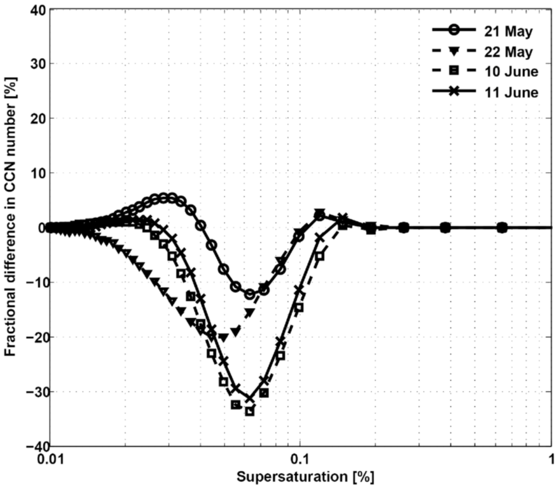

Σχήμα 7.41: *Οι διαφορές στους λόγους ενεργοποίησης $\Delta\phi(s)$ κατά μήκος του φάσματος των υπερκορεσμών για όλες τις περιπτώσεις.*

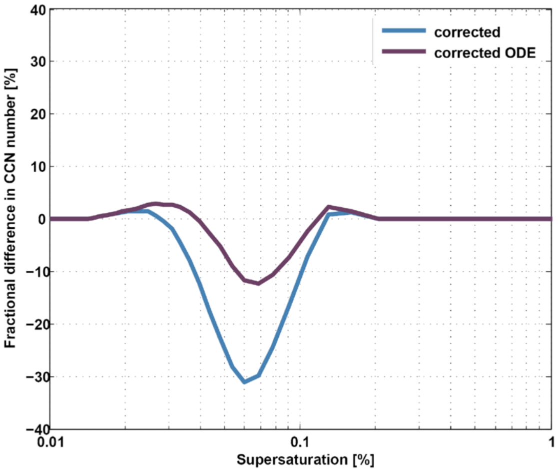

Σχήμα 7.42: *Ποσοστιαίες διαφορές στον αριθμό των ΠΣΝ πριν και μετά την εφαρμογή της εκτιμήτριας μέγιστης πιθανοφάνειας.*

εκτός από τη μέση τιμή όλες οι πιθανές τιμές της χαρακτηριστικής ταχύτητας που συνοψίζονται στον Πίνακα 7.7 έχουν θεωρηθεί. Στον Πίνακα 7.8 παρουσιάζονται τα αποτελέσματα. Ο μέγιστος υπερκορεσμός εμφανίζεται για την περίπτωση της 22 Μαΐου. Αυτό οδηγεί σε ένα ποσοστό ενεργοποίησης νεφοσταγονιδίων έως 82%. Επομένως, ο χαρακτηρισμός των σωματιδίων της 22 Μαΐου ως τα πιο αποδοτικά στην δημιουργία νέφωσης επιβεβαιώνεται από την παραμετροποίηση σαν αληθής.

Ο αριθμός των νεφοσταγονιδίων επηρεάζεται πολύ λίγο από τις μη σταθερές λύσεις του προβλήματος αντιστροφής, επομένως οι ανακτούμενες ποσότητες δεν είναι ευαίσθητες στις μη μοναδικές κατανομές των σωματιδίων. Σε όλες τις περιπτώσεις, ο αριθμός των νεφοσταγονιδίων εκτιμάται για ένα μέγιστο υπερκορεσμό στο διάστημα [0.13-0.31]. Για αυτούς τους υπερκορεσμούς βλέπουμε ότι ο λόγος ενεργοποίησης νεφοσταγονιδίων δεν παρουσιάζει υπερεκτίμηση ή υποεκτίμηση. Συγκεκριμένα όταν εφαρμόζεται και η εκτιμήτρια μέγιστης πιθανοφάνειας στις κατανομές μεγέθους, η διαφοροποίηση στο λόγο ενεργοποίησης νεφοσταγονιδίων είναι μικρότερη του 5%.

Πίνακας 7.7: *Στατιστικά από τις συναρτήσεις πυκνότητας πιθανότητας της κατακόρυφης συνιστώσας του ανέμου.*

	Ημερίσιο (ανοδικά και καθοδικά ρεύματα)			**Μόνο ανοδικά ρεύματα**			**Ταυτόχρονα με την αντιστροφή**
Μέση τιμή μ	*mean*	*min*	*max*	*mean*	*min*	*max*	
21 Μαΐου	0.0	-0.1	0.3	0.4	0.0	0.3	0.9
22 Μαΐου	-0.2	-0.2	0.0	0.1	0.1	0.1	-0.2
10 Ιουνίου	-0.3	-0.1	-0.3	0.1	0.2	0.1	-0.3
11 Ιουνίου	-0.2	-0.3	-0.2	0.3	0.2	0.3	-0.3
Διασπορά σ	*mean*	*min*	*max*	*mean*	*min*	*max*	
21 Μαΐου	0.8	0.3	1.2	0.9	0.4	1.2	1.1
22 Μαΐου	0.7	0.4	1.2	0.5	0.4	0.5	0.6
10 Ιουνίου	0.8	0.5	1.1	0.8	0.5	1.1	0.7
11 Ιουνίου	0.7	0.3	1.2	1.0	0.8	1.2	0.3
Χαρακτηριστική ταχύτητα $w^{\star}$	*mean*	*min*	*max*	*mean*	*min*	*max*	
21 Μαΐου	0.6	0.2	1.0	0.7	0.3	1.0	0.9
22 Μαΐου	0.6	0.3	1.0	0.4	0.3	0.4	0.5
10 Ιουνίου	0.6	0.4	0.9	0.6	0.4	0.9	0.6
11 Ιουνίου	0.6	0.2	1.0	0.8	0.6	1.0	0.2

Πίνακας 7.8: *Παράμετροι ενεργοποίησης νεφοσταγονιδίων*

	21 Μαΐου	**22 Μαΐου**	**10 Ιουνίου**	**11 Ιουνίου**
Μεγ. υπερκορεσμός (%)	[0.13, 0.26]	[0.15, 0.31]	[0.14, 0.19]	[0.13, 0.26]
Νεφοσταγονίδια (m^{-3})	[285, 453]	[270, 324]	[539, 655]	[281, 476]
Λόγ. ενεργοποίησης (%)	[62, 98]	[82, 98]	[70, 90]	[58, 98]

7.2 Δεύτερη μέθοδος: Υπολογισμός της ροής μεταφοράς σωματιδίων κατακόρυφα στο ΑΟΣ

Η μεταφορά των αιωρούμενων σωματιδίων στο ΑΟΣ παρουσιάζει πολυπλοκότητα και μέχρι τώρα δεν έχει μελετηθεί συστηματικά με μεθόδους ενεργητικής τηλεπισκόπησης. Τελευταία έχει παρουσιαστεί ιδιαίτερο ενδιαφέρον από την κοινότητα του ACTRIS/EARLINET να παρέχουν καθ΄ ύψος τη ροή των σωματιδίων μέσα στο ΑΟΣ. Συνεργιστικές μετρήσεις από ένα ελαστικό σύστημα lidar σωματιδίων και ένα σύστημα Doppler lidar μπορούν να χρησιμοποιηθούν για την ανάκτηση αυτής της πληροφορίας. Μία μέθοδος υλοποιήθηκε πρόσφατα μέσα στο ανέφελο ΑΟΣ σε ξηρές ατμοσφαιρικές συνθήκες (χαμηλή σχετική υγρασία) αναφέρεται στην [147]. Εδώ, προσπαθήσαμε να επεκτείνουμε την εφαρμογή της μεθόδου σε μία περίπτωση με εμφάνιση νέφωσης στην κορυφή του ΑΟΣ όπου κατά την μεταφορά των σωματιδίων κατακόρυφα, διογκώνονται και μεγαλώνουν σε μέγεθος λόγω των υδρατμών που προσλαμβάνουν γύρω τους.

Από την βάση δεδομένων του πειράματος HygrA-CD, χρησιμοποιήσαμε τις ταυτόχρονες ημερήσιες μετρήσεις στον σταθμό ‘Δημόκριτος’ της 11ης Ιουνίου. Η ποσοτικοποίηση της κατακόρυφης μεταφοράς σωματιδίων προυποθέτει ότι και τα δύο συστήματα lidar μετρούν τον ίδιο ατμοσφαιρικό όγκο. Το lidar AIAS λειτουργεί στο μήκος κύματος 532 nm και τα γεωμετρικά

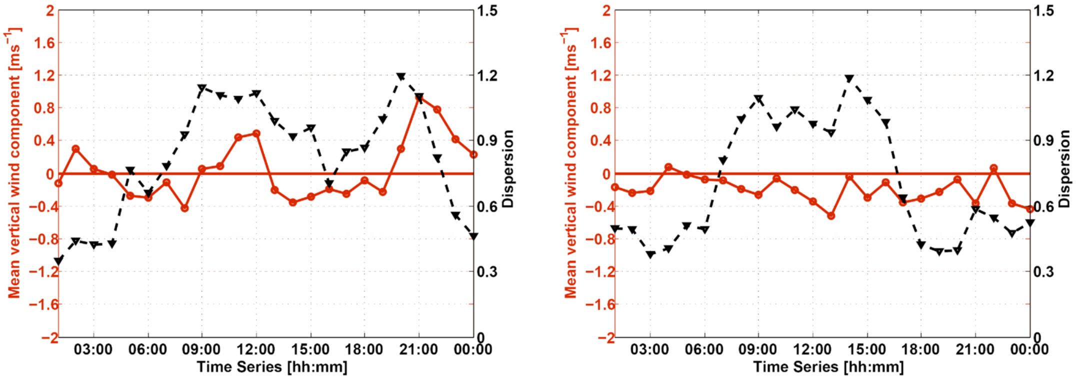

(a) **21 May** (b) **22 May**

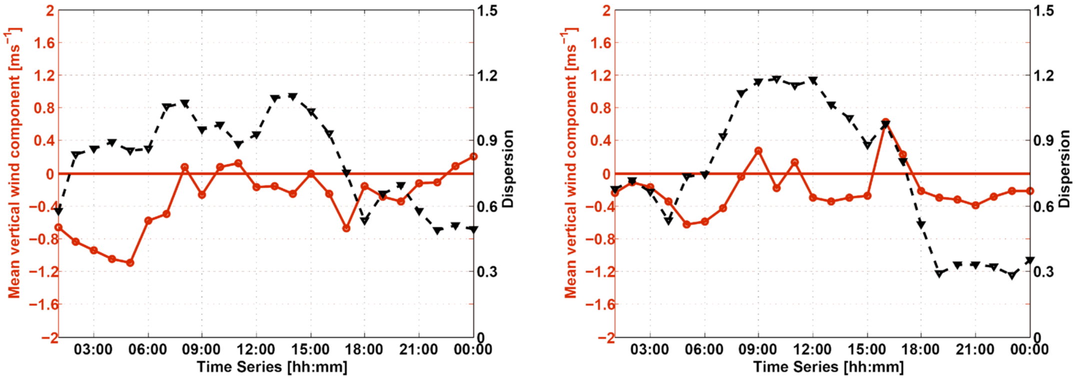

(c) **10 June** (d) **11 June**

Σχήμα 7.43: *Στατιστικά από τις συναρτήσεις πυκνότητας πιθανότητας της κατακόρυφης ταχύτητας. Η κόκκινη γραμμή είναι η μέση τιμή της ταχύτητας και η μαύρη γραμμή η διασπορά ως προς τη μέση τιμή.*

χαρακτηριστικά του πομπού και δέκτη μας επιτρέπουν την ανάκτηση του συντελεστή οπισθοσκέδασης σωματιδίων πάνω από τα 300 m από την επιφάνεια του εδάφους. Ο ρυθμός δειγματισμού του ελαστικά οπισθοσκεδαζόμενου σήματος είναι 20 MHz και οδηγεί στην κατακόρυφη διακριτική ικανότητα των 7.5 m. Η χρονική διακριτική ικανότητα του συστήματος lidar ορίστηκε ίση με 100 s με σκοπό να επιτευχθεί ένας ικανοποιητικά καλός σηματοθορυβικός λόγος. Το τελευταίο μας επέτρεψε να ανακτήσουμε τις διακυμάνσεις του συντελεστή οπισθοσκέδασης σωματιδίων β με σφάλμα της τάξης ~15% [97]. Ο συντελεστής οπισθοσκέδασης εκτιμήθηκε από τη μέθοδο Klett [51,115] κάνοντας υπόθεση ως προς το λόγο lidar S. Επιλέξαμε την τιμή S=45 sr επειδή ήταν η πιο συχνά παρατηρούμενη τιμή κατά τη διάρκεια του πειράματος (βλέπε Σχήμα 6.27). Το σύστημα Doppler lidar είναι ένα εμπορικό σύστημα που χρησιμοποιεί σύμφωνη ετερόδυνη πηγή laser με δυνατότητες σάρωσης στις τρεις διαστάσεις το οποίο κατασκευάστηκε από την εταιρία HALO Photonics, η καλή λειτουργία του οποίου έχει πιστοποιηθεί στο [99]. Το συγκεκριμένο σύστημα lidar έχει τη δυνατότητα να λειτουργεί με έναν σύνθετο τρόπο σάρωσης που μας επιτρέπει να μετρούμε την κατακόρυφη συνιστώσα της ταχύτητας w με σφάλμα μικρότερο από 0.1 ms^{-1} [151]. Η κατακόρυφη χωρική διακριτική ικανότητα είναι 30 m και η χρονική διακριτική ικανότητα 14 s.

Για μετρήσεις τυρβώδους μεταφοράς χρησιμοποιείται πολύ συχνά η τεχνική συσχέτισης στροβιλισμών. Η συγκεκριμένη τεχνική επιτρέπει τον άμεσο υπολογισμό της ροής των αερολυμάτων μέσα στο ΑΟΣ και μπορεί να συσχετιστεί με την διακύμανση της μάζας από το έδαφος μέχρι την κορυφή του ΑΟΣ. Η μεθοδολογία απαιτεί τον υπολογισμό της συνδιακύμανσης της κατακόρυφης συνιστώσας του ανέμου w' και του συντελεστού οπισθοσκέδασης β'. Μία προυπόθεση για την εφαρμογή της μεθόδου είναι η λεγόμενη 'παγωμένη τύρβη' που πληρείται μέσα από την υπόθεση του Taylor. Στην πράξη, όταν μελετούμε οποιαδήποτε μετεωρολογική παράμετρο, οι χρονικές διακυμάνσεις στο μέσο εκφράζονται ως μία απλή μεταφορά των χωρικών διακυμάνσεων υπό την επίδραση της ταχύτητας που είναι ίση με την ένταση του ανέμου. Το τελευταίο μας επιτρέπει να συνδέσουμε την κλίμακα του χρόνου και της συχνότητας αυτής της παραμέτρου με την χωρική του κλίμακα του μήκους κύματος ή του κυματαριθμού [153].

Από την βάση δεδομένων του πειράματος HygrA-CD, επιλέξαμε την περίπτωση της 11ης Ιουνίου για να εφαρμόσουμε την παραπάνω τεχνική. Ο λόγος είναι ότι εκείνη την ημέρα παρατηρήθηκε νέφωση και ταυτόχρονα καλή ανάμειξη στην κατώτερη ατμόσφαιρα. Η κατάσταση ανάμειξης χαρακτηρίζεται από τον καθ΄ ύψος λόγο ανάμειξης των υδρατμών. Στο Σχήμα 7.44, ο λόγος ανάμειξης είναι σχεδόν σταθερός και ίσος με 9 gkg^{-1} από το έδαφος έως τα 2000 m ύψος. Αυτό είναι μία ένδειξη ενός καλά αναμεμιγμένου ΑΟΣ λόγω της προγενέστερης επίδρασης τυρβώδους ροής μέσα στο ΑΟΣ. Σχετικά με το σωματιδιακό φόρτο, η συγκεκριμένη ημέρα χαρακτηρίστηκε από σχετικά υψηλό ΟΒΑ(500 nm)>0.17 και έναν εκθέτη ΑΕ(440/870 nm) περίπου 1.5-1.6 (βλέπε Σχήμα 7.45). Η χρονοσειρά των μετρήσεων σταματά περίπου στις 07:30 UTC λόγω του σχηματισμού νέφωσης που δημιουργούν πρόβλημα στις μετρήσεις με το ηλιακό φωτόμετρο. Το σύστημα AIAS ανίχνευσε τα πρώτα νέφη λίγο πρίν τις 08:00 UTC σε ένα ύψος περίπου 1900 m. Επομένως, το χρονικό παράθυρο που χρησιμοποιήθηκε για την μελέτη της τυρβώδους κατακόρυφης μεταφοράς των σωματιδίων είναι μεταξύ 06:40-07:45 UTC.

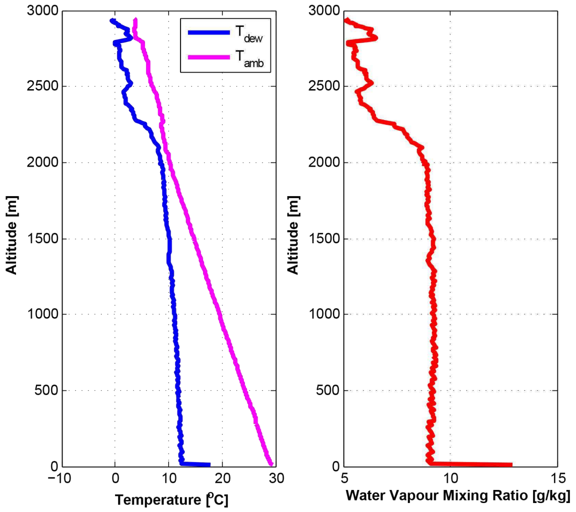

Σχήμα 7.44: *Ραδιοβόλιση στις 11 Ιουνίου 2014, 12:00 UTC. Το αριστερό γράφημα δείχνει εξωτερική θερμοκρασία και θερμοκρασία δρόσου, το μεσαίο γράφημα δείχνει τον λόγο ανάμειξης υδρατμών και το δεξιό γράφημα δείχνει την ενθαλπία του ανερχόμενου αέρα.*

Οι μετρήσεις της ροής σωματιδίων καθ΄ ύψος μπορούν να πραγματοποιηθούν κάτω από την υπόθεση ότι η συγκέντρωση των σωματιδίων είναι ομοιογενής στις οριζόντιες x,y-διευθύνσεις πάνω από τα συστήματα lidar. Η εγκυρότητα αυτής της υπόθεσης εξερευνήθηκε μέσα από το μοντέλο WRF. Οι διακυμάνσεις της μάζας αιωρούμενων σωματιδίων πάνω από τα συστήματα lidar είναι κυρίως λόγω κατακόρυφης μεταφοράς των σωματιδίων μέσα στην ατμοσφαιρική στήλη αέρα και οι διακυμάνσεις λόγω οριζόντιας μεταφοράς μπορούν να παραληφθούν. Η ένταση εκπομπής από τις πηγές των σωματιδίων φαίνεται να παραμένει προσεγγιστικά σταθερή για την περίοδο 06:00 και 12:00 στα Σχήματα 7.46(α) και 7.46(β).

Η κατακόρυφη ροή σωματιδίων κυρίως οφείλεται στους μεγάλους στροβίλους με μέγεθος παρόμοιο με αυτό του βάθους του ΑΟΣ. Δεδομένου ότι η τύρβη μπορεί να εκφραστεί σε διαφορετικές κλίμακες, είναι αρκετά χρήσιμο να κατασκευάσουμε το ενεργειακό φάσμα το οποίο

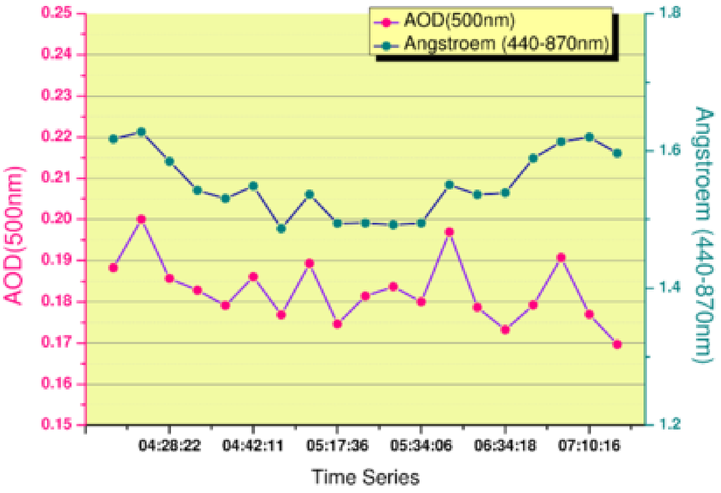

Σχήμα 7.45: *ΟΒΑ και ΑΕ από τα δεδομέναν του ηλιακού φωτόμετρου (11 Ιουνίου 2014)*

εκφράζει πόση κινητική ενέργεια είναι αποθηκευμένη στον στροβιλισμό ανάλογα με τον μέγεθος/κυματαριθμό k. Το ενεργειακό φάσμα του συντελεστή οπισθοσκέδασης παρουσιάζεται στο Σχήμα 7.47 για δύο διαφορετικά ατμοσφαιρικά στρώματα σε ύψη 720 και 810 m για το χρονικό διάστημα 06:40-07:45 UTC. Το φάσμα φαίνεται να καλύπτει το μεγαλύτερο μέρος από την αδρανειακή υποπεριοχή που ακολουθεί την υπόθεση του Kolmogorov για την ομογενή και ισοτροπική τύρβη [155]. Ο νόμος του -5/3 έχει προσαρμοστεί πάνω στα δεδομένα για το φάσμα των συχνοτήτων $8 \times 10^{-3} - 2 \times 10^{-2}$ Hz. Σε υψηλότερες συχνότητες παρατηρούμε μία πιο επίπεδη συμπεριφορά που οφείλεται στον θόρυβο ο οποίος επικρατεί σε εκείνο στο τμήμα του φάσματος [156]. Πράγματι, περιοριζόμαστε από την συχνότητα δειγματοληψίας των 100 Hz και δεν μπορούμε να μελετήσουμε μικρότερες δομές τύρβης.

Η συνεισφορά των τυρβώδη ροών κατά μήκος των στροβίλων μπορεί να ποσοτικοποιηθεί μέσω του διαφάσματος των w' και β'. Στην περίπτωσή μας, οι συχνότητες που συνεισφέρουν στην κατακόρυφη μεταφορά είναι στο εύρος $1 \times 10^{-3} - 2 \times 10^{-2}$ Hz (βλέπε Σχήμα 7.48). Με την υπόθεση Taylor για την παγωμένη τύρβη, βρίσκουμε ότι αυτές οι συχνότητες αντιστοιχούν σε μεγέθη στροβίλων από 450 έως 8000 m. Τα μήκη κύματος λ των στροβιλισμών μπορούν να υπολογιστούν από τη μέση ταχύτητα του ανέμου που ήταν 8 ms^{-1}. Επικρατεί ανοδική κατακόρυφη μεταφορά σωματιδίων όταν το διάφασμα έχει θετικό πρόσιμο, δηλαδή για στροβίλους μεγέθους 450-1500 m. Αυτοί οι στροβιλισμοί έχουν παρόμοιο μέγεθος με αυτό του βάθους του ΑΟΣ και αυτό εξηγεί την καλή κατακόρυφη ανάμειξη μετά το τοπικό μεσημέρι.

Η συγκέντρωση μάζας των αερολυμάτων σε ξηρές συνθήκες (χαμηλή σχετική υγρασία) μπορεί να βρεθεί από τον συντελεστή οπισθοσκέδασης των σωματιδίων. Όμως, σε ατμοσφαιρικές συνθήκες με υψηλή σχετική υγρασία αναμένουμε ότι ο συντελεστής οπισθοσκέδασης ενισχύεται λόγω της αυξημένης ποσότητας νερού στα σωματίδια [158, 159, 160]. Η μέση τιμή του συντελεστή οπισθοσκέδασης στο χρονικό παράθυρο 06:40-07:45 UTC παρουσιάζεται στο Σχήμα 7.49. Είναι φανερό ότι σε ύψος 1800 m υπήρξε ενίσχυση του συντελεστή οπισθοσκέδασης, η οποία αιτιολογείται βλέποντας τα επίπεδα σχετικής υγρασίας καθ' ύψος (βλέπε Σχήμα 7.50). Η σχετική υγρασία πάνω από τα 1800 m ξεπερνά το 80%. Στο ίδιο γράφημα βλέπουμε τη δυναμική θερμοκρασία καθ' ύψος όπου πάνω από τα 2000 m εμφανίζει μία θετική βαθμίδα και συνεπώς οι κατακόρυφες μεταφορές πάνω από αυτό το ύψος περιορίζονται.

Πρίν προχωρήσουμε στον υπολογισμό της ροής των σωματιδίων, είναι απαραίτητο να απαλλάξουμε τον συντελεστή οπισθοσκέδασης από την επίδραση της υγρασίας. Γι αυτό ανακτήσαμε

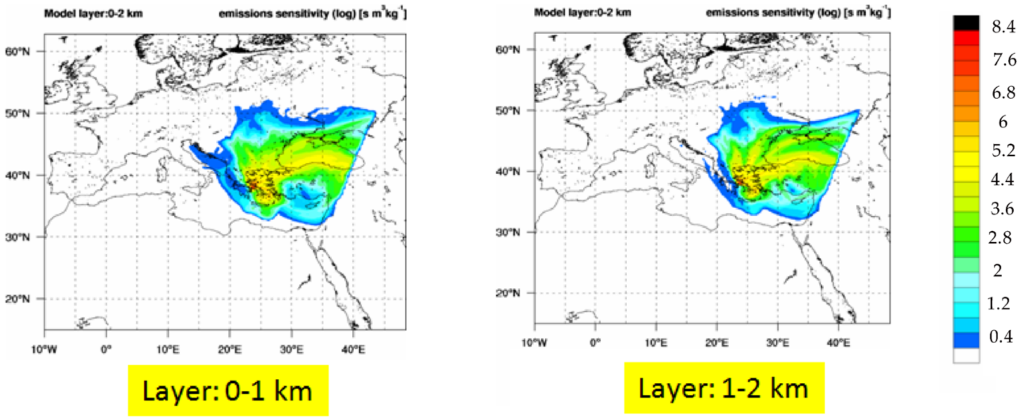

(a) 06:00 UTC

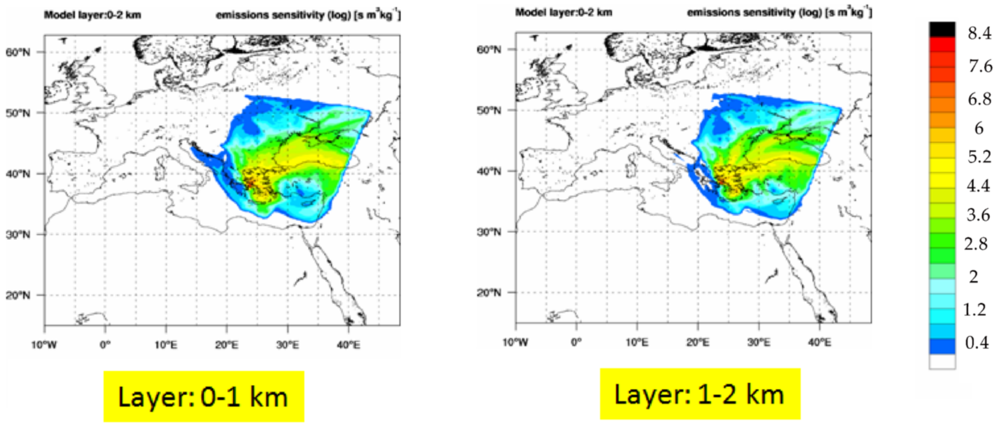

(b) 12:00 UTC

Σχήμα 7.46: *Ευαισθησία εκπομπών από το μοντέλο WRF στις 06:00 και 12:00 UTC για τα ατμοσφαιρικά στρώματα 0-1 km και 1-2 km (αέριες μάζες που έφθασαν πάνω από την Αθήνα στις 11 Ιουνίου 2014)*

το παράγοντα ενίσχυσης του συντελεστή οπισθοσκέδασης θεωρώντας δεδομένα του β και του RH για την περιοχή 2100-2500 m. Υποθέτουμε ότι σε αυτή την περιοχή οι περισσότερες από τις διαφοροποιήσεις στο συντελεστή οπισθοσκέδασης παρατηρούνται λόγω διαφοράς στο RH. Η υπόθεση αυτή επιβεβαιώνεται από την θετική βαθμίδα της δυναμικής θερμοκρασίας (βλέπε Σχήμα 7.50). Το ύψος αναφορά που χρησιμοποιήθηκε ήταν τα 2500 m όπου η σχετική υγρασία είναι 65%. Εφαρμόζοντας την παραμετροποίηση Hänel για έναν εκθέτη γ=0.85, πετύχαμε πολύ καλή προσαρμογή του μοντέλου πάνω στα δεδομένα για σχετικές υγρασίες 65-70% και 80-90%. Για την περιοχή RH μεταξύ 70-80% ο παράγοντας ενίσχυσης εκτιμάται από τα δεδομένα lidar να είναι μεγαλύτερος από τον παραμετροποιημένο παράγοντα. Αυτό πιθανότητα παρατηρείται επειδή η συγκέντρωση αερολύματος αυξάνεται από ανώτερα ή κατώτερα στρώματα της ατμόσφαιρας. Η ανακτούμενη τιμή για τον εκθέτη γ βρέθηκε ίση με 0.85 που είναι μία μέση τιμή των τιμών 0.47-1.35 που βρέθηκαν για αστικά σωματίδια στην πόλη του Παρισιού [162].

Στην περίπτωση των ξηρών ατμοσφαιρικών συνθηκών όπου το RH παραμένει σχετικά σταθερό σε σχέση με το ύψος και πάντοτε κάτω από 40%, οποιαδήποτε διακύμανση στο συντελεστή οπισθοσκέδασης σωματιδίων οφείλεται σε μεταβολή της συγκέντρωσης των σωματιδίων

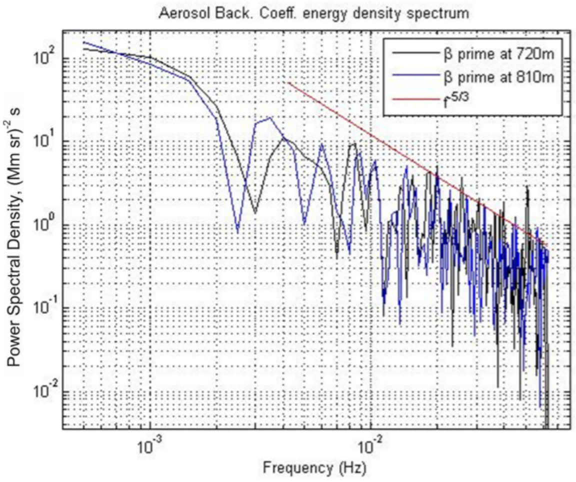

Σχήμα 7.47: *Συνάρτηση φασματικής πυκνότητας ισχύος του συντελεστή οπισθοσκέδασης στα ύψη 720 και 810 m για το χρονικό παράθυρο 06:40-07:45 UTC (11 Ιουνίου 2014)*

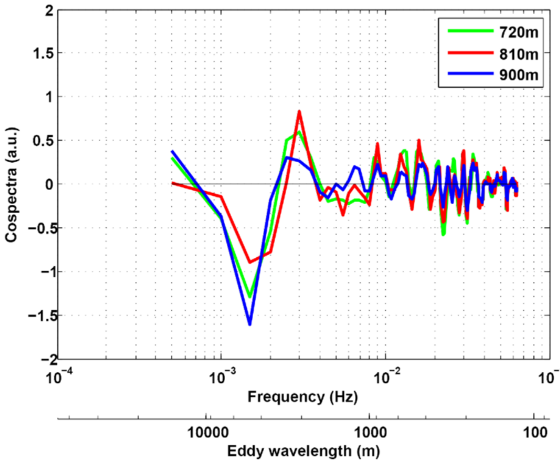

Σχήμα 7.48: *Διάφασμα των διακυμάνσεων του συντελεστή οπισθοσκέδασης των σωματιδίων και της κατακόρυφης συνιστώσας του ανέμου.*

ενώ στην περίπτωση της υγρής ατμόσφαιρας, μία αύξηση του συντελεστή οπισθοσκέδασης δεν συνεπάγεται απόλυτα και αύξηση των σωματιδίων. Γι΄ αυτό και διορθώσαμε το συντελεστή οπισθοσκέδασης από τα φαινόμενα ενίσχυσης λόγω υψηλού RH όπως φαίνεται στο Σχήμα 7.51. Οι διαφορές ανάμεσα στον διορθωμένο συντελεστή και τον αρχικό είναι ιδιαίτερα εμφανείς σε μεγαλύτερα ύψη (π.χ. στα 1200 m μετά τη διόρθωση ο συντελεστής οπισθοσκέδασης είναι δύο φορές μικρότερος από τον αρχικό συντελεστη).

Η ροή των σωματιδίων λόγω κατακόρυφης μεταφοράς υπολογίσθηκε μέσω της συνδιακύμανσης $C_{w,\beta}$ που είναι θετική όταν έχουμε ανοδικές κινήσεις και αρνητική όταν έχουμε καθοδικές κινήσεις. Η ροή των σωματιδίων παρουσιάζεται στο Σχήμα 7.52 για τα ύψη 700-1300 m. Η μετατροπή του συντελεστή οπισθοσκέδασης σωματιδίων β σε μάζα σωματιδίων έγινε μέσω του αλγορίθμου LIRIC χρησιμοποιώντας χαρακτηριστικές πυκνότητες για τα λεπτοειδή και χονδροειδή σωματίδια. Τελικά η ροή μάζας σωματιδίων που παρουσιάζεται στο Σχήμα 7.53

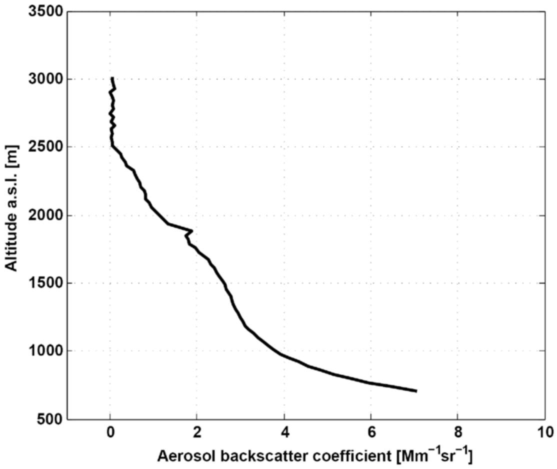

Σχήμα 7.49: *Μέση τιμή του συντελεστή οπισθοσκέδασης των αιωρούμενων σωματιδίων* $\overline{\beta}(z)$ *στο χρονικό παράθυρο 06:40-07:45 UTC (11 Ιουνίου 2014)*

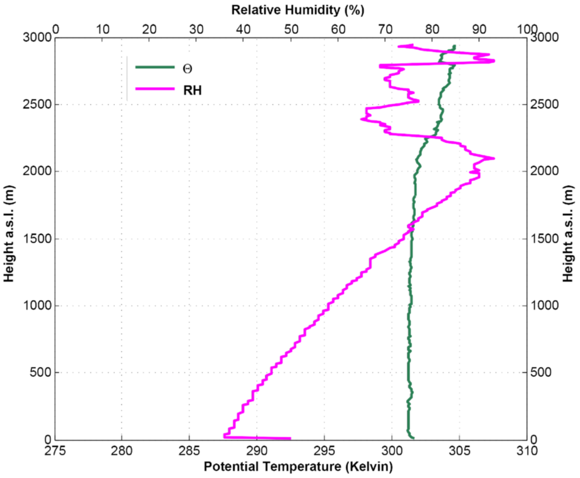

Σχήμα 7.50: *Δυναμική θερμοκρασία και σχετική υγρασία καθ' ύψος από δεδομένα ραδιοβολίσεων στις 12:00 UTC (11 Ιουνίου 2014)*

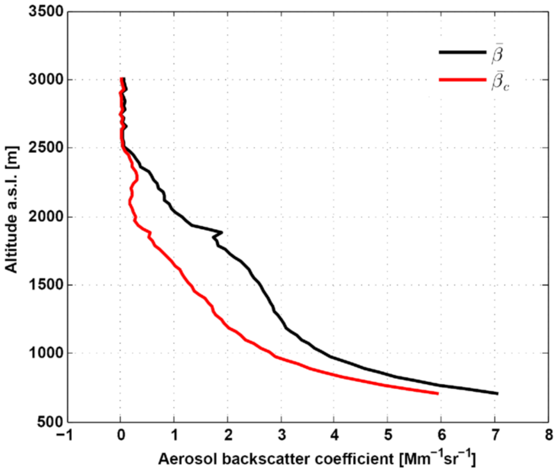

Σχήμα 7.51: *Μέση τιμή του συντελεστή οπισθοσκέδασης των αιωρούμενων σωματιδίων διορθωμένος από την επίδραση της σχετικής υγρασίας (11 Ιουνίου 2014)*

προέκυψε από έναν μέσω παράγοντα μετατροπής $\overline{C}$=23.5 $\mu g\ m^{-3} Mmsr$. Οι ανακτούμενες τιμές που κυμαίνονται στο εύρος 0.5-2.4 $\mu g\ m^{-2}s^{-1}$ στο ανώτερο ενεργό ΑΟΣ (800-1300 m) φαίνονται πολύ λογικές και χαρακτηριστικές για ΑΟΣ με παρουσία ανοδικών θερμικών ρευμάτων. Η μέση ροή μάζας είναι προσεγγιστικά 1 $\mu g\ m^{-2}s^{-1}$ που αντιστοιχεί σε ένα ρυθμός επαγωγής του ΑΟΣ ίσο με 100 $m\ h^{-1}$, ο οποίος ήταν ο μέσος ρυθμός αύξησης του ΑΟΣ στην Αθήνα τις αργότερες πρωινές ώρες (07:00-07:30 UTC) την καλοκαιρινή περίοδο.

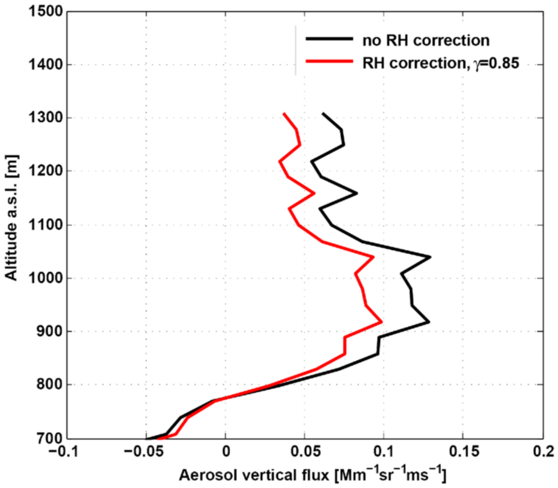

Σχήμα 7.52: *Υπολογισμός της κατακόρυφης ροής αερολύματος για το χρονικό παράθυρο 06:40-07:45 UTC (11 Ιουνίου 2014)*

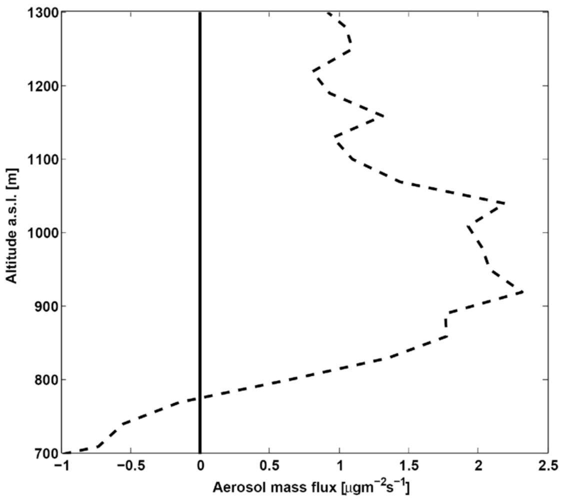

Σχήμα 7.53: *Εκτίμηση της ροής μάζας αερολύματος (11 Ιουνίου 2014)*

Κεφάλαιο 8: Επίλογος και μελλοντικές προοπτικές

Ο στόχος της παρούσας διδακτορικής διατριβής ήταν να μελετηθεί η επίδραση των αιωρούμενων σωματιδίων στις ιδιότητες των νεφών υπό την επίδραση τύρβης στο ΑΟΣ. Τα κυριότερα ευρύματα σχετίζονται με την ανάπτυξη νέφωσης στην περιοχή της κορυφής του ΑΟΣ όπως αυτά προέκυψαν από το πείραμα HygrA-CD. Παρατηρήθηκε ανάπτυξη νέφωσης τις ημέρες με βαθύ ΑΟΣ (~2-2.5 km). Στην Αθήνα, εμφανίζεται συχνά βαθύ ΑΟΣ όταν επικρατούν οι Ετησίες, όταν δηλαδή επικρατούν μέτριας προς ισχυρής έντασης άνεμοι από Βόρειες διευθύνσεις. Τότε, οι αέριες μάζες που φθάνουν στην ΕΠΑ προέρχονται από την Κωσταντινούπολη και τις βιομηχανικές ζώνες γύρω από την Μαύρη Θάλασσα, και συνεπώς μεταφέρουν πολλούς αέριους ρύπους. Παρόλο που υπάρχουν μεγάλες συγκεντρώσεις σωματιδίων στο ΑΟΣ, πιθανότατα οι συγκεντρώσεις ΠΣΝ που δημιουργούνται να μην είναι υψηλές. Μία πιθανή εξήγηση είναι ότι τα σωματίδια ανταγωνίζονται για τον ίδιο υπερκορεσμό και τελικά τα αερολύματα που είναι πλούσια σε ανόργανα στοιχεία ενεργοποιούνται επειδή είναι πιο υγροσκοπικά.

Σαν μελλοντικό βήμα, προτίνουμε να μελετηθούν και να χαρακτηρισθούν αυτές οι μεταφερόμενες αέριες μάζες ως προς την υγροσκοπικότητά τους. Τότε, μία μελέτη συσχέτισης ανάμεσα στον ρυθμό μεγένθυσης της διαμέτρου των σωματιδίων και την ενίσχυση στο συντελεστή οπισθοσκέδασης μπορεί να μας παρέχει ένα μεγάλο αριθμό από περιπτώσεις για να επιβεβαιώσουμε την τεχνική υπολογισμού της κατακόρυφης ροής σωματιδίων.

Για τις ημέρες που χαρακτηρίσθηκαν από ένα ρηχό ΑΟΣ (<1-1.5 km υπό Ν-ΝΔ ροές ανέμου), ο υπερκορεσμός δεν επιτεύχθηκε σε κανένα σημείο μέσα στο ΑΟΣ. Σε όλες τις περιπτώσεις με ροή αερίων μαζών από Ν-ΝΔ διευθύνσεις, η ατμόσφαιρα ήταν πολύ ξηρή και το επίπεδο που ξεκινούσε η συμπύκνωση των υδρατμών ήταν σε μεγάλο υψόμετρο εκτός του ΑΟΣ. Η διερεύνηση της ποσότητας των υδρατμών στο κατώτερο στρώμα της ατμόσφαιρας θα μας δώσει μία ένδειξη για το πόσο ξηρή είναι η ατμόσφαιρα επειδή τα σωματίδια που επικρατούν είναι η ερημική σκόνη από την Σαχάρα. Δεδομένου ότι τα σωματίδια σκόνης είναι μεγάλα σε μέγεθος, μπορούν να ενεργοποιηθούν σε νεφοσταγονίδια ακόμα και σε χαμηλότερα επίπεδα υπερκορεσμού. Επομένως, η μελέτη της περιεκτικότητας υδρατμών στην ατμόσφαιρα σε συνδυασμό με τη δυναμική του ΑΟΣ θα μας δώσουν απάντηση ως προς το πόσο συχνά δεν μπορεί να επιτευχθεί η συμπύκνωση στην ατμόσφαιρα και υπό ποιές συνθήκες.

Το βάθος το ΑΟΣ φαίνεται να είναι αντιστρόφως ανάλογο από την ταχύτητα του ανέμου όταν οι ροή του αέρα είναι από ΝΔ-Δ-ΒΔ διευθύνσεις. Τις ημέρες με μέτριας έντασης ανέμους, το ΑΟΣ δεν ξεπέρασε τα 2 km, ενώ στις περιπτώσεις με ισχυρούς ανέμους από ΝΔ-Δ-ΒΔ διευθύνσεις, το ύψος του ΑΟΣ θα ήταν μεγαλύτερο από 1.2 km. Η επίδραση της τύρβης στο βάθος του ΑΟΣ πρέπει να μελετηθεί περισσότερο για αυτές τις περιπτώσεις. Η πολύπλοκη τοπογραφία της Αθήνας ίσως να παίζει έναν κρίσιμο ρόλο στην δημιουργία νέφωσης όταν οι αέριες μάζες φθάνουν από παρόμοιες διευθύνσεις.

Ως ένα γενικό συμπέρασμα, το πείραμα HygrA-CD υπογράμμισε την σημασία των ταυτόχρονων μετρήσεων των αερολυμάτων και της δυναμικής του ΑΟΣ με σκοπό την κατανόηση της δημιουργίας νέφωσης στην περιοχή της κορυφής του ΑΟΣ. Ο αριθμός των νεφοσταγονιδίων αρχικά ορίζεται από την κατακόρυφη ταχύτητα του ανέμου, δεύτερον από την συγκέντρωση αιωρούμενων σωματιδίων και τελικά από την χημική σύσταση των αερολυμάτων. Στο μέλλον, παρόμοια πειράματα θα μας επιτρέψουν να εμβαθύνουμε στη μελέτη των αλληλεπιδράσεων μεταξύ αιωρούμενων σωματιδίων και νεφοσταγονιδίων που οδηγουν σε βροχή, καθώς αρκετά ερωτήματα παραμένουν ανοικτά ιδιαίτερα σχετικά με τα μικτής φάσης νέφη και τα νέφη πάγου.

List of Symbols

Greek Symbol	**Description**	**Units**
α_{aer}	aerosol extinction coefficient	m^{-1}
β_{aer}/β_p	aerosol backscatter coefficient	$m^{-1}sr^{-1}$
β_{att}	attenuated backscatter coefficient	$m^{-1}sr^{-1}$
β_m	molecular backscatter coefficient	$m^{-1}sr^{-1}$
γ	lapse rate	K/km
Γ_{adiab}	adiabatic lapse rate	K/km
δ_{m}	linear molecular depolarization ratio	
δ_{p}	linear particle depolarization ratio	
δ_{v}	linear volume depolarization ratio	
ϵ	kinetic energy dissipation rate	m^2s^{-3}
η_L	lidar optical efficiency	
ζ_{sph}	sphericity	
θ	scattering angle	rad
Θ	potential temperature	K
Θ_v	virtual potential temperature	K
κ	hygroscopic parameter	
λ	wavelength	m
ν	kinematic viscosity	m^2s^{-1}
μ_v	chemical potential for vapor species	J/kg
μ_w	chemical potential for water species	J/kg
ρ	air density	kg/m^3
ρ_{aer}/ρ_p	aerosol mass density	kg/m^3
ρ_w	water density	kg/m^3
σ	surface tension	J/m^2
σ_r	molecular extinction coefficient	m^{-1}
$\sigma_{s/a}$	surface tension of the solution/air interface	J/m^2
σ_s	scattering cross section	m^2
τ	transmittance	
τ_{aer}	aerosol optical depth	
ϕ	azimuthal angle	rad
ω	angular frequency	rad/s
$\overline{\omega}$	single scattering albedo	
Ω	solid angle	sr

Latin Symbol	**Description**	**Units**
Å	Ångström	
c_p	heat capacity of air	$Jkg^{-1}K^{-1}$
C_s	speed of sound	ms^{-1}
C^V	columnar volume concentration	m^3/m^2
D	particle diameter	m
d	dry particle diameter	m
D	diffusion coefficient	
e	vapor pressure	Pa
e_s/p^s	vapor saturation pressure	Pa
E	turbulence kinetic energy	m^2s^{-2}
E	collision efficiency	
E'	coalescence efficiency	
E_0	energy of transmitted laser pulse	W
E_i	incident electric field	V/m
E_l	internal electric field	V/m
E_s	scattered electric field	V/m
$f/\tilde{v}$	frequency	Hz
$f_M(D_p)$	mass distribution function	gm^{-1}/m^3
$f_N(D_p)$	number distribution function	m^{-1}/m^3
$f_S(D_p)$	surface area distribution function	m/m^3
$f_V(D_p)$	volume distribution function	m^2/m^3
G	Gibbs free energy	J
k	wavenumber	m^{-1}
$l/\Delta H_v$	latent heat of condensation	J/g
$\boldsymbol{\mathcal{L}}$	length scale PBL/eddy length	m
L_0	characteristic eddy length	m
m_v	vapor mass	kg
m_w	water mass	kg
M_a	molecular weight of air	g/mol
M_w	molecular weight of water	g/mol
n, m	refractive index	
n_w	number density	m^{-3}
N	total particle number	m^{-3}
N_d	total cloud droplet number	m^{-3}
N_{Ra}	molecular number density	m^{-3}
p	pressure	Pa
P	lidar signal	W
q	specific humidity	kg/kg
r	particle radius	m
r/r_L	mixing ratio of water vapor/liquid water in the dry air	g/kg

Latin Symbol	**Description**	**Units**
Q_e	Mie extinction efficiency	
Q_s	Mie scattering efficiency	
Ri	Richardson number	
Ri_b	bulk Richardson number	
Ri_f	flux Richardson number	
s	supersaturation	
s_c	critical supersaturation	
$\mathbf{S}$	Stokes vector	
S	total aerosol surface area	m^2/m^3
S	entropy	J/K
S_β	backscatter power spectral density	$m^{-2}sr^{-2}s$
S_k	spectral energy density	$m^{-2}sr^{-2}s$
S_λ	lidar ratio	sr
t	time	s
T	temperature	K
v	degree of ionic dissociation of the solute	
$\boldsymbol{\mathcal{V}}$	velocity scale PBL	ms^{-1}
V_0	characteristic eddy velocity	ms^{-1}
V_c/V_f	coarse-/fine-mode particle volume	m^3/m^3
V/V_t	total particle volume	m^3/m^3
w	vertical velocity	ms^{-1}
w_l	liquid water content of cloud	g/m^3
y	impact parameter	m
z	altitude, height	m

Constant	**Description**	**Units**
α_k	Kolmogorov's constant	
c_0	speed of light	ms^{-1}
g	gravitational constant	ms^{-2}
h	Planck's constant	kgm^2s^{-1}
k	Boltzmann's constant	J/K
R	ideal gas constant	$Jmol^{-1}K^{-1}$

List of Abbreviations

Abbreviation	Description
ACTRIS	Aerosols, Clouds, and Trace gases Research InfraStructure
AE	Ångström Exponent
AERONET	AErosol RObotic NETwork
AOD	Aerosol Optical Depth
APD	Avalanche Photo-Diode
BB	Biomass Burning
BC	Black Carbon
BL	Boundary Layer
BR	Backscattering Ratio
BRFAA	Biomedical Research Foundation Academy of Athens
CAPE	Convective Available Potential Energy
CAT	Clear Air Turbulence
CCN	Cloud Condensation Nuclei
CDSD	Cloud Droplet Size Distribution
DBS	Doppler Beam Swinging
DEM	National Centre for Scientific Research “DEMOKRITOS”
DMS	dimethylsulfide
EARLINET	European Aerosol Research LIdar NETwork
EKF	Extended Kalman Filter
EZ	Entrainment Zone
FT	Free Troposphere
FWHM	Full Width at Half Maximum
GAA	Greater Athens Area
GCM	General Circulation Model
HNMS	Hellenic National Meteorological Service
HR-Tof-AMS	High-Resolution Time-of-flight Aerosol Mass Spectrometer
HTDMA	Hygroscopic Tandem Differential Mobility Analyzer
HygrA-CD	Hygroscopic Aerosols to Cloud Droplets
HYSPLIT	HYbrid Single Particle Lagrangian Integrated Trajectory
ITaRS	Initial Training for atmospheric Remote Sensing
IFF	Interference Filter
IR	Infrared
LCL	Lifting Condensation Level
lidar	Light Detection and Ranging

LIRIC	LIdar Radiometer Inversion Code
LWC	Liquid Water Content
ML	Mixed Layer
MODIS	Moderate Resolution Imaging Spectroradiometer
NA	Numerical Aperture
ND	Neutral Density
NKUA	National and Kapodistrian University of Athens
NOA	National Observatory of Athens
NTUA	National Technical University of Athens
OC	Organic Carbon
OD	Optical Density
ODE	Optimal Distribution Estimator
PBL	Planetary Boundary Layer
PBS	Polarizing Beam Splitter
pdf	probability density function
PMT	Photomultiplier Tube
POM	Particulate Organic Matter
RH	Relative Humidity
RL	Residual Layer
RR	Rotational Raman
SBL	Stable Boundary Layer
SNR	Signal-to-Noise Ratio
SSA	Single-Scattering Albedo
UTC	Universal Time Coordinated
UV	Ultraviolet
VAD	Vertical Azimuth Display
VRR	Vibrational Rotational Raman
WRF	Weather Research and Forecasting

Contents

List of Figures

List of Tables

CHAPTER 1

The Planetary Boundary Layer

The PBL is the lowest part of the atmosphere wherein the majority of the human activities take place. A widely known definition for the PBL has been given by Stull (1988) [20] as following:
"The planetary boundary layer is that part of troposphere which is directly influenced by the presence of the earth's surface and responds to surface forcings with a timescale of about an hour or less".

1.1 Structure of the PBL

The structure of the PBL and its diurnal variation is presented in Figure 1.1. The physical mechanisms which contribute to the diurnal variation of the PBL structure are forcings such as evaporation and transpiration, heat transfer, frictional drag, pollutant emission and terrain induced flow modification. During daytime, there is a statically-unstable Mixed Layer (ML) which reaches its maximum depth in late afternoon. At night, a statically Stable Boundary Layer (SBL) forms under a statically neutral Residual Layer (RL). The RL contains the pollutants and moisture from the previous ML, but is not very turbulent. The layer close to the surface is the so-called surface layer. This layer is also known as the constant flux layer since turbulent fluxes are relatively uniform with height. The surface layer occupies approximately 10% of the Boundary Layer (BL) regardless of whether it is part of a ML or SBL. The free troposphere is clearly separated from the ML by the so-called Entrainment Zone (EZ). During nighttime, turbulence is diminished in the entrainment zone but a nonturbulent separation layer called the capping inversion remains [21].

Mixed Layer

The stronger dynamic characteristic of the ML is that of turbulence. Eddies of many different scales govern within the PBL and, hence, they are responsible for the transport of heat, momentum, water vapor and pollutants vertically. Usually, turbulence in the PBL is convectively driven even though a real well-ML can only occur in the presence of strong winds. The main source of convection is the ground surface since the air just above the surface is heated by the solar radiation and thermal plumes are being formed. In a cloudy boundary layer, radiative cooling from the top of the cloud layer is another convective source leading to

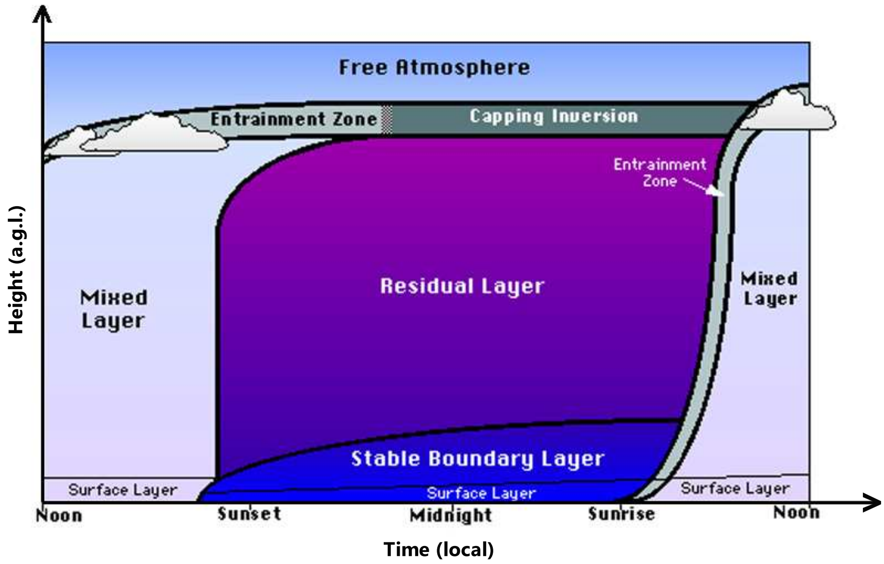

Σχήμα 1.1: *Structure of the PBL and its diurnal variation [20]*

thermals of cool air sinking from the cloud top. An example of simultaneous presence of such sources is a cool stratocumulus topped ML advected over warmer ground.

Apart from convection, another cause of turbulence initiation is the wind shear across the top of the ML. In particular, wind shear is responsible for the production of Clear Air Turbulence (CAT) and seems to be connected with the formation and breakdown of waves in the air, the so-called Kelvin-Helmholtz waves.

At the top of the ML, a stable layer known as the entrainment zone is responsible for the restriction of turbulence domain which functions as a cap for the rising thermals. For this reason, it is also called as capping inversion layer by referring to the temperature inversion that mostly happens at this height. Moreover, this inversion layer is responsible for the trapping of pollutants within the ML. Very frequently atmospheric gases and aerosols are used as tracers for the determination of ML height. In addition, water vapor mixing ratios tend to decrease with height because soil and plant moisture is evaporated and dry air is entrained towards the surface. Often, profiles of potential temperature and moisture are used to characterize the ML top [22].

Residual Layer

About half an hour before sunset, the thermals stop forming and atmospheric stability almost diminishes eddies' effectiveness. The ML gives its place to the RL which maintains its initial mean state variables and concentration variables very similar to ones of ML.

The RL often stays for a while in the morning before being entrained into the new ML. When the top of the ML reaches the base of the former's day RL, the ML growth becomes faster.

Stable Boundary Layer

The depth of the RL decreased with time. This can be explained by the fact that the bottom portion of the RL is transformed by its contact with the ground to a SBL. The SBL tends to suppress turbulence, however the developing nocturnal jet[1] enhances wind shears that tend to generate turbulence. During turbulent periods mixing becomes possible even at the SBL and during nonturbulent periods, the flow becomes decoupled from the surface. In this case, the top of the SBL is not well discriminated from the RL.

1.2 Different states of the PBL

The state of the PBL can be characterized as (a) unstable, (b) neutral or (c) stable [23]. Profiles of lapse rate $\gamma = {}^{-dT}/_{dz}$ with respect to the adiabatic lapse rate Γ_{adiab} and vertical gradient of potential temperature Θ are widely used for the characterization of the PBL state as Figure 1.2 illustrates.

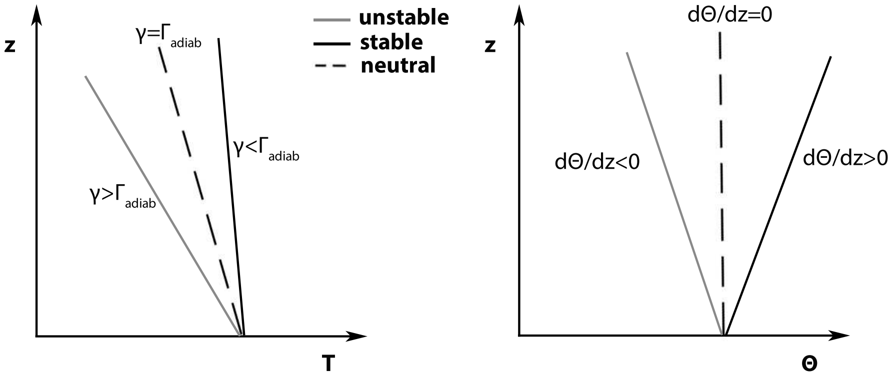

Σχήμα 1.2: *States of the PBL: (a) neutral: there is no temperature inversion and the lapse rate γ is equal to the adiabatic one Γ_{adiab}, (b) stable: there is a positive temperature gradient and γ is lower than Γ_{adiab} and (c) unstable: there is a negative temperature gradient and γ is higher than Γ_{adiab}.*

The main characteristics of each PBL state are summarized below:
neutral: there is no temperature inversion and the lapse rate γ is equal to the adiabatic one Γ_{adiab}. This is a state which occurs when sensible and latent heat flux from the surface are negligible. Then, turbulence is exclusively formed due to wind shear stress and not due to any ascending thermals. This state is rarely true during the day, however, a neutral PBL is generally observed in late afternoons.
stable: occurs usually during night time when the surface of the earth functions as a sink of heat. The air closer to the ground gets colder than the air at higher altitudes a positive temperature gradient occurs. In this case, the prevailing forces due to density difference subtract energy to the atmosphere which may result to nullification of the turbulence in the PBL.
unstable: occurs usually in the morning and noon when earth's surface functions as a source of heat and thermal plumes are formed. Such thermals may also take place in the marine PBL when the air close to the surface is more humid than the air above. Thus, instability which is indicated by a negative temperature gradient result to enhancement of turbulence in the PBL since the system is fed with energy.

Often, the characterization of PBL stability can be done through the gradient Richardson number *Ri* [24]:

---

[1] nocturnal jet or low-level jet is a physical phenomenon which occurs when the wind at ground level is moderate and the winds aloft accelerate to supergeostrophic speeds.

$$Ri = \frac{g}{\Theta}\frac{\frac{d\Theta}{dz}}{\left(\frac{du}{dz}\right)^2} \tag{1.1}$$

For a zero Richardson number the PBL is characterized as neutral, whereas a positive and a negative Ri implies a stable and unstable state, respectively.

1.2.1 Cloud development over the Planetary Boundary Layer

In general, clouds form when an ascending air parcel becomes saturated. Saturation only occurs by adding water, by cooling or by mixing processes. In particular, cumuliform clouds form in statically unstable air and are grouped as active clouds. Cumuliform clouds form within convective updrafts rising from the ground. The principle behind this mechanism is that unstable air tends to turbulently stabilize itself, unless there is continuous destabilization from the ground, due to the solar radiation hitting the surface. The highest thermals may reach their Lifting Condensation Level (LCL) if the atmosphere is rich to H_2O content. Other type of clouds close to the surface are formed by updrafts caused by turbulence due to wind shear. In reality, both buoyancy and shear contribute to these updrafts. All these type of clouds are developing in the entrainment zone as also illustrated in Figure 1.1 [25].

1.3 Formation and maintenance of turbulent flow in the PBL

As it is well-know from fluid mechanics, there are two states of the air flow in the atmosphere; the laminar and the turbulent flow. In the PBL, the flow is generally turbulent and the production of turbulence is either mechanically induced or thermally induced or even the product of the contribution of both. Several concepts that are of value when we speak about turbulence in the PBL are discussed below:

1. Turbulence is stationary if its statistical properties are time invariant. In simple words, stationarity condition is only satisfied if the mean value of a random variable is the same for a given averaging period.

2. Turbulence is homogeneous if the field is statistically invariant in all three dimensions. This may be approximately true in the horizontal dimension but it cannot be true in the vertical.

3. Turbulence is isotropic if the field is statistically invariant to axis rotation and reflection. By definition, an isotropic turbulence should be always homogeneous. In fact, PBL turbulence is quite anisotropic due to surface roughness and buoyancy effects.

The complexity of a turbulent flow implies the consideration of two components for any atmospheric quantity $s(x,t)$; the mean flow component $\overline{s}$ and a rapidly oscillating turbulent component s'. This convention was introduced by Reynolds (1895). Simply, we refer to the average $\overline{s}$ and the fluctuation s' of the random variable $s(x,t)$

$$s = \overline{s} + s' \tag{1.2}$$

with properties

$$\overline{s'} = 0 \tag{1.3}$$

$$\overline{ws} = \overline{w}\overline{s} + \overline{w's'} \tag{1.4}$$

$$\overline{w+s} = \overline{w} + \overline{s} \tag{1.5}$$

$$\overline{as} = a\overline{s} \tag{1.6}$$

where a is a constant. The first- and second-order moment of the random variable s is the mean value $\overline{s}$ and the variance $\overline{s'}$ respectively. The covariance[2] $\overline{w's'}$, where w the vertical wind component is an important quantity which is widely used in Section 1.3.1 representing flux[3] terms.

The set of equations governing the flow consists of three equations for the conservation of momentum (i.e., the Navier-Stokes equation), an equation for the conservation of mass (the continuity equation), an equation for the conservation of thermal energy (first law of Thermodynamics), an equation for the conservation of moisture (the humidity equation) and the equation of state (the gas law)[21]. For brevity reasons, in the current thesis only the continuity equation for the conservation of mass is included. The compressible form for any substance x_j with instantaneous advective velocity u_j is

$$\frac{\partial \rho}{\partial t} + \frac{\partial(\rho u_j)}{\partial x_j} = 0. \tag{1.10}$$

By considering the total derivative form $\frac{\mathrm{d}}{\mathrm{d}t} = \frac{\partial}{\partial t} + u_j \frac{\partial}{\partial x_j}$ Eq. (1.10) becomes

$$\frac{\mathrm{d}\rho}{\mathrm{d}t} + \rho\frac{\partial(u_j)}{\partial x_j} = 0 \tag{1.11}$$

The "shallow convection" assumption $\frac{1}{\rho}\frac{\mathrm{d}\rho}{\mathrm{d}t} \ll \frac{\partial u_j}{\partial x_j}$ may lead to the incompressible form of Eq. (1.11)

$$\frac{\partial(u_j)}{\partial x_j} = 0 \tag{1.12}$$

Such an approximation is possible only if (a) $\boldsymbol{\mathcal{V}} \ll 100m/s$, (b) $\boldsymbol{\mathcal{L}} \ll 12km$, (c) $\boldsymbol{\mathcal{L}} \ll C_s^2/g$ and (d) $\boldsymbol{\mathcal{L}} \ll C_s/f$ where $\boldsymbol{\mathcal{V}}$ and $\boldsymbol{\mathcal{L}}$ are typical velocity and length scales for the PBL, C_s the speed of sound and f the frequency of any pressure waves that may exist. Generally in mesoscale phenomena these conditions are met.

1.3.1 Turbulent Kinetic Energy Budget

As it is already mentioned above, the primary source of boundary layer turbulence is the wind structure and the temperature profile close to Earth's surface. If the lapse rate is unstable, turbulence is convectively generated. If it is stable, convection is suppressed and

---

[2] In statistics, the covariance is a measure of how much two random variables fluctuate together.

[3] Any ensemble average of the temporal derivative $\overline{\frac{\mathrm{d}s}{\mathrm{d}t}}$ can be written in flux notation:

$$\begin{aligned}\overline{\frac{\mathrm{d}s}{\mathrm{d}t}} &= \overline{\frac{\partial s}{\partial t}} + \nabla\cdot(\overline{\mathbf{u}s}) && (1.7)\\ &= \frac{\partial}{\partial t}\overline{(\overline{s}+s')} + \frac{\partial}{\partial x}\overline{(\overline{u}+u')(\overline{s}+s')} + \frac{\partial}{\partial y}\overline{(\overline{v}+v')(\overline{s}+s')} + \frac{\partial}{\partial z}\overline{(\overline{w}+w')(\overline{s}+s')} && (1.8)\\ &= \overline{\frac{\partial s}{\partial t}} + \nabla\cdot(\overline{\mathbf{u}}\overline{s}) + \frac{\partial}{\partial dx}\overline{u's'} + \frac{\partial}{\partial dy}\overline{v's'} + \frac{\partial}{\partial dz}\overline{w's'} && (1.9)\end{aligned}$$

with $\mathbf{u} = u\hat{\mathbf{i}} + v\hat{\mathbf{j}} + w\hat{\mathbf{k}}$. The last three terms are the eddy correlation terms in the three directions. Usually, the vertical flux divergence is dominant and the contribution of the terms $\frac{\partial}{\partial dx}\overline{u's'}$,$\frac{\partial}{\partial dy}\overline{v's'}$ can be neglected.

the instability associated with wind shear is responsible for the production of PBL turbulence. The generating processes of turbulence in the PBL can be well parameterized through the turbulent kinetic energy budget. By definition, turbulent kinetic energy per unit mass is given as

$$\bar{E} = \frac{\left(\overline{u'^2 + v'^2 + w'^2}\right)}{2} \tag{1.13}$$

where u, v, w are the x- , y- and z-component of the wind vector. The temporal variation of energy E is formulated as

$$\frac{\mathrm{d}E}{\mathrm{d}t} = S + B + T - \epsilon \tag{1.14}$$

where S is the production rate of turbulence due to wind shear effects

$$S = -\overline{u'w'}\left(\frac{\partial u}{\partial z}\right) - \overline{v'w'}\left(\frac{\partial v}{\partial z}\right) \tag{1.15}$$

with the statistical covariances $\overline{u'w'}$ and $\overline{v'w'}$ refer to the x- and y-direction kinematic eddy flux of W-momentum B is the energy production rate due to buoyancy effects

$$B = \frac{g}{\theta_v}\overline{w'\theta'_v} \tag{1.16}$$

with the statistical covariance $\overline{w'\theta'_v}$ being the vertical kinematic eddy heat flux, where θ_v[4] the virtual potential temperature. Hence, this buoyancy flux could be further analysed to the sensible and latent heat flux components.

$$\overline{w'\theta'_v} = \overline{w'\theta'} + 0.61\bar{\theta}\overline{w'q'} \tag{1.17}$$

The contribution of S term in the production of turbulent kinetic energy is significant near the surface layer and at the top of the mixing layer. It is proven that the ratio $-B/S$ is approximately equal to the flux Richardson number

$$Ri_f = \frac{g}{\theta_v}\frac{\overline{w'\theta'_v}}{\left(\overline{u'w'}\frac{\partial\bar{u}}{\partial z} + \overline{v'w'}\frac{\partial\bar{v}}{\partial z}\right)} \tag{1.18}$$

When the Richardson number is negative then both terms S and B have a contribution to the energy production in the turbulent boundary layer. When Ri_f has a positive value, the buoyancy term B subtract energy from the atmosphere and turbulence might reduce. There is always a threshold for Ri_f such as turbulent flow is developed in the PBL if and only if $Ri_f < Ri_f^{cr}$ [26].

The vertical transport term T in flux form

$$T = -\frac{\partial\left(\overline{w'E} + \frac{\overline{w'p'}}{\rho}\right)}{\partial z} \tag{1.19}$$

where ρ is the air density and $\frac{\partial\overline{p'w'}}{\partial z}$ the pressure transport term. Integrating over the whole depth of the PBL, the transport term T becomes zero.

The dissipation rate ϵ in Eq. (1.13) is the primary sink of turbulent kinetic energy. It expresses the rate at which the produced turbulent kinetic energy is converted into thermal internal energy.

---

[4] The virtual potential temperature is mathematically defined as $\theta_v = \theta(1 + 0.61r + r_L)$ with θ expresses the actual potential temperature, r and r_L the mixing ratio of water vapor and liquid water in the dry air respectively.

1.3.2 Turbulent energy spectrum

In the case of homogeneous and isotropic turbulence, Kolmogorov (1941) showed that turbulent kinetic energy has a spectral dependence. Figure 1.3 illustrates the energy spectrum as a function of eddy wavenumber k_w in the vertical. The (a) region is the energy containing part of the spectrum which is basically the large scale of turbulence where energy is produced by wind shear, friction or/and buoyancy. The energy that is fully developed at these large scales is not dissipated. On the contrary, through an energy cascade mechanism the kinetic energy carried by large eddies is transfered to newly induced eddies of smaller scales. This (b) region of spectrum is called the inertial sub-range. Within this part of the spectrum, under the Taylor's hypothesis of frozen turbulence [27], Kolmogorov showed that the spectral energy density of turbulent kinetic energy follows a $-5/3$ power law.

$$S\left(k_w\right) = \frac{\mathrm{d}E\left(k_w\right)}{\mathrm{d}k_w} \sim \alpha_{k_w} \epsilon^{2/3} {k_w}^{-5/3} \tag{1.20}$$

where α_k is the Kolmogorov's constant, and k_w is the wavenumber related to the eddy length scale L, as $k_w = 2\pi/L$.

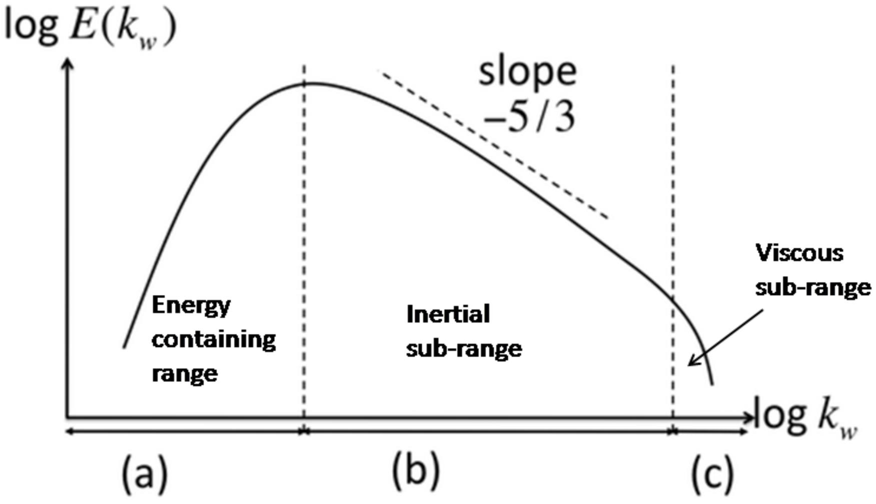

Σχήμα 1.3: *Energy spectrum of turbulence*

The (c) part of the spectrum is called the viscous sub-range. The turbulent kinetic energy is now carried from eddies of very small scales where viscous effects become important. The kinematic viscosity of the fluid ν can effectively dissipate the kinetic energy into internal energy. This is the second hypothesis that Kolmogorov introduced for very high wavenumbers and describes the universal microscale length of turbulence $\eta = \left(\frac{\nu^3}{\epsilon}\right)^{1/4}$.

1.3.3 Kinetic Energy Dissipation Rate from a Doppler lidar

The energy enters the turbulent atmosphere as a result of variations in the mean vertical wind component. In continuation to Section 1.3.2, the outer length scale of turbulent eddies L_0 supply the turbulent atmosphere with kinetic energy equal to V_0^3/L_0, where V_0 is the characteristic velocity for an eddy of size L_0. The respective energy dissipation to themal energy is of the order of $\epsilon \approx \nu V_0^2/L_0^2$ and it is negligible with respect to the corresponding kinetic energy. The eddies of such large scales are unstable and break down to smaller scale eddies ($L_1 < L_0$). The smaller eddies are unstable too and transfer their kinetic energy to even smaller eddies and so on ($L_n < ... < L_2 < L_1 < L_0$). This energy cascade process demonstrates that the kinetic energies per unit of mass and time of all scales are approximately equal. While the size becomes smaller, the dissipation $\nu V_n^2/L_n^2$ increases until the eddy becomes to a critical size l_0 where the kinetic energy is of the same order with the dissipation rate from kinetic energy to molecular thermal energy.

$$\frac{V_0^3}{L_0} \approx \frac{V_1^3}{L_1} \approx \frac{V_2^3}{L_2} \approx ... \approx \frac{V_n^3}{L_n} \approx \frac{\nu V_0^2}{l_0} \approx \epsilon \tag{1.21}$$

The kinetic energy dissipation rate ϵ can be estimated from a vertically pointing Doppler Light Detection and Ranging (lidar). The method is based on the assumption that turbulence is exclusively responsible for the broadening in vertical velocity spectra [28]. The variance of the observed mean Doppler velocity (i.e., the vertical wind component w) contains the ϵ information.

$$\begin{aligned} \overline{w'^2} &= \int_{k_0}^{k_1} S(k)\, dk \qquad (1.22) \\ &= -\frac{3}{2}\alpha\epsilon^{2/3}\left(k_1^{-2/3} - k^{-2/3}\right) \qquad (1.23) \\ &= \frac{3\alpha}{2}\left(\frac{\epsilon}{2\pi}\right)^{2/3}\left(L^{2/3} - L_1^{2/3}\right) \qquad (1.24) \end{aligned}$$

If both length scales L and L_1 lie within the inertial sub-range, the energy dissipation rate can be estimated directly from $\overline{w'^2}$.

In Figures 1.4 and 1.5, several quantities derived by the lidar backscattered signal are presented for a case of cloud-topped PBL. The cloud layer present at the PBL as a result of the turbulent flow can been distinguished at the top colorplot of Figure 1.4 (showing the attenuated backscatter coefficient). The retrieved ϵ is presented in the colorplot just below β. The retrieval of ϵ was possible through the measurements of vertical wind component and the respective uncertainty which are both illustrated in Figure 1.5. Large values of epsilon at around 03:00 UTC (06:00 local time) have a smaller associated fractional error as can be seen by the bottom colorplot of Figure 1.4. The fractional error in dissipation rate is calculated by

$$\frac{\Delta\epsilon}{\epsilon} = \frac{3\Delta\overline{w'}}{\overline{w'}} + \frac{\Delta L}{L} \tag{1.25}$$

where $\Delta\overline{w'}$ denotes the measurement error in the variance. This is basically due to low contamination of solar background noise to the lidar backscattered signal. The main source of turbulence should be the wind shear at this time of the day. Later in the day, at around 09:00 UTC (12:00 local time) the PBL reaches its maximum depth and clouds are still forming at the capping inversion layer. The production of turbulence should be a contribution of both wind shear and buoyancy.

1.4 Determination of the PBL height

The accurate determination of the PBL height has been studied by use of lidar remote sensing. The range-resolved backscattered signal $P(z)$ of elastic lidars contains information about the height of aerosol layers (see Chapter 3, Section 3.3). By considering the capping inversion layer as a physical border for the aerosols to move higher, aerosols can be considered as good tracers of the mixing layer height. In literature, several methods have been proposed for capturing of the convective PBL top.

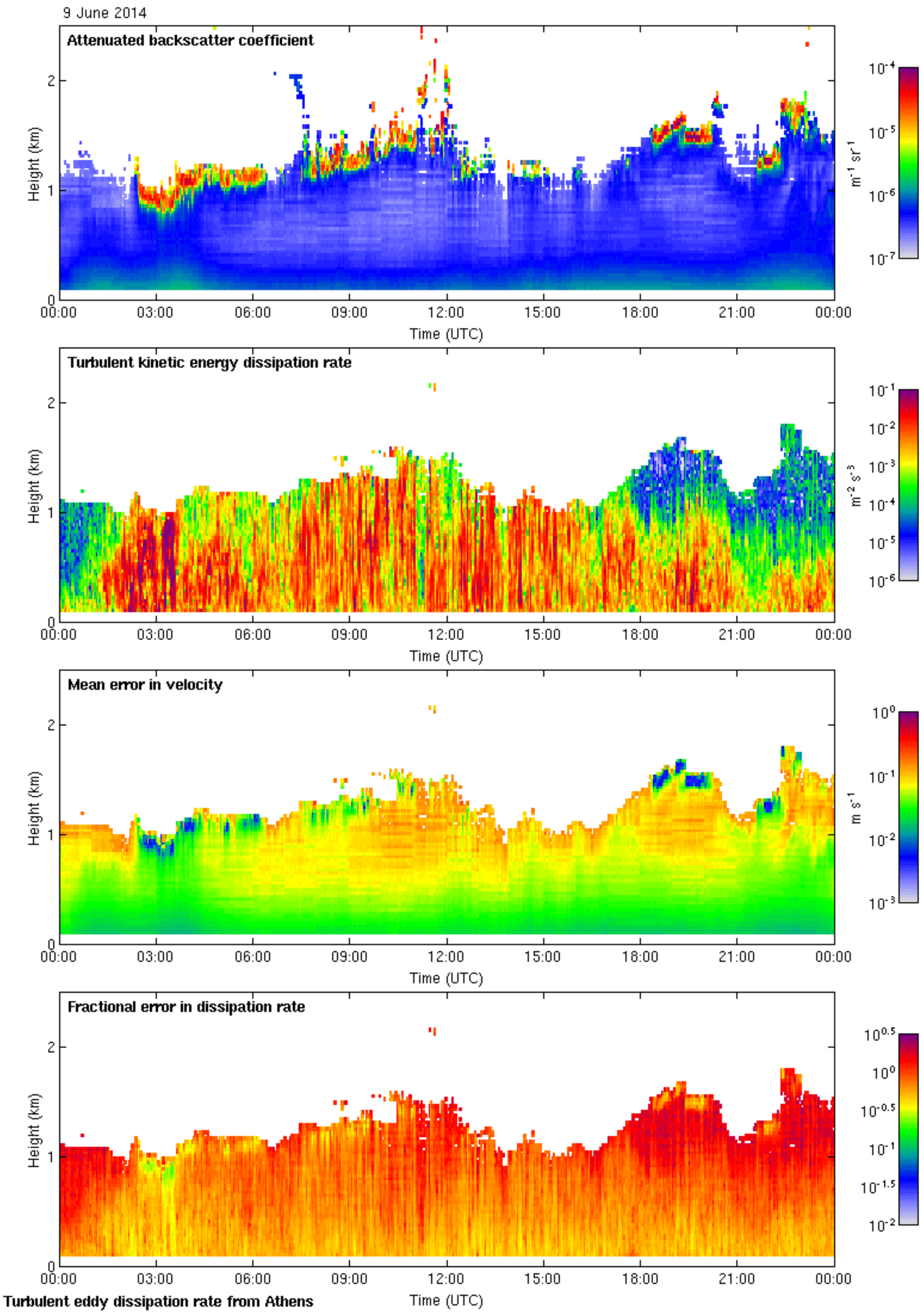

Σχήμα 1.4: *Range-resolved quantities from a Doppler lidar: the top colorplot depicts the attenuated backscatter coefficient. Just below, the ϵ dissipation rate is retrieved by the variance of vertical wind. The corresponding fractional error in the dissipation rate is associated to the mean error in vertical velocity and hence to the signal-to-noise ratio at a particular range gate [28].*

Gradient technique

This method is based on the fact that a sudden drop in the range-corrected signal lidar $P(z)\,z^2$ vertical profile means the geometric edge of an aerosol layer which usually occurs in the presence of a temperature inversion. The exact height of this sudden reduction in the lidar signal can be derived if the first derivative of the lidar signal with respect to height is

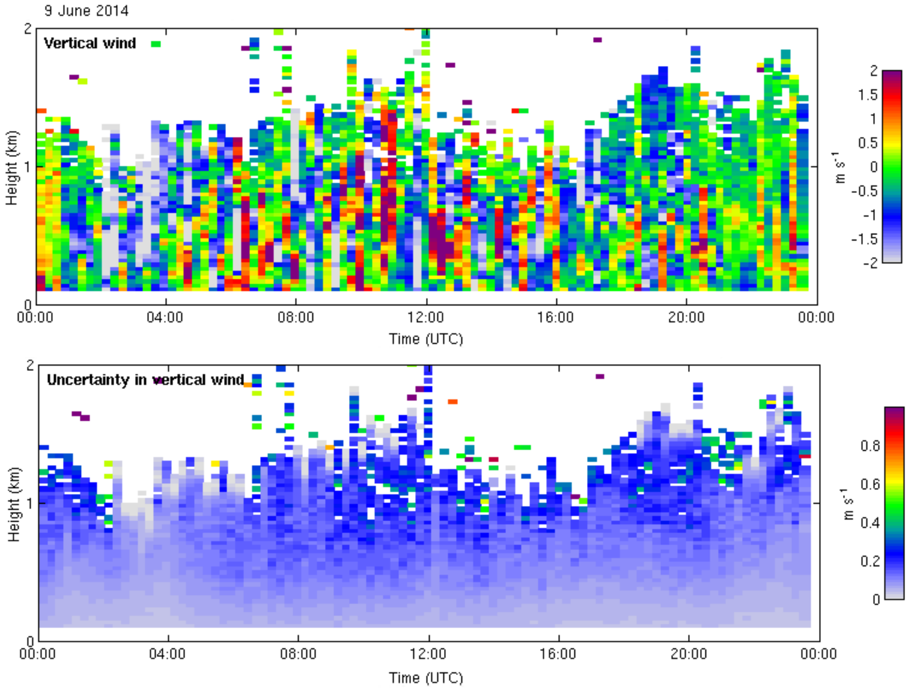

Σχήμα 1.5: *Vertical wind component from Doppler lidar: the top colorplot depicts the spatio-temporal variation of vertical wind component and the associated error is shown just below [28].*

calculated. Then, the PBL top is determined by a negative maximum [29].

$$z_{GM} \approx min\left(\frac{\mathrm{d}\left(P\left(z\right)z^{2}\right)}{\mathrm{d}z}\right) \tag{1.26}$$

Inflection point technique

The inflection point technique[30] is very similar to the gradient technique with the only difference that the second derivative of the lidar signal with respect to height should be calculated.

$$z_{IP} \approx min\left(\frac{\mathrm{d}^{2}\left(P\left(z\right)z^{2}\right)}{\mathrm{d}z^{2}}\right) \tag{1.27}$$

As a gerenal comment, it seems that this method is less accurate than the gradient method.

Haar wavelet transform technique

The wavelet transform method [31] has a slightly different concept. The lidar signal is supposed to be correlated with a function of a certain form like the Haar function here. The mathematical formulation of the wavelet correlation $W_f\left(a,b\right)$ for a certain window $[z_{min}, z_{max}$ is

$$W_f\left(a,b\right) = \frac{1}{a}\int_{z_{min}}^{z_{max}}\{P\left(z\right)z^{2}H\left(\frac{z-b}{a}\right)\}dz \tag{1.28}$$

with the Haar function being

$$H\left(\frac{z-b}{a}\right)=\begin{cases}1, & b-\frac{a}{2}\leq z\leq b\\ -1, & b<z\leq b+\frac{a}{2}\\ 0, & \text{otherwise}\end{cases}\tag{1.29}$$

where b defines the center of Haar function and is called translation of the function and a denotes the spatial extent or the so-called dilation of the function. The edge of the aerosol layer is denoted as a maximum in the convolution of lidar signal with Haar function

$$z_{HWT}\approx max\left(W_f\left(a,b\right)\right)\tag{1.30}$$

for $z_{min} < b < z_{max}$. This is lately considered as a stable and more accurate method for automatic identification of mixing layer tops.

The above methods have been compared with respect to their accuracy in capturing PBL top in cloud-free and cloudy conditions. In Figure 1.6 a typical convective cloud-topped PBL is illustrated. The color scale in arbitrary units demonstrates the range-corrected lidar signal at 1064 nm. The highest values denoted with red color indicate very strong backscattered signal from an atmospheric substance (e.g., clouds). Low values shown with blue color imply weaker light backscattering by air molecules and aerosols. All intermediate colors between blue and red mean higher aerosol concentrations in the atmosphere.

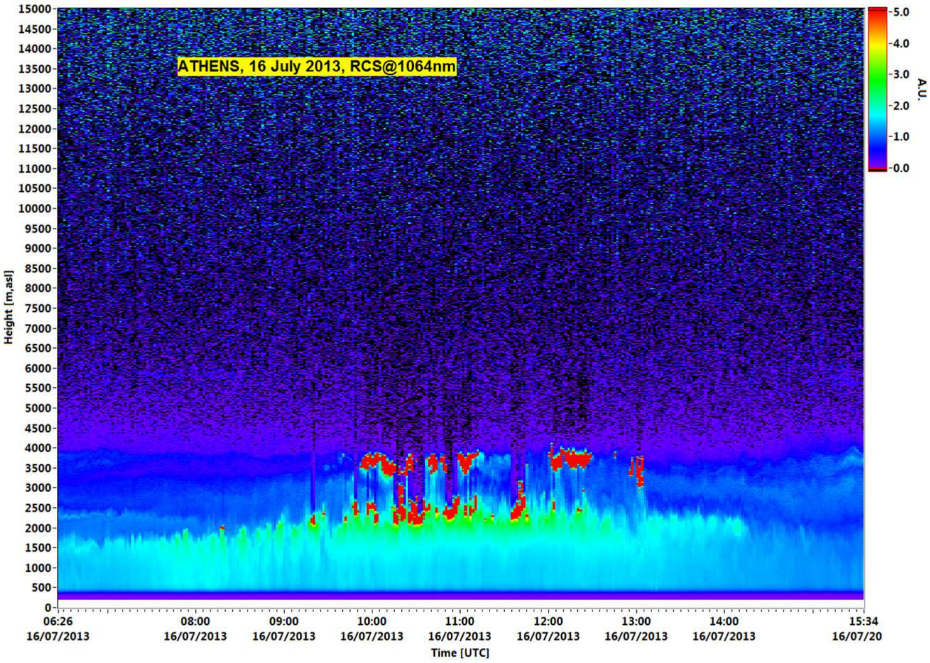

Σχήμα 1.6: *Cloud-topped PBL. The colorplot illustrates the time series of the range-resolved range-corrected lidar signal at 1064 nm. In this case of 16 July 2013, fair-weather clouds (the so-called cumuli) have been formed at the capping inversion layer of the convective PBL.*

As an example, the above methods are applied to two time intervals in the case of Figure 1.6. The first time interval of 06:45-07:00 UTC (i.e., 09:45-10:00 local time) corresponds to cloud-free sky whereas the second of 08:15-08:30 UTC (i.e., 11:15-11:30 local time) corresponds to cloudy atmosphere. The determination of PBL top is more accurate in the case of cloud-free conditions as it is shown in Figure 1.7. In the lidar profiles, there are two local minima/maxima at 1700 m and 2500 m which could be considered as the PBL top. The reason why the PBL top has been determined at approximately 1700 m and not around 2500 m is the a-posteriori information of a cloud presence with a base lower than 2500 m. The PBL top could not appear at a height higher than the cloud base. At a later timeslot, the presence of clouds in the lidar profiles makes the precise determination of PBL top more difficult. In Figure 1.8, we could not precisely identify the PBL top by applying any of the aforementioned methods. In fact, the strong backscattering from the cloud base might prohibit the successful discrimination of aerosol layer edge. For this reason, we frequently assume that cloud layer base coincides with the mixing layer top. Therefore, in the cloudy conditions of Figure 1.8, the PBL top has been determined at 2000 m.

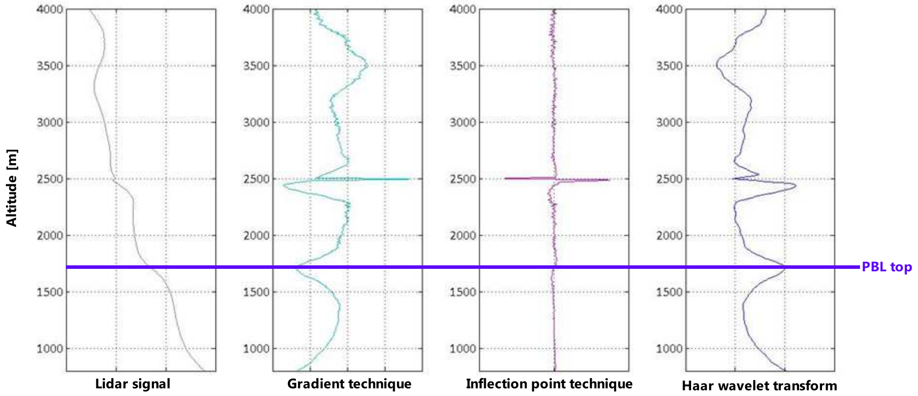

Σχήμα 1.7: *PBL top in cloud-free sky. The lidar profile corresponds to the time period 06:45-07:00 UTC (i.e., 09:45-10:00 local time) from the case study of 16 July 2013 shown in Figure 1.6. The first panel from left shows a profile of range-corrected lidar signal from 800 m (full overlap function) up to 4 km height. The gradient technique, inflection point and Haar wavelet transform methods have been applied to the lidar profile and is illustrated in panels above. PBL top seems to be approximately at 1700 m height above sea level.*

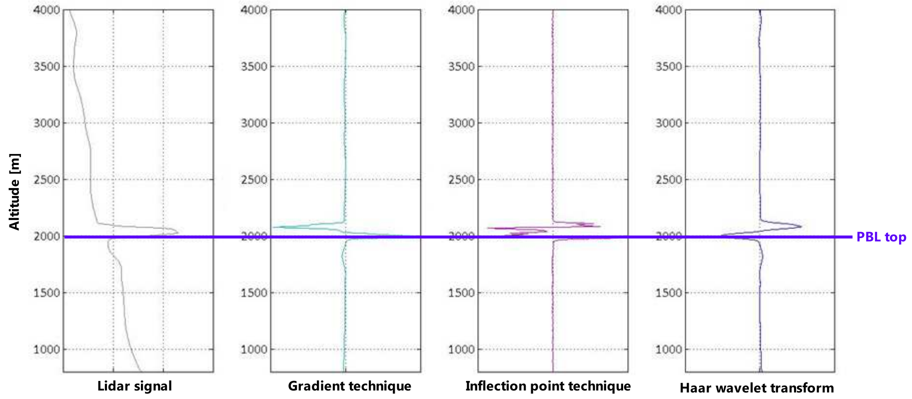

Σχήμα 1.8: *PBL top in cloudy sky. The lidar profile corresponds to time period 08:15-08:30 UTC (i.e., 11:15-11:30 local time) from the case study of 16 July 2013 shown in Figure 1.6. Similar to Figure 1.7 the panels from left to right depict a profile of range-corrected lidar signal from 800 m (full overlap function) up to 4 km, the gradient technique, inflection point and Haar wavelet transform methods applied to the lidar profile respectively. PBL top has been difficult to be identified for such a lidar profile because of the cloud layer at 2 km. Consequently, the PBL top has been determined to coincide with the cloud base at approximately 2 km height above sea level.*

Using lidar remote sensing for the continuous capturing of PBL top, an estimation of the entrainment rate is possible. For this specific convective PBL of Figure 1.6, the entrainment rate has been estimated of around 200 mh^{-1}.

Recently, the Extended Kalman Filter (EKF) technique [32] has been applied to the NTUA lidar data [33]. Against classical techniques, the EKF approach is based on estimating four time-adaptive coefficients of a erf-like curve model $h\left(z\right)$

$$h\left(z;z_{bl},\alpha,A,c\right)=\frac{A}{2}\{1-erf\left[\frac{\alpha}{\sqrt{2}}\left(z-z_{bl}\right)\right]\}+c, \tag{1.31}$$

where z_{bl} is an initial guess of the PBL height, α is the entrainment zone scaling factor, A is the amplitude of the erf transition, and c is the average molecular background at the bottom of the free troposphere. The PBL height over Athens in early summer (e.g., 15 May-22 June) showed a daytime maximum of 2.57 km during Etesian flows (N-NE wind directions) and a minimum of 0.37 km during Saharan dust flows (SW-S wind directions) [33].

In addition, apart from the PBL height determination from lidar data, radio soundings are reliable for the accurate PBL height derivation under various atmospheric conditions by calculating the bulk Richardson number Ri_b [34], [35], [36]. Ri_b at a certain altitude z is given as a function of the potential temperature and wind speed at this altitude and the surface [37]

$$Ri_b\left(z\right)=\frac{\frac{g}{\theta_{v0}}\left(\theta_v\left(z\right)-\theta_{v0}\right)z}{u^2\left(z\right)+v^2\left(z\right)}, \tag{1.32}$$

where θ_{v0} and $\theta_v\left(z\right)$ is the virtual potential temperature at the surface and at altitude z, respectively, g/θ_{v0} is the buoyancy parameter and $u(z)$, $v\left(z\right)$ are the two horizontal wind components at the altitude z. The PBL height is found at the altitude in which Ri_b exceeds a certain critical value Ri_{bc}. The optimal Ri_{bc} value varies with respect to the application. Typically, a Ri_b value larger than 0.25 is needed for the unstable PBLs [38]. In a recent study [39], the authors found that Ri_{bc} increases as the PBL becomes more unstable: 0.24 for strongly SBLs, 0.31 for weakly SBLs, and 0.39 for unstable boundary layers.

Chapter 2

Aerosol-cloud interactions and their impact to climate change

Atmospheric particles or particular matter may be solid or liquid with diameters from 0.002 μm to 100 μm. The lower bound is not strictly defined because there is no accepted criterion at which a cluster of molecules consist a particle. The upper bound corresponds to particles (like drizzle or sand) which are so large that they cannot remain suspended in the atmosphere for a long period because it does not have negligible terminal velocity. Larger particles in the atmosphere are usually produced in the form of precipitation (e.g., rain drops with diameter in the order of mm) and fall out of the atmosphere very fast. The atmospheric processes which result to interactions between aerosol and clouds are still unknown. This lack of knowledge adds more uncertainty in the prediction of future climate from the numerical models.

2.1 Climate change: state-of-the-art

After the industrial revolution, aerosol concentrations have been significantly increased and the response of the climate system to this sharp increase of emissions is still not well-predicted. Consequently, we need to improve our understanding of the role of aerosols and cloud droplets in the climate system. A recent overview of our current knowledge on the topic is summarized in [40]. It address many questions with respect to lack of experimental data to improve the General Circulation Models (GCMs). Provided that aerosol microphysics can be accurately measured in-situ, retrieval algorithms for vertically profiling aerosol optical properties with means of ground-based and space-borne remote sensing instruments should be developed. From the radiative forcing point-of-view, cloud microphysics (i.e., liquid water path and cloud fractional coverage) is the dominant contribution to planetary albedo that needs to be simulated in climate models. Cloud droplet concentration is the key microphysical mediator of aerosol - cloud interactions in warm clouds. It is governed by two factors: (a) the size of the aerosols that activate and (b) the updraft velocity of the air that transports the aerosols to the aerosol of activation. The most advanced GCMs represent the warm cloud formation using mechanistic parameterizations that use updraft velocity, particle size distribution and particle composition to predict the Cloud Droplet Size Distribution (CDSD).

The observations of aerosol-cloud relationships are still very limited [41], [42], [43]. Aerosol hygroscopicity required to account for humidity-dependent aerosol optical property changes when there are conditions in the atmosphere which initiate cloud formation. This is a barrier for deriving remote sensing observations in a systematic basis [44]. The number of activated cloud drops at cloud base depends on the aerosol CCN supersaturation activation spectrum and the cloud base updraft velocity. From satellite measurements AOD has been considered correlated to CCN [45]. However, because of no other options, AOD has been used as a proxy for CCN number. However, such an approach comes with many disadvantages:

- aerosols smaller than 0.1 μm in diameter are indistinguishable from molecular scattering from air molecules, whereas aerosols larger than ∼0.05 μm often serve as CCN especially in pristine environments, where small absolute changes in aerosol loading lead to large relative changes in cloud properties;
- aerosol swelling at high Relative Humidity (RH) causes uncertainty in determining the size distribution and total dry mass of particulate matter [46];
- cloud contamination of aerosol retrievals can exist [47];
- cloud-scattered light can alias nearby aerosol retrievals;
- the observed AOD are column integrated quantities and may come from aerosol layers other that those which interact with cloud base.
- clouds obscure the aerosol signal beneath them [48]

2.2 Aerosols: characterization and properties

Aerosols are defined as relatively stable suspensions of solid or liquid particles in a gas. Particles may be either directly emitted into the atmosphere or formed in the atmosphere via photochemical reactions. The former particles are called primary while the latter are called secondary particles. The formation mechanism for primary aerosols is twofold (a) *bulk-to-particle conversion* (e.g., mineral dust, pollen) and (b) *liquid-to-particle conversion* (e.g., sea salt). Secondary aerosols form only within the atmosphere from precursor substances like gases, hence through the physical mechanism is *gas-to-particle conversion*. Through physical and chemical aging processes, when the thermodynamic state of the atmosphere permits it, aerosols functions as CCN and enhance cloud development processes. Aerosols lifetime is generally short from few days to few weeks and they are transported to remote regions following always the wind trajectories. Finally, they are removed from the atmosphere via either dry deposition due to the gravitation force or wet deposition in the form of precipitation. Aerosols' life cycle is schematically illustrated in Figure 2.1.

It is common to discriminate atmospheric aerosols with respect their size range and their origin. We usually make a distinction between “fine” and “coarse” particles referring to particles smaller and larger than 1 μm respectively. In fact, particles falling in “fine” mode are further classified to the “nucleation”, “Aitken” and “accumulation” mode. The nucleation mode refers exclusively to secondary particles and its formation involves the nucleation of a new phase (liquid or solid) from a supersaturated gas phase. The other modes consist of both primary and secondary aerosols. Table 2.1 provides the most common aerosol types with respect to their size.

Aerosol sources have been grouped into two big classes; the *anthropogenic sources* due to emissions from industry and power plants and the *natural sources*. The most common aerosols of natural origin are mineral dust, sea salt, biological aerosols like bacteria and pollen. Aerosols of anthropogenic origin include sulfates, nitrates, Black Carbon (BC) and particular organic matter. Sulfates may also originate from natural sources through dimethylsulfide (DMS) which is emitted by phytoplankton species after their death. Due to the high concentration of oxygen to the atmospheric, DMS by its reaction with O_2 produce sulfur dioxide SO_2 and a

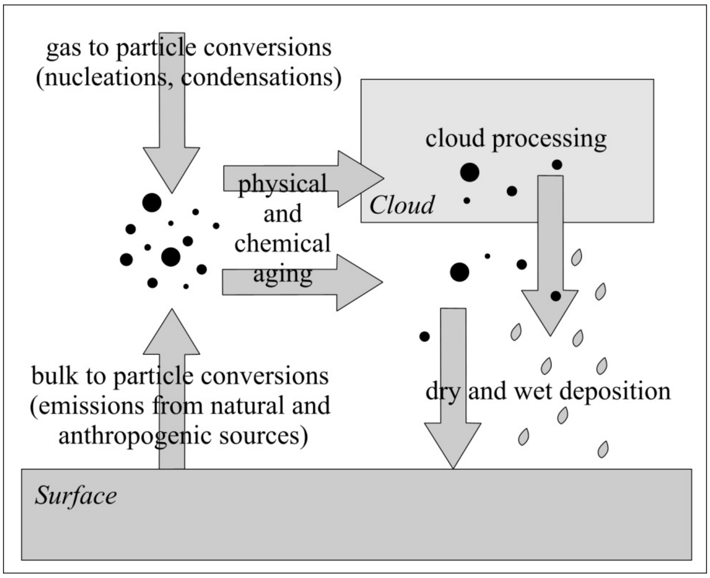

Σχήμα 2.1: *Life cycles of aerosols: sources and sinks [49]*

secondary product is sulfate SO_4^{2-}. Moreover, apart from the ocean, DMS is also released to the atmosphere through vegetation. Last but not least, volcanoes (via eruption and continuous degassing) may be substantial natural sources of SO_2 which functions as an effective sulfate precursor. SO_2 is mainly emitted to the atmosphere through anthropogenic activities among which ship emissions and fossil fuel combustion are the most dominant. Biomass Burning (BB) is an important source for BC and Particulate Organic Matter (POM); main products of incomplete combustion of biomass. High concentrations of BC and POM are due to fossil fuel combustion. The anthropogenic activities are also responsible for nitrates NO_x although one small portion of such emissions comes from natural sources; lightning and the soil which produces NO [50], [51].

Πίνακας 2.1: *Aerosol modes and possible types per mode*

Aerosol mode	**Diameter Range** [μm]	**Type**
Nucleation	$10^{-3} - 10^{-2}$	secondary aerosols
Aitken	$10^{-2} - 10^{-1}$	soot, sulfuric acid, organics
Accumulation	$10^{-1} - 1$	ammonium sulfate, ammonium nitrate, organics, smoke from BB or fires
Coarse	$1 - 10$	mineral dust, sea salt, pollen
Giant	$10 - 100$	mineral dust, sea salt

2.2.1 Chemical composition

The chemical composition of the aerosol stems from the mixing state among its different chemical components. The discrimination between externally and internally mixed aerosols is usually convenient however the true mixing state stands between these two extremes.

Frequently, we use the population mixing state to define the distribution of chemical compounds across the particle population and the morphological mixing state to express the distribution of chemical compounds within and on the surface of the particle.

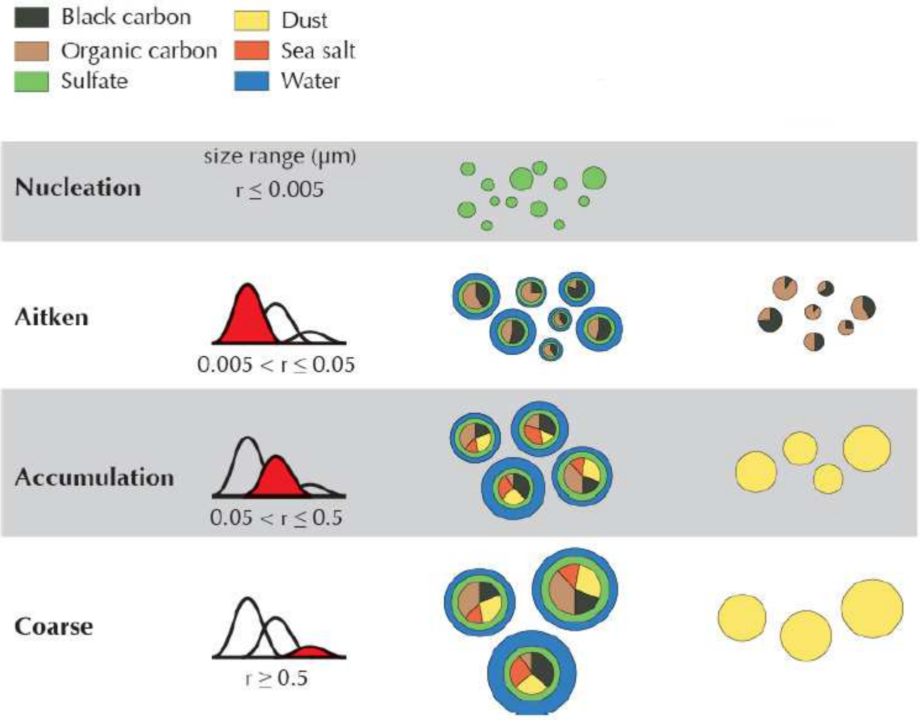

Σχήμα 2.2: *Aerosol mixing state Versus size range for the compounds: BC, OC, Sulfate, Dust and Sea salt. Internally-mixed soluble aerosols of a radius larger than 0.005 μm have an affinity to water. Picture was adapted from [50].*

The exact chemical composition depends strongly on the geographical location however, the most probable chemical components with respect to size range are summarized in Figure 2.2. Mineral dust is generally insoluble when is in pure form, close to the emitting sources. Nevertheless, when mineral dust is internally mixed with soluble components, like sea salt, the resulting aerosol becomes prone to water uptake. In nature, the internally-mixed particles can be decomposed into an insoluble and hydrophobic component, like Organic Carbon (OC), and a soluble and hygroscopic component, like sulfate.

Global distribution of aerosols

Aerosols are globally distributed as shown in Figure 2.3. The largest values of AOD appear in Asia and the tropical regions of Africa. The estimated contributions from different aerosol types in selected regions are shown in pie diagrams. In general, there is large spatial and temporal variability in global aerosol composition. Remote sensing from both space and ground together with in situ observations have substantially advanced an understanding of geographical aerosol distribution, but there are still large uncertainties especially in the characterization of aerosol chemical composition with respect to anthropogenic emissions [52].

2.2.2 The size distribution function

In this section, aerosols are characterized with respect to their size distribution signature. An aerosol composed of particles of a single size is called monodisperse, while an aerosol composed of particles of multiple sizes is called polydisperse [55]. The aerosol size distribution is most

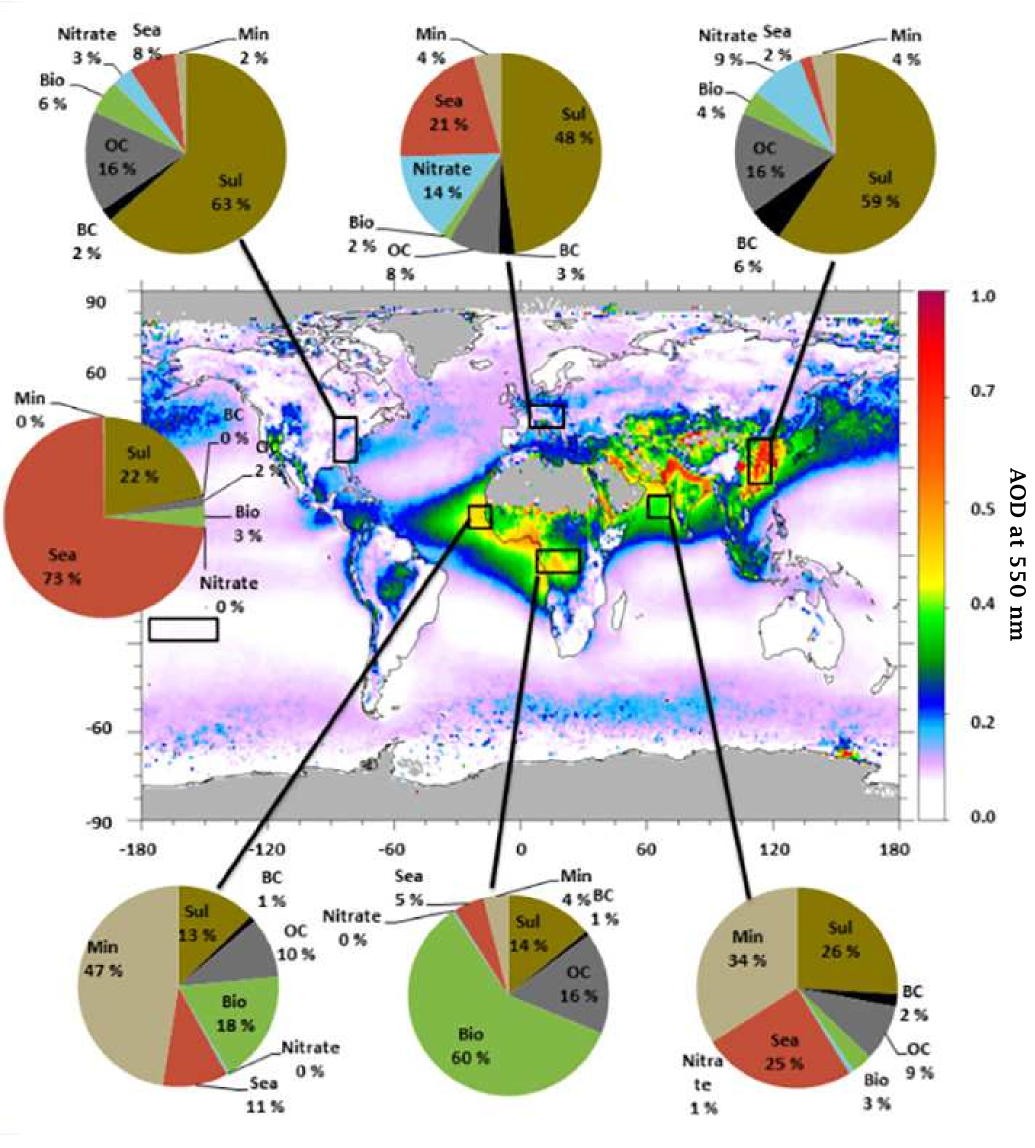

Σχήμα 2.3: *Global aerosol distribution as seen by Moderate Resolution Imaging Spectroradiometer (MODIS). AOD at 550 nm averaged over the 10-year period 2001-2010 [53]. Pie charts show how various aerosol types contribute to the total AOD for different regions, as estimated by a global aerosol model [54]. Aerosol types are Sul (sulfate), BC and OC from fossil fuel usage, Bio (OC and BC from BB), Nitrate, Sea (sea salt), and Min (mineral dust). Gray areas indicate lack of MODIS data. Some aerosol types, e.g. sulfate, have enhanced contributions to AOD due to hygroscopic growth. Picture was adapted from [52].*

frequently presented in the form of the number distribution function $f_N(D_p)$ $[\mu m^{-1} cm^{-3}]$ such as $f_N(D_p)\,dD_p$ expresses the number of particles per cm^3 of air having diameters in the range $[D_p,\ D_p + dDp]$. The total number of particles is estimated as the integration over all size ranges

$$N = \int_0^{\infty} f_N(D_p)\,dD_p \tag{2.1}$$

By differentiating both sides of Eq. (2.1) with respect to size we end up to the number distribution function $f_N(D_p)$

$$\frac{\mathrm{d}N}{\mathrm{d}D_p} = f_N(D_p) \tag{2.2}$$

Frequently, instead of the $f_N(D_p)$ notation, we use the normalized size distribution $\bar{f}_N(D_p) = \frac{f_N(D_p)}{N}$ $[\mu m^{-1}]$ such as the mathematical expression $\bar{f}_N(D_p)\,dD_p$ denotes the fraction of the total number of particles with diameter in the range $[D_p,\ D_p + dD_p]$ per cm^3 of air. In general, it is more convenient to express the number distribution as a function of $\ln D_p$ (or $\log D_p$) $f_N(\ln D_p)$ cm^{-3} in order $f_N(\ln D_p)\,d\ln D_p$ describes the number of particles with sizes within the range $[\ln D_p,\ \ln D_p + d\ln D_p]$[1]. Now the total number concentration is

$$N = \int_{-\infty}^{\infty} f_N(\ln D_p)\,d\ln D_p \tag{2.3}$$

and then in correspondence to Eq. (2.2)

$$\frac{\mathrm{d}N}{\mathrm{d}\ln D_p} = f_N(\ln D_p) \tag{2.4}$$

Provided that $\frac{\mathrm{d}\ln D_p}{\mathrm{d}D_p} = \frac{1}{D}$, the transition from linear space function $f_N(D_p)$ to logarithmic space function $f_N(\ln D_p)$ implies their relation

$$f_N(\ln D_p) = \frac{\mathrm{d}N}{\mathrm{d}\ln D_p} = \frac{\mathrm{d}N}{\mathrm{d}D_p}\frac{\mathrm{d}D_p}{\mathrm{d}\ln D_p} = D_p\frac{\mathrm{d}N}{\mathrm{d}D_p} \tag{2.5}$$

Since $f_N(D_p)$ is generally a log-normal distribution, $f_N(\ln D_p)$ will appear as a Gaussian distribution.

Analogous to the number distribution function the surface area $f_S(D_p)$ and volume distribution distribution function $f_V(D_p)$ can be expressed as under the assumption of spherical particles.

$$f_S(D_p) = 4\pi\left(\frac{D_p}{2}\right)^2 f_N(D_p) \tag{2.6}$$

$$f_V(D_p) = \frac{4\pi}{3}\left(\frac{D_p}{2}\right)^3 f_N(D_p) \tag{2.7}$$

Depending on the research application different aerosol property is useful. For instance, aerosol number distribution is important for the estimation of CCN number and CDSD. In radiative transfer models, total surface area is the preferred aerosol property [56].

---

[1] $f_N(D_p)$ notation is not preferable for two reasons: (1) dependence of the distribution on the size width dD_p and (2) the size width dD_p is universal along the whole range of diameters D_p and thus the tail of the distribution is not well represented. For example, if the considered size width is $dD_p = 1\mu m$, the number concentration around diameter 10 μm would be negligible in comparison to aerosol number around $1\mu m$ (i.e., $f_N(D_p = 10\mu m) \ll f_N(D_p = 1\mu m)$. However, with introducing the $f_N(\ln D_p)$ notation the size width in a logarithmic scale becomes dimensionless and increases as much as the diameter increases.

Like in Eq. (2.1), the total aerosol surface area S $[\mu m^2 cm^{-3}]$ and volume V $[\mu m^3 cm^{-3}]$ can be calculated

$$S = \pi \int_0^\infty D_p^2 f_N(D_p)\, dD_p = \int_0^\infty f_S(D_p)\, dD_p \tag{2.8}$$

$$V = \frac{\pi}{6} \int_0^\infty D_p^3 f_N(D_p)\, dD_p = \int_0^\infty f_V(D_p)\, dD_p \tag{2.9}$$

Sometimes, we refer to the aerosol size distribution moments to define the total number N, surface area S and volume V as the zeroth, second and third moment of the distribution respectively.

Since usually we consider different orders of size magnitude, the log notation is generally more convenient for surface area $f_S(\ln D_p)$ and volume size distributions $f_V(\ln D_p)$ too. The different forms of representation for the same aerosol is illustrated in Figure 2.4.

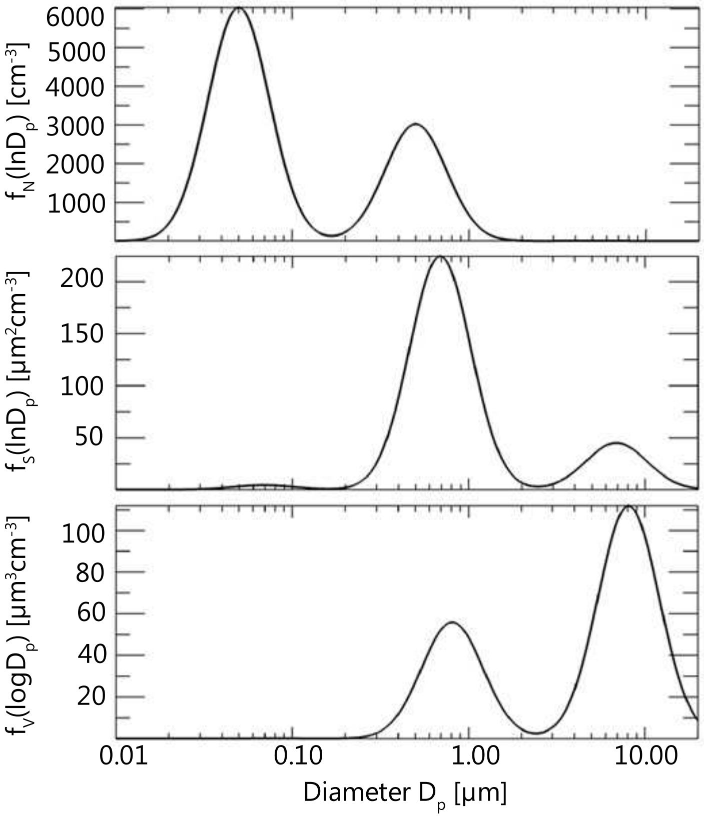

Σχήμα 2.4: *Aerosol size distribution: number, surface area and volume function.*

In specific applications, we need to produce the aerosol mass distribution function with respect to particle diameter $f_M(D_p)$ if all particles have the same density ρ_p $[\mu g \mu m^{-3}]$

$$f_M(D_p) = \rho_p f_V(D_p) = \frac{\pi \rho_p D_p^3}{6} f_N(D_p) \tag{2.10}$$

2.3 Formation of cloud droplets from activated aerosols

The atmospheric aerosols serve as potential CCN when water vapor condenses around them. The exact number of CCN depends on the supersaturation of the ascending air parcel and then maximum supersaturation implies the fraction of the CCN which turn to cloud droplets. Liquid water droplets are present in warm and mixed-phase clouds below the 0° isotherm. In general, we are interested in geometrical characteristics and microstructure of warm clouds. The complete drop size spectrum is a important microphysical property, sufficient to retrieve the total cloud droplet number concentration. The spatial homogeneity of the cloud in the vertical is evaluated through its Liquid Water Content (LWC). Typically, in warm clouds like cumuli, LWC increases with height above the cloud base, reaches a maximum at the upper half of a cloud and decreases towards the cloud top [57].

In this thesis, we focus on PBL clouds of cumuli type. A frequent discrimination of such clouds is through the PBL environment where they form and develop. We observe differences within clouds developed above land, the continental clouds, and those developed above oceans, the marine clouds. Most of marine clouds have concentrations in the order of few hundreds while continental clouds may contain droplets which exceed one hundred droplets per cm^3 of air. Such differences in clouds are related to the efficiency of continental aerosols to act as CCN. With respect to their LWC, marine and continental cumuli are very similar. Hence, the droplet size distributions in marine cumulus should be of a wider variance than in continental cumulus. This is an indirect effect that aerosols may have on clouds by modifying their microphysical properties in the presence of polluted air masses [57].

The next sections describe the growth mechanisms which take place in low level clouds; growth by condensation and growth by collision-coalescence.

2.3.1 Growth by condensation

Cloud droplet formation is via homogeneous nucleation[2], where water vapor becomes condensed and forms liquid water droplet. Such droplet is formed initially by random collisions of H_2O. The equilibrium of the system *“droplet-surrounding water vapor”* ensures the survival of this droplet as a competition between condensation and evaporation. The Gibbs free energy equation describes thermal and mechanical equilibrium of the system *“droplet-surrounding water vapor”*

$$dG = -SdT + Vdp + (\mu_v - \mu_w)\,dm_v + \sigma dA \tag{2.11}$$

where the first term SdT is related to the energy loss due to temperature change of a system with entropy S, the second term $Vdp + (\mu_v - \mu_w)\,dm_v$ describes the enthalpy change of the system as the summation of pressure difference dp in the air volume V and the internal energy of the system for the diffusion of mass from vapor to liquid water phase is expressed with the term $(\mu_v - \mu_w)\,dm_v$ where μ_v, μ_w are the chemical potentials for vapor and water species respectively and $dm_v = -dm_w = -n_w dV_w$ with n_w and V_w the number density and volume of the droplet. The last term σdA represents the mechanical work which performs a spherical droplet in association with its surface tension σ to the vapor-droplet interface area dA [58].

The chemical potential difference between vapor and liquid phase can be expressed in terms of vapor e and saturation vapor pressures e_s

$$\mu_v - \mu_w = KT \ln\left(\frac{e}{e_s}\right) \tag{2.12}$$

with K denoting the Boltzmann constant. Under isothermal and isobaric conditions the first two terms of Eq. (2.11) can be nullified [59] and by incorporating Eq. (2.12) the required Gibbs free energy change for the formation of a spherical droplet of radius r_d is given as

---

[2] Nucleation process is any physical process in which a free energy barrier needs to be overcome like in phase transition (e.g, vapor-to-liquid transition, liquid-to-ice transition).

$$\Delta G\left(r_d\right) = -4\pi r_d^2\sigma - \frac{4}{3}\pi r_d^3 n_w KT \ln\left(\frac{e}{e_s}\right) \tag{2.13}$$

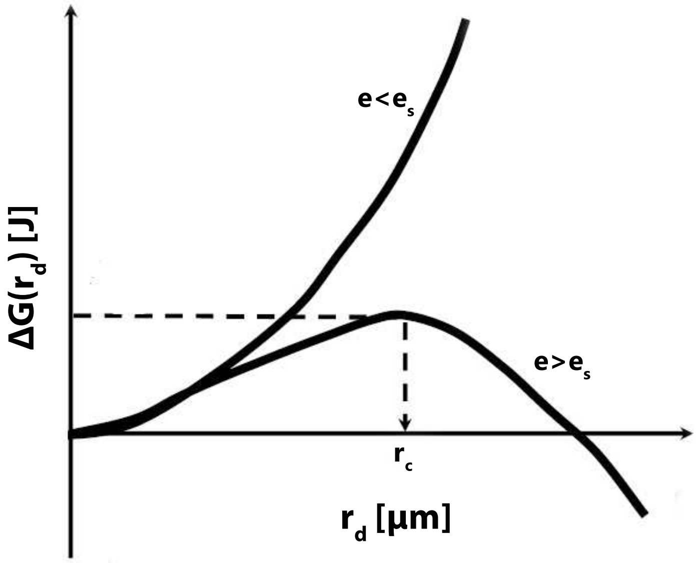

Σχήμα 2.5: *Gibbs free energy as a function of droplet radius for sub-saturated ($e < e_s$) and super-saturated ($e > e_s$) conditions. Picture adapted from [60].*

Droplet formation is only favored for $e > e_s$ when supersaturation occurs. This is because for saturation $e = e_s$ and sub-saturation $e < e_s$, Gibbs free energy increases monotonically with respect to droplet radius r_d as shown in Figure 2.5. On the contrary, for supersaturated conditions, $\Delta G\left(r_d\right)$ posseses a maximum at a critical radius r_c, beyond which the free energy decreases and condensation is more efficient than evaporation. Any droplet with radius larger than the critical radius will become activated and grow through condensation of water vapor. The critical radius can be defined through the Kelvin's formula for a certain temperature and vapor pressure of the air

$$r_c = \frac{2\sigma}{n_w KT \ln\left(\frac{e}{e_s}\right)} \tag{2.14}$$

In a true atmosphere, homogeneous nucleation cannot result to cloud droplet formation because the required supersaturation to activate a droplets is never reached. Instead, cloud droplets are being formed through heterogeneous nucleation, when water vapor condenses onto an aerosol activated as CCN. Only a small fraction of tropospheric aerosols act as CCN because aerosols may be of a very small radius, hydrophobic or even insoluble. In general aerosols can be classified as hygroscopic, neutral or hydrophobic. Nucleation on a neutral aerosol requires almost the same supersaturation as homogeneous nucleation. The hygroscopic particles serve generally as good CCN because they are soluble and have an affinity for water [61].

Cloud droplet activation

The role of CCN in cloud droplet formation by condensation, as stated above, is essential. Kelvin's equation (2.14) expresses saturation vapor pressure as a function of size. Raoult's law added a reduction in the equilibrium vapor pressure in the presence of dissolved materials. A non-volatile dissolved substance tends to lower the equilibrium vapor pressure of a liquid.

The effect is explained by the fact that when solute is added to a liquid, some of the liquid molecules in the surface layer are replaced by solute molecules. If the vapor pressure of the solute is less than that of the solvent[3], the vapor pressure is reduced in proportion to the amount of solute present. This effect can effectively decrease the equilibrium vapor pressure over a droplet. Therefore, a solution droplet can be in equilibrium with an environment at much lower supersaturation than a pure water droplet of the same size. The equilibrium vapor pressure of a solution droplet decreases by a factor $^{B}/_{r_d^3}$

$$\frac{e^{sol}}{e_s} = 1 - \frac{B}{r_d^3} \tag{2.15}$$

where B[4] depends exclusively on the type of solute for a given solvent (i.e., water in this case).

The curvature effect on the equilibrium vapor pressure can be included if we express Kelvin's equation (2.14) in terms of molar units [62]. The exponential curvature term which expresses the increase in saturation ratio over a droplet as compared to a plane surface should be added in Eq. (2.15).

$$\frac{e^{sol}}{e_s} = \left(1 - \frac{B}{r_d^3}\right) \exp\left(\frac{A}{r_d}\right) \tag{2.17}$$

where A is a constant for droplet liquid which depends on the absolute temperature of the droplet and its immediate surroundings

$$A = \frac{2\sigma M_w}{\rho_w RT} \tag{2.18}$$

with R being the ideal gas constant.

A good approximation for the Kelvin effect is to accept only the first two terms of the series expansion of the exponential function (2.17)

$$\frac{e^{sol}}{e_s} = 1 + \frac{A}{r_d} - \frac{B}{r_d^3} \tag{2.19}$$

The resultant total curve is called Köhler curve [63] and is presented in Figure 2.6. The curve shows that the solution effect is dominant when the radius is small, so that a very small solution droplet is in equilibrium with the vapor at RH<100%. If the RH gets increased, the droplet will grow until it finds its thermal equilibrium. Up to slightly above the level of RH~100%, any increase in the ambient humidity will always permit to the particle to grow to its equilibrium size. However, at the point that RH increases enough to reach the critical saturation ratio S_c (i.e., the peak of the curve in Figure 2.6), the droplet can grow beyond its equilibrium size r_c. Up this r_c size, the droplet is in a stable equilibrium with its environment: any change in saturation ratio allows the droplet to reach its equilibrium through the competing mechanisms of condensation and evaporation. But beyond the critical size r_c, the Kelvin term of Eq. (2.17) dominates and the equilibrium turns to unstable: the vapor diffuses to the droplet causing increase in its size without the need of increasing the ambient saturation ratio. Now the condensation nucleus is called *activated*. The critical values for radius and saturation ratio are those for which the Köhler curve gets a maximum

---

[3] Solvent is called a substance that dissolves a solute.

[4] B expresses the Köhler hygroscopicity coefficient

$$B = \frac{vM_w\rho_s}{M_s\rho_w} \tag{2.16}$$

where M_s and ρ_s is the molecular mass and density of solute, M_w and ρ_w the molecular weight and density of water and v the degree of ionic dissociation of the solute [57].

$$r_c = \left(\frac{3B}{A}\right)^{1/2} \tag{2.20}$$

$$S_c = 1 + \left(\frac{4A^3}{27B}\right)^{1/2} \tag{2.21}$$

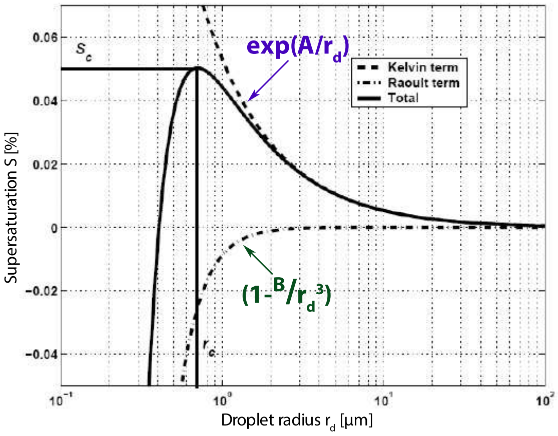

Σχήμα 2.6: *Köhler curve: the two contributions from the curvature (Kelvin) effect and solution (Raoult) effect are shown here. The critical supersaturation S_c is found at the peak of the curve. The critical supersaturation splits the droplet radius domain into two regions: (1) the stable equilibrium $r_d < r_c$ where droplet may grow in size for increased RH level but then returns to the initial size and (2) the unstable equilibrium $r_d > r_c$ where droplet enters the zone where is now considered an activated particle meaning that its radius will keep on growing. Picture was adapted from [64].*

The growth by condensation does not continue indefinitely because many droplets compete for the available water vapor in the environment [65]. The consequence on the drop size distribution is the narrow width in the dispersion of the distribution.

Growth rate of droplet size due to condensation

For an ambient saturation ratio $S = {}^{e}/_{e_s}$ the rate of increase in droplet radius due to condensation is given as

$$\frac{\mathrm{d}r_d}{\mathrm{d}t} = \frac{1}{r_d}\frac{(S-1)}{F_k + F_d} \tag{2.22}$$

where $F_k = \left(\frac{l}{RT} - 1\right)\frac{l\rho_l}{KT}$[5] is the thermodynamic-heat conduction term and $F_d = \frac{\rho_l RT}{De_s(T)}$[6] is the vapor diffusion term. The rate of growth is inversely proportional to the radius of the droplet. This explains the fact that growth by condensation initially is large but after a time interval that droplet reaches larger size, the rate of growth significantly drops. We observe a narrowing effect in drop size spectra meaning that droplet growth by condensation results to a monodispersed distribution.

---

[5] Latent heat of condensation l is the heat per unit mass needed to make the change from vapor to liquid phase.

[6] The diffusion coefficient D is the rate of mass flow of water vapor (and normal to) a unit area in the presence of a unit gradient in water vapor density.

2.3.2 Growth by collision-coalescence

Cloud droplets do not grow enough to produce raindrops with the mechanisms described in the previous section. The responsible mechanism for the further growth of droplets is the collision and coalescence of droplets. Collision can occurs when a large droplet (the collector) due to the force of gravity applied on it collides with smaller droplets which may lie in its path.

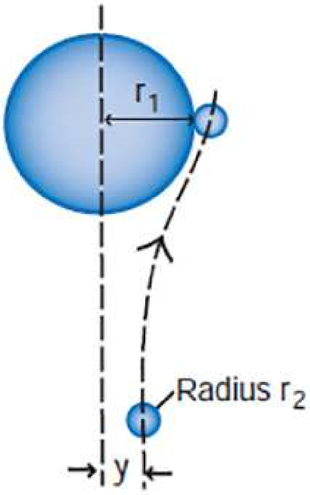

Σχήμα 2.7: *Description of a collision. The collector droplet with radius* r_1 *due to its large size falls down due to the gravity. The collecting drop with radius* r_2 *may have a successful collision with the collector drop if the impact parameter* y *is smaller than* (r_1+r_2) *[57].*

Suppose a collector drop of radius r_1 which overtakes a smaller droplet of radius r_2, like in Figure 2.7. As the collector drop approaches the droplet, the later will tend to follow the streamlines around the collector drop and, hence no collision occurs. An effective collision cross section depends on the critical distance between the center fall line of the collector drop and the center of the potential collecting droplet. This parameter y known as the maximum impact parameter is estimated at a large distance from the collector drop. Only if the distance of centers between the two droplets (r_1+r_2) is smaller than y, the collision will be successful. Hence, the effective collision cross section of the collector drop for droplets of radius r_2 is πy^2 and the geometrical collision cross section is $\pi(r_1+r_2)^2$. Finally, the collision efficiency E for a droplet of radius r_2 with a drop of radius r_1 is given as the ratio of effective over geometrical collision cross section

$$E = \frac{y^2}{(r_1+r_2)^2} \tag{2.23}$$

The collision efficiency depends significantly on the ratio $\frac{r_2}{r_1}$. When $\frac{r_2}{r_1} \gg 1$, the collision efficiency is low since the collecting droplet tends to follow the streamlines around the collector drop. Larger collecting droplets might move nearly in a straight line rather than on the streamlines around the collector drop and collision efficiency increases. In cases that fraction $\frac{r_2}{r_1}$ increases from 0.6 to 0.9, the collision efficiency drops for smaller collector drops because the terminal fall velocities of collector and collecting droplet become similar and thus relative fall velocity becomes small. Finally, when $\frac{r_2}{r_1} \sim 1$ collision efficiency tends to increase again as two nearly equal sized drops interact strongly to produce a closing relative velocity.

A small droplet may collide with a much larger one but then coalescence fails. This is typical when air is trapped between the touching surfaces of the two droplets. Coalescence

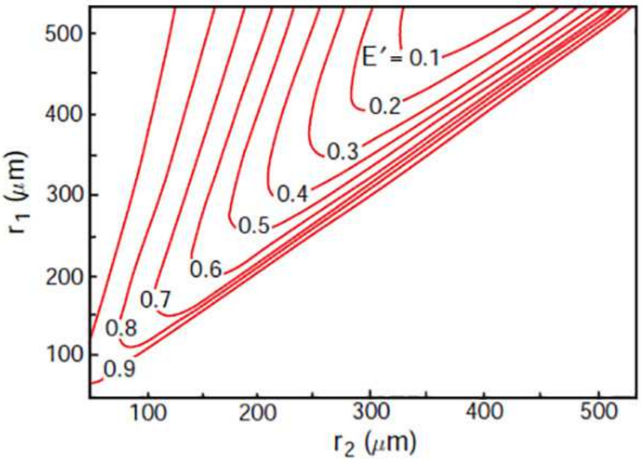

Σχήμα 2.8: *Coalescence efficiency E' for several size pairs of collector drops r_1 and colliding droplet r_2 [57].*

will occur only if the cushion of air is squeezed out before the collecting droplets rebounds at the collector's surface. The coalescence efficiency E' is then defined as the fraction of collisions which result to coalescence over total number of collisions. Coalescence efficiency depends on the relation of collector's radius r_1 versus collecting droplet's radius r_2 as illustrated in Figure 2.8. E' increases when the collector droplet collides with small droplets. As the colliding droplets increase in size, coalescence efficiency decreases until the point that collector droplet and collecting droplet become comparable in size where E' suddenly increases. Moreover, it has been observed that electrically charged droplets become more prone to coalescence.

Growth rate of droplet size due to collision-coalescence

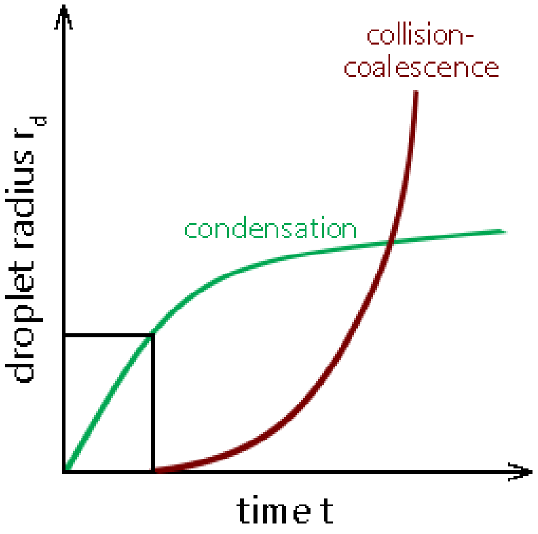

Σχήμα 2.9: *Growth rate of droplet radius with respect to time for two mechanisms: (1) Condensation expressed by Eq. (2.22) (2) Collision-Coalescence expressed by Eq. (2.24).*

Lets' assume $E' = 1$ and v_1, v_2 the terminal velocity of collector and collecting droplet respectively under the condition $v_1 \gg v_2$. The rate of increase in the radius of a collector drop due to collisions will be given as

$$\frac{\mathrm{d}r_1}{\mathrm{d}t} = \frac{v_1 w_l E}{4\rho_l} \tag{2.24}$$

where w_l is the LWC of cloud droplets of radius r_2 and ρ_l is the liquid water density. Unlike the droplet growth due to condensation, droplet growth due to collision-coalescence is a accelerating process responsible for the vertical development of clouds.

Figure 2.9 illustrates the growth rate of droplet radius with respect to time. The growth of cloud droplets due to condensation is the first mechanisms which takes place in cloud formation. When the droplet is small, the growth rate is large in accordance to Eq. (2.22). When the cloud droplet gets large enough ($r_d \sim 20\mu m$), the second mechanism of collision-coalescence is activated in the cloud. With time, the growth rate due to condensation gets very slow and the mechanisms becomes weak whilst the growth rate due to collision-coalescence is expressed by a function which becomes asymptote to y-axis. The latter explains the accelerating behavior of this mechanism which is further strengthened by the presence of turbulence in warm deep-convective clouds.

CHAPTER

3

Remote sensing of the atmosphere

Remote sensing is the science of making inferences about objects from measurements, made at a distance, without coming into physical contact with the objects under study. In general, remote sensing includes any method which uses a force field (i.e., acoustic, gravity, magnetic, electromagnetic etc.) in order to retrieve remotely information about an object. In atmospheric studies, remote sensing has received quite an attention, in the last decades, because of the many possibilities to retrieve information about the structure and the constitution of the atmosphere with a high vertical resolution (i.e. few meters depending on the instrument and the application). In the current work, lidar is the fundamental active remote sensing instrument which was used to study the structure of the lower troposphere (including the PBL) and to retrieve the optical and microphysical properties of aerosols.

3.1 Atmospheric lidar

A simplified representation of a lidar set-up is demonstrated in Figure 3.1. The transmission unit consists of a pulsed laser source, followed by a series of high reflection mirrors, and a beam expander which sends the collimated laser beam, vertically, up to the atmosphere. Part of the transmitted radiation is scattered by the atmospheric components (i.e., gases, molecules, aerosols, clouds) backward to the lidar system, where it is collected by a telescope. The backscattered laser light is driven to an optical analyzer where the optical signal is first spectrally separated, amplified and transformed to an electrical signal. Finally, the signal is digitized and stored in a computer unit for further signal processing and analysis.

3.1.1 Elastic aerosol lidar

The elastic backscatter lidar is the most common type of such system. The characterization of a lidar system, as an elastic one, demonstrates the principle of operation. The laser transmitter emits a beam at specific wavelengths and a receiving telescope collects the photons/signals which are elastically backscattered by the atmospheric molecules and particles. Elastic scattering is the process which occurs when the detected wavelength is the same with the transmitted one. In the current study, three wavelengths are emitted by a Nd:YAG laser in the atmosphere covering a wide part of the spectrum from the ultraviolet ($\lambda = 355$ nm) to the infrared ($\lambda = 1064$ nm) including the visible region ($\lambda = 532$ nm) too. Using these three wavelengths we are able to detect different types of aerosols, with the assumption that these aerosols are treated as spheres in order to be consistent with the Mie scattering theory.

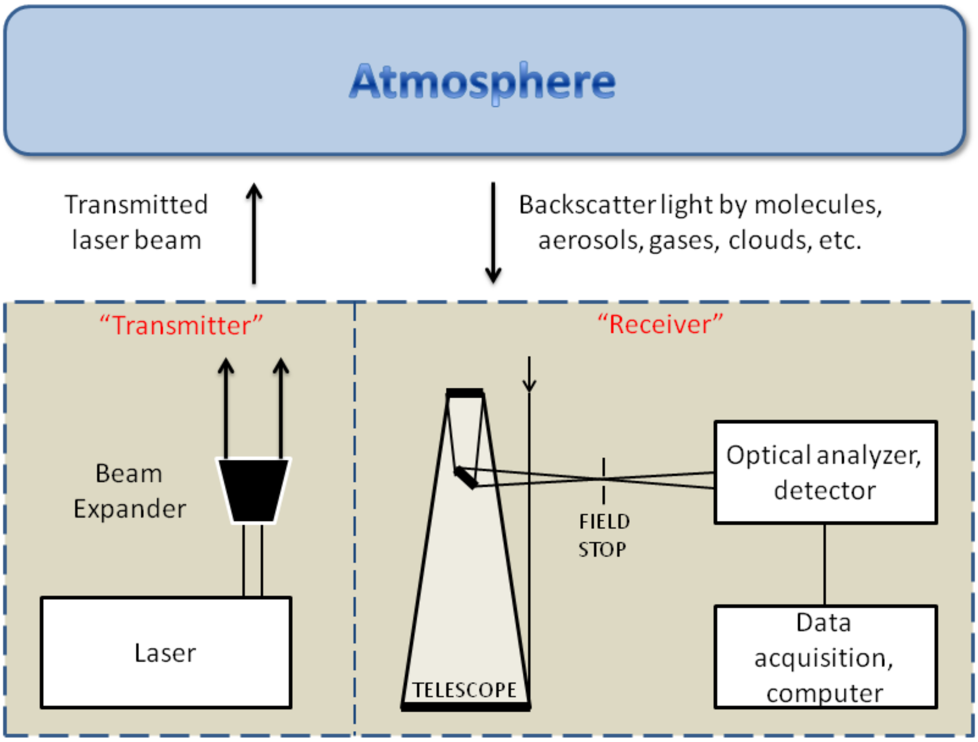

Σχήμα 3.1: *Lidar schematic configuration*

3.1.2 The NTUA Raman lidar EOLE

The NTUA Raman lidar system is called EOLE. The transmitting unit of EOLE is illustrated in Figure 3.2. The laser source is a pulsed solid state Nd:YAG (Neodymium-doped Yttrium Aluminium Garnet) laser (Spectra-Physics LAB-170-10 model). The primary laser beam is emitted at 1064 nm with 10 Hz repetition frequency. The energy of each laser pulse is, at the beginning, 850 mJ. The second and third harmonic frequencies of the Nd:YAG system (at 532 nm and 355 nm, respectively) are generated with the use of two non-linear KD*P (Potassium Dideuterium Phosphate) crystals. The laser beam has a Gaussian profile, a 10 mm diameter and its beam divergence is lower than 0.5 mrad. The characteristics of the first, second and third harmonic beams are summarized in Table 3.1.

Πίνακας 3.1: *Characteristics of laser harmonic beams*

	1064.2 nm	532 nm	354.93 nm
Energy per pulse (mJ)	260	300	240
Pulse duration (ns)	10	9	8
Degree of linear polarization (%)	>90% H-polarized	>90% H-polarized	>90% V-polarized

At the beginning of each measurement, while the laser is getting heated, the energy of the laser beam is controlled by an energy meter (see Figure 3.2). With the use of a 100% reflective

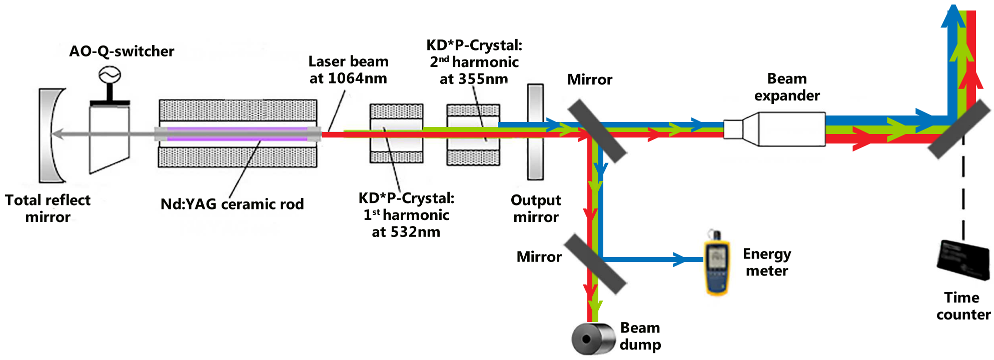

Σχήμα 3.2: *EOLE lidar Transmit Unit*

dichroic mirror only the laser beam at 355 nm is guided to the energy meter, whereas the other two laser beams at 532 and 1064 nm are transmitted through the mirror and guided to a beam dump. When the laser is sufficiently heated, the laser system is turned to the *Q-Switch* mode. The basic turning mirror is rotated 90° around its axis permitting to the three laser beams (at three wavelengths) to be expanded with a factor of 3 and then transmitted to the atmosphere via a highly reflective mirror (reflection coefficient of 99.9% at all three wavelengths). The beam expander is of a Galilean type. The simplest design of a Galilean beam expander consists of a concave lens followed by a convex lens as presented in Figure 3.3. The magnification power is defined by the ratio of the outgoing beam diameter D_{out} over the incoming beam diameter D_{in}. The EOLE beam expander consists of four lenses; three made of Barium crown $[N-BaK_2]$ and one of Calcium Fluoride $[CaF_2]$ manufactured by Dorotek GmbH. It has a magnification power of a factor 3 and thus, the outgoing expanded beam has a diameter of 30 mm. Likewise, the beam divergence is 3 times smaller (0.17 mrad Full Width at Half Maximum (FWHM) at 95% of energy) than the one of the incoming laser beam. The final turning mirror (manufactured by Laseroptik GmbH), which guides the laser beam to the atmosphere, is highly reflective at all operational wavelengths when the incident angle of the laser beam to the mirror is 45°.

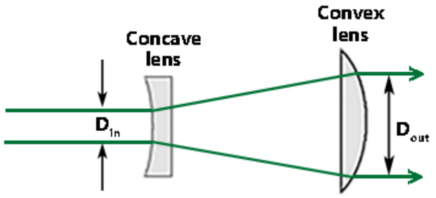

Σχήμα 3.3: *Beam expander: Galilean type*

The receiver unit of EOLE is illustrated in Figure 3.4. A telescope of Cassegrain type collects the backscattered light. At the bottom of the telescope there is a concave parabolic mirror of diameter d=300 mm and focal length f=600 mm. Hence, the telescope has a half-angle divergence θ of approximately 244 mrad. A simple illustration of the telescope focal point is given in Figure 3.5. The parabolic mirror has a substrate of magnesium fluoride $[MgF_2]$, an inorganic compound which increases the reflectivity at the spectral region of 355-1064 nm. On top of the MgF_2 a substrate of silicon dioxide $[SiO_2]$ protects the former. Finally, the reflectivity of the telescope mirror is above 85% for light beams at the detected

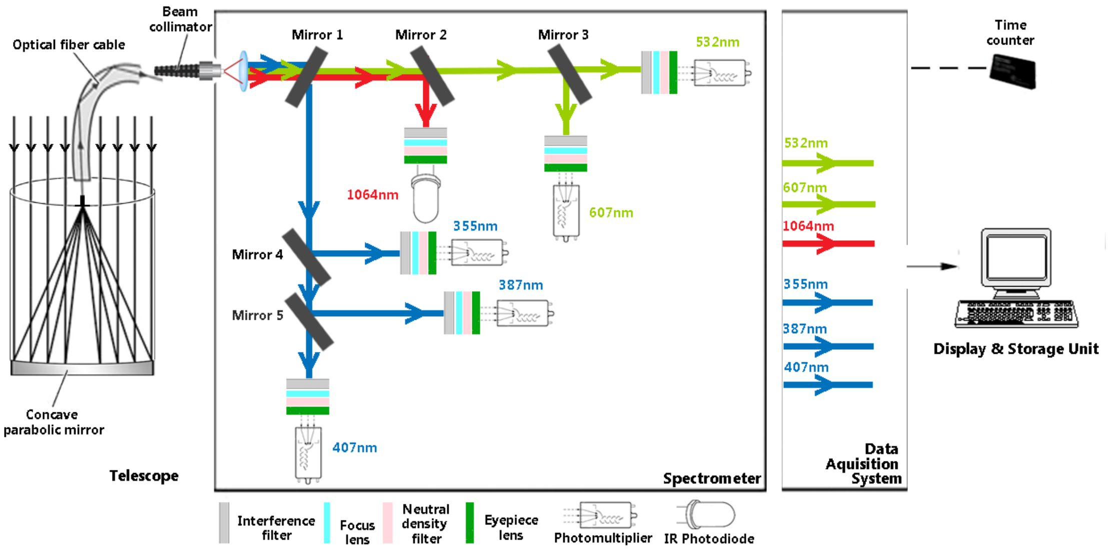

Σχήμα 3.4: *EOLE lidar Receiver Unit*

wavelengths (in particular lower reflectivity of 85% at 1064 nm and higher reflectivity of 98% at 355 nm).

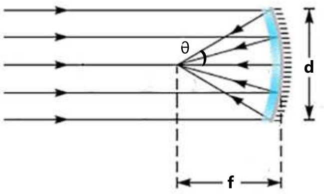

Σχήμα 3.5: *Focal length of a concave parabolic mirror*

The collected light is guided to the detection unit through an optical fiber. The latter is mounted to a base which can be mechanically adjusted at the focal point of the telescope mirror. The optical fiber is of a SiO_2 type manufactured by A.R.T. Photonics GmbH. The core of the fiber has a diameter of 1.5 while the cladding (with refractive index $n_2 > n_1$) is of a 1.6 mm diameter. A schematic configuration for the propagation of light in an optical fiber is presented in Figure 3.6. A light beam will be guided correctly through the fiber only if the light beam enters the core with an angle lower than a certain angle which is called acceptance cone angle of the fiber ϕ_a. Otherwise, the light beam will be lost in the cladding. The maximum angle of acceptance indicates the Numerical Aperture (NA) of the fiber which is a simplified measure of fiber's light gathering capacity. The NA is mathematically expressed as the sine of the acceptance cone angle. The NA of EOLE optical fiber has been estimated equal to 0.22±0.02 and the resulting final field of view of the EOLE system is 1.5 *mrad* (FWHM).

The received light which propagates through the optical fiber passes through a beam collimator before entering to the optical detection unit. The collimated light beam is splitted into several beams via a series of dichroic filters (beamsplitters), as can be seen in Figure 3.4. All beamsplitters have been manufactured by Omega Optical and their optical characteristics

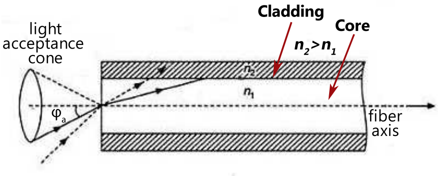

Σχήμα 3.6: *Light propagation in an optical fiber cable [66]*

(i.e., Reflectivity (R) and Transmissivity (T)) are presented in Table 3.2.

Πίνακας 3.2: *Beamsplitters of EOLE Optical Detection Unit: Reflectivity (R) and Transmissivity (T) of dichroic filters shown in Figure 3.4*

	355 nm	387 nm	407 nm	532 nm	607 nm	1064 nm
Mirror 1	$R >$ 95.0%	$R >$ 95.0%	$R >$ 95.0%	$T = 88.5\%$	$T = 87.5\%$	$T = 85\%$
Mirror 2				$T = 85.0\%$	$T = 88.5\%$	$R =$ 99.9%
Mirror 3				$T = 91.5\%$	$R =$ 99.0%	
Mirror 4	$R =$ 99.0%	$T = 82.0\%$	$T = 82\%$			
Mirror 5		$R =$ 96.5%	$T = 76.0\%$			

The spectrally separated light beams are transmitted through a series of optical filters so as the intensity of the backscattered signal as well as the atmospheric background noise are both reduced. These optical filters consist of a narrow-band Interference Filter (IFF), followed by a focusing lens and a/some Neutral Density (ND) filter(s). The ND filters (manufactured by Melles Griot-CVI) aim to reduce the signal intensity of the elastically-backscattered light beams at 355, 532 and 1064 nm. Finally, an eyepiece lens is used right before the light beam enters the photo-detectors. Thus, the Signal to Noise Ratio (SNR) is certainly increased provided that the narrow spectral width of the interference filters allow only the detected wavelengths to be transmitted through the filter. The optical characteristics of the interference filters are presented more precisely in Table 3.3.

Πίνακας 3.3: *Optical characteristics of interference filters used in EOLE Optical Detection Unit as depicted in Figure 3.4*

Detected wavelength [nm]	Transmissivity [%]	Optical Density	Bandwidth [nm]
354.9	47.5	5	1
386.6	77	8	0.9
407.5	51	10	0.41
532	45	0.5	4
607.4	78	8	1.06
1064	45.7	4	0.97

In principle, the transmissivity (T), the Optical Density (OD) and the spectral width are the critical criteria for the selection of the IFF. The OD of an interference filter demonstrates the blocking ability of the filter with respect to the amount of radiation which is transmitted through it. Mathematically speaking it is related to the filter percent transmission (T) as $OD = -\log_{10}(\frac{T}{100})$. The bandwidth of a filter is a wavelength range used to indicate the part of the spectrum that light beam is transmitted through it. It is also referred as FWHM. The focusing lenses have a focal length of 40 mm and a diameter 25.4 mm. The ND filters are only used at the backscattered lidar signals at 355, 532 and 1064 nm, to reduce their amplitude, as there is a strong elastic backscattering component from the lower layers of the atmosphere. This leads to saturation on the data acquisition unit and hence, ND filters are necessary as light intensity attenuators. The current ND filters used in EOLE detection unit are able to attenuate the collected light up to 70%. Figure 3.4 shows the presence of ND filters at all detected wavelengths. The ND filters used at 387, 407 and 607 nm reduce the collected light only up to 20%, the inelastic backscattered light from atmospheric gases is, in general, weak. The eyepiece lens consists of two plano-convex lenses (doublet type[1]) manufactured by Thorlabs S.A. The effective focal length is 29.79 mm for all wavelengths, except for 1064 nm where the total focal length is 14.89 mm. This difference results from the use of an avalanche photodiode which has a detection cross-section of 1.5 mm, much smaller than the one of photomultipliers (used at all other wavelengths) which is 5 mm. The use of an eyepiece lens is certainly important because of the inhomogeneity of radiation's spatial distribution when reaching the receiving area of the photo-detectors. When eyepiece lenses are used, the advantages are: · the spatial inhomogeneity problem at the photocathode of the photomultiplier is eliminated and · the range-dependence of the lidar backscattering effect on the final image at the photocathode is significantly decreased (i.e., backscattered signal from lower altitudes does not appear at different spots on the detector effective area than backscattered signal from higher altitudes) [67], [68].

The PMTs used are manufactured by Hamamatsu S.A. (type R7400: P and Y series). The photocathode of photomultipliers is an alloy multialkali (Na-K-Sb-Cs)[2] with quantum efficiency[3] of 12% at 532 nm, 20% at 387 and 407 nm, 22% at 607 nm and 23% at 355 nm. The Avalanche Photo-Diode (APD) used for the detection of the 1064 nm radiation is provided, also, by Hamamatsu S.A. (model APD-1.5).

The detected backscattered light at all mentioned wavelengths from UV to the near IR, as exiting from the PMTs and the APD enters the data acquisition system which is implemented either as analog detection mode or photon counting detection mode. At the analog detection mode, the pulse when exits the PMT is being recorded as output current, whereas at the photon counting detection mode, all the produced photoelectrons by the PMT are recorded as counts. The latter detection mode is more accurate under low SNRs and provides high stability of the lidar signal. The photon counting mode is applicable only to lidar signals backscattered from higher altitudes (e.g. $>$ 4-5 km) because at low altitudes the PMTs cannot detect photoelectrons which arrive at a very high rate due to the so-called dead time.

In EOLE system, the lidar signals at 355, 532 and 1064 nm are being detected both in the analog and photon counting mode, while the signals at 387, 407 and 607 nm are detected only in the photon counting mode. The EOLE data acquisition system is manufactured by LICEL GmbH. In particular, when the signal is detected in analog mode the digitization of the signal is required. The Analog-to-Digital conversion is feasible with an accuracy of 12 bits for 8192 time bins with the possibility of integrating up to 4000 pulses. Provided that the

---

[1] Doublet lens: sequence of two plano-convex lenses with their convex sides to osculate aside. In this design the two lenses are paired together such as spherical and chromatic aberrations are reduced when light ray is transmitted through a doublet lens.

[2] Na: Sodium - K: Potassium - Sb: Antimony - Cs: Cesium

[3] Quantum efficiency, expressed as a percent, is the number of photoelectrons emitted from the photocathode divided by the number of incident photons.

laser pulse repetition frequency is 10 Hz, in order to achieve a signal with a time resolution of 100 seconds, 1000 pulses are integrated in each recording. With a 20 MHz sampling rate of the EOLE' transient recorders, the resulting raw spatial resolution is 7.5 m. The amplitude range of the detected analog signals is in the order of 40-150 mV. The photon counting detector consists of a three-order pre-amplifier followed by a signal discriminator of 64 tuning levels. The maximum theoretical photon counting rate is 250 MHz; however the actual rate is of the order of 50 MHz due to the photomultiplier dead time constrain. For the accurate recording of the backscattered laser photons, the operation of the detection unit should remain within its "linear" region. The upper limit of the recording rate is set obeying to the dead time constrain which has been measured equal to 6.5 ns (i.e., recording rate of 153 MHz). High energy photons which may originate from cosmic rays should also be excluded, using the relevant discrimination levels.

3.2 Depolarization lidar

It is well known that backscattering from spherical particles maintains the polarization state of the incident polarized light beam. The polarization lidar technique makes use of this property by using a laser source which generates a linearly polarized light beam and a receiver with the discrimination capability between the two components of the backscattered light: the parallel polarized and the perpendicular to the primary laser beam polarized component. The signal discrimination is done with a Polarizing Beam Splitter (PBS) cube which directs the perpendicular-polarized component of the backscatter signal to one channel and the parallel one to the other. The calibrated ratio of these two components is known as the depolarization ratio. Depolarization ratio measurements provide information about the shape of the particles and the cloud phase (i.e., discrimination between liquid and ice phase).

For a depolarization lidar, the lidar equation should be splitted into two:

$$P^{\parallel}(R,\lambda) = \frac{E_0(\lambda)\,\eta_L^{\parallel}(\lambda)\,O^{\parallel}(R,\lambda)}{R^2}\beta^{\parallel}(R,\lambda)\exp\left[-2\int_0^R \alpha^{\parallel}(\zeta,\lambda)\,d\zeta\right] \tag{3.1}$$

$$P^{\perp}(R,\lambda) = \frac{E_0(\lambda)\,\eta_L^{\perp}(\lambda)\,O^{\perp}(R,\lambda)}{R^2}\beta^{\perp}(R,\lambda)\exp\left[-\int_0^R \left(\alpha^{\parallel}(\zeta,\lambda)+\alpha^{\perp}(\zeta,\lambda)\right)d\zeta\right] \tag{3.2}$$

Eq. (3.1) refers to the co-polarized component; the backscattered signal which has the same state of polarization with the transmitted laser beam, while Eq. (3.2) refers to the cross-polarized component; the backscatted signal which has perpendicular to the transmitted laser beam state of polarization.

The ratio of the cross-polarized component $P^{\perp}$ over the co-polarized component $P^{\parallel}$ determines the so-called linear volume depolarization ratio δ_v.

$$\delta_v = \frac{P^{\perp}}{P^{\parallel}} = \frac{\beta^{\perp}}{\beta^{\parallel}}\exp\left[\tau^{\parallel}-\tau^{\perp}\right] \tag{3.3}$$

where $\tau^{\parallel}$ and $\tau^{\perp}$ is the atmospheric transmission of co-polarized and cross-polarized light, respectively

$$\tau^{\parallel} = -2\int_0^R \alpha^{\parallel}(\zeta,\lambda)\,d\zeta \tag{3.4}$$

$$\tau^{\perp} = -\int_0^R \left(\alpha^{\parallel}(\zeta,\lambda)+\alpha^{\perp}(\zeta,\lambda)\right)d\zeta \tag{3.5}$$

The atmospheric transmission is not dependent on light polarization state and thus since $\tau^{\parallel}=\tau^{\perp}$, Eq. (3.3) which consists from the contribution of aerosol and molecules becomes

$$\delta_v = \frac{\beta^{\perp}}{\beta^{\parallel}} = \frac{\beta_p^{\perp} + \beta_m^{\perp}}{\beta_p^{\parallel} + \beta_m^{\parallel}} \tag{3.6}$$

By introducing the linear molecular and particle depolarization ratio $\delta_m = \frac{\beta_m^{\perp}}{\beta_m^{\parallel}}$, $\delta_p = \frac{\beta_p^{\perp}}{\beta_p^{\parallel}}$ respectively, Eq. (3.7) can be reformulated to

$$\delta_v = \frac{\delta_m(\delta_p + \beta_m) + \delta_p(\beta_m\delta_m + \beta_p)}{\beta_m(1+\delta_p) + \beta_p(1+\delta_m)} \tag{3.7}$$

which can be solved for linear particle depolarization ratio δ_p

$$\delta_p = \frac{\beta_m(\delta_v - \delta_m) + \beta_p\delta_v(1+\delta_m)}{\beta_m(\delta_m - \delta_v) + \beta_p(1+\delta_m)} \tag{3.8}$$

By introducing the backscatter ratio $\mathbf{R} = \frac{\beta_\mathbf{m} + \beta_\mathbf{p}}{\beta_\mathbf{m}}$ as the ratio of total backscatter coefficient to the molecular backscatter coefficient Eq. (3.8) reformulates to

$$\delta_p = \frac{\mathbf{R}\delta_v(1+\delta_m) - \delta_m(1+\delta_v)}{\mathbf{R}(1+\delta_m) - (1+\delta_v)} \tag{3.9}$$

Therefore, the determination of δ_p requires the calculation of the molecular backscatter coefficient and the molecular depolarization ratio. The former can be estimated from a nearby radiosounding, while the latter is only a function of the interference filters bandwidth in the detection unit and hence, it can be considered as a calibration constant for each depolarization lidar [69]. This calibration factor may also depend on atmospheric temperature if the rotational Raman spectrum is partially included in the signal [70].

3.2.1 Calibration technique for depolarization lidar

The most trustworthy calibration technique of a depolarization lidar has been recently proposed by [71]. Let P^s, P^p be the parallel and perpendicular power component with respect to the incident plane of the PBS respectively. Then, ϕ is the angle between the plane of laser polarization and the incident plane of the PBS. The cross-polarized signal is measured either in the reflected path after the PBS cube for $\phi = 0°$ or in the transmitted path for $\phi = 90°$. Correspondingly, the co-polarized signal can be measured in the reflected path for $\phi = 90°$ and in the transmitted path for $\phi = 0°$.

$$P^s(\phi) = P^{\parallel}\sin^2(\phi) + P^{\perp}\cos^2(\phi) \tag{3.10}$$

$$P^p(\phi) = P^{\parallel}\cos^2(\phi) + P^{\perp}\sin^2(\phi) \tag{3.11}$$

Let the PBS cube, like in the one in Figure 3.7, have a reflectivity R_p, R_s and transmittance T_p, T_s for the parallel (p) and perpendicular (s) plane of polarization, respectively. Now, let P^R and P^T be the power of the lidar signal measured in the reflected and transmitted path right after the PBS, respectively.

$$P^R(\phi) = V_R(P^p(\phi)R_p + P^s(\phi)R_s) \tag{3.12}$$

$$P^T(\phi) = V_T(P^p(\phi)T_p + P^s(\phi)T_s) \tag{3.13}$$

where V_R and V_T are the corresponding amplification factors in the reflected and transmitted path which include the optical transmittance of the receiver and the electronic amplification. The ratio of the recorded signal P^R, P^T is finally expressed

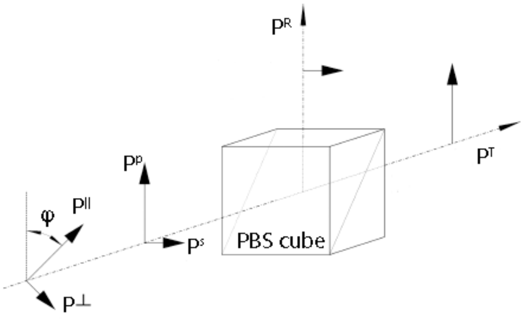

Σχήμα 3.7: *Power components in the detection unit in a polarization lidar. Figure was adapted from [71].*

$$\delta^{\star}(\phi)=\frac{V_R}{V_T}\frac{\left[1+\delta_v\tan^2(\phi)\right]R_p+\left[tan^2(\phi)+\delta_v\right]R_s}{\left[1+\delta_v\tan^2(\phi)\right]T_p+\left[tan^2(\phi)+\delta_v\right]T_s} \tag{3.14}$$

Name $V^{\star}=\frac{V_R}{V_T}$ as the relative amplification factor and solve Eq. (3.15) with respect to $V^{\star}$

$$V^{\star}=\delta^{\star}(\phi)\frac{\left[1+\delta_v\tan^2(\phi)\right]T_p+\left[tan^2(\phi)+\delta_v\right]T_s}{\left[1+\delta_v\tan^2(\phi)\right]R_p+\left[tan^2(\phi)+\delta_v\right]R_s} \tag{3.15}$$

For the determination of factor $V^{\star}$ can be done via the so-called ±45°-calibration method, subsequent lidar signals at angles $\phi=+45°$ and $\phi=-45°$ are recorded [71]. At these angles, the power components P^s and P^p are equal as results from Eq. (3.10), (3.11). Provided that $tan(+45°)=tan(-45°)\,1$, Eq. (3.15) writes

$$V^{\star}=\sqrt{\delta^{\star}(\phi=+45°)\,\delta^{\star}(\phi=-45°)\frac{T_p+T_s}{R_p+R_s}} \tag{3.16}$$

3.3 Aerosol optical properties from a multi-wavelegth elastic lidar

3.3.1 Aerosol Backscatter Coefficient

The backscatter coefficient $\beta(R,\lambda)$ defines the scattering coefficient at the backward direction (i.e., at a scattering angle of $\theta=180^o$). This parameter determines the strength of the lidar return at the operational wavelength λ at a distance R far from the lidar. The mathematical expression of backscatter signal is:

$$\beta(R,\lambda)=\sum N_j(R)\frac{d\sigma_{j,sca}}{d\Omega}(\pi,\lambda)[m^{-1}sr^{-1}], \tag{3.17}$$

where N_j denotes the concentration of scattering "particles" of kind j in the illuminated volume and $d\sigma_{j,sca}(\pi,\lambda)/d\Omega$ is the "particles" differential scattering cross section for the backward direction.

Nevertheless, since this backscatter coefficient denotes the backscattered light from both aerosols and molecules in the atmosphere, the contribution of molecules to the total backscatter could be defined so as the aerosol backscatter coefficient can be estimated. The most commonly used method for calculating the aerosol backscatter coefficient is the Fernald-Klett method exclusively described in literature [72], [73]. The main uncertainty for the accurate calculation of aerosol backscatter coefficient in this method are introduced by the assumption of the lidar ratio value, which is characteristic for the type of the detected aerosols. Another uncertainty can be introduced by the calibration height where aerosol contribution in the backscatter profile is considered negligible [74].

3.3.2 Klett method

The lidar equation due to elastic backscatter by air molecules and aerosol properties is given by:

$$P(R,\lambda) = \frac{E_0\eta_L}{R^2} O(R)\,\beta(R) \exp\left[-2\int_0^R \alpha(r)\,dr\right], \tag{3.18}$$

where $P(R)$ is the backscattered lidar signal received from distance R due to Rayleigh and particle scattering, E_0 is the energy of the transmitted laser pulse, η_L is the optical efficiency of the lidar system (efficiencies of the optical and detection units), $O(R)$ is the geometrical form function at distance R, $\beta(R)$ is the backscatter coefficient due to aerosol and molecules, $\alpha(r)$ is the extinction coefficient due to aerosol and molecules.

Eq. (3.18) can be reformulated to the range corrected signal $S(R)$

$$S(R) = P(R,\lambda)\,R^2 = E_0\eta_L O(R)\left[\beta_{aer}(R) + \beta_{mol}(R)\right] \exp\left[-2\int_0^R \left[\alpha_{aer}(r) + \alpha_{mol}(r)\right] dr\right]. \tag{3.19}$$

By introducing the S_λ of aerosols (which depends on their size distribution, shape and chemical composition) $S_\lambda(R) = \frac{\alpha_{aer}(R)}{\beta_{aer}(R)}$ and of molecules $S_{mol}(R) = \frac{\alpha_{mol}(R)}{\beta_{mol}(R)} = \frac{8\pi}{3} sr$, the multiplication of both sides of S_λ with Eq. (3.19) leads to

$$\begin{aligned} S(R)\,S_\lambda(R) &= E_0\eta_L O(R)\,S_\lambda(R)\left[\beta_{aer}(R) + \beta_{mol}(R)\right] \exp\left[-2\int_0^R \left[\alpha_{aer}(r) + \alpha_{mol}(r)\right] dr\right] \\ &= E_0\eta_L O(R)\,Y(R) \exp\left[-2\int_0^R \left[\alpha_{aer}(r) + \alpha_{mol}(r)\right] dr\right], \end{aligned} \tag{3.20}$$

with $Y(R) = S_\lambda(R)\left[\beta_{aer}(R) + \beta_{mol}(R)\right]$.

The exponential term of Eq. (3.20) can be reformulated as

$$\begin{aligned} A &= \exp\left[-2\int_0^R \left[\alpha_{aer}(r) + \alpha_{mol}(r)\right] dr\right] \\ &= \exp\left[-2\int_0^R \left[S_\lambda(r)\,\beta_{aer}(r) + S_{mol}\beta_{mol}(r)\right] dr\right] \\ &= \exp\left[-2\int_0^R \left[S_\lambda(r)\,\beta_{aer}(r) + S_\lambda(r)\,\beta_{mol}() - S_\lambda(r)\,\beta_{mol}() + S_{mol}\beta_{mol}(r)\right] dr\right] \\ &= \exp\left[-2\int_0^R \left[S_\lambda(r)\left[\beta_{aer}(r) + \beta_{mol}(r)\right] - \beta_{mol}(r)\left[S_\lambda(r) - S_{mol}\right]\right] dr\right] \\ &= \frac{\exp\left[-2\int_0^R Y(r)\,dr\right]}{\exp\left[-2\int_0^R \beta_{mol}(r)\left[S_\lambda(r) - S_{mol}\right] dr\right]}. \end{aligned} \tag{3.21}$$

Then, Eq. (3.21) writes

$$S(R)\,S_\lambda(R) \exp\left[-2\int_0^R \beta_{mol}(r)\left[S_\lambda(r) - S_{mol}\right] dr\right] = E_0\eta_L Y(R) \exp\left[-2\int_0^R Y(r)\,dr\right] \tag{3.22}$$

Taking the natural logarithm on both sides of Eq. (3.22) leads to

$$\begin{aligned}
&\ln\left(S\left(R\right)S_{\lambda}\left(R\right)\exp\left[-2\int_0^R \beta_{mol}\left(r\right)\left[S_{\lambda}\left(r\right)-S_{mol}\right]dr\right]\right)\\
&=\ln\left(E_0\eta_L Y\left(R\right)\exp\left[-2\int_0^R Y\left(r\right)dr\right]\right)\\
&=\ln\left(E_0\eta_L\right)+\ln\left(Y\left(R\right)\right)+\ln\left(\exp\left[-2\int_0^R Y\left(r\right)dr\right]\right)\\
&=\ln\left(E_0\eta_L\right)+\ln\left(Y\left(R\right)\right)-2\int_0^R Y\left(r\right)dr \qquad (3.23)
\end{aligned}$$

Differentiation of Eq. (3.23) with respect to range R results to

$$\begin{aligned}
&\frac{d\left[\ln\left[S\left(R\right)S_{\lambda}\left(R\right)\exp\left[-2\int_0^R \beta_{mol}\left(r\right)\left[S_{\lambda}\left(r\right)-S_{mol}\right]dr\right]\right]\right]}{dR}=\\
&=\frac{d\ln\left(E_0\eta_L\right)}{dR}+\frac{d\ln Y\left(R\right)}{dR}-2\frac{d\left[\int_0^R Y\left(r\right)dr\right]}{dR}=\\
&=\frac{1}{Y(R)}\frac{d\left(Y\left(R\right)\right)}{dR}-2Y\left(R\right) \qquad (3.24)
\end{aligned}$$

To solve the Eq. (3.24), we need a boundary condition which is formulated at the reference height R_0 where the contribution of the aerosol backscatter to the total backscatter is negligible, thus the total backscatter at the reference height is exclusively due to molecules presence

$$Y\left(R_0\right)=S_{\lambda}\left(R_0\right)\left[\beta_{aer}\left(R_0\right)+\beta_{mol}\left(R_0\right)\right] \qquad (3.25)$$

If the variable $M\left(R\right)=S\left(R\right)S_{\lambda}\left(R\right)\exp\left[-2\int_0^R \beta_{mol}\left(r\right)\left[S_{\lambda}\left(r\right)-S_{mol}\right]dr\right]$ is introduced, then $K\left(R\right)=\frac{d(\ln M(R))}{dR}=\frac{1}{M(R)M'(R)}$ and Eq. (3.24) becomes:

$$\frac{dY}{dR}-K\left(R\right)Y=-2Y^2 \qquad (3.26)$$

The above differential equation is a Bernoulli type. For the solution of such form d.e., look at appendix A. The solution of Eq. (3.24) for the boundary condition (4.18) gives the aerosol backscatter coefficient

$$\begin{aligned}
&\beta_{aer}\left(R\right)+\beta_{mol}\left(R\right)=\\
&=\frac{S\left(R\right)\exp\{-2\int_{R_0}^R\left[L_{aer}\left(r\right)-L_{mol}\right]\beta_{mol}\left(r\right)dr\}}{\frac{S(R_0)}{\beta_{aer}(R_0)+\beta_{mol}(R_0)}-2\int_{R_0}^R L_{aer}\left(r\right)S\left(r\right)\exp\{-2\int_{R_0}^r\left[L_{aer}\left(r'\right)-L_{mol}\right]\beta_{mol}\left(r'\right)dr'\}dr}. \qquad (3.27)
\end{aligned}$$

3.4 Aerosol optical properties from a multi-wavelegth Raman lidar

The main advantage of a Raman lidar in comparison to an elastic one is that allows the independent retrieval of the aerosol extinction and backscatter coefficients, without any assumption of the aerosol S_{λ}.

EOLE has been used for the retrieval of aerosols' optical properties using the Raman technique. The Raman lidar equation includes the backscatter coefficients $\beta_{mol}(\lambda,z)$, $\beta_{aer}(\lambda,z)$ and extinction coefficients $\alpha_{mol}(\lambda,z)$, $\alpha_{aer}(\lambda,z)$ of molecules and aerosols respectively. The solution of this differential equation with making use of the Raman channels has been proposed [75] for the simultaneous retrieval of the aerosols' backscatter and extinction coefficients at $\lambda = 355$ nm and $\lambda = 532$ nm. The inelastic Raman signals are only due to the scattering from Nitrogen N_2 molecules and therefore the backscattering cross-section determines the intensity of the signals.

In 1928, Sir Raman observed the frequency-shifted lines in the spectrum of scattered light [76]. The frequency shift relative to the incident light corresponds to the vibrational and rotational frequencies of the scattering molecules. The frequency shift can be towards lower energies $\lambda_{Ra} > \lambda_0$ (Stokes lines) or higher energies $\lambda_{Ra} < \lambda_0$ (anti-Stokes lines). The total Raman spectrum of a diatomic molecule can be seen in Figure 3.8. When the scattered light is coherent to the incident light, Rayleigh scattering occurs which is much stronger than the Raman scattering. When only molecular rotations occur, the Rotational Raman (RR) lines are just around the Rayleigh line. However, the Vibrational Rotational Raman (VRR) lines are better separated in frequency from the incident light. VRR lines consist of Q, S and O branches. The anti-Stokes lines are weaker than the Stokes lines and usually cannot be observed.

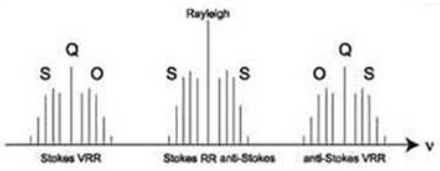

Σχήμα 3.8: *Raman spectrum of a diatomic molecule. The Rayleigh line is at the same frequency of the incident photon. Just around the Rayleigh line, the rotational Stokes and anti-Stokes lines lie to the left towards lower energies and to the right towards higher energies respectively [77].*

A molecule is always at a specific vibrational-rotational energy. The frequency shift which is caused by the change in vibrational, rotational or vibrational-rotational energy level of the scattering molecule is estimated by

$$\Delta\tilde{v} = \tilde{v}_i - \tilde{v}_s = \frac{\Delta E}{hc_0}, \tag{3.28}$$

where $\tilde{v}_i$[4] is the frequency of the incident photon, $\tilde{v}_s$ is the frequency of the scattered photon, ΔE is the difference between the molecular energy levels, h is Planck's constant and c_0 the speed of light in vacuum [78].

3.4.1 Rotational Vibrational Raman Spectra

Figure 3.9 illustrates the rotational-vibrational Raman spectra for several atmospheric molecules such as silicon dioxide (SiO_2), oxygen (O_2), nitrogen (N_2) and water vapor (H_2O) in gas, liquid and solid phase. The incident light at 355 nm excites the atmospheric nitrogen molecules which emits light at the Stokes line of 387 nm. When the incident beam is at 532 nm, the Raman scattered photon is detected at 607 nm. The Raman lidar can also detect Raman lines of water vapor at 407 nm when incident light beam is at 355 nm.

---

[4] In spectroscopy, the wavenumber $\tilde{v} = 1/\lambda$ $[cm^{-1}]$ is preferred.

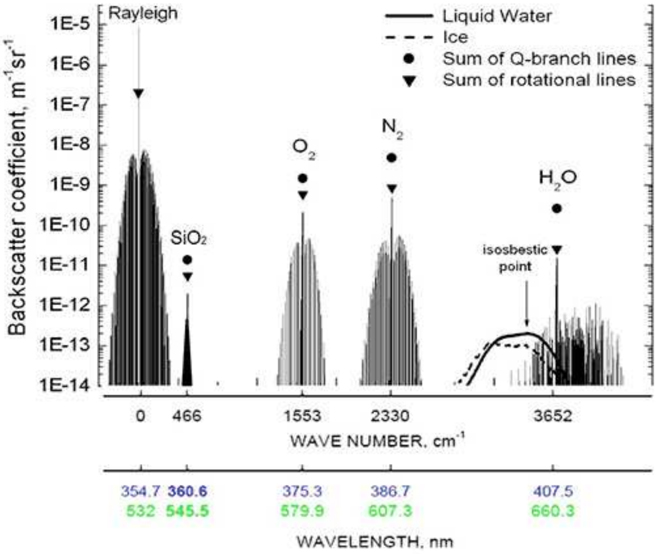

Σχήμα 3.9: *Rotational Vibrational Raman lines. The Raman backscatter spectrum of the atmosphere for incident laser wavelength of 355 and 532 nm. Picture was adapted from [79].*

3.4.2 Raman method

The determination of particle extinction coefficient from molecular backscatter signals is certainly straightforward using the Raman technique. Let's introduce the system constant $C = E_0 \eta_{\lambda_{Ra}} O(\lambda_{Ra}, z)$, the transmitted energy of the laser pulse E_0, efficiencies at optical and detection units $\eta_{\lambda_{Ra}}$ and the overlap function $O(\lambda_{Ra}, z)$. Then, the lidar equation for the molecular backscatter signal is formulated as

$$P(\lambda_{Ra}, z) = \frac{C}{z^2} \beta_{Ra}(\lambda_0, z) \exp\{-\int_0^z [\alpha(\lambda_0, \zeta) + \alpha(\lambda_{Ra}, \zeta)] d\zeta\}, \tag{3.29}$$

where $\beta_{Ra}(z, \lambda_0)$ is the molecular backscatter coefficient calculated as the product of the nitrogen molecular number density N_{Ra} and the molecular differential cross section $\frac{d\sigma_{Ra}(\phi)}{d\Omega}$ with scattering angle $\phi = \pi$ if only backscattering is considered

$$\beta_{Ra}(z, \lambda_0) = N_{Ra} \frac{d\sigma_{Ra}}{d\Omega}(\pi, \lambda_0). \tag{3.30}$$

Provided that $\beta_{Ra} \equiv \beta_{mol}$, by substituting Eq. (3.30) to Eq. (3.29),

$$P(\lambda_{Ra}, z) = \frac{C}{z^2} N_{Ra}(z) \frac{d\sigma_{Ra}}{d\Omega}(\pi, \lambda_0) \exp\{-\int_0^z [\alpha(\lambda_0, \zeta) + \alpha(\lambda_{Ra}, \zeta)] d\zeta\} \tag{3.31}$$

and by taking the natural logarithm in both sides of Eq. (3.31),

$$\ln\left[P(\lambda_{Ra}, z) z^2\right] = \ln\left[C N_{Ra}(z) \frac{d\sigma_{Ra}}{d\Omega}(\pi, \lambda_0) \exp\{-\int_0^z [\alpha(\lambda_0, \zeta) + \alpha(\lambda_{Ra}, \zeta)] d\zeta\}\right], \tag{3.32}$$

where $S(\lambda_{Ra}, z) = P(\lambda_{Ra}, z) z^2$ is the range corrected signal.

However, the logarithm of system constant C and molecular backscatter coefficient can be reformulated as

$$\ln C = \ln[E_0 \eta_{\lambda_{Ra}} O(\lambda_{Ra}, z)] = \ln(E_0 \eta_{\lambda_{Ra}}) + \ln O(\lambda_{Ra}, z) = c_1 + \ln O(\lambda_{Ra}, z), \tag{3.33}$$

$$\ln\left[N_{Ra}(z)\frac{d\sigma_{Ra}}{d\Omega}(\pi,\lambda_0)\right]=\ln N_{Ra}(z)+\ln\frac{d\sigma_{Ra}}{d\Omega}(\pi,\lambda_0)=\ln N_{Ra}(z)+c_2. \tag{3.34}$$

If we substitute Eq. (3.33) and 3.34 in Eq. 3.32,

$$\begin{aligned}\ln S(\lambda_{Ra},z)&=c_1+\ln O(\lambda_{Ra},z)+\ln N_{Ra}(z)+c_2+\ln\left[\exp\{-\int_0^z[\alpha(\lambda_0,\zeta)+\alpha(\lambda_{Ra},\zeta)]\,d\zeta\}\right]\\&=\ln O(\lambda_{Ra},z)+\ln N_{Ra}-\int_0^z[\alpha(\lambda_0,\zeta)+\alpha(\lambda_{Ra},\zeta)]\,d\zeta+c_3,\end{aligned} \tag{3.35}$$

with $c_3=c_1+c_2$.
Rearrangement of Eq. (3.35) gives

$$\begin{aligned}\int_0^z[\alpha(\lambda_0,\zeta)+\alpha(\lambda_{Ra},\zeta)]\,d\zeta&=\ln O(\lambda_{Ra},z)+\ln N_{Ra}-\ln S(\lambda_{Ra},z)+c_3\\&=\ln O(\lambda_{Ra},z)+\ln\frac{N_{Ra}}{S(\lambda_{Ra},z)}+c_3.\end{aligned} \tag{3.36}$$

Differentiation of Eq. (3.36) with respect to range z

$$\frac{d}{dz}\int_0^z[\alpha(\lambda_0,\zeta)+\alpha(\lambda_{Ra},\zeta)]\,d\zeta=\frac{d}{dz}\ln\frac{N_{Ra}}{S(\lambda_{Ra},z)}+\frac{d}{dz}O(\lambda_{Ra},z) \tag{3.37}$$

finally writes

$$\alpha(\lambda_0,z)+\alpha(\lambda_{Ra},z)=\frac{d}{dz}\ln\frac{N_{Ra}}{S(\lambda_{Ra},z)}+\frac{d}{dz}O(\lambda_{Ra},z). \tag{3.38}$$

The term $A=\frac{d}{dz}O(\lambda_{Ra},z)$ can be nullified for long ranges where overlap function is equal to 1. At altitudes of incomplete overlap, the term A writes

$$\frac{d}{dz}\ln O(\lambda_{Ra},z)=\frac{1}{O(\lambda_{Ra},z)}\frac{d}{dz}O(\lambda_{Ra},z) \tag{3.39}$$

and correction for the overlap effect is needed. Nevertheless, for ranges of full overlap $z\geq z_{f.o.}$, Eq. (3.38) writes

$$\alpha_{aer}(\lambda_0,z)+\alpha_{aer}(\lambda_{Ra},z)=\frac{d}{dz}\ln\frac{N_{Ra}}{S(\lambda_{Ra},z)}-\alpha_{mol}(\lambda_0,z)-\alpha_{mol}(\lambda_{Ra},z). \tag{3.40}$$

Let's introduce the Ångström exponent Å(z) as

$$\frac{\alpha_{aer}(\lambda_0,z)}{\alpha_{aer}(\lambda_{Ra},z)}=\left(\frac{\lambda_{Ra}}{\lambda_0}\right)^{\mathring{A}(z)}. \tag{3.41}$$

Substitution of Eq. (3.41) to 3.40 results to

$$\alpha_{aer}(\lambda_0,z)+\left(\frac{\lambda_0}{\lambda_{Ra}}\right)^{\mathring{A}(z)}\alpha_{aer}(\lambda_0,z)=\frac{d}{dz}\ln\frac{N_{Ra}}{S(\lambda_{Ra},z)}-\alpha_{mol}(\lambda_0,z)-\alpha_{mol}(\lambda_{Ra},z) \tag{3.42}$$

which gives the final mathematical expression for the aerosol extinction coefficient $\alpha_{aer}(\lambda_0,z)$

$$\alpha_{aer}(\lambda_0, z) = \frac{\frac{d}{dz} \ln \frac{N_{Ra}}{S(\lambda_{Ra}, z)} - \alpha_{mol}(\lambda_0, z) - \alpha_{mol}(\lambda_{Ra}, z)}{1 + \left(\frac{\lambda_0}{\lambda_{Ra}}\right)^{\mathring{A}(z)}}. \tag{3.43}$$

From the Raman equation and the elastic backscatter equation, the aerosol backscatter coefficient can be retrieved from signals $P(\lambda_0, z)$, $P(\lambda_{Ra}, z)$, $P(\lambda_0, z_0)$ and $P(\lambda_{Ra}, z_0)$ with z_0 being a reference height where the contribution of aerosols backscatter is negligible to the total backscattered signal. Hence, for ranges of full overlap $z \geq z_{f.o.}$, the aforementioned four signals

$$P(\lambda_0, z) = \frac{E_0 \eta_L}{z^2} \left[\beta_{aer}(\lambda_0, z) + \beta_{mol}(\lambda_0, z)\right] \exp\left[-2 \int_0^z \alpha_{mol}(\lambda_0, \zeta) + \alpha_{aer}(\lambda_0, \zeta)\right] \tag{3.44}$$

$$P(\lambda_0, z_0) = \frac{E_0 \eta_L}{z_0^2} \left[\beta_{aer}(\lambda_0, z_0) + \beta_{mol}(\lambda_0, z_0)\right] \exp\left[-2 \int_0^{z_0} \alpha_{mol}(\lambda_0, \zeta) + \alpha_{aer}(\lambda_0, \zeta)\right] \tag{3.45}$$

$$P(\lambda_{Ra}, z) = \frac{E_0 \eta_L}{z^2} \beta_{Ra}(\lambda_0, z) \exp\left[- \int_0^z \left[\alpha(\lambda_0, \zeta) + \alpha(\lambda_{Ra}, \zeta)\right] d\zeta\right], \tag{3.46}$$

$$P(\lambda_{Ra}, z_0) = \frac{E_0 \eta_L}{z_0^2} \beta_{Ra}(\lambda_0, z) \exp\left[- \int_0^z \left[\alpha(\lambda_0, \zeta) + \alpha(\lambda_{Ra}, \zeta)\right] d\zeta\right] \tag{3.47}$$

lead to the solution of aerosol backscatter coefficient through the following expression

$$\begin{aligned} &\beta_{aer}(\lambda_0, z) + \beta_{mol}(\lambda_0, z) \\ &= \left[\beta_{aer}(\lambda_0, z_0) + \beta_{mol}(\lambda_0, z_0)\right] \frac{P(\lambda_0, z) P(\lambda_{Ra}, z_0)}{P(\lambda_0, z_0) P(\lambda_{Ra}, z)} \frac{N_{Ra}(z)}{N_{Ra}(z_0)} \frac{T(\lambda_{Ra}, z)}{T(\lambda_0, z)}, \end{aligned} \tag{3.48}$$

where $T(\lambda, z) = \exp\left[-\int_{z_0}^{z} \left(\alpha_{aer}(\lambda, \zeta) + \alpha_{mol}(\lambda, \zeta)\right) d\zeta\right]$ for $\lambda = \lambda_0, \lambda_{Ra}$.

3.5 Lidar data pre-processing: General corrections

The data pre-processing is always performed before the retrieval of the aerosol optical properties. It ensures that lidar signals are corrected for all instrumental effects. The pre-processing procedure is systematically performed to all raw signals with the NTUA in-house software. All analog signals should be corrected for trigger delay, atmospheric background and electronic noise while photon-counting signals should be corrected only for dead-time effect.

3.5.1 Corrections of analog signals

Trigger delay correction: The data acquisition unit gets a trigger from the laser system to start recording the lidar signal. A delay between the actual time of the outgoing laser pulse and the time at which the acquisition system starts to record the lidar signal is called trigger delay and it is a systematic electronic delay. This trigger delay implies a systematic shift on the atmospheric range gates which finally causes a systematic error in the range-correction of the lidar signal. The latter might propagate to the calculation of the final aerosol properties. The error becomes significant in the aerosol extinction coefficient estimation with the Raman method in the near range [80].

Atmospheric background correction: A raw lidar signal also contains atmospheric background noise, such as sunlight and cosmic noise. The atmospheric background is not range dependent. Therefore, it should be determined at the very far range of the lidar profile, where the transmitted laser beam has been totally attenuated and hence only solar and cosmic noise might be present.

Electronic noise correction: Electronic signal background results from electronic effects (electronic noise) of the signal detection and the data acquisition unit. These electronic distortions consist of a temporally constant part and a range-dependent oscillating part. Some of the random electronic noise is filtered out of the final profile just by integrating several raw lidar signals. However, there is another component of the electronic noise which is synchronized with the laser pulse upon its repetition frequency. This component is removed from the useful signal after subtraction of the so-called zero/dark signals. These type of signals are recorded by lidar data acquisition unit when the receiving telescope is fully covered in such a way that atmospheric light cannot reach the photomultiplier tubes.

3.5.2 Corrections at photon counting signals

Dead time correction: In any detector system, there is a certain amount of time that is required to discriminate and process a single photon. If a second photon arrives during this time, it will not be counted. The minimum amount of time which is required such as both photon arrivals are counted is referred to as the *dead time*. Because of the random nature of the arrival times of photons, some backscattered photons will not be counted. A dead time correction is necessary to account for those photons that arrive during the time required for the scalar to record a previous photon arrival. The number of uncounted photons is significant at short ranges since the backscattering from the lower atmospheric layers is strong and leads the system to saturation.

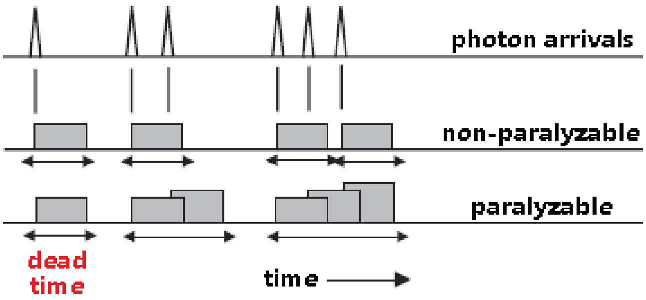

Σχήμα 3.10: *Dead time in paralyzed and nonparalyzed detection systems*

In Figure 3.10 two types of detection systems are illustrated. The non-paralyzable counting system takes a fixed dead time interval for a photon recording. Any other photon which arrives during this interval is ignored and thus system overall dead time never becomes longer. This is important because two photons which arrive in time separated by at least the dead time interval will be counted. If N_m is taken to be the system measured count rate, N_a is the actual count rate and τ is the dead time, then the total fraction of the time that is dead is $N_m\tau$, so that the rate at which a photon gets ignored is $N_aN_m\tau$. The corrected count rate is determined by $N_a = \frac{N_m}{(1-N_mT)}$. On the contrary, in a paralyzable detection system, any photon that arrives within the recording time of a prior photon extends the dead time of the first by its own dead time. The measured count rate for this type of electronic system is $N_m = N_a \exp(-N_aT)$. This expression is not invertible to determine the actual count rate and for a given measured count rate there exist two values of the actual count rate that will produce the measured rate for a given dead time [81].

3.5.3 Overlap Function

The transmitted laser beam cannot be totally within the receiver field-of-view. By looking to the geometry of a bi-axial lidar system as illustrated in Figure 3.11, the effect of overlap function on lidar backscattered signal is eliminated above a certain altitude. This is the minimum distance of full overlap where the overlap function $O(R)$ equals 1. To minimize the distance of full overlap, the laser beam is transmitted to the atmosphere with a small tilted angle. Above that range, the backscattered light beam is totally captured by the receiver telescope. However, at any lower altitude from ground to this full overlap range, the backscattered signal is affected by the incomplete overlap function (i.e., $O(R) < 1$).

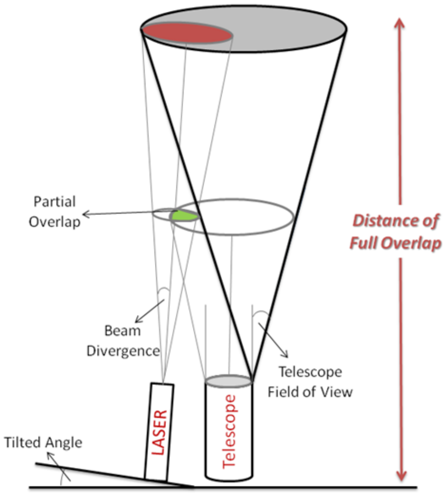

Σχήμα 3.11: *The incomplete overlap problem: the transmitted laser beam is not fully within the telescope field-of-view.*

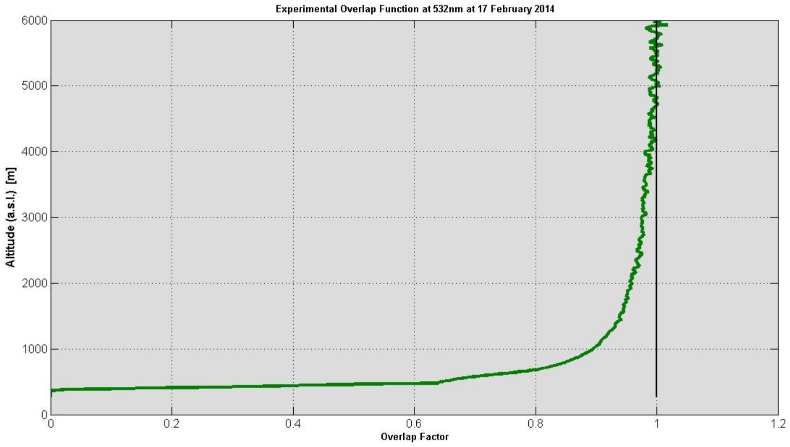

Σχήμα 3.12: *Experimental overlap: overlap function has been determined according to the method proposed by [82].*

The distance of full overlap can be defined from a ray-tracing simulation package by considering the geometrical and optical characteristics of transmitter and receiver units (i.e., the divergence of the laser beam, the telescope field of view, the imaging properties of the receiver system and the distance between the laser beam and the telescope axis). This is called the theoretical overlap function that the system has been designed to achieve. Nevertheless, it is often noticeable that real experimental overlap function can significantly differ from the theoretical one. The main reason for this discrepancy is systems misalignment issues. A method for the experimental determination of overlap function has been proposed by [82]. The method is based on the fact that the aerosol backscatter coefficient as estimated by the Raman method does not depend on the overlap function whereas in Klett method the same coefficient is only overlap function dependent. If the solution of Klett method is done for a S_λ close to the mean value of S_λ estimated by Raman method, the two aerosol backscatter coefficients should have similar values for ranges higher than the full overlap distance and become different for ranges lower than the full overlap distance.

The overlap function can be determined from the following expression:

$$O(R,\lambda) = \begin{cases} \dfrac{1}{1+\dfrac{\beta_{aer,Raman}(R,\lambda)-\beta_{aer,Klett}(R,\lambda)}{\beta_{aer,Raman}(R,\lambda)+\beta_{mol}(R,\lambda)}} & \text{if } R < R_{f.o.} \\ 1 & \text{if } R \geq R_{f.o.} \end{cases} \tag{3.49}$$

After several N iterations the final overlap function writes

$$O'(R,\lambda) = \prod_{i=1}^{N} O'_i(R,\lambda) \tag{3.50}$$

The experimental overlap of EOLE lidar system has been determined by the method of [82] and it is depicted in Figure 3.12. Then, this experimental overlap will be applied to correct the aerosol optical profiles down to 1.2 km.

CHAPTER 4

Light scattering from atmospheric substances

Interaction of light with matter is the physics domain of interest for laser remote sensing. Light emitted towards an object may be scattered or absorbed by the object depending on the optical properties of the object with respect to the frequency band of the interacting radiation. Scattering and absorption are both processes which subtract energy from the incoming radiation. We usually refer to this energy reduction by the term extinction. In Chapter 3 where the lidar principle was described, several concepts related to aerosol optical properties (i.e., extinction and backscattering coefficient) were first introduced. In this chapter, the scattering theory will be demonstrated for atmospheric particles (Rayleigh and Mie scattering). Clouds are opaque (Geometric scattering) to electromagnetic radiation in the ultraviolet, visible and near infrared spectral region which is the operational frequency spectrum of the lidar source because such beam is able to interact only with smaller than cloud droplets particles. There are two large classes of problems in the theory of interaction of light with particles; the forward problem and the inverse problem. The former describes the electromagnetic field which is induced around a particle with specified characteristics (i.e., shape, size and composition) when is illuminated by a beam of known frequency, amplitude and polarization state. The inverse problem refers to the retrieval of the characteristics (i.e., shape, size and composition) of a particle from the properties of the electromagnetic field around the particle.

4.1 Scattering theory

Let's consider a single particle of arbitrary shape, size and orientation that is illuminated by a plane electromagnetic wave. If we define the incident field E_i in a Cartesian coordinate system $(x,\, y,\, z)$ determined by the orthogonal basis vectors $\hat{e}_x$, $\hat{e}_y$, $\hat{e}_z$ with the orthogonality property $\|\hat{e}_x\| = \|\hat{e}_y\| = \|\hat{e}_z\| = 1$ and $\langle \hat{e}_x, \hat{e}_y \rangle = \langle \hat{e}_y, \hat{e}_z \rangle = \langle \hat{e}_z, \hat{e}_x \rangle = 0$, the direction of propagation of the incident light is along the positive part of z-axis, the *forward direction*. Then, the scattered field E_s is formulated in the spherical polar coordinate system $(r,\, \theta,\, \phi)$ defined by the orthogonal basis vectors $\hat{e}_r$, $\hat{e}_\theta$, $\hat{e}_\phi$. The forward direction $\hat{e}_z$ together with the scattering direction $\hat{e}_r$ define the scattering plane. The incident field of a plane wave can be mathematically formulated with two components of polarization; the parallel-polarized component $E_i^{\|}$ and the cross-polarized component $E_i^{\perp}$ such as the total incident field is expressed as

$$E_i = \left(E_0^{\|} \hat{e}_i^{\|} + E_0^{\perp} \hat{e}_i^{\perp} \right) \exp\left(ikz - i\omega t \right) = E_i^{\|} \hat{e}_i^{\|} + E_i^{\perp} \hat{e}_i^{\perp} \tag{4.1}$$

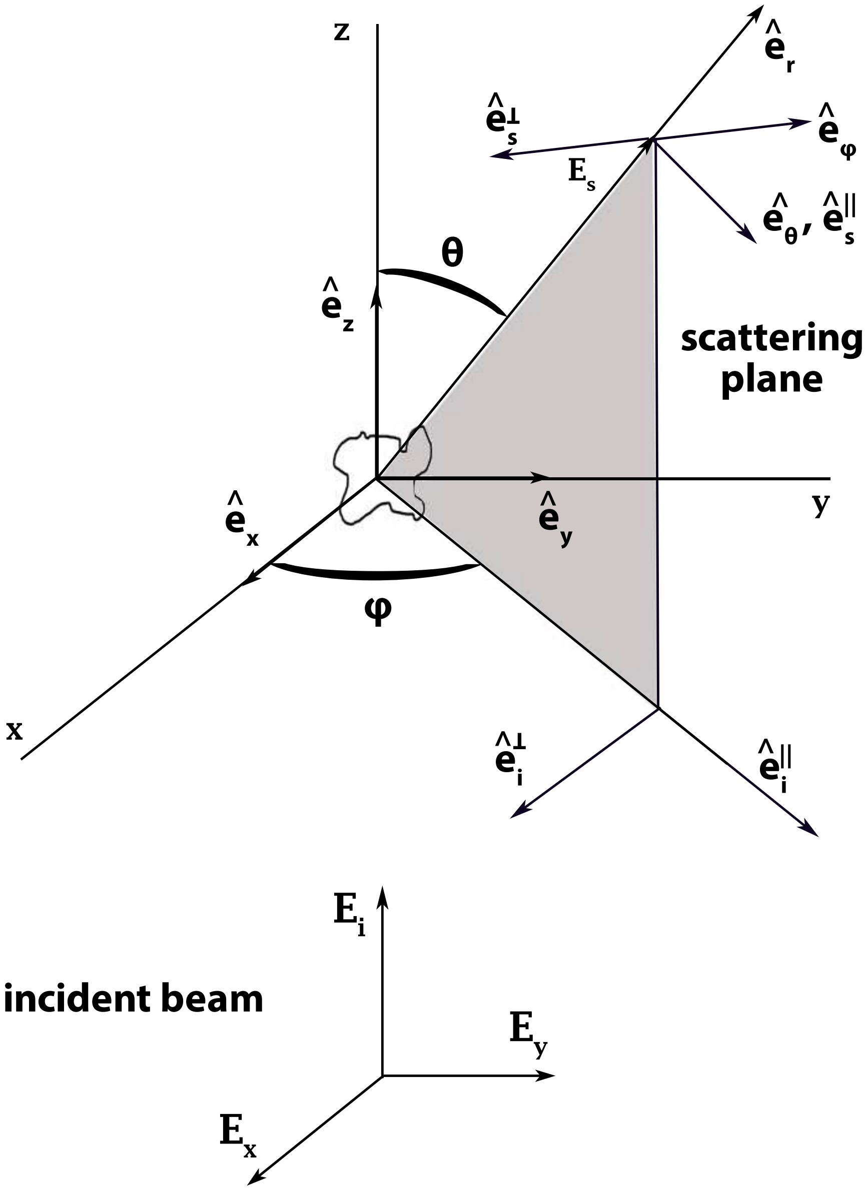

Σχήμα 4.1: *Scattering by an aerosol. The incident field is partially polarized. Picture was adapted from [83].*

From Eq. (4.1), the incident field can be formulated by the orthogonal basis $\hat{e}_i^{||}$, $\hat{e}_i^{\perp}$

$$\hat{e}_i^{||} = \cos\phi \hat{e}_x + \sin\phi \hat{e}_y \tag{4.2}$$

$$\hat{e}_i^{\perp} = \sin\phi \hat{e}_x - \cos\phi \hat{e}_y \tag{4.3}$$

$$\hat{e}_z = \hat{e}_i^{\perp} \times \hat{e}_i^{||} \tag{4.4}$$

Alternatively, the orthogonal basis $\hat{e}_i^{||}$, $\hat{e}_i^{\perp}$ can be expressed with respect to polar coordinates

$$\hat{e}_i^{||} = \sin\theta\hat{e}_r + \cos\theta\hat{e}_\theta \tag{4.5}$$

$$\hat{e}_i^{\perp} = -\hat{e}_\phi \tag{4.6}$$

The co- and cross-polarized components of the incident field E_i are given in accordance to Eq. (4.2), (4.8)

$$E_i^{||} = \cos\phi E_x + \sin\phi E_y \tag{4.7}$$

$$E_i^{\perp} = \sin\phi E_x - \cos\phi E_y \tag{4.8}$$

$$\tag{4.9}$$

The scattered field in the far-field[1]

$$\mathbf{E}_s = E_s^{||}\hat{e}_s^{||} + E_s^{\perp}\hat{e}_s^{\perp} \tag{4.10}$$

with

$$\hat{e}_s^{||} = \hat{e}_\theta \tag{4.11}$$

$$\hat{e}_s^{\perp} = -\hat{e}_\phi \tag{4.12}$$

$$\hat{e}_r = \hat{e}_s^{\perp} \times \hat{e}_s^{||} \tag{4.13}$$

and the scattered field related to the incident field $E_i^{||}$, $E_i^{||}$ is given as

$$\begin{pmatrix} E_s^{||} \\ E_s^{\perp} \end{pmatrix} = \frac{e^{ik(r-z)}}{-ikr} \begin{pmatrix} S_2 & S_3 \\ S_4 & S_1 \end{pmatrix} \begin{pmatrix} E_i^{||} \\ E_i^{\perp} \end{pmatrix} \tag{4.14}$$

where the elements S_j of the amplitude scattering matrix depend, in general, on the scattering angle θ and the azimuthal angle ϕ.

Spherical particles have a scattering matrix of the simplest type in which $S_3(\theta) = S_4(\theta) = 0$

$$\begin{pmatrix} E_s^{||} \\ E_s^{\perp} \end{pmatrix} = \frac{e^{ik(r-z)}}{-ikr} \begin{pmatrix} S_2 & 0 \\ 0 & S_1 \end{pmatrix} \begin{pmatrix} E_i^{||} \\ E_i^{\perp} \end{pmatrix} \tag{4.15}$$

Eq. (4.15) is the fundamental equation describing the scattered field around a sphere as a function of the polarized incident field.

Amplitude scattering matrix

The scattering amplitudes $S_1(\theta)$ and $S_2(\theta)$ are given by Mie theory [85]

$$S_1(\theta) = \sum_{n=1}^{\infty} \frac{2n+1}{n(n+1)} \left[\alpha_n \pi_n (cos\theta) + b_n \tau_n (\cos\theta)\right] \tag{4.16}$$

$$S_2(\theta) = \sum_{n=1}^{\infty} \frac{2n+1}{n(n+1)} \left[b_n \pi_n (cos\theta) + \alpha_n \tau_n (\cos\theta)\right] \tag{4.17}$$

The complex Mie coefficients α_n and b_n can be found from the boundary conditions at the surface of the sphere

---

[1] At large distances from the origin ($kr \gg 1$), the scattered electric field $\mathbf{E}_s$ is almost transverse ($\hat{\mathbf{e}}_r \cdot \mathbf{E}_s \simeq 0$) and has an asymptotic form [84].

$$\left(\mathbf{E}_i + \mathbf{E}_s - \mathbf{E}_l\right) \times \hat{\mathbf{e}}_{\mathbf{r}} = 0, \tag{4.18}$$

where $\mathbf{E}_l$ is the internal field inside the sphere. The boundary condition of Eq. (4.18), in θ-, ϕ-component form is

$$E_{i\theta} + E_{s\theta} = E_{l\theta} \tag{4.19}$$

$$E_{i\phi} + E_{s\phi} = E_{l\phi}. \tag{4.20}$$

The Mie coefficients are finally expressed through spherical Bessel functions of order n evaluated for the arguments: (1) size parameter $x = 2\pi r/\lambda$; (2) the refractive index of the sphere relative to the ambient medium m. The Mie angular functions π_n and τ_n are related to the Legendre polynomials P_n^1

$$\pi_n\left(cos\theta\right) = \frac{1}{sin\left(\theta\right)} P_n^1\left(cos\theta\right) \tag{4.21}$$

$$\tau_n\left(cos\theta\right) = \frac{\mathrm{d}}{\mathrm{d}\theta} P_n^1\left(cos\theta\right) \tag{4.22}$$

Finally, the Mie scattering Q_s and extinction Q_e efficiencies can be derived from the scattering amplitudes from the Forward-Scattering Theorem (i.e., for scattering amplitudes $S_1\left(0°\right)$ and $S_2\left(0°\right)$) [86], [87]

$$Q_s = \frac{2}{x^2} \sum_{n=1}^{\infty} \left(2n+1\right) \left(\left|\alpha_n\right|^2 + \left|b_n\right|^2\right) \tag{4.23}$$

$$Q_e = \frac{2}{x^2} \sum_{n=1}^{\infty} \left(2n+1\right) Re\left(\alpha_n + b_n\right) \tag{4.24}$$

The proposed maximum number of terms in the infinite series is $n_{max} = x + 4x^{\frac{1}{3}} + 2$ [83].

Scattering phase matrix

The intensity and the state of polarization of a light beam are fully described by its Stokes vector $\mathbf{S}$ = (I, Q, U, V). The four elements of this vector are called Stokes parameters and characterize the total intensity I, Q and U are measures of the orientation of the ellipse relative to the x-axis and V is a measure of circularity of the polarization (left- or right-handed circular polarization). The Stokes parameter of a plane monochromatic wave are not completely independent but are related to the quadratic Stokes identity [88]

$$I^2 = Q^2 + U^2 + V^2 \tag{4.25}$$

Except for natural light, in all other cases, light is partially polarized. The unpolarized light has Stokes parameters Q=U=V=0 and I=1. The linearly-polarized light along x-axis has Stokes parameters I=Q=1 and U=V=0. When light has its Stokes parameters Q=U=0, a positive V describes a left-handed circular polarization while a negative V shows a right-handed circular polarization. Finally, for elliptical polarization, a non-negative V parameter is required. Different elliptical polarization states occur for the combinations of U=0, Q≠0 and Q=0, U≠0. The aforementioned particular cases of linear, circular and elliptical polarization are demonstrated in Figure 4.2.

By interposing various polarizers between particle and detector and recording the irradiances, we obtain the Stokes parameters of the light scattered by a particle through the

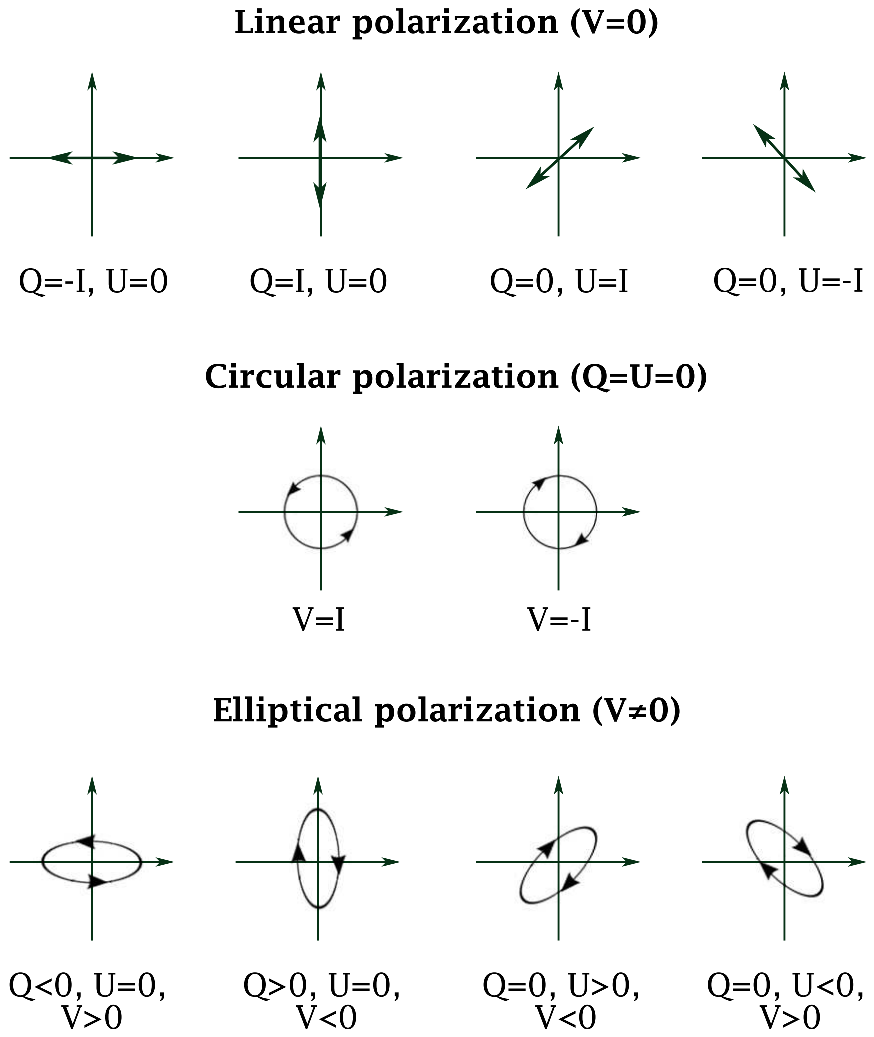

Σχήμα 4.2: *Plane polarization states: particular cases of linear, circular and elliptical polarization. The plane electromagnetic wave propagates towards the reader. Picture was adapted from [88].*

so-called scattering phase matrix F, which is the phase function with polarization. Suppose the intensity and state of polarization of the incident field is described by the Stokes vector $\mathbf{S}_i = (I_i,\, Q_i,\, U_i,\, V_i)$. Then, the corresponding Stokes vector of the scattered field $\mathbf{S}_s = (I_s,\, Q_s,\, U_s,\, V_s)$ for randomly oriented particles is [87], [86]

$$\begin{pmatrix} I_s \\ Q_s \\ U_s \\ V_s \end{pmatrix} = \frac{\sigma_s}{2\pi r^2} F \begin{pmatrix} I_i \\ Q_i \\ U_i \\ V_i \end{pmatrix}, \tag{4.26}$$

where σ_s is the scattering cross section and the scattering matrix is given as

$$F(\theta) = \begin{pmatrix} F_{11}(\theta) & F_{12}(\theta) & 0 & 0 \\ F_{12}(\theta) & F_{22}(\theta) & 0 & 0 \\ 0 & 0 & F_{33}(\theta) & -F_{34}(\theta) \\ 0 & 0 & F_{34}(\theta) & F_{44}(\theta) \end{pmatrix}. \tag{4.27}$$

For spherical particles $F_{11}(\theta) = F_{22}(\theta)$ and $F_{33}(\theta) = F_{44}(\theta)$ and each element $F_{ij}(\theta)$ can be expressed by the scattering amplitude functions $S_1(\theta)$ and $S_2(\theta)$. The scattering matrix becomes a diagonal matrix for exact backscattering because $F_{12}(\theta=180°)=F_{34}(\theta=180°)=0$. Therefore, polarization does not affect the intensity component of the phase matrix F_{11}.

4.2 Inversion of lidar optical data

A multi-wavelength Raman lidar allows the independent determination of particle backscatter, $\beta(\lambda)$, and extinction coefficient, $\beta(\lambda)$. These optical data are related to the physical particle properties by Fredholm integral equations of the first kind

$$\beta(\lambda_i) = \int_0^\infty K_\beta(m,r,\lambda_i)\, f(r)\, dr \tag{4.28}$$

$$\alpha(\lambda_i) = \int_0^\infty K_\alpha(m,r,\lambda_i)\, f(r)\, dr \tag{4.29}$$

The kernel functions $K_{\beta,\alpha}(m,r,\lambda_i)$ are pre-calculated for spherical particles of complex refractive index $m = m_R - im_I$ and radius r when interacting with radiation of wavelength λ_i. The kernel functions are expressed via the backscatter and extinction efficiencies $Q_{\beta,\alpha}(m,r,\lambda_i)$ of Eq. (4.23) and (4.24) [89]

$$K_{\beta,\alpha}(m,r,\lambda_i) = \pi r^2 Q_{\beta,\alpha}(m,r,\lambda_i)\,. \tag{4.30}$$

The inversion process is performed in order to retrieve the integrand $f(r)$ of Eq. (4.28) and (4.29) [90], [91]. The latter is the particle size distribution expressed as the number of particles per unit volume between r and $r+dr$. The particle optical data $g_j(\lambda_i)$ are expressed using a generalized integral equation by reformulating Eq. (4.28) and (4.29) as

$$g_j(\lambda_i) = \int_{r_{min}}^{r_{max}} K_j(m,r,\lambda_i)\, f(r)\, dr, \tag{4.31}$$

with r_{min} and r_{max} denote the lower and the upper limits of the particle radii.

By its nature, the inversion of lidar data is an ill-posed problem [89]. The solution of such problems is only found by numerical methods using regularization techniques [92], [93]. If the optical data are distorted, Eq. (4.31) becomes

$$g_p^\delta = \int\limits_{r_{min}}^{r_{max}} K_p(m,r)\, f^\delta(r)\, dr, \tag{4.32}$$

with subscript $p = j,\lambda$ referring to the kind and number of optical data. The distorted function $f^\delta(r)$ of Eq. (4.32) is sufficiently well approximated by

$$f^\delta(r) = \tilde{f}^\delta(r) + \epsilon = \sum_{j=1}^{N} C_j B_j(r) + \epsilon. \tag{4.33}$$

Therefore, the solution is approximated by $\tilde{f}^\delta(r)$ with an associated uncertainty equal to ϵ. The approximated solution is constructed via the base functions $B_j(r)$ which are of a triangular shape. Mathematically, the base functions are expressed as

$$B_j(r) = \begin{cases} 0 & r < r_{j-1} \\ 1 - \frac{r_j - r}{r_j - r_{j-1}} & r_{j-1} < r \le r_j \\ 1 - \frac{r - r_j}{r_{j+1} - r_j} & r_j < r \le r_{j+1} \\ 0 & r > r_{j+1} \end{cases}$$

The coefficients C_j in the sum of Eq. (4.33) are the weighting factors for the respective base functions. The total number of base functions is N and the inversion is performed in the size range $[r_0,\, r_{N+1}]$ for r_j equally separated points. Usually 8 triangular base functions are sufficient in order to reconstruct the aerosol size distribution. Hence, the existing difficulty in the inversion is how to calculate the proper weight coefficients C_j in Eq. (4.33). The optical data g_p^δ can be reformulated from the combination of Eq. (4.32) and (4.33) as

$$g_p^\delta = \sum_{j=1}^{N} A_{pj}\left(m\right) C_j + \epsilon_p \tag{4.34}$$

where $A_{pj}\left(m\right)$ is the kernel matrix which is given from the individual kernel functions $K_p\left(m,r\right)$ and the respective base function $B_j\left(r\right)$

$$A_{pj}\left(m\right) = \int_{r_{min}}^{r_{max}} K_p\left(m,r\right) B_j\left(r\right) dr \tag{4.35}$$

and the corresponding errors ϵ_p of the distorted optical data g_p^δ

$$\epsilon_p = \int_{r_{min}}^{r_{max}} K_p\left(m,r\right) \epsilon\left(r\right) dr. \tag{4.36}$$

In vector format, the optical data are written as $\mathbf{g}^\delta = \left[g_p^\delta\right]$, the weighting coefficients $\mathbf{C} = \left[C_j\right]$ and the errors $\boldsymbol{\epsilon}^\nabla = \left[\epsilon_p\right]$. Then, Eq. (4.34) writes in the form

$$\mathbf{g}^\delta = A\mathbf{C} + \boldsymbol{\epsilon}^\nabla, \tag{4.37}$$

where $A = \left[A_{pj}\right]$ is the weight matrix consisting of the elements of Eq. (4.35). The vector of weighting coefficients can be found from the above equation as

$$\mathbf{C} = A^{-1}\mathbf{g}^\delta + \boldsymbol{\epsilon}', \tag{4.38}$$

with $\boldsymbol{\epsilon}' = -A^{-1}\boldsymbol{\epsilon}^\nabla$ being the error vector.

The solution space consists of all possible weight coefficients C_j which reproduce the input optical data within the discrepancy limit. In general, the solution is unstable and, thus, the approximate solution $\tilde{f}^\delta$ may not succeed to represent well the accurate solution f. Then, the instability of the solution is suppressed by regularization.

Following Eq. (4.31), the exact optical data are produced when $\hat{A}$ operator is applied to the exact solution f.

$$g = \hat{A} f. \tag{4.39}$$

If the true optical data are approximated by g^δ, the solution space can be restricted by reducing the largest acceptable discrepancy δ between the exact data g and the approximated data g^δ

$$\left\| g - g^\delta \right\| \leq \delta$$

Through the regularization technique, the approximate optical data g^δ with corresponding discrepancy δ are those for which the approximate solution $\tilde{f}^\delta$ converges to the accurate solution f when the discrepancy δ goes to zero

$$\lim_{\delta \to 0} \tilde{f}^\delta = f. \tag{4.40}$$

Let's introduce the function $M^\gamma\left[f, g^\delta\right]$

$$M^{\gamma}\left[f, g^{\delta}\right] = \left\|\hat{A}f - g^{\delta}\right\| + \gamma\Gamma(f),$$

with γ being a Lagrange multiplier (i.e., a non negative regularization parameter) and $\Gamma(f)$ the penalty term which stabilizes the solution on the particle size distributions f [93]. The penalty term is defined as

$$\Gamma(f) = \mathbf{C}^{T} H \mathbf{C}, \tag{4.41}$$

with matrix H being the smoothing matrix which for 8 base functions becomes

$$H = \begin{pmatrix} 1 & -2 & 1 & 0 & 0 & 0 & 0 & 0 \\ -2 & 5 & -4 & 1 & 0 & 0 & 0 & 0 \\ 1 & -4 & 6 & -4 & 1 & 0 & 0 & 0 \\ 0 & 1 & -4 & 6 & -4 & 1 & 0 & 0 \\ 0 & 0 & 1 & -4 & 6 & -4 & 1 & 0 \\ 0 & 0 & 0 & 1 & -4 & 6 & -4 & 1 \\ 0 & 0 & 0 & 0 & 1 & -4 & 5 & -2 \\ 0 & 0 & 0 & 0 & 0 & 1 & -2 & 1 \end{pmatrix}. \tag{4.42}$$

The minimization of $M^{\gamma}\left[\tilde{f}^{\delta}_{\gamma}, g^{\delta}\right]$ leads to the equation:

$$A^{T}A\mathbf{C} - A^{T}g^{\delta} + \gamma H\mathbf{C} = 0. \tag{4.43}$$

Now, the weighting coefficients can be found from the above linear equation

$$\mathbf{C} = \left(A^{T}A + \gamma H\right)^{-1} A^{T}g^{\delta}. \tag{4.44}$$

In the final determination of the weight vector, the smoothing matrix is important because it describes the physical constraint that size distributions do not oscillate significantly within a narrow particle size range. The Lagrange multiplier γ determines the degree of smoothing and hence, the strength of H. Many different methods have been proposed for the selection of the proper Lagrange multiplier, like the maximum-likelihood method, the Bayesian approach, the generalized cross-validation method and the minimum discrepancy principle [94], [95], [96]. The most widely used in lidar inversion algorithms is the minimum discrepancy principle.

CHAPTER 5

Optimization processes for aerosol retrievals

The aerosol retrievals from combined remote sensing instruments belong to a class of ill-posed inverse problems. Ill-posed problems cannot be solved without the use of an *a priori* information [97], [98], [92], [99], [100]. In this chapter, passive and active optical remote sensing observations are used synergistically in order to calculate volume concentration profiles for fine- and coarse-mode aerosol. The lidar signals used as an input to a specific algorithm, consider only the three elastic channels (355 nm, 532 nm, 1064 nm). The code used (LIRIC) requires also as an input the sun-photometric data, briefly introduced in Section 5.1. The fundamentals of the algorithm are presented in Section 5.2 and, finally, in the last Section 5.3 the results from an implementation of the inversion code on specific case studies are discussed.

5.1 Sun-photometers

Sunphotometers are mainly automated sky-scanning radiometers, operated at multiple wavelengths; they measure the direct solar irradiance and sky radiance at the ground level. Direct calculation of the aerosol optical depth for the atmospheric column is possible at various bands provided cloud-free sky conditions. Furthermore, inversion algorithms applied to sun-photometer data are able to provide the microphysical properties of aerosols including the volume particle size distribution with radii range 0.05 up to 15 μm. The logarithmic size distribution considers two modes; one for fine particles and a second one for coarse particles.

CIMEL CE-318-NEDPS9 is an 8-wavelength (340, 380, 440, 500, 675, 870, 1020 and 1640 nm) sun photometer, operating within NASA's AErosol RObotic NETwork (AERONET) [101]. Radiometric measurements are classified in two categories: (1) direct-sun and (2) almucantar (scanning) measurements. Direct sun measurements are performed with a frequency of 15 min. The almucantar measurements are performed only in almost-clear-sky conditions. Thus, the frequency of almucantar measurements depends on the sky cloud fraction. However, in most cases, under favorable meteorological conditions, approximately two to six measurements are successful per day. All the retrieved quantities are derived by solving the vector radiative transfer equation for a plane-parallel multi-layered atmosphere. Those quantities are the AOD (with an uncertainty of 0.01-0.02) [3], and the atmospheric column aerosol microphysical properties [102], [103], [104], such as: the particle volume distribution (with an uncertainty of 15-35%) at 22 size bins, the fractional volume of non-spherical particles, the complex refractive index (with an uncertainty of 0.025-0.050 and 0.03 for the real and imaginary part respectively), the Single-Scattering Albedo (SSA) (with an uncertainty lower than 0.03 for the cases of high AOD (i.e., AOD>0.2) and the Ångström exponent (with an uncertainty of 0.03-0.04) [105], [106].

The exact set of radiometer data which are recalculated before inserting the inversion code are:

- The total columnar volume concentration

  $$\hat{C}_k^V = \int_{r_{min,k}}^{r_{max,k}} \frac{dV_k(r)}{d\ln r} d\ln r; \tag{5.1}$$

  with $r_{min,k}$ and $r_{max,k}$ being the minimum and the maximum radius of the kth aerosol mode.
- the aerosol volume size distribution $V_k(r)/d\ln r$ for each aerosol mode;
- the complex refractive indices at the operating wavelengths;
- the "sphericity", ζ_{sph} which is defined as the ratio of spherical particle's volume to the total volume;
- aerosol optical depth of each k^{th} aerosol mode, $\hat{E}_k(\lambda_j)$;
- the single scattering albedo for each k^{th} aerosol mode, $\varpi_k(\lambda)$;
- the elements of the backscattering matrix, $P_{x,x}^k(\lambda, 180°)$;
- aerosol extinction and backscatter coefficients for the k^{th} aerosol mode, a_k and b_k respectively.

5.2 LIdar-Radiometer Inversion Code (LIRIC)

The inversion code LIRIC is structured along three processes: (i) parameterization of the scatterer under investigation (i.e. development of the aerosol layer model); (ii) derivation of the optical aerosol properties from the aerosol model (i.e., construction of the calculated input signals with specified parameters); and (iii) retrieval of the parameters which minimize discrepancies between the measured and the calculated input signals. In particular, the structure of LIRIC algorithm is illustrated in Figure 5.1.

Preprocessing of lidar data

The lidar signals for j receiving channels are inserted to the software and the range-corrected normalized lidar signals $L_j^*(h)$ are calculated

$$L_j^*(h) = \frac{S_j^*(\lambda_j, h)}{\hat{S}_j^*(\lambda_j, h)} \exp\left(-2\tau_r(\lambda_j, h, h_{ref})\right). \tag{5.2}$$

The set of lidar signals, $L_j^*(h)$, constitutes the measured lidar vector $\mathbf{L}^*$. The measured $\mathbf{L}^*$ and model estimated L should be related to the retrieved quantity $c_k(h)$ via the following equation:

$$\mathbf{L}^* = L(\lambda, c_k(h), a_k, b_k) + \mathbf{\Delta}_L, \tag{5.3}$$

where $\mathbf{\Delta}_L$ is the vector of measurement uncertainties.

In addition, the covariance matrix $\mathbf{\Omega}_L$ is constructed in this module. $\mathbf{\Omega}_L$ is a diagonal matrix which contains the variances of differences between the components $\mathbf{L}^*$ and L.

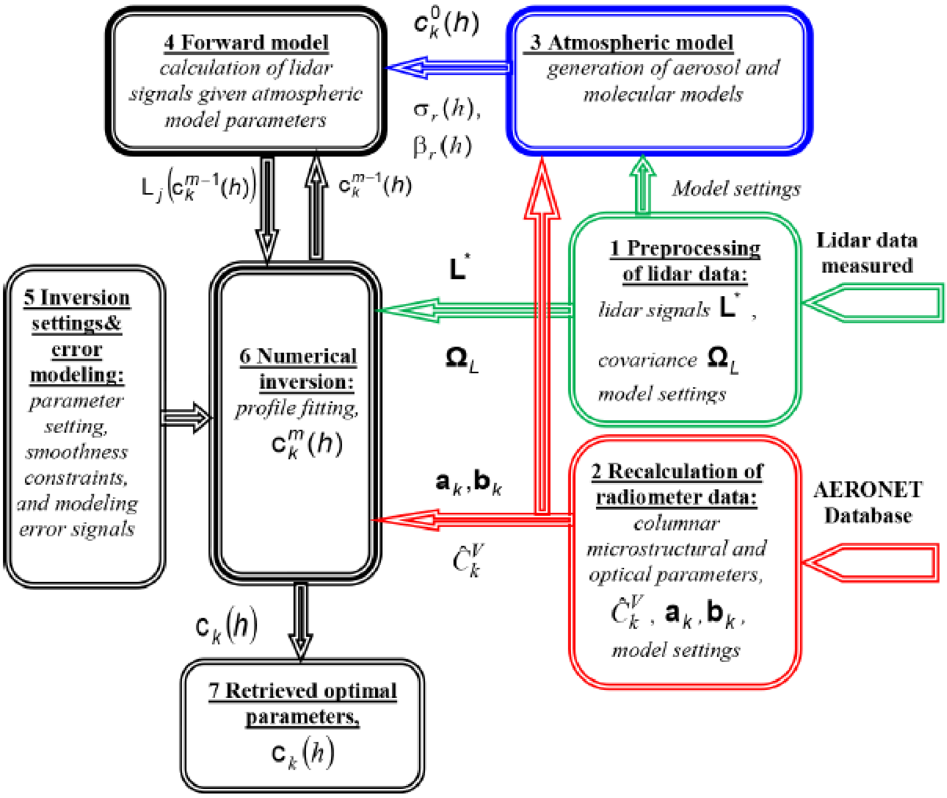

Σχήμα 5.1: *Flowchart of LIRIC algorithm. Picture was taken from [107].*

Recalculation of radiometer data

At this module, all AERONET products of either Level 1.5 or Level 2.0 are inserted to the algorithm aiming to calculate the "measured" columnar volume concentrations of aerosol modes $\hat{\mathbf{C}}^{*V}$ which is mathematically formulated as

$$\hat{\mathbf{C}}^{*V} = \mathbf{Hc} + \mathbf{\Delta}_V, \tag{5.4}$$

where $\mathbf{H}$ is the convolution matrix for integrating the vertically resolved concentration and $\mathbf{\Delta}_V$ is the vector of the sun-photometer volume concentration $\hat{\mathbf{C}}^{*V}$ uncertainties. Then, the k^{th} component of the vector $\hat{\mathbf{C}}^{*V}$ is defined by the following equation

$$\hat{\mathbf{C}}^{*V}(c_k(h_i)) = \sum_{i=1}^{I} c_k(h_i)\Delta h_i + \Delta_{V,k}, \tag{5.5}$$

where $c_k(h_i)$ are the vertical profiles of aerosol mode concentrations.

Atmospheric model

The input of this module comes from module 1. The type of lidar measurement, sounding wavelength, geographical coordinates of the measurement site are some of the setting parameters for the atmospheric model. At this stage, the generation of aerosols and molecular models is materialized. The output parameters are the initial profiles of the aerosol-mode concentration, $c_k^0(h)$ and the molecular extinction and backscatter coefficients $\sigma_r(\lambda, h)$ and $\beta_r(\lambda, h)$, respectively.

Forward model

The Forward model uses all the outputs of the atmospheric model of Module 3 and calculates arrays of lidar signals, $L_j\left(c_k^{m-1}(h)\right)$ and columnar volume concentrations, $\hat{C}^{V,m-1}$ with known aerosol concentration profiles, $c_k^{m-1}(h)$, where m is the number of iterations in the inversion process of module 6.

Inversion setting & error modeling

This module is responsible to generate all the required input information for the numerical inversion module. Such information regards the inversion parameters, the constraints on the smoothness characteristics and the error signals for the sensitivity test.

Numerical inversion & retrieved optimal parameters

This module aims to perform the fitting of volumetric aerosol concentration profiles $c_k^{m-1}(h)$ for the retrieved aerosol model, by taking measured data and *a priori* information. Provided that the aerosol concentration profiles are retrieved through an optimization algorithm, the fundamental mathematical expressions should be briefly discussed. The optimization is being done out of a minimization of the following functional:

$$\Psi(\mathbf{L}^*,\hat{\mathbf{C}}^{*V},\mathbf{c}_k(h))=\Psi_1(\mathbf{L}^*,\mathbf{c}_k(h))+\Psi_2(\hat{\mathbf{C}}^{*V},\mathbf{c}_k(h))+\Psi_3(\mathbf{c}_k(h))) \tag{5.6}$$

The first function Ψ_1 relates the measured lidar data $\mathbf{L}^*$ with the model estimated ones L by calculating the covariance matrix of their differences from Eq. (5.3). The second function Ψ_2 demands that the calculated data $\mathbf{Hc}$ from the retrieved volume concentration profiles are as closer as possible to the radiometric data $\hat{\mathbf{C}}^{*V}$. Finally, the third function Ψ_1 asks for the smoothness constrains related to the *a priori* information. Smoothing is required for assuring stable results in ill-posed problems. In aerosol applications, smoothing is most commonly done by use of second derivatives [102].

5.3 Application of LIRIC on case studies over Athens

The LIRIC algorithm has been used for the derivation of microphysical properties for several type of aerosols [108]. Interesting studies on volcanic ash and dust particles enhance the importance of this inversion code in the aerosol remote sensing community [109], [110]. Lately, LIRIC software has been proved to be a dynamic tool for investigating dust model performance using synergistic European Aerosol Research LIdar NETwork (EARLINET)/AERONET dust concentration retrievals [111]. In this section, results from the evaluation of the LIRIC algorithm performance are discussed. Two cases of dust event occurred over the Athens basin on 5 and 10 June 2013 are explicitly presented. Section 5.3.1 is devoted on the lidar measurements of the period May-July 2013 which were available for testing the LIRIC algorithm. In section 5.3.2, the concentration profiles retrieved by LIRIC are presented, as well as the aerosol backscatter coefficients from the Klett method, as compared with the ones retrieved from LIRIC. Finally, in section 5.3.3, sensitivity tests examine the robustness of LIRIC algorithm with respect to the uncertainties of input parameters.

5.3.1 Lidar Measurements

One year prior to the HygrA-CD campaign, scheduled for the period May-June of 2014, lidar measurements were performed during the same period of the year in order to be used for testing LIRIC mostly for cases of cloud-topped PBL. The following Table 5.1 summarizes the meteorological conditions (wind: long-transport aerosols, cloud cover) and the aerosol load over Athens during those measurements. Two dominant wind directions result to different aerosol conditions above Athens. These directions have been separated to *Southern* versus *Northern* winds. The time series of the range-corrected signals at 1064 nm are presented in Fig. 5.2 for such two cases.

Πίνακας 5.1: *Lidar measurements for the period May - July 2013. Characterization of the measurements has been done upon three categories: Wind Direction, Aerosol Type and Cloud Presence.*

Date	Wind Conditions	Aerosol Type	Cloud Presence
28 May	Southern wind	Saharan dust at 2-4km	Precipitating clouds
29 May	Southern wind	Saharan dust at 1-2 km	Very few clouds
05 June	Mild southern wind	Saharan dust at 2-4 km	Clouds present at 2-4km. Few cirrus at 9km
10 June	Mild southern wind	Saharan dust at 2-5km	Cloud-free sky
19 June	Strong northern wind. Etesians Mildwind	Marine + Urban	Cloud-free sky
26 June	Mild wind	Urban	Presence of low clouds at 2-3km in the afternoon
4 July	Northern wind (N-NE). Local Etesians	Marine + Urban	Low clouds in the afternoon
11 July	Northern wind. Etesians	Marine + Urban	Low clouds in the afternoon
16 July	Northern wind. Etesians	Marine + Urban	Low clouds in the afternoon

- On 28 May, cirrus clouds were present during the day which even precipitated later in the evening. Due to the complicated meteorological conditions and the continuous presence of clouds as it is seen in the Fig. 5.2(a), the corresponding lidar signals cannot be used for LIRIC inversion.

- The dust event of 29 May could be used in LIRIC algorithm. However, dust particles were only present at low altitudes $z<2000$ m and, thus, the lidar signals should be first overlap-corrected. In addition, the dust layer appeared in the PBL and this makes the retrieval of two-mode aerosol concentration profiles an extremely complex process.

- For 4 July and 11 July, radiometric data are completely missing and, therefore, LIRIC retrieval is not possible.

- For 19 June, aerosol load is very low. In particular, from the sunphotometer data the AOD at 675 nm was found equal to 0.062. Moreover, PBL was quite shallow that day. Therefore, LIRIC retrieval is not possible.

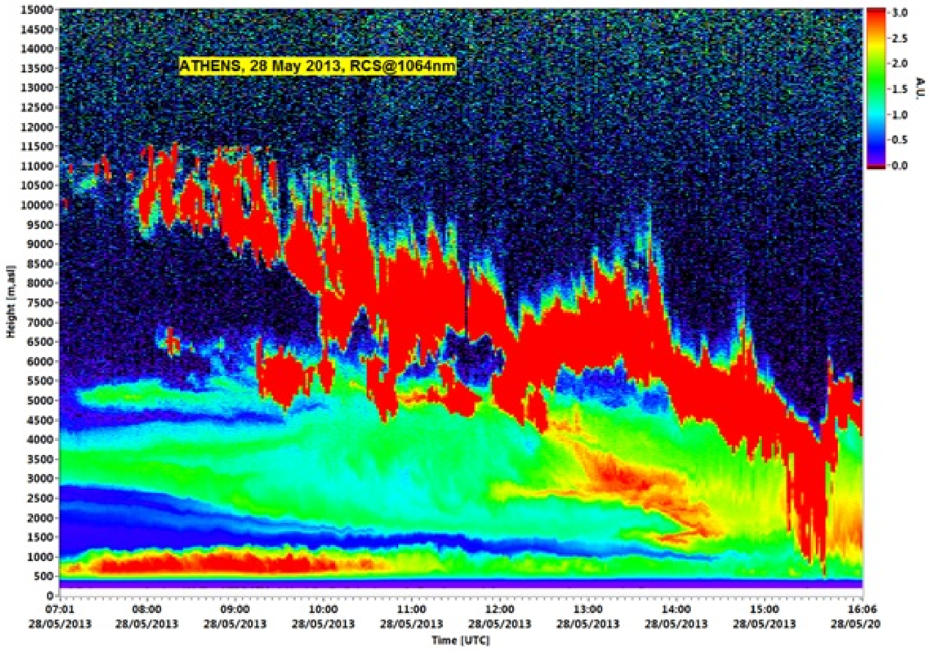

(a) Southern winds: 28 May

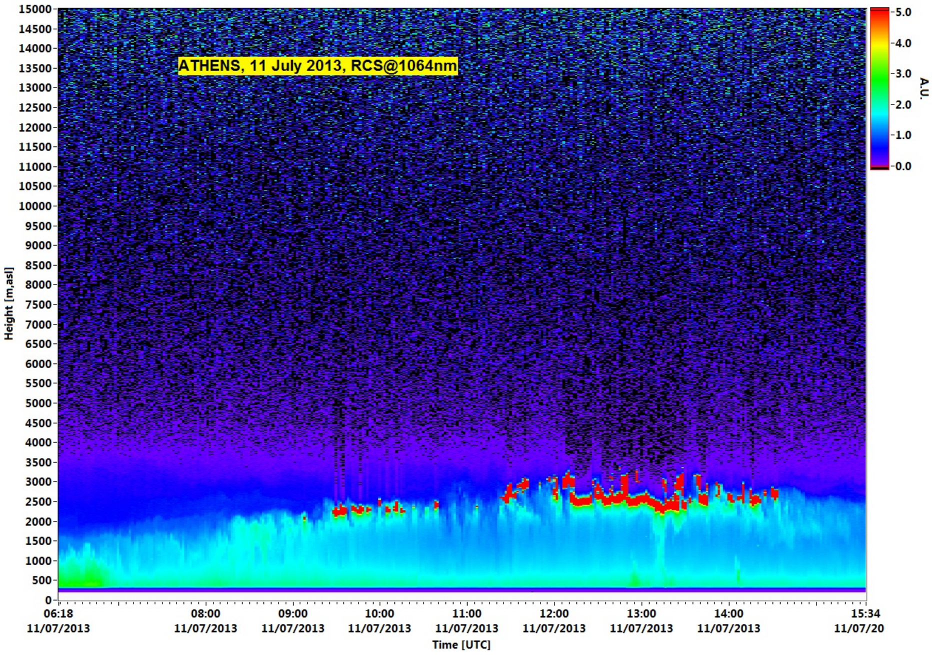

(b) Northern winds: 11 July

Σχήμα 5.2: *Spatio-temporal evolution of the range-corrected lidar signals of two totally different meteorological conditions (Northern Vs Southern winds), bringing totally different aerosol type above Athens. Both colorplots include clouds.* (**a**) *Low synoptic southern wind rich in Saharan dust (28 May): Cirrus clouds precipitate in the afternoon.* (**b**) *Etesians system bringing a mixture of maritime and urban aerosols from the North (11 July): Low clouds appear above the PBL in the afternoon.*

5.3.2 Vertical concentration profile

The vertical profiles of volume concentration $\mathbf{c}_k(h)$ have been optimized through the minimization of the objective function (5.6). When the algorithm converges fast (i.e., in about 10

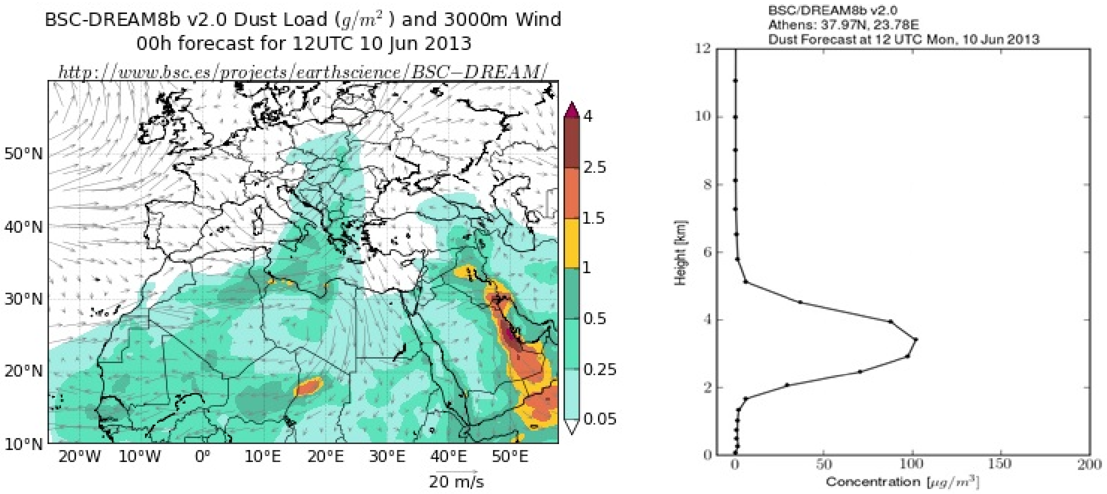

(a) Dust load

(b) Dust concentration

Σχήμα 5.3: *Dust forecast for 10 June 2013 provided by BSC-DREAM model:* (**a**) *Dust load in* $\mu g/m^3$ *and* (**b**) *Dust concentration profile in* $\mu g/m^3$.

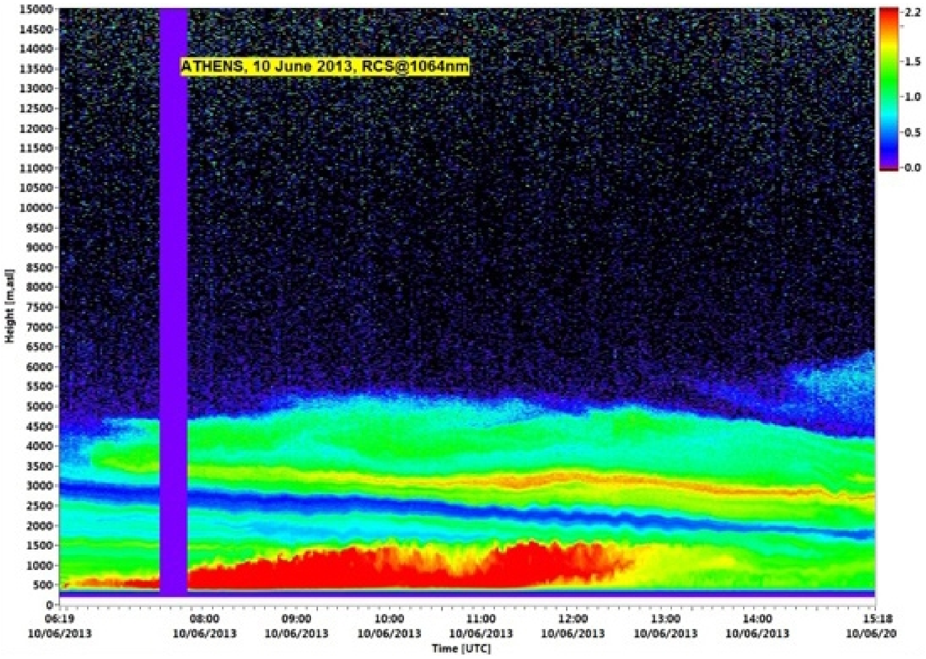

Σχήμα 5.4: *Spatio-temporal evolution of the range-corrected lidar signal at 1064 nm over Athens on 10 June 2013*

iterations), the solutions for fine and coarse mode are in general good and stable. Nevertheless, the fact that the optimization was successful is not a sufficient evidence to guarantee that the retrieved values are physically meaningful too. To strengthen the validity of the retrieved profile, a direct comparison between the aerosol backscatter profile as calculated by the well-known Klett method, versus the one retrieved back from the LIRIC output data. The formula for estimating the aerosol backscatter profile is

$$\beta_{aer}(\lambda, h_i) = c_f(h_i) b_f(\lambda) + c_c(h_i) b_c(\lambda), \tag{5.7}$$

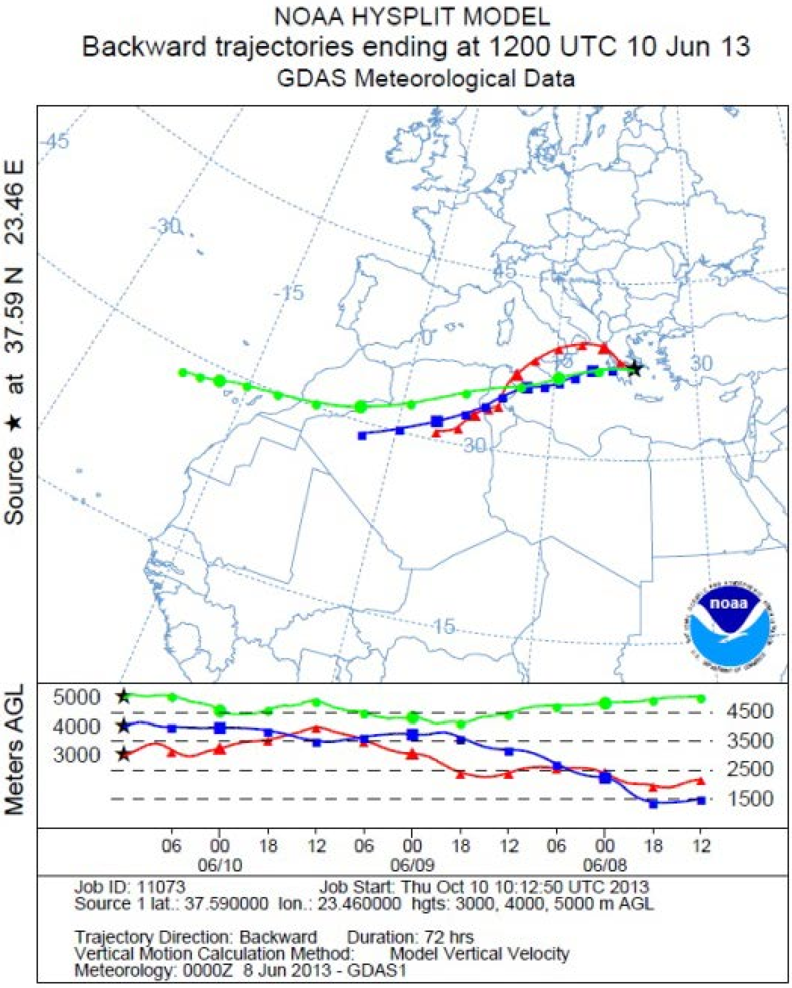

Σχήμα 5.5: *Airmass backward trajectories arriving over Athens on 10 June 2013*

where $c_{f,c}(h_i)$ is the volume concentration profile for fine- and coarse-mode aerosols and $b_{f,c}(\lambda)$ are the backscatter coefficients for fine and coarse mode aerosols at a specified wavelength λ.

Dust event of 10 June 2013

The dust event of 10 June over Athens was forecasted by the BSC-DREAM model (cf. Fig. 5.3(a)). The dust layer was expected at 2-5 km above sea level with a maximum mass concentration of 100 $\mu g/m^3$ (Fig. 5.3(b)). Indeed, the NTUA lidar detected a dust layer above the PBL located between 2000 and 5000 m at 12:00 UTC (cf. Fig. 5.4). The air mass back trajectories arriving at that time over Athens (cf. Fig. 5.5) show that the source region of these aerosol layers is the Saharan desert. Another strong argument regarding the constitution of the aerosol layer comes from sun photometer data. In Fig. 5.6, all the measurements after 08:26 UTC (light blue line) showed high concentration of coarse non-spherical aerosols in the atmospheric column resulting to an AOD(675 nm) of about 0.19. The sun photometer data at 12:26 UTC combined with one hour integrated lidar signals (12:00 - 13:00 UTC) are then used as input to the LIRIC algorithm. The output results after a successful optimization of the algorithm is the volume concentration profile depicted in Fig. 5.7. The vertical profiles of volume concentration seem to be trustworthy above 1500 m, since we observe a good agreement on the retrieved aerosol backscatter coefficient profiles between LIRIC and Klett

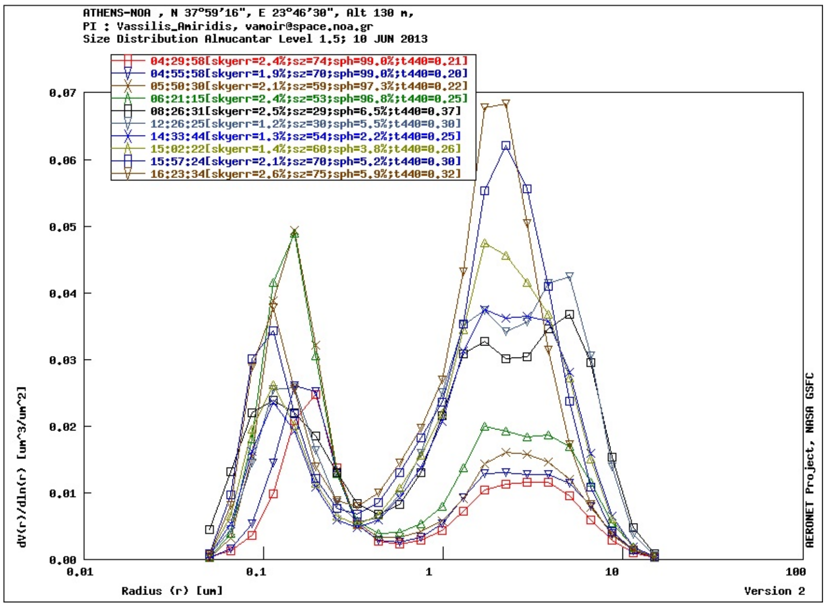

Σχήμα 5.6: *Volumetric size distribution of aerosols obtained by CIMEL on 10 June 2013*

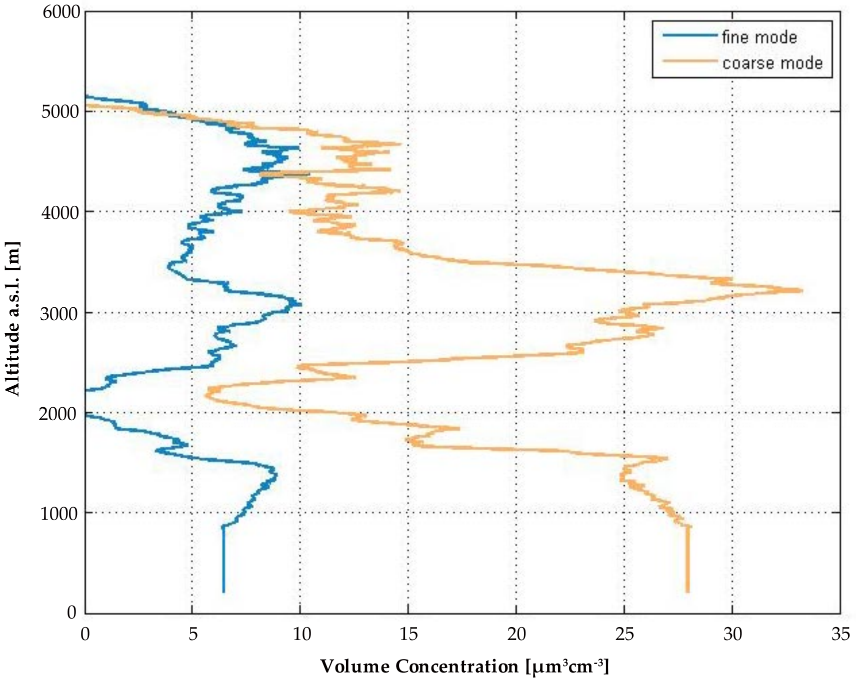

Σχήμα 5.7: *Volume concentration profiles for two aerosol modes retrieved through LIRIC on 10 June 2013*

retrievals, above approximately 1500 m (cf. Fig. 5.8).

Dust event of 5 June 2013

The dust event of 5 June over Athens was not very intense according to the BSC-DREAM model, which forecasted quite low dust load over Greece with a maximum mass concentration

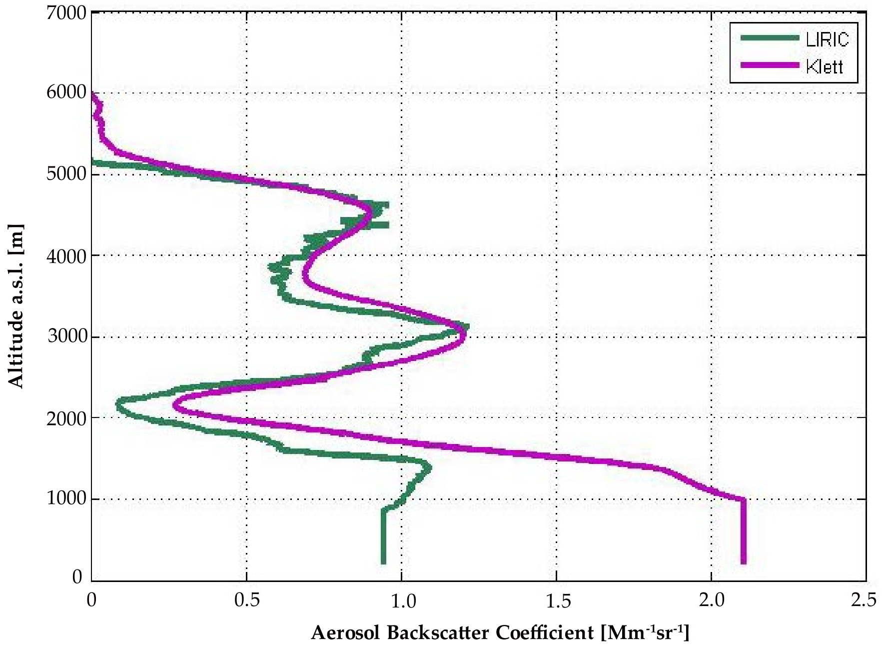

Σχήμα 5.8: *Aerosol backscatter profiles calculated by Klett and LIRIC on 5 June 2013*

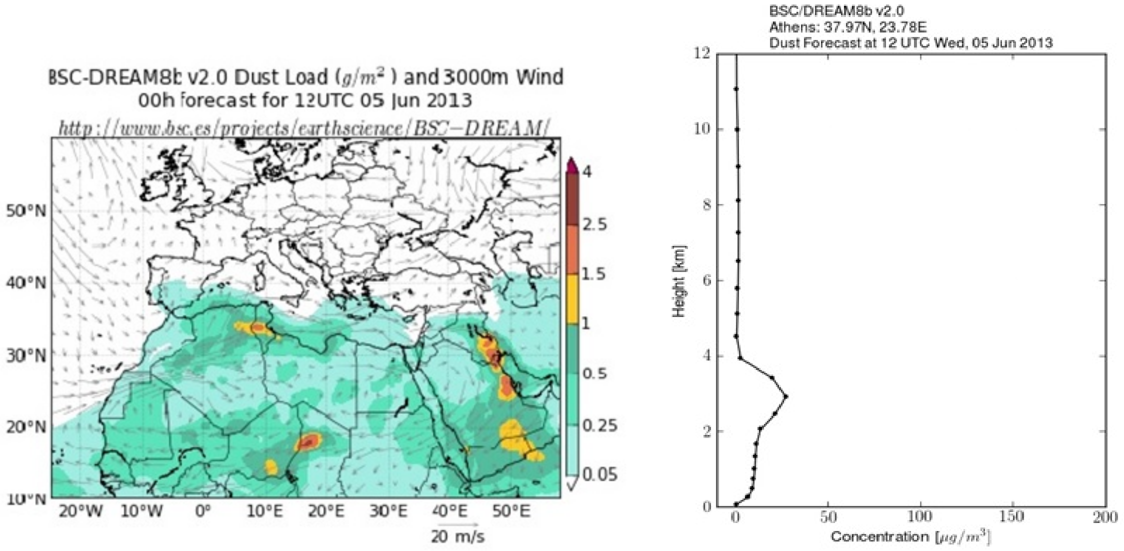

(a) Dust load

(b) Dust concentration

Σχήμα 5.9: *Dust forecast for 5 June 2013 provided by BSC-DREAM model:* (**a**) *Dust load in* $\mu g/m^3$ *and* (**b**) *Dust concentration profile in* $\mu g/m^3$.

of about 25 $\mu g/m^3$ (cf. Fig. 5.9(a)). The dust layer was forecasted to arrive over Athens at around 2000 - 4000 m height. Indeed, from Fig.5.10, an aerosol layer was observed between 2000 and 4000 m height. Nevertheless, due to the presence of clouds during that day, the

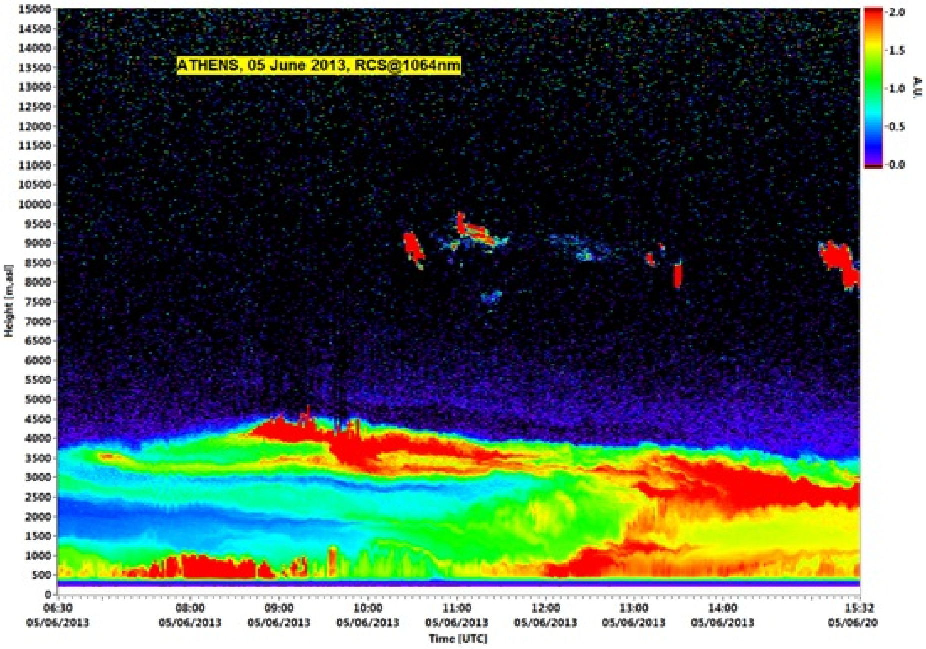

Σχήμα 5.10: *Spatio-temporal evolution of the range-corrected lidar signal at 1064 nm over Athens on 5 June 2013*

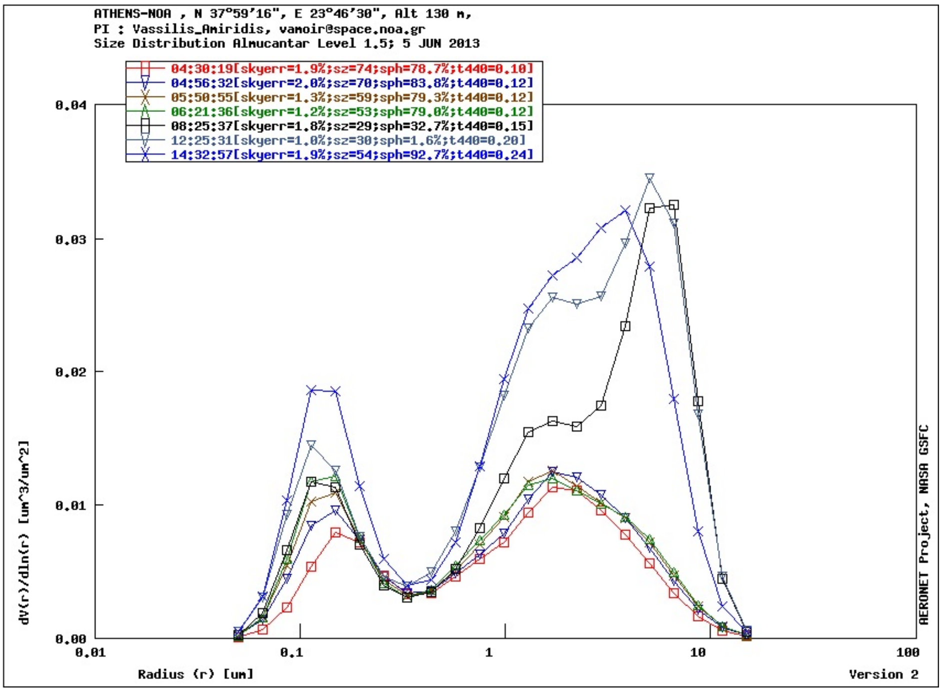

Σχήμα 5.11: *Volumetric size distribution of aerosols obtained by CIMEL on 5 June 2013*

retrieval of the volume concentration profile using LIRIC is possible only for the period 07:40 - 08:20 UTC. Hence, 40-min lidar signals combined with the sunphotometer data of 08:25 UTC (cf. Fig. 5.11) were used for the aerosol volume concentration retrieval; the LIRIC retrieved profiles, shown in Fig. 5.12 are compared to the back-calculated aerosol backscatter coefficient profiles (Klett and LIRIC) shown in Fig. 5.13. In that figure the presence of the

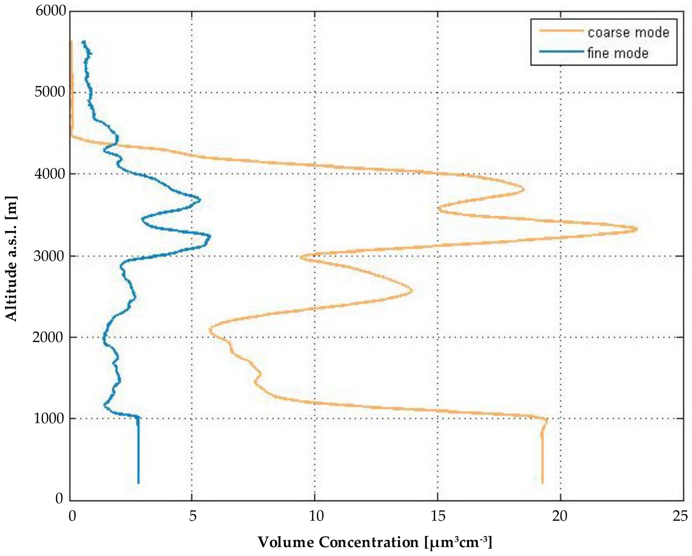

Σχήμα 5.12: *Volume concentration profiles for two aerosol modes retrieved through LIRIC on 5 June 2013*

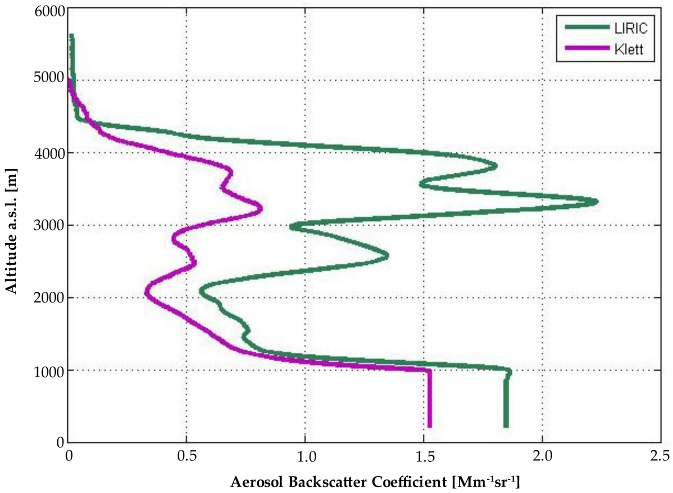

Σχήμα 5.13: *Aerosol backscatter profiles calculated by Klett and LIRIC on 5 June 2013*

dust layer structure between 2000 - 4000 m is well captured although LIRIC overestimates the backscatter coefficient up to a factor of 3, compared to Klett' within the aerosol layer. However, below 1200 m the two aerosol backscatter coefficients do not show significant differences. In general, we can say that LIRIC fails to find the correct dust concentration when the aerosol optical depth is quite low (e.g. AOD(675nm)$<$0.10) and the mass of the dust concentration from BSC-DREAM model is also quite low (e.g. 4 times lower than in the case of 10 June for which the results were optimal within the dust layer).

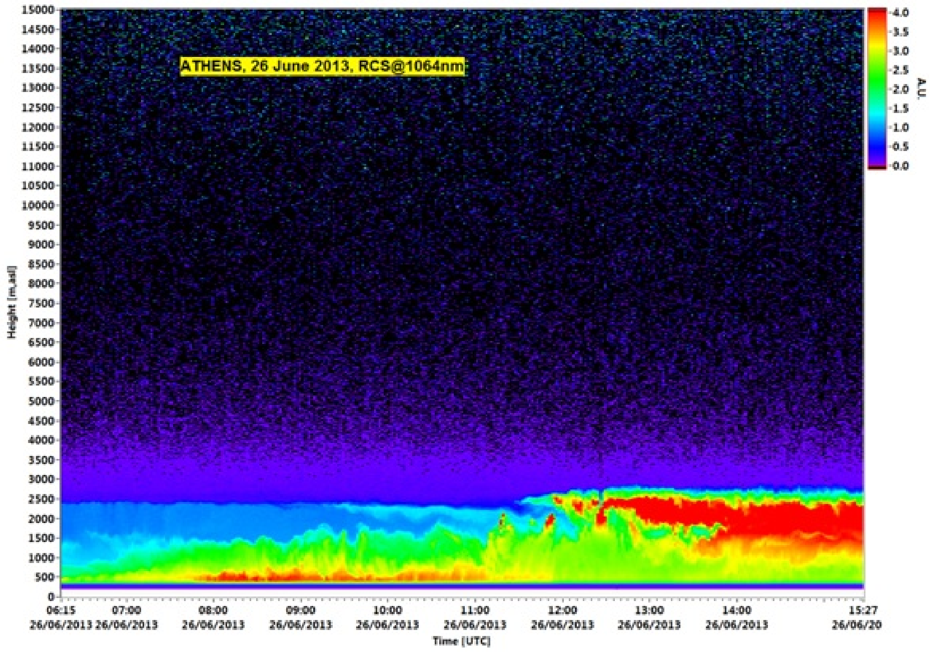

Σχήμα 5.14: *Spatio-temporal evolution of the range-corrected lidar signal at 1064 nm over Athens on 26 June 2013*

5.3.3 Sensitivity analysis

Sensitivity analysis is common in systems or models which are taken as black boxes. Therefore, sensitivity analysis has been performed in the LIRIC algorithm to check the robustness of its results. Such an approach could show how uncertainties in the input parameters of a mathematical model could have a significant impact on the output uncertainties. LIRIC profiler retrieval is a tool which could indeed be considered as a black box by the end-user. The main uncertainties that were included in this work are:

- uncertainty of the reference / calibration height. This height is an assumption introduced when the input lidar signal is processed at an earlier stage (pre-processed) before the optimization. By convention, this height is defined as the altitude above which aerosol concentration is negligible compared to molecular contribution. The portion of aerosol presence above that height is described by the so-called lidar Backscattering Ratio (BR), defined as:

$$BR(z) = \frac{\beta_{aer}(z) + \beta_{mol}(z)}{\beta_{mol}(z)}. \tag{5.8}$$

- uncertainties of the weighting coefficients used during the optimization. LIRIC tool lets the user define: (1) the weighting coefficients related to the lidar signals at all elastic wavelengths, (2) the total concentration of fine and coarse-mode aerosols and (3) the smoothness of aerosol concentration vertical profile of fine and coarse-mode.

Uncertainties on the calibration height

Our sensitivity analysis tests proved out that uncertainties stemming from different values of the reference height might not introduce significant difference on the retrieved vertical profiles of the aerosol volume concentration in some cases with high AOD values (e.g., 26 June 2013, 08:10 - 08:40 UTC). On the other hand, different values of the reference height could introduce uncertainties to the retrieved aerosol concentration profiles in days characterized by a lower AOD as shown in the case of 5 June 2013 (07:40 - 08:20 UTC).

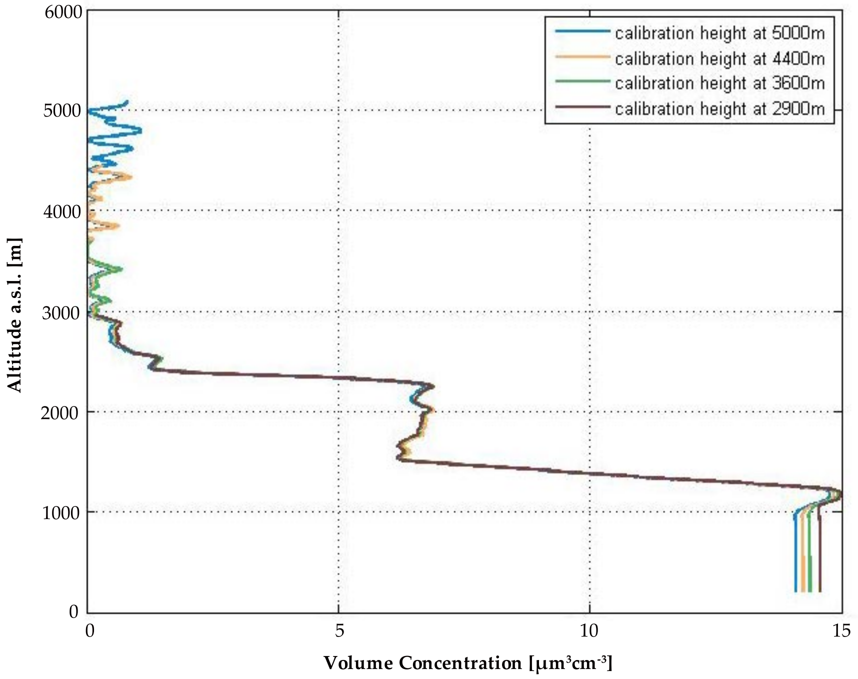

(a) Fine-mode aerosol

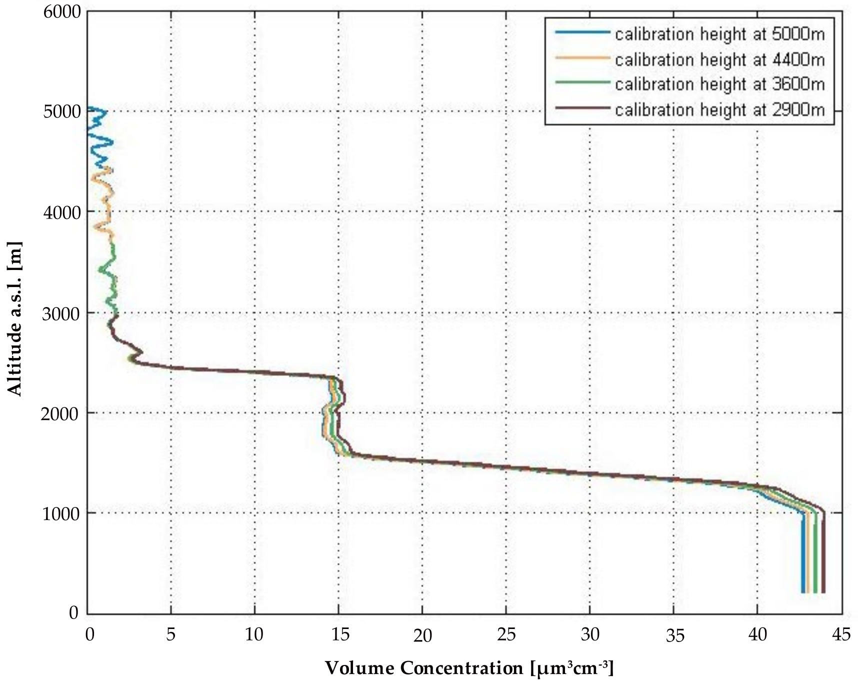

(b) Coarse-mode aerosol

Σχήμα 5.15: *Comparative figures showing the influence of reference height on the fine and coarse-mode aerosol volume concentration profiles on 26 June 2013.*

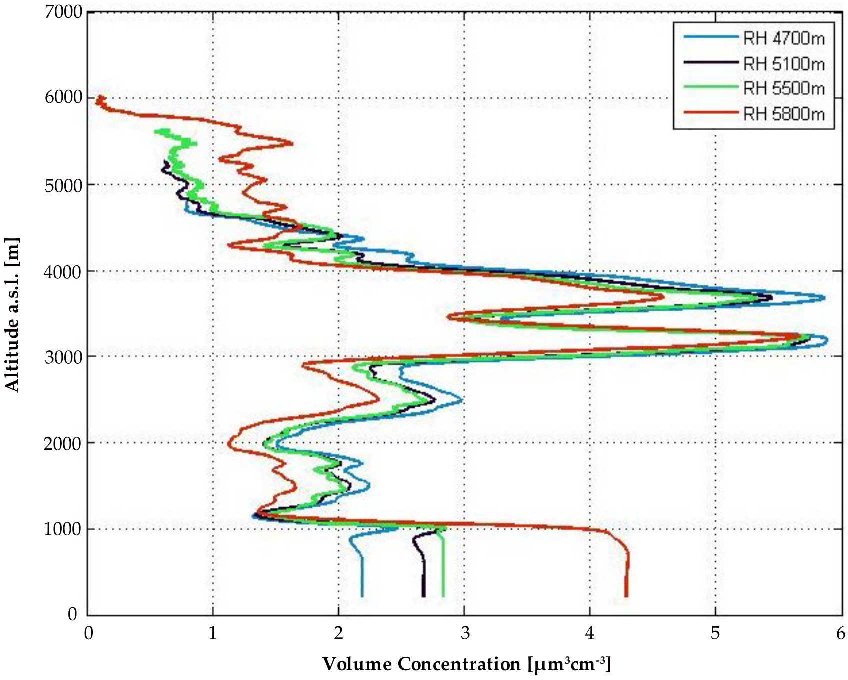

(a) Fine-mode aerosol

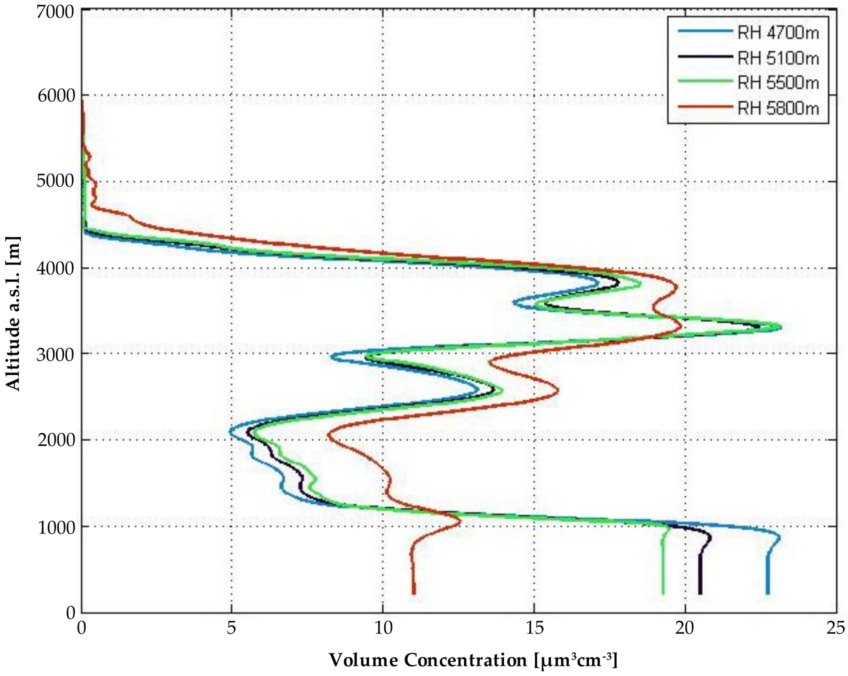

(b) Coarse-mode aerosol

Σχήμα 5.16: *Comparative figures showing the influence of reference height on the fine and coarse-mode aerosol volume concentration profiles on 5 June 2013.*

26 June 2013: In this day the reference height is chosen between 2900 and 5000 m. From Figs. 5.15(a) and 5.15(b) we do not see significant differences on the retrieved (fine-and coarse-mode) aerosol volume concentration profiles, except below 1200 m height. An explanation for this robust behavior is that the aerosol load at 08:10 - 08:40 UTC was within the PBL (cf. Fig. 5.14 and the AOD from CIMEL had a value >0.10 at 675 nm).

5 June 2013: In this day (shown in Fig. 5.10 and characterized by less significant aerosol load, with an AOD of 0.09 at 675 nm) the reference height is chosen between 4700 and 5800 m. Even though the range is narrower in this case, the relatively small distance values of the reference height (between 5500 m and 5800 m) could lead to large discrepancies between the aerosol volume concentration profiles. In particular, the coarse-mode concentration profile (cf. Fig. 5.16(b)) for a reference height of 5800 m (depicted with the red curve) changed significantly at the atmospheric layer at 3000 - 4000 m compared to the ones corresponding to reference heights of 4700, 5100 and 5500 m. We should also note that while increasing the reference height, the concentration of coarse-mode aerosols seems to increase across the whole vertical profile, while concentration of fine-mode aerosols has been decreased below the 4000 m height.

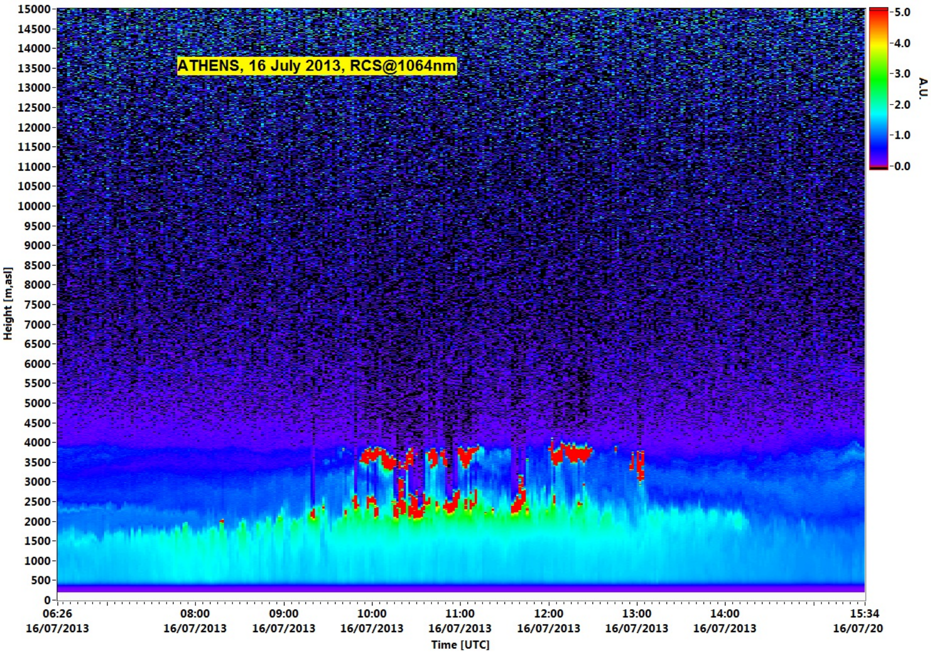

Σχήμα 5.17: *Spatio-temporal evolution of the range-corrected lidar signal at 1064 nm over Athens on 16 July 2013*

Uncertainties on the weighting coefficients

Several other sensitivity tests have been performed to check the influence of the fine-mode and coarse-mode concentration weighting coefficients values on the retrieved aerosol volume concentration profiles. The chosen day for these tests is the 16^{th} of July 2013, where cloud formation above PBL was present. The spatio-temporal evolution of the range-corrected lidar signal at 1064 nm, for that day is shown in Fig. 5.17. The sensitivity tests refer to the period of 08:30 - 09:00 UTC.

The different values (uncertainties) of the fine-mode total concentration weighting coefficient do influence the retrieved aerosol volume concentration profiles when the weighting coefficient has a value lower than 1.7. Hence, we could certainly argue that there is an upper bound for this weighting coefficient above which any further increase will leave both fine-mode and

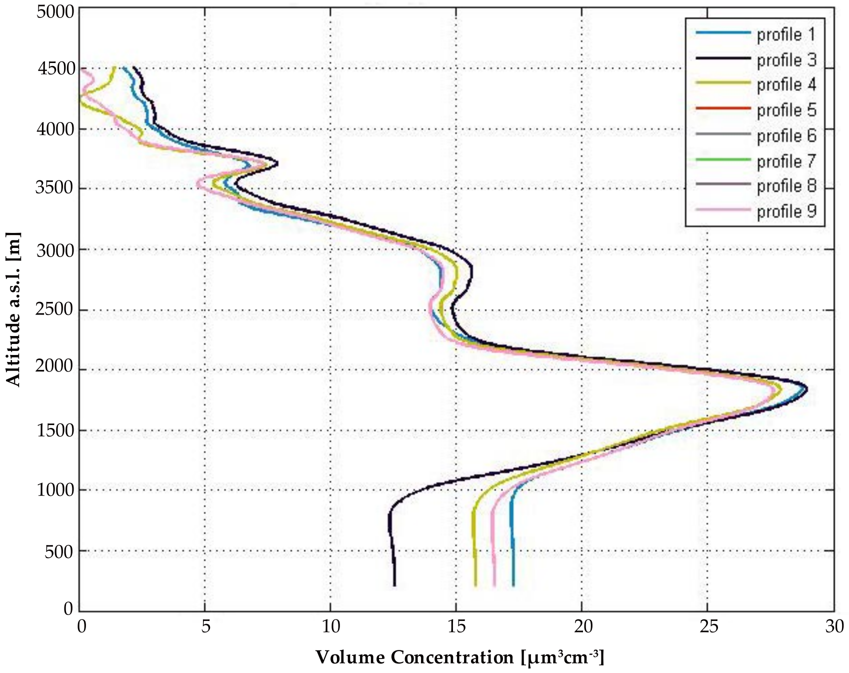

(a) Fine-mode aerosol

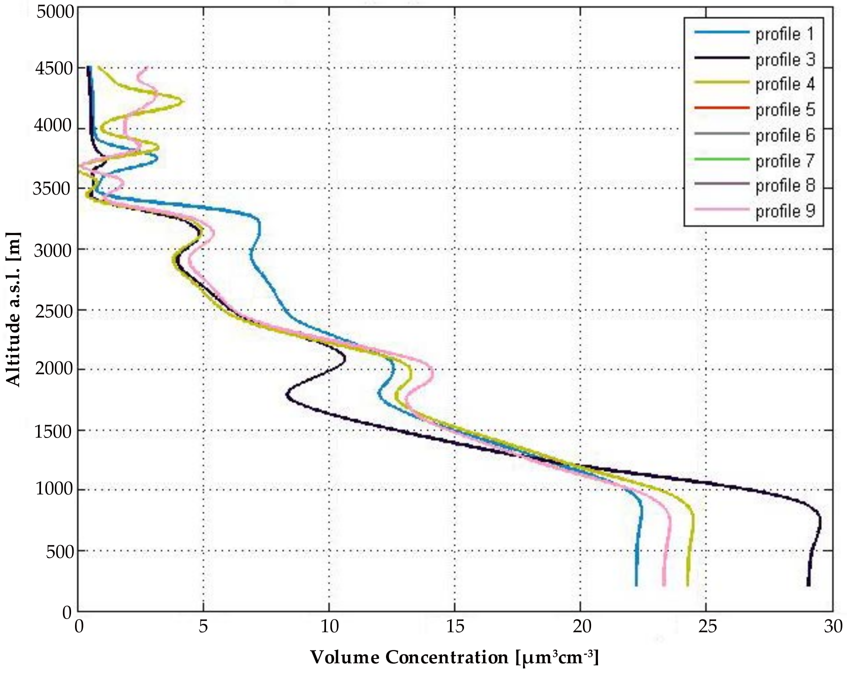

(b) Coarse-mode aerosol

Σχήμα 5.18: *Comparative figures showing the influence of increasing fine-mode concentration weighting coefficient on the fine and coarse-mode aerosol volume concentration profiles on 16 July 2013.*

coarse-mode concentration profiles almost unchanged. For this reason, the profiles numbered 5, 6, 7, 8 and 9 are almost identical (cf. Fig. 5.18).

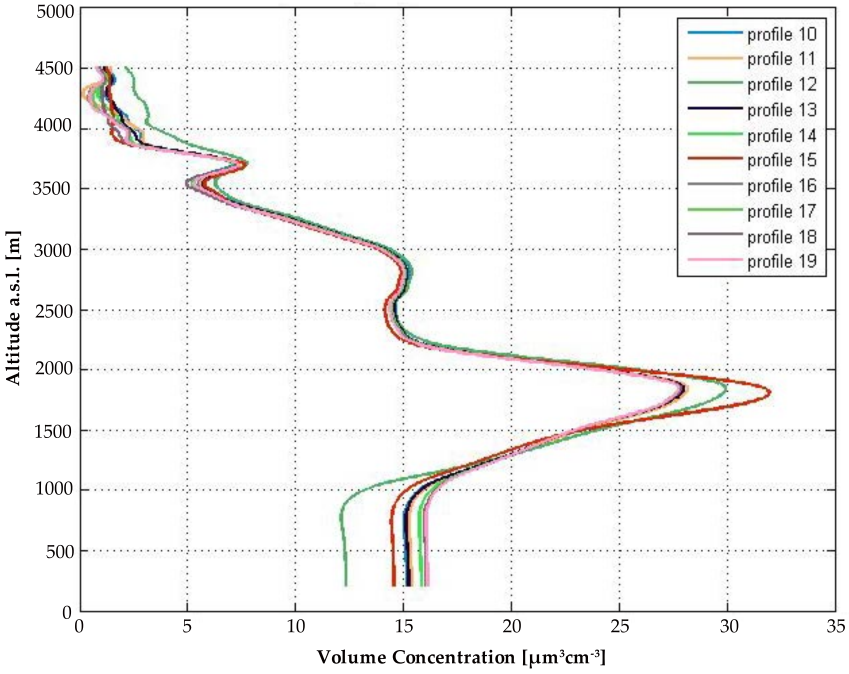

(a) Fine-mode volume aerosol

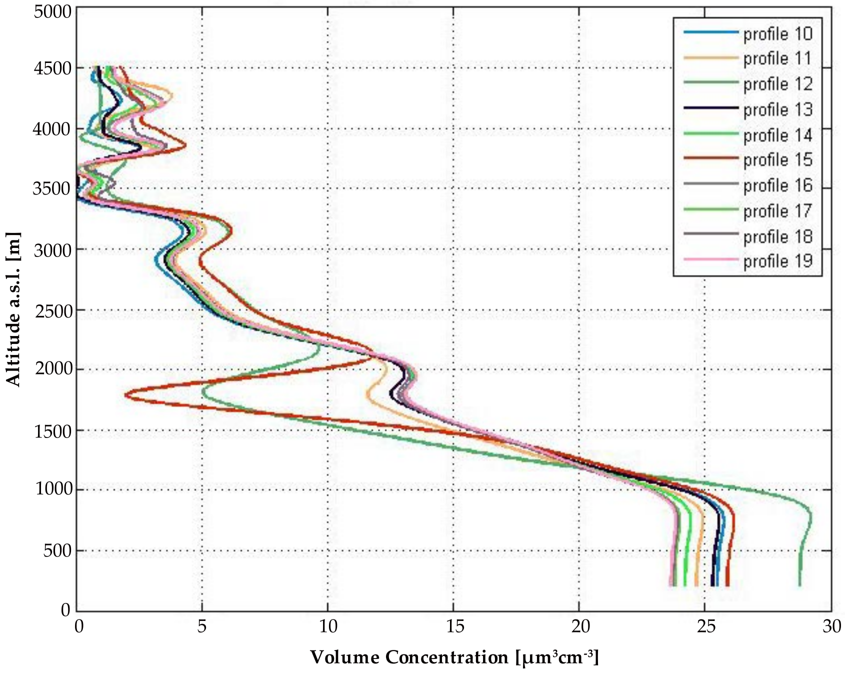

(b) Coarse-mode aerosol

Σχήμα 5.19: *Comparative figures showing the influence of increasing coarse-mode concentration weighting coefficient on the fine and coarse-mode aerosol volume concentration profiles on 16 July 2013.*

On the other hand, the different values of the coarse-mode total concentration weighting coefficients have strong impact on the retrieved aerosol volume concentration profiles. In this case (cf. Fig. 5.19), there is no upper bound for the weighting coefficient which would result to identical profiles again above 1000 m. Any increment from the range 0.2 - 4.2 (corresponding to profiles 10 to 19 in Fig. 5.19) will have a significant effect on the retrieved aerosol volume concentration profiles. In this figure, we see that the retrieved coarse-mode aerosol volume concentration profiles are essentially more sensitive different values of the weighting coefficients, as we saw in the cases depicted in Figs. 5.18 and 5.19.

CHAPTER 6

Experimental Campaign 2014

An international experimental campaign named HygrA-CD has been carried out in the Greater Athens Area (GAA), Greece in the period 15 May-22 June 2014. The major objectives of the campaign are discussed below (section 6.1). The site location is described in section 6.2 while the instrumentation network is presented in section 6.3. Finally, the prevailing meteorological conditions over the GAA are summarized in section 6.4 while an overview of the general findings is given in section 6.5.

6.1 General description

The HygrA-CD campaign (hygracd.impworks.gr) was conceived to study the aerosol-cloud droplet link under convective PBL cloud formation, being part of the Initial Training in Atmospheric Remote Sensing (ITARS) project. A noteworthy aspect of the campaign was the coordinated attempt to strengthen the links between the remote sensing and in-situ observation communities, to resolve the physico-chemical properties of aerosols-CCNs and the dynamical and geometrical properties of clouds, which together with well-established modeling frameworks, would provide a comprehensive view of the aerosol-cloud droplet formation process. A simplified schematic of the different aerosol-meteorology factors-cloud interactions leading to cloud formation near the top of the PBL is presented in Figure 6.1. Aerosols activated as CCNs are transported upwards in a convective PBL, from ground to near the top of the PBL where they form clouds over the LCL. Figure 6.2 shows a conceptual view of the mechanisms leading to cloud development as studied in the frame of HygrA-CD and main instrumentation/models involved.

6.1.1 Scientific Objectives

The major scientific objectives of the HygrA-CD campaign were:

- the characterization of aerosol properties both at ground and aloft in the lower troposphere
- the quantification of aerosols number concentration and its efficiency of being CCN active at water vapor supersaturation levels relevant to ambient clouds, and
- the quantification of tropospheric water vapor content variability

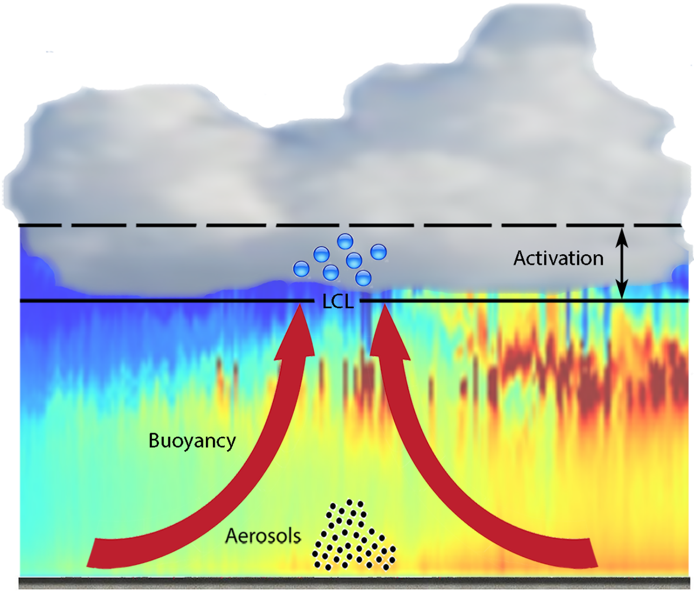

Σχήμα 6.1: *HygrA-CD: Schematic representation of the physical processes present in the cloud-topped PBL [112].*

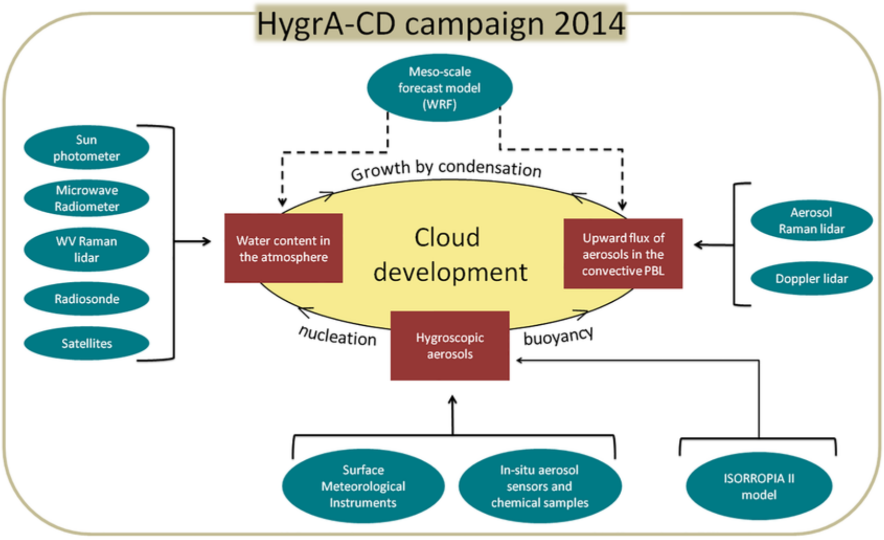

Σχήμα 6.2: *Physical processes studied in the HygrA-CD campaign. Synergy of in-situ ground-based instrumentation and remote sensors has been examined for the better understanding of the physical processes in the cloud-topped PBL. A numerical weather prediction model (i.e., Weather Research and Forecasting (WRF)) and an aerosol model (i.e., ISORROPIA II) have been used to predict atmospheric quantities which were not directly measured by the available instrumentation [112].*

- the study of cloud dynamics, tropospheric water vapor content and low-cloud variability related to atmospheric state
- the retrieval of non-precipitating cloud properties.

In general the HygrA-CD dataset allowed us to better understand the role of aerosols and meteorological conditions under which clouds are formed near the top and above the PBL over the urban site of Athens. Specifically, in the framework of this thesis, we have mainly focused in the following aspects:

1. Synergy between in-situ aerosol instruments at ground level and remote sensing instruments (i.e., aerosol lidar) within a well-mixed PBL [113].
2. Study the dynamics of the PBL (i.e., monitoring updrafts and downdrafts) using a Doppler and Raman lidar [114], [115], [116].
3. Explore the dependence of aerosols properties on the formation of cloud droplets in relation to the existing thermodynamic state of the atmosphere.

6.2 The Greater Athens Area

The GAA is located in the Attica peninsula (around 37°58′ N and 23°43′ E) and hosts a very large urban agglomeration of about 3.8 million inhabitants within about 415 km^2. GAA presents a very complex topography, being surrounded by four major mountains Egaleo (468 m) and Parnitha (1413 m) to the northwest, Penteli (1109 m) to the north and Hymettus (1026 m) to the east and with a major opening to the sea on the south-western part (Saronikos Gulf). These four mountains act as physical barriers, giving a small opening inland to the north-east. This part is a very important one as it gives access to a persistent northeast wind flow, called Etesian winds, mainly during summer period (May-August). A synoptic description of the prevailing flow dynamics in the GAA is given by [117].

The field campaign has been materialized in several locations of GAA. In total six research institutes and universities participated in the experiment and hosted different instrumentation. Figure 6.3 shows the location of the measuring sites. The altitude of each station is given in parenthesis (in meters above sea level: a.s.l.). Much of the instrumentation was located at two major experimental sites: the NTUA (37.97° N, 23.79° E, 212 m a.s.l.) and the National Centre for Scientific Research "DEMOKRITOS" (DEM) (37.99° N, 23.82° E, 275 m a.s.l.). Several other instruments were deployed at the Biomedical Research Foundation of the Academy of Athens (BRFAA) (37.93° N, 23.8° E, 130 m a.s.l.), the National Observatory of Athens (NOA) (38.06° N, 23.86° E, 495 m a.s.l.), the National Kapodistrian University of Athens (NKUA) (37.96° N, 23.73° E, 280 m a.s.l.) and the Hellenic National Meteorological Service (HNMS) (37.98° N, 23.72° E, 10 m a.s.l.).

6.3 Instrumentation & Synergies

To fulfill the HygrA-CD objectives a suite of various instruments (Figure 6.2) of complementary nature (in situ and active/passive remote sensing) was deployed in GAA to characterize the role of aerosols into the cloud formation, especially in the vicinity of the PBL. The suite of the instrumentation deployed for the HygrA-CD is summarized in Tables 6.1 and 6.2 for remote sensing and in-situ instruments respectively. Apart from the name of the instrument, information on the location and the period of operation is provided in these Tables. For remote sensors both the spatial and time resolution are given while for in-situ instruments only the time resolution is provided. The type of physical parameters derived from such instruments is provided in the second column of these Tables.

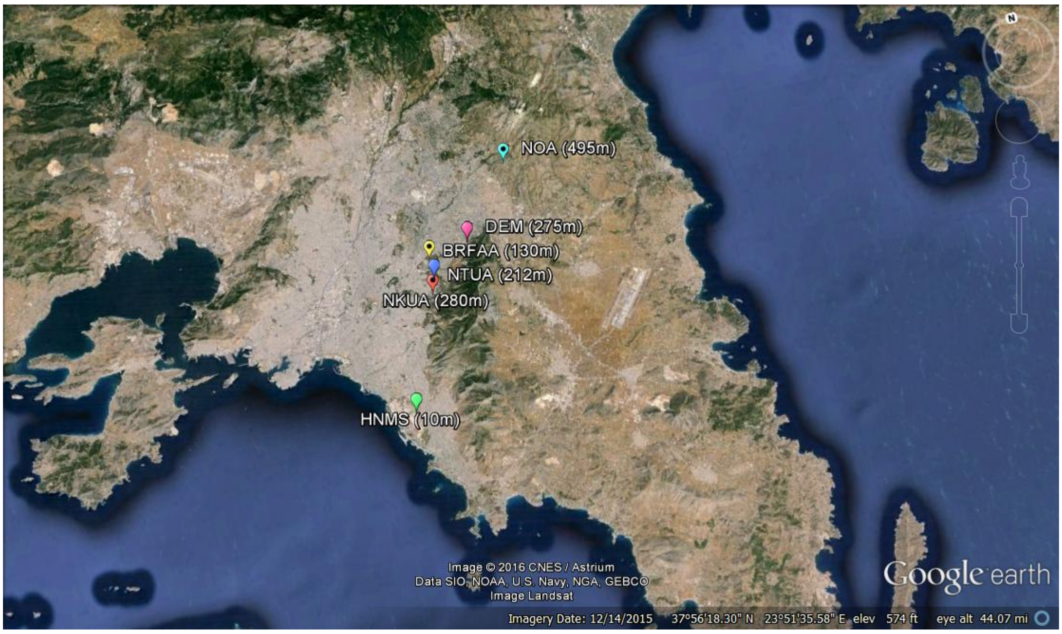

Σχήμα 6.3: *Instrumentation network shown on a map of Athens basin. All six participants in the campaign are show: (1) NTUA with blue icon, (2) DEM with pink icon, (3) BRFAA with yellow icon, (4) NOA with cyan icon, (5) NKUA with red icon and (6) HNMS with green icon. The corresponding distances between NTUA and the several other institutions have been calculated and are the following: NTUA from DEM* **4km***, NTUA from BRFAA* **2km***, NTUA from NOA* **10km***, NTUA from NKUA* **1km** *and NTUA from HNMS* **12km***.*

6.4 Prevailing meteorological conditions over Athens Basin

To obtain a general idea about the origin of the air masses arriving over the GAA during the campaign period, we performed a cluster analysis of the backward air mass trajectories from Hybrid Single Particle Lagrangian Integrated Trajectory (HYSPLIT) model, using the clustering technique provided by [118]. These runs were performed for a 96 hours backwards period starting at 12:00 UTC of each campaign date. The arrival heights over Athens are 0.5, 1, 2, 3 and 4 km. A cluster analysis of all trajectories (195 in total) for all arriving heights indicates the prevalence of three synoptic flow patterns during the campaign namely continental (72.3%), Etesians (14.4%) and Saharan (13.3%). Detailed information on the prevailing meteorological conditions over GAA can be found in [112].

6.5 Overview of the major findings

Provided that the general findings of the campaign are summarized in the review paper [112], in this section we will briefly present the HygrA-CD results related to our work. At first, the characterization of aerosols optical properties has been performed with the use of active remote sensing (i.e., lidar) and passive remote sensing (i.e., sun-photometer) techniques. The origin of the detected aerosol layers has been identified through the HYSPLIT model [119]. Moreover, the thermodynamic state of the atmosphere has been defined from Skew-T LogP diagrams produced based on radiosonde data. Finally, the wind field (wind speed and direction) within the PBL for the whole campaign has been retrieved from a Doppler lidar [112].

6.5.1 Vertical profiling of aerosols

The aerosol Raman lidar EOLE and the elastic depolarization lidar AIAS have been used to retrieve the aerosols' optical properties. The aerosol extensive optical properties like the backscatter and extinction coefficients at 355 nm and 532 nm have been retrieved using the Raman method [75] and the backscatter coefficient at 1064 nm using the Klett technique [73], [120]. The extensive properties depend on the aerosol type and load in the atmospheric layer whereas the intensive properties refer only on the aerosol type and are independent on the amount of aerosols in the layer. With the term intensive aerosol properties we refer to:

- the extinction-to-backscatter ratio, the so-called lidar ratio $S_\lambda(\lambda, z) = \frac{\alpha_{aer}(\lambda,z)}{\beta_{aer}(\lambda,z)}$, which is a proxy of aerosols' absorption capacity and size.
- the Ångström exponent (AE) related to extinction:

$$\text{Å}_{\lambda_1/\lambda_2}(\mathrm{z}) = \frac{\ln\left[\frac{\alpha(\lambda_1,z)}{\alpha(\lambda_2,z)}\right]}{\ln\left[\frac{\lambda_2}{\lambda_1}\right]} \tag{6.1}$$

, which expresses the wavelength dependence of the aerosols extinction coefficient and can be used as a proxy of the aerosols size (e.g., small particles have a large wavelength dependence and therefore a large Angström exponent).

The vertical profiles of the extensive (3β+2α) and intensive optical properties ($2S$ and 3AE) have been retrieved for 20 days during the HygrA-CD campaign and are shown below.

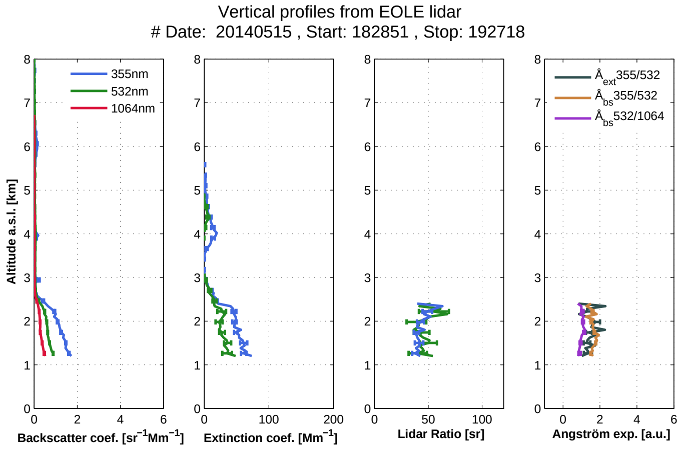

Σχήμα 6.4: *Vertical profiles of aerosol optical properties (15 May). From left to right, first graph shows aerosol backscatter coefficient, second graph shows aerosol extinction coefficient, third graph shows aerosol S_λ and fourth graph shows AE.*

Optical properties of the detected aerosol layers

The optical properties of detected aerosol layers are presented in Table 6.3. The intensive optical properties of each layer are the S_λ at 355 and 532 nm and the AE-extinction related. These two parameter were both retrieved from EOLE Raman lidar. The linear particle depolarization ratio (δ_p) is a parameter which was retrieved from AIAS depolarization lidar. The S_λ, AE and δ_p are also illustrated in Figs 6.24 and 6.25, respectively. The lidar classification scheme over our site consider the air mass origin and the respective values of S_λ (355 and 532 nm), AE and δ_p in conjunction with typical experimental values found in literature (e.g, [121], [122], [123], [124], [125], [126], [127]). The observed aerosol were classified as mixed

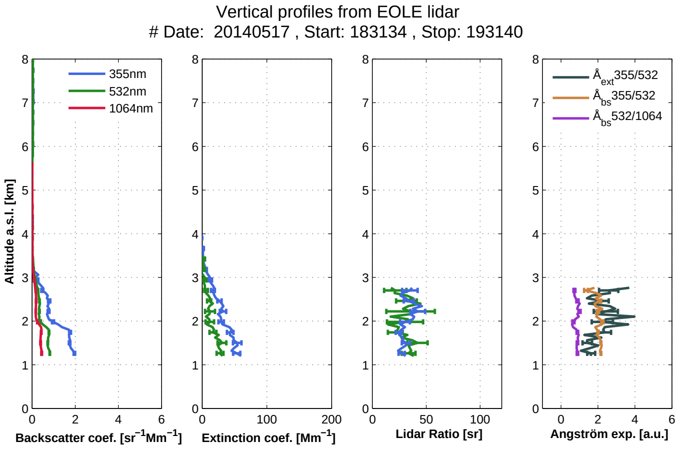

Σχήμα 6.5: *Vertical profiles of aerosol optical properties (17 May). From left to right, first graph shows aerosol backscatter coefficient, second graph shows aerosol extinction coefficient, third graph shows aerosol* S_λ *and fourth graph shows AE.*

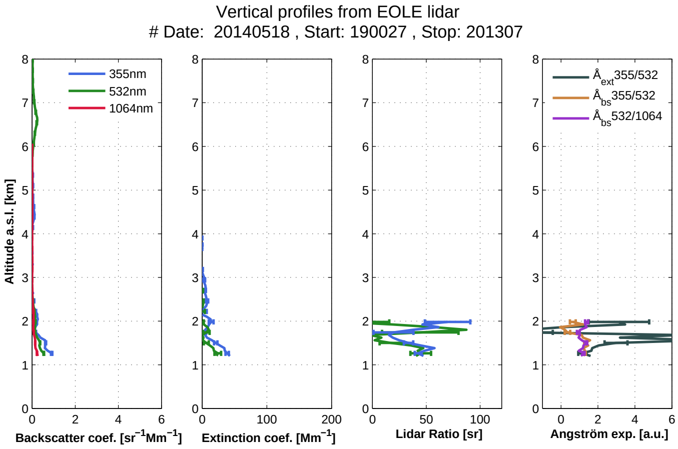

Σχήμα 6.6: *Vertical profiles of aerosol optical properties (18 May). From left to right, first graph shows aerosol backscatter coefficient, second graph shows aerosol extinction coefficient, third graph shows aerosol* S_λ *and fourth graph shows AE.*

dust, continental, mixed biomass burning, mixed Arctic-continental-biomass burning, mixed continental-marine, and Asian dust-biomass burning-continental. For each of the tropospheric aerosol layers (up to 5 km height) identified by lidar within HygrA-CD, we performed an individual 9-day backward trajectory analysis for the base, center and top of the layer at the lidar measurement time (see Appendix B) in order to define the air mass origin. When smoke particles were identified by the lidar, we cross-checked this information from MODIS data [128], [129]. The DREAM [130] and WRF-Flexpart models were also used to identify those cases where Saharan dust was advected above GAA.

Moreover, especially from the S_λ parameter, the Figs 6.26 and 6.27 show that a S_λ of 40 sr and 45 sr within the PBL was the most frequently observed at 355 nm and 532 nm, respectively. This S_λ value could be typical for an mixture of anthropogenic with marine. Similar S_λ is sometimes observed when dust is advected from Saharan desert, however they are detected more frequently at the Free Troposphere (FT) rather than within the PBL. The argument of detecting mixture of anthropogenic and marine aerosols is enhanced by the histograms in Figs 6.28 and 6.29 which indicate occurrences of small and spherical aerosols within PBL characterized by an AE > 1.2 and a $\delta_p < 5\%$.

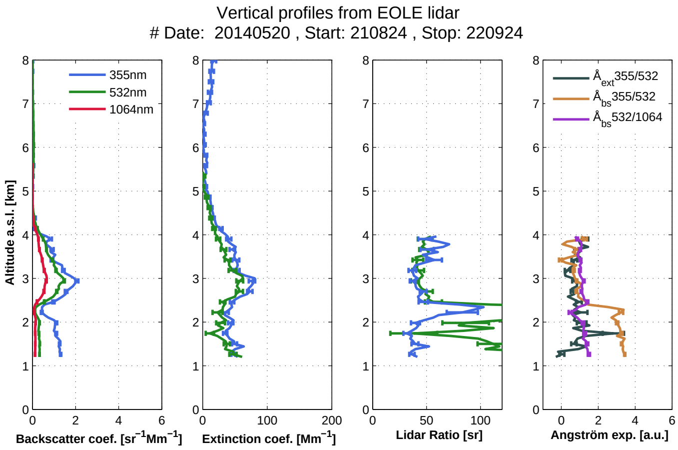

Σχήμα 6.7: *Vertical profiles of aerosol optical properties (20 May). From left to right, first graph shows aerosol backscatter coefficient, second graph shows aerosol extinction coefficient, third graph shows aerosol S_λ and fourth graph shows AE.*

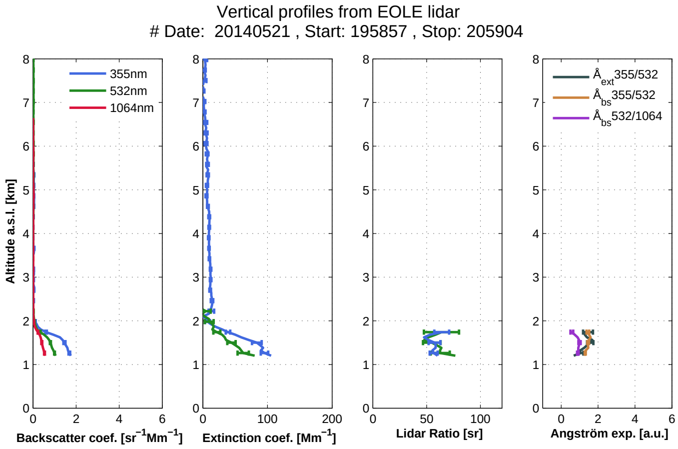

Σχήμα 6.8: *Vertical profiles of aerosol optical properties (21 May). From left to right, first graph shows aerosol backscatter coefficient, second graph shows aerosol extinction coefficient, third graph shows aerosol S_λ and fourth graph shows AE.*

From the integration of aerosol extinction coefficient, we can also retrieved the AOD as follows:

$$\tau_{aer}(\lambda) = \int_{z=0}^{z=TOA} \alpha(z,\lambda)dz \tag{6.2}$$

The AOD at 355 nm and 532 nm are illustrated in Figure 6.30. They are both indicators of the aerosol load in an atmospheric column at nighttime. The nighttime AOD can be compared to the AOD at daytime which is retrieved from CIMEL sunphotometer and are shown in Figure 6.31. The results indicate an increased AOD when Saharan dust is present. It seems that dust particles were not able to act as CCNs and lead to cloud formation at the PBL top during the campaign. Therefore, the AOD cannot be a single indicator for cloud droplet activation. The question is whether dust particles are efficient to act as CCNs and the thermodynamic conditions do not favor activation or dust aerosols do not act as CCN. The answer is given by exploring the state of the atmosphere when air masses from W-SW directions reach the GAA.

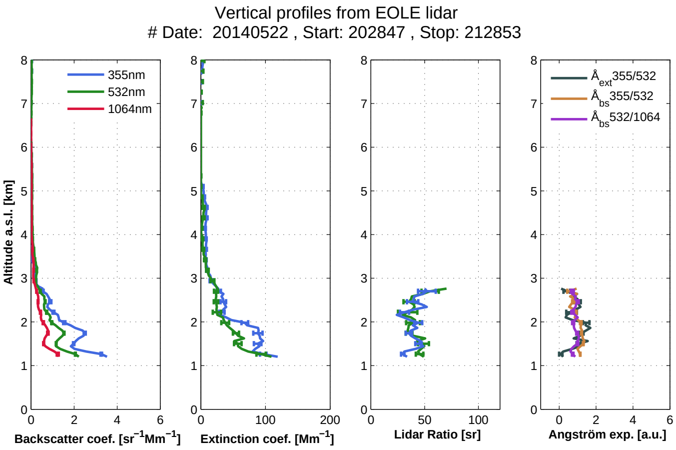

Σχήμα 6.9: *Vertical profiles of aerosol optical properties (22 May). From left to right, first graph shows aerosol backscatter coefficient, second graph shows aerosol extinction coefficient, third graph shows aerosol* S_λ *and fourth graph shows AE.*

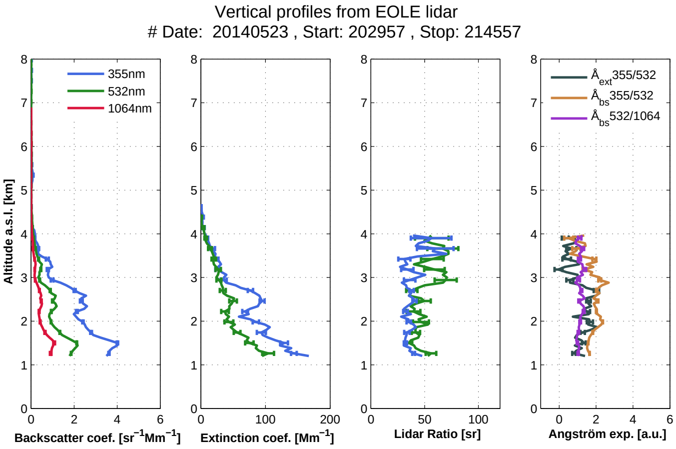

Σχήμα 6.10: *Vertical profiles of aerosol optical properties (23 May). From left to right, first graph shows aerosol backscatter coefficient, second graph shows aerosol extinction coefficient, third graph shows aerosol* S_λ *and fourth graph shows AE.*

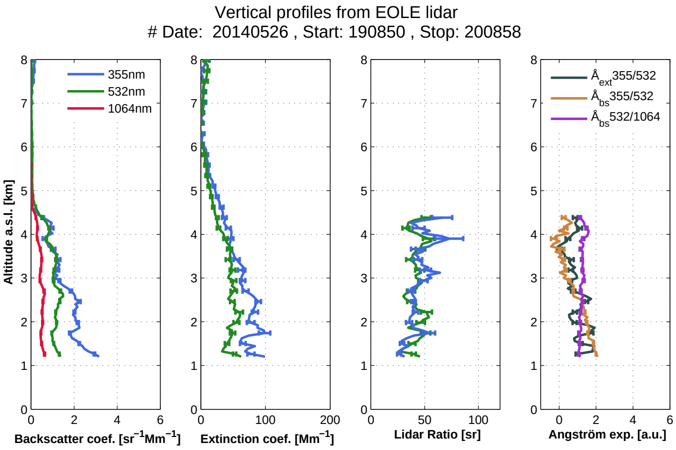

Σχήμα 6.11: *Vertical profiles of aerosol optical properties (26 May). From left to right, first graph shows aerosol backscatter coefficient, second graph shows aerosol extinction coefficient, third graph shows aerosol* S_λ *and fourth graph shows AE.*

Πίνακας 6.1: *Remote sensors operated during the HygrA-CD campaign. The first column names the sensor. The next four columns provide the information on the physical parameter retrieved by the instrument, the raw spatio-temporal resolution, the location and the period of operation. The last column gives some reference for the instrument.*

Instrument	**Parameter retrieved**	**Raw resolution**	**Site**	**Period of operation**	**Ref.**
Aerosol depolarization lidar (AIAS)	Aerosol backscatter coefficient, volume particle depolarization ratio, linear particle depolarization ratio	Spatial: 7.5 m, Time: 100 s	DEM	15.05-22.06	[1]
Aerosol Raman lidar (EOLE)	Aerosol backscatter coefficient, aerosol extinction coefficient	Spatial: 7.5 m, Time: 100 s	NTUA	15.05-22.06	[2]
Sun photometer	Aerosol optical depth, Ångström exponent, aerosol size distribution, effective radius, single scattering albedo	Time: 15 min	BRFAA	15.05-17.06	[3], AERONET
Wind Doppler lidar	Wind speed and direction, Doppler velocity, energy dissipation rate	Spatial: 30 m, Time: 24 s	DEM	15.05-17.06	[4]
Microwave radiometer	Temperature and humidity profiles, integrated water vapor, liquid water path	Spatial: 200 m (0-2 km), 400 m (2-5 km), 800 m (5-10 km), Time: 1 s	NTUA	15.05-20.06	[5], [6], [7
Ceilometer	Attenuated backscatter, mixing layer height, cloud base	Spatial: 5 m, Time: 30 s	DEM	15.05-22.06	[8]
Weather radar	Doppler velocity (radial) and spectral width, horizontal and differential reflectivity, differential phase shift, co-polar correlation, Rainfall rate and droplet size distribution (for droplet diameters > 0.3 mm)	Spatial horizontal: 120 m (24 km range), Spatial vertical: 12-25 m (from 0.5-12.5 km), Time: 1 min	NOA	23.05-17.06	[9], [10]
Radiosonde	Temperature, pressure, RH, wind (speed and direction), height	Spatial: 20 m, Time: 0.4-20 s	HNMS	15.05-22.06	[11], Vaisala

Πίνακας 6.2: *In-situ instruments operated during the HygrA-CD campaign. The first column names the instrument. The next four columns provide the information on the physical parameter retrieved by the instrument, the raw time resolution, the location and the period of operation. The last column gives some reference for the instrument when it is available.*

Instrument	**Parameter retrieved**	**Time resolution**	**Site**	**Period of operation**	**Ref.**
PM_1	PM_1 mass concentration	1 min	NTUA	15.05-22.06	N/A
PM_{10}	PM_{10} mass concentration	1 min	NTUA	15.05-22.06	N/A
SMPS-OPC	Aerosol size distribution	5 min	DEM, NTUA	15.05-22.06	[12], [13]
CCN counter	CCN number concentration, κ-parameter under supersaturation	10 min	DEM	18.06-22.06	[14]
Nephelometer	Aerosol total scattering coefficient and backscattering coefficient	1 min	DEM	15.05-22.06	[15]
Aethalometer	Equivalent black carbon concentration	5 min	DEM	15.05-22.06	[16]
EC/OC	Elemental/organic carbon concentration	3 hours	DEM	15.05-22.06	[17], [18]
Ion Chromatographer	Water soluble ions in aerosol samples	3-5 hours	NTUA	21.05-07.06	[19]
Meteorological station	Temperature, pressure, RH, wind (speed and direction)	10 min	NTUA, NOA, HNMS	15.05-22.06	N/A

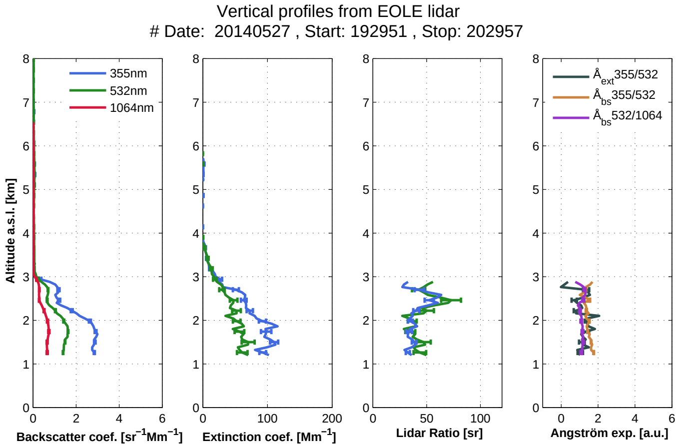
Vertical profiles from EOLE lidar
Date: 20140527 , Start: 192951 , Stop: 202957

Σχήμα 6.12: *Vertical profiles of aerosol optical properties (27 May). From left to right, first graph shows aerosol backscatter coefficient, second graph shows aerosol extinction coefficient, third graph shows aerosol* S_λ *and fourth graph shows AE.*

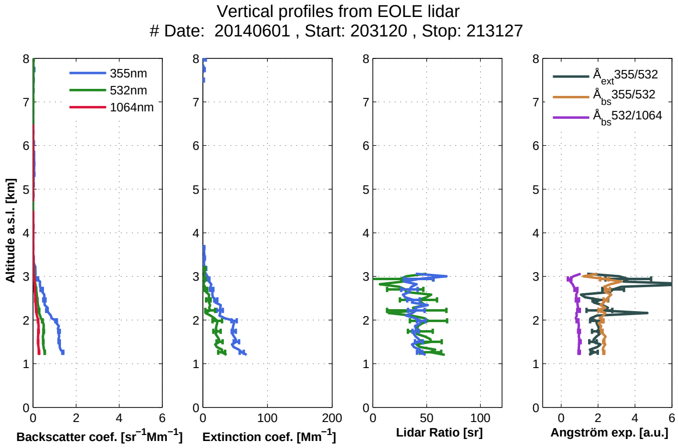

Σχήμα 6.13: *Vertical profiles of aerosol optical properties (1 June). From left to right, first graph shows aerosol backscatter coefficient, second graph shows aerosol extinction coefficient, third graph shows aerosol S_λ and fourth graph shows AE.*

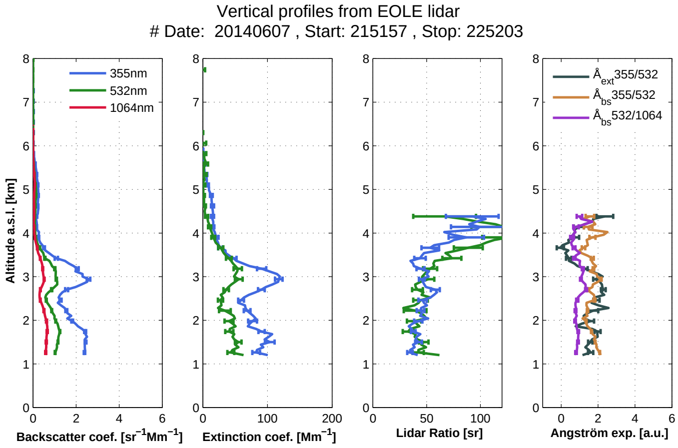

Σχήμα 6.14: *Vertical profiles of aerosol optical properties (7 June). From left to right, first graph shows aerosol backscatter coefficient, second graph shows aerosol extinction coefficient, third graph shows aerosol S_λ and fourth graph shows AE.*

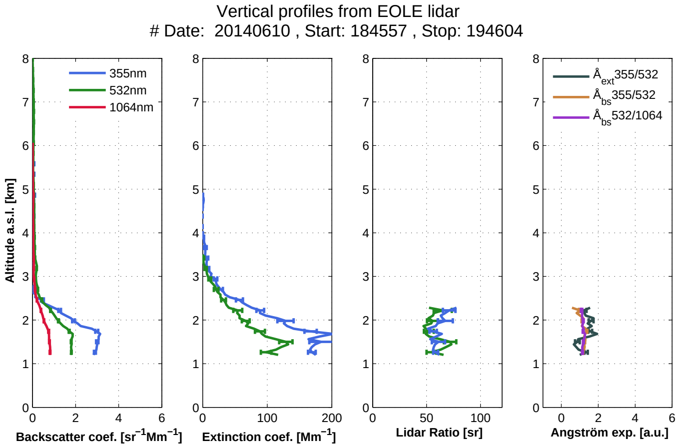

Σχήμα 6.15: *Vertical profiles of aerosol optical properties (10 June). From left to right, first graph shows aerosol backscatter coefficient, second graph shows aerosol extinction coefficient, third graph shows aerosol S_λ and fourth graph shows AE.*

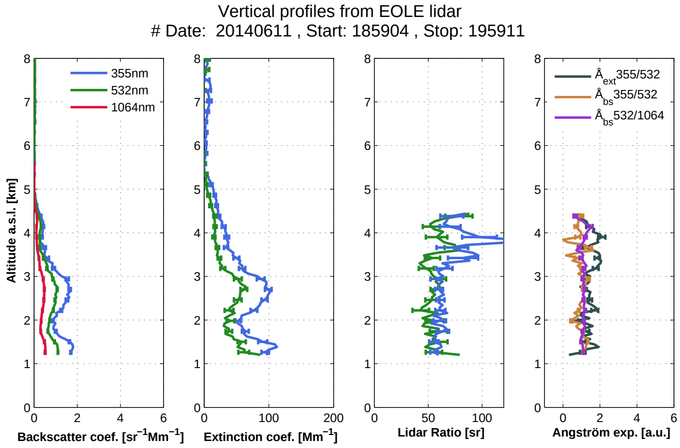

Σχήμα 6.16: *Vertical profiles of aerosol optical properties (11 June). From left to right, first graph shows aerosol backscatter coefficient, second graph shows aerosol extinction coefficient, third graph shows aerosol* S_λ *and fourth graph shows AE.*

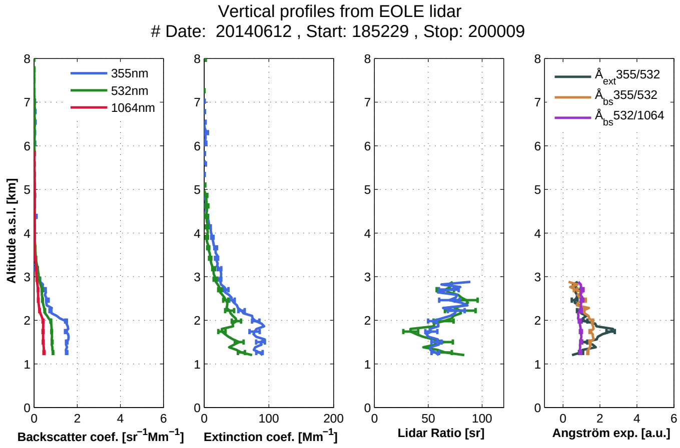

Σχήμα 6.17: *Vertical profiles of aerosol optical properties (12 June). From left to right, first graph shows aerosol backscatter coefficient, second graph shows aerosol extinction coefficient, third graph shows aerosol* S_λ *and fourth graph shows AE.*

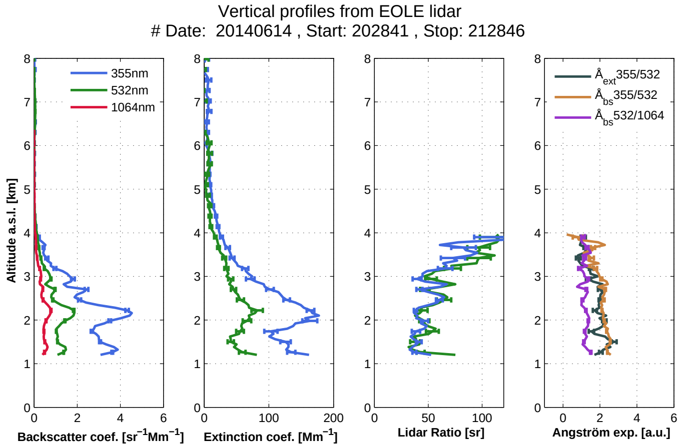

Σχήμα 6.18: *Vertical profiles of aerosol optical properties (14 June). From left to right, first graph shows aerosol backscatter coefficient, second graph shows aerosol extinction coefficient, third graph shows aerosol* S_λ *and fourth graph shows AE.*

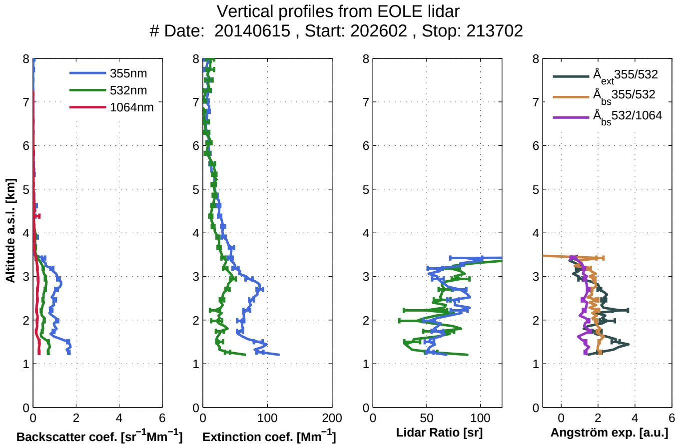

Σχήμα 6.19: *Vertical profiles of aerosol optical properties (15 June). From left to right, first graph shows aerosol backscatter coefficient, second graph shows aerosol extinction coefficient, third graph shows aerosol* S_λ *and fourth graph shows AE.*

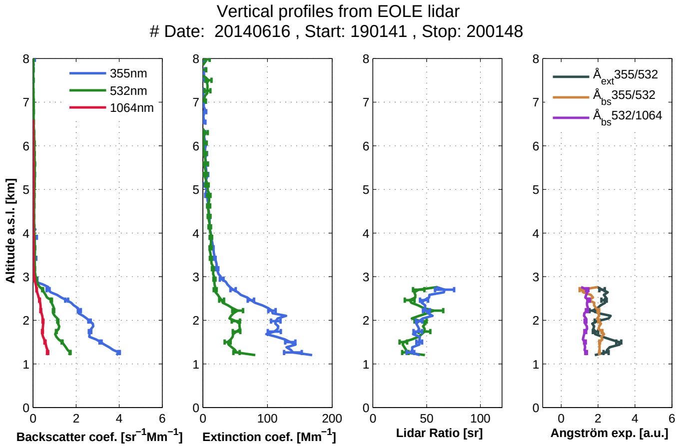

Σχήμα 6.20: *Vertical profiles of aerosol optical properties (16 June). From left to right, first graph shows aerosol backscatter coefficient, second graph shows aerosol extinction coefficient, third graph shows aerosol* S_λ *and fourth graph shows AE.*

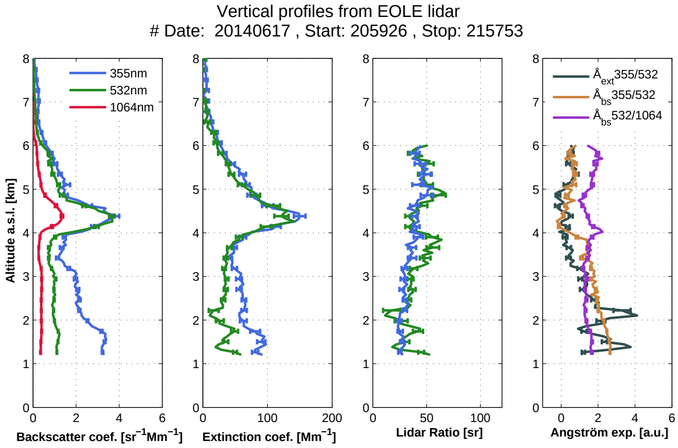

Σχήμα 6.21: *Vertical profiles of aerosol optical properties (17 June). From left to right, first graph shows aerosol backscatter coefficient, second graph shows aerosol extinction coefficient, third graph shows aerosol* S_λ *and fourth graph shows AE.*

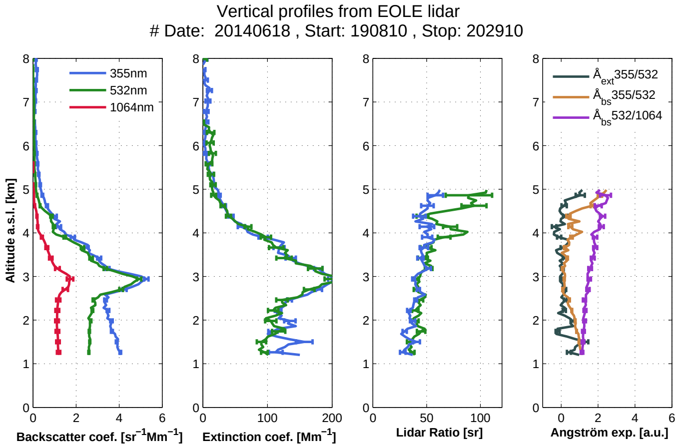

Σχήμα 6.22: *Vertical profiles of aerosol optical properties (18 June). From left to right, first graph shows aerosol backscatter coefficient, second graph shows aerosol extinction coefficient, third graph shows aerosol* S_λ *and fourth graph shows AE.*

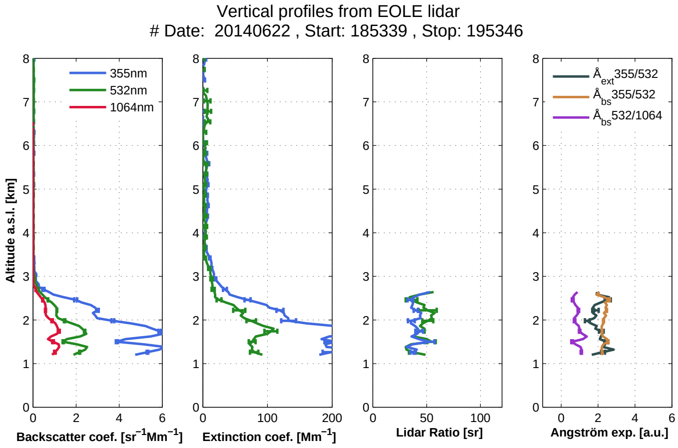

Σχήμα 6.23: *Vertical profiles of aerosol optical properties (22 June). From left to right, first graph shows aerosol backscatter coefficient, second graph shows aerosol extinction coefficient, third graph shows aerosol* S_λ *and fourth graph shows AE.*

Πίνακας 6.3: *Intensive optical properties from the HygrA-CD database. The first column refers to the dates of the campaign that EOLE lidar signals were processed with the use of the Raman method. The AOD at 355nm and 532nm are given in the second column. The third column shows the position of the aerosol layers (i.e., base and top) detected in the retrieved vertical profiles.The fourth and fifth columns refer to the S_λ and AE within the detected aerosol layers. Finally, the sixth column provides information on the linear particle depolarization ratio values provided by AIAS. AIAS was operational only daytime and therefore the detected aerosol layers during nighttime may differ slightly in the FT but more significantly within the PBL.*

Date [dd/mm]	**AOD**		**Layer [km]**	S_λ **[sr]**		**AE**	δ_p **[%]**
	355nm	**532nm**		**355nm**	**532nm**		
15/05	0.06	0.04	1.2-2.0	41±2	44±5	1.5±0.3	1.1±0.9
			2.0-2.4	50±8	54±9	1.3±0.5	-
17/05	0.09	0.08	1.2-1.8	28±3	34±6	1.7±0.4	1.4±0.2
			2.0-2.5	37±5	33±7	2.4±0.7	1.2±0.3
18/05	0.03	0.02	1.2-1.5	46±8	38±11	1.9±0.6	2.3±0.1
20/05	0.20	0.16	2.5-3.2	41±3	47±5	0.6±0.2	28.4±2.6
			3.4-4.0	61±8	48±4	1.0±0.2	-
21/05	0.05	0.03	1.2-1.7	56±5	60±8	1.3±0.3	2.3±0.2
22/05	0.10	0.07	1.2-1.5	40±8	46±3	0.8±0.6	4.7±0.2
			1.6-2.0	40±3	38±6	1.3±0.3	6.9±0.6
23/05	0.28	0.24	1.3-2.8	35±3	43±5	1.5±0.4	14.0±2.5
26/05	0.28	0.24	3.0-4.0	53±9	44±5	0.5±0.3	-
27/05	0.13	0.08	1.2-2.0	35±3	40±6	1.3±0.3	25.1±3.7
			2.0-2.5	44±9	51±16	1.1±0.4	28.1±3.1
01/06	0.1	0.08	1.2-2.5	40±5	46±10	2.0±0.6	6.3±0.1
07/06	0.27	0.19	1.2-1.7	39±3	45±7	1.6±0.3	4.8±1.2
			2.5-3.2	51±5	47±5	2.0±0.3	2.9±0.5
10/06	0.19	0.11	1.2-2.1	59±4	58±8	1.3±0.4	6.4±0.7
11/06	0.22	0.12	1.2-2.1	59±4	55±9	1.2±0.4	2.0±0.1
			2.1-3.0	62±3	54±5	1.4±0.2	0.9±0.4
12/06	0.13	0.08	1.2-2.0	56±4	55±14	2.0±0.5	8.9±0.4
			2.1-2.8	73±8	76±7	1.4±0.1	11.3±1.7
14/06	0.34	0.19	1.3-1.7	37±3	41±7	2.2±0.4	5.7±0.1
			2.3-2.9	55±9	60±8	1.9±0.2	6.8±0.8
15/06	0.22	0.16	1.7-3.2	70±12	67±11	1.9±0.2	-
16/06	0.26	0.19	1.3-2.7	46±8	40±8	2.3±0.4	7.1±1.4
17/06	0.38	0.33	4.0-4.8	40±4	42±8	0.1±0.3	24.9±6.0
18/06	0.42	0.41	2.5-3.5	44±4	46±5	0.1±0.1	19.0±2.0
22/06	0.33	0.21	1.2-2.5	40±5	44±8	2.0±0.4	1.8±0.5

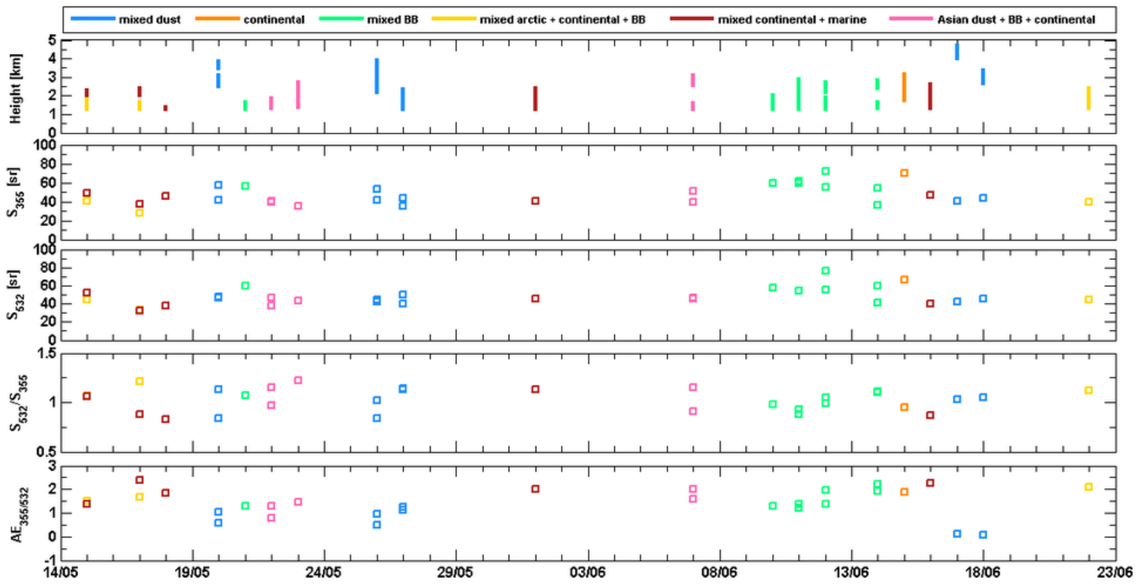

Σχήμα 6.24: *Aerosol layers optical properties for the whole period of the campaign from EOLE Raman lidar.* S_λ *and AE are shown in the plots for all the detected aerosol layers.*

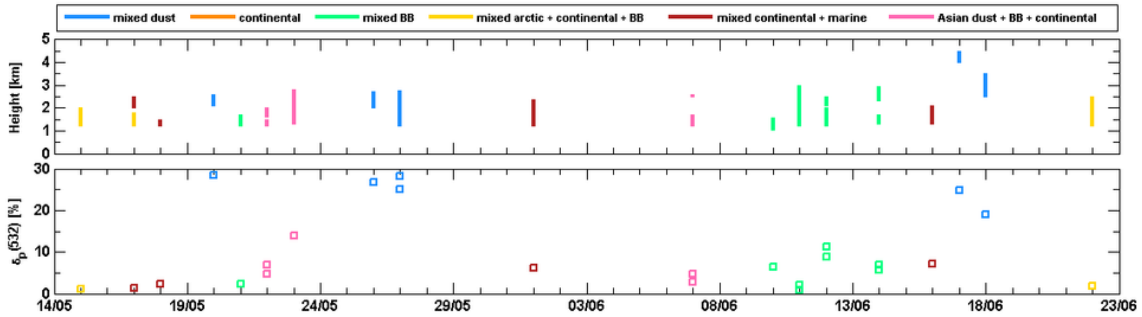

Σχήμα 6.25: *Linear particle depolarization ratio at 532nm is presented for all the detected aerosol layers during the campaign provided by AIAS lidar.*

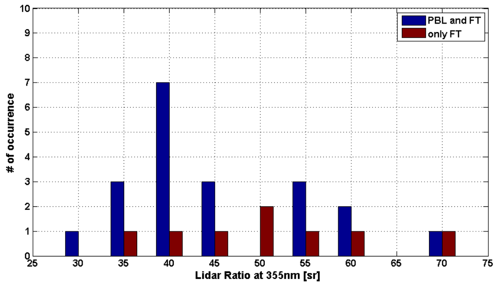

Σχήμα 6.26: *Histogram of* S_λ *at 355nm.*

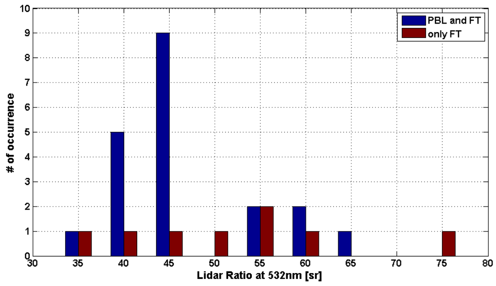

Σχήμα 6.27: *Histogram of* S_λ *at 532nm.*

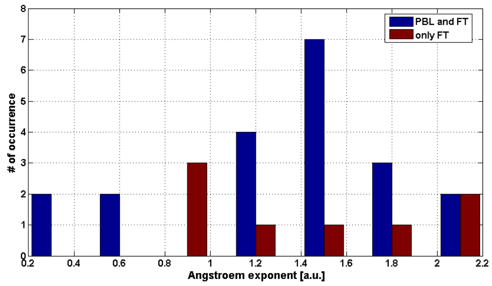

Σχήμα 6.28: *Histogram of* $AE_{355/532}$.

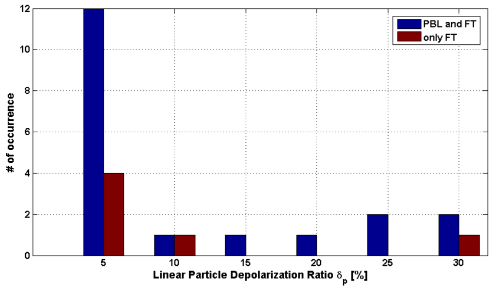

Σχήμα 6.29: *Histogram of the linear particle depolarization ratio at 532nm.*

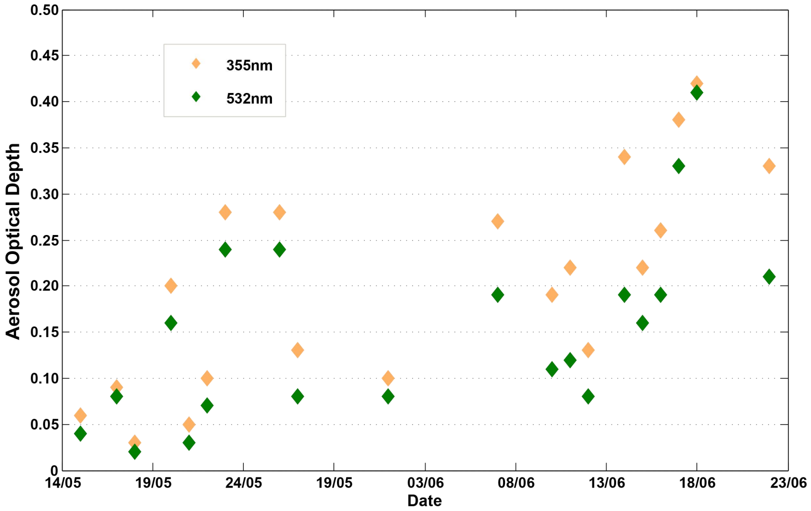

Σχήμα 6.30: *Daily evolution of the AOD at 355 nm and 532 nm, as measured by the EOLE.*

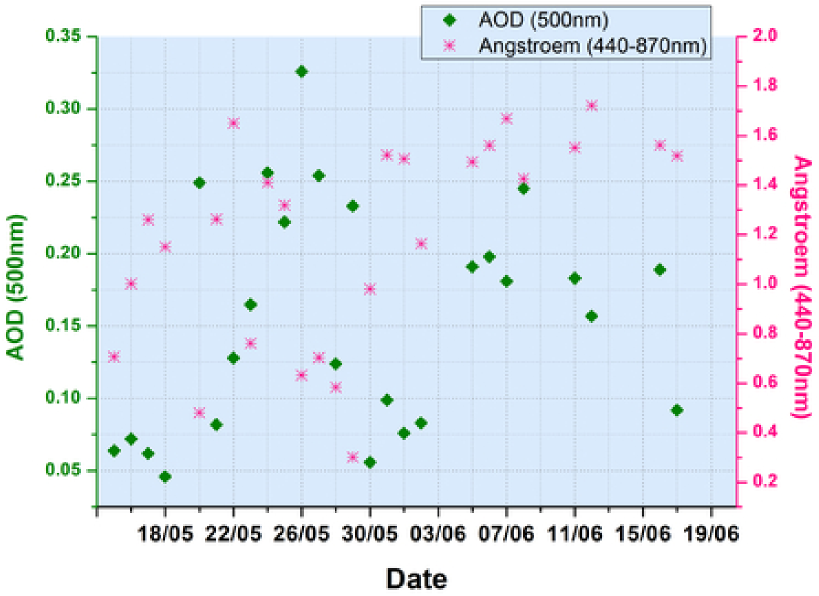

Σχήμα 6.31: *Daily evolution of the AOD at 500 nm and* $AE_{440/870}$ *as measured by the sunphotometer.*

6.6 The thermodynamic state of the atmosphere

The thermodynamic state of the atmosphere can be easily characterized when radiosonde data are available for the study area. This characterization is based on Skew-T Log-P diagrams and the relative vertical profiles of the due point temperature, water vapor mixing ratio and enthalpy [131]. The basic physical parameter retrieved from the soundings is the LCL above which condensation starts for the ascending air parcel. Any lifting above that point results to water phase change from vapor to liquid and the air parcel behaves as a pseudo-adiabatic system which releases latent heat with the ambient environment. Therefore, when cloud starts to form, at this level we observe a sharp negative gradient in the water vapor mixing ratio and the enthalpy vertical profile above LCL. Provided that radiosonde launches were not available everyday at noon, we will comment on the thermodynamic conditions of the days as summarized in Table 6.4. The case of the 22nd of May is a typical example of cloud formation. The LCL was identified at 1660 m ($\sim$ 840 hPa) (cf. Fig 6.34) and the cloud formed at an altitude of about 1900 m as shown in Figure 6.35. In that day the boundary layer was rich in water vapor with an almost homogeneously mixed PBL with water vapor mass mixing ratio of 8 g/kg of dry air. Very similar thermodynamic conditions appeared in the case of June 11th, where the mean water vapor mixing ratio ($\sim$ 9 g/kg) was invariant from ground level up to the LCL at $\sim$ 2000 m height (cf. Figure 6.49). In that case, the LCL was in the vicinity of PBL top and cloud formation occurred. In both days, the air masses arriving over the GAA were advected from N-NE directions and were combined with AOD(500 nm)>0.1 and AE>1.6-1.7 (cf. Figure 6.31); therefore these air masses contained medium-to-high aerosol load of small particles. An interesting case of cloud formation is also observed on the 30th of May, with low aerosol load and large particles (AOD(500 nm)$\sim$0.05 and AE<1). In this case, the air parcel reaches supersaturation at an altitude of 1050 m. In any case, the critical parameter of cloud formation is the Convective Available Potential Energy (CAPE) which was very high in that day ($\sim$2300 J/kg).

Πίνακας 6.4: *Thermodynamic parameters from radiosonde launches*

Date [dd/mm]	**LCL height [m]**	**Temperature [C]**	**CAPE [J/kg]**
21/05	2000	7	4
22/05	1660	11	668
23/05	1390	12	0
27/05	1410	14	0
30/05	1050	15	2295
02/06	1500	9	0
05/06	1090	15	0
08/06	1990	9	863
11/06	1360	15	863

6.7 Wind field in the PBL

Apart from the aerosols ability to act as CCN according to their properties, the wind field plays a determinant role in the cloud development in several ways:

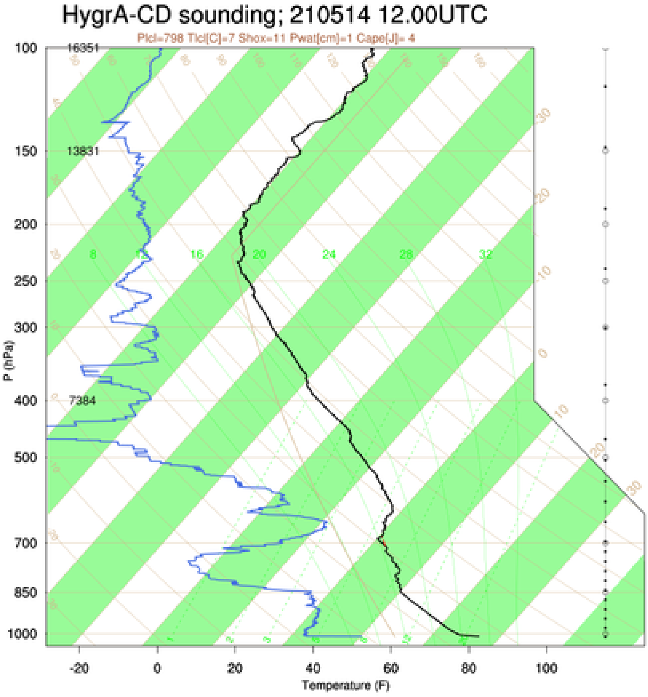

Σχήμα 6.32: *SkewT-logP diagram, 21 May 2014 at 12:00 UTC*

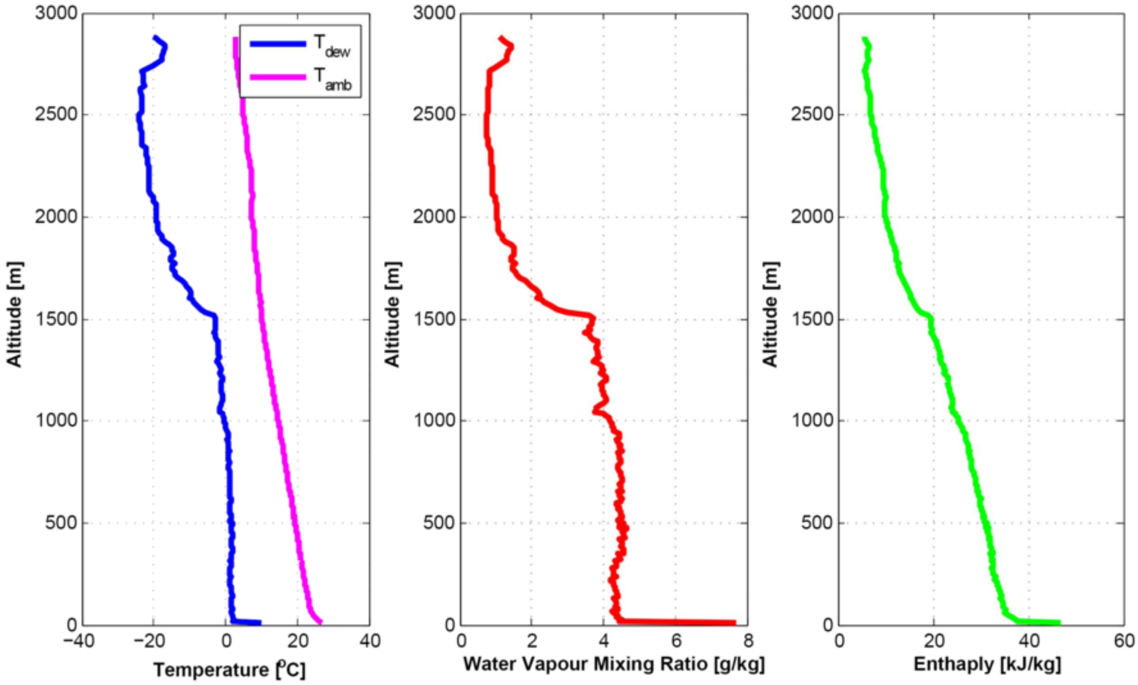

Σχήμα 6.33: *Vertical profiles from radiosonde, 21 May 2014 at 12:00 UTC. Left graph shows temperature and due point temperature, middle graph shows water vapor mixing ratio and right graph shows the enthalphy of air parcel.*

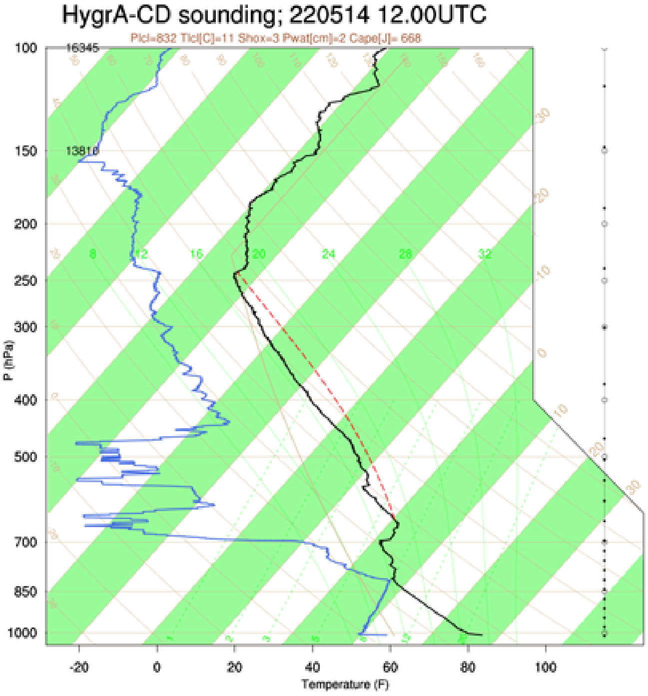

Σχήμα 6.34: *SkewT-logP diagram, 22 May 2014 at 12:00 UTC*

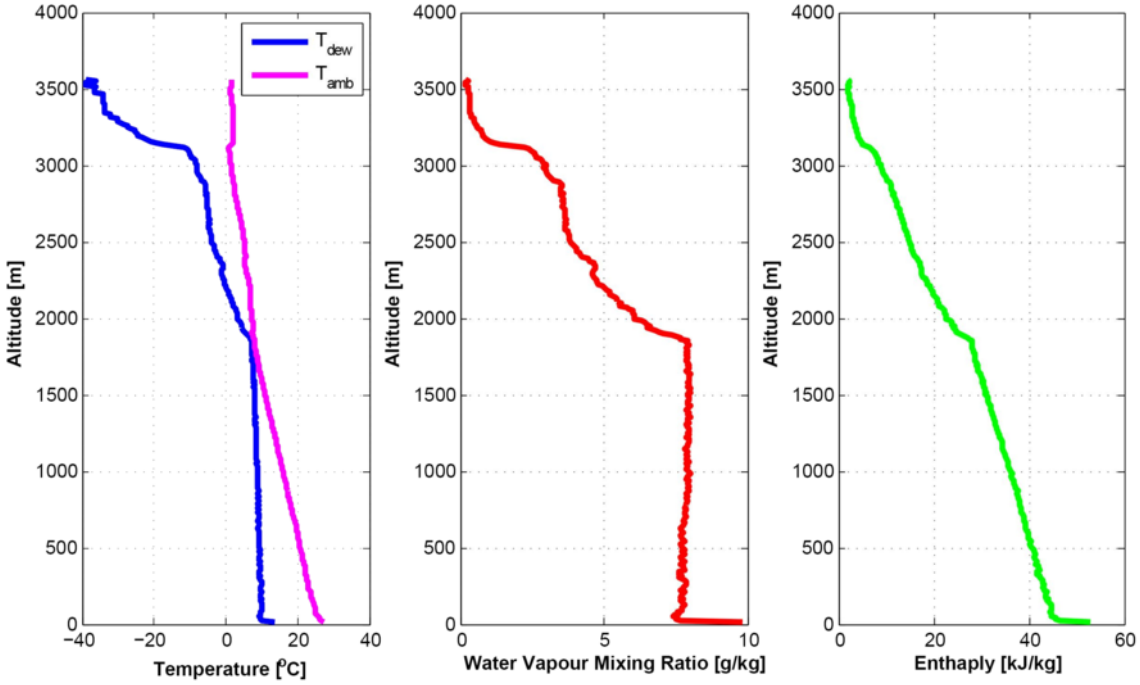

Σχήμα 6.35: *Vertical profiles from radiosonde, 22 May 2014 at 12:00 UTC. Left graph shows temperature and due point temperature, middle graph shows water vapor mixing ratio and right graph shows the enthalphy of air parcel.*

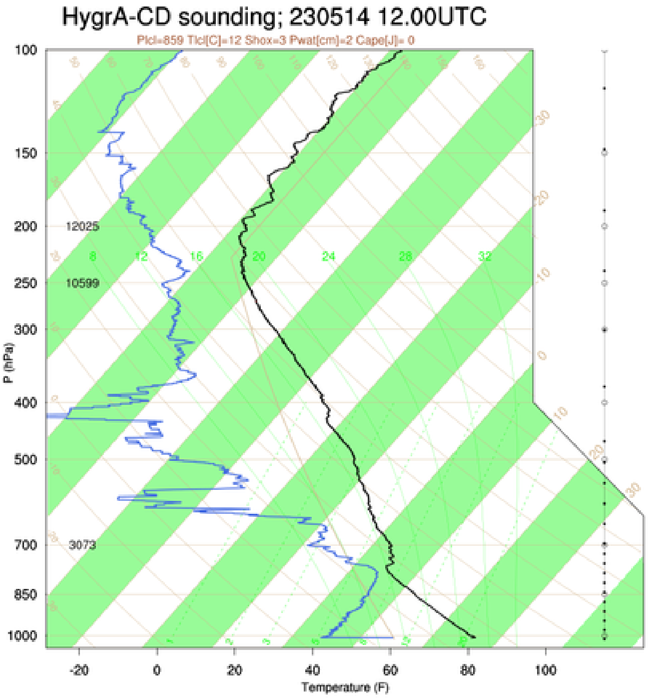

Σχήμα 6.36: *SkewT-logP diagram, 23 May 2014 at 12:00 UTC*

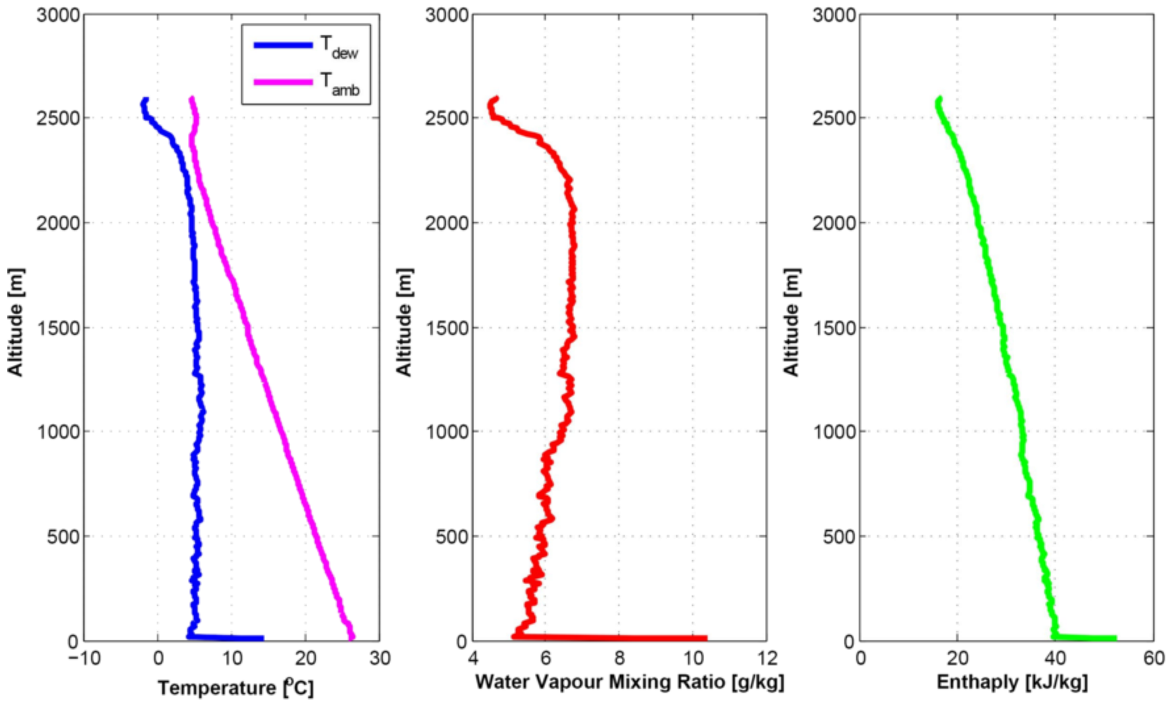

Σχήμα 6.37: *Vertical profiles from radiosonde, 23 May 2014 at 12:00 UTC. Left graph shows temperature and due point temperature, middle graph shows water vapor mixing ratio and right graph shows the enthalphy of air parcel.*

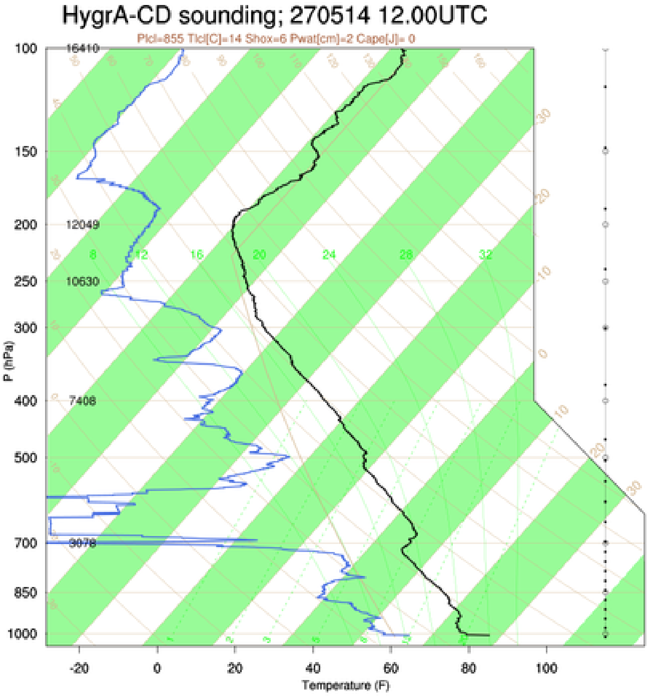

Σχήμα 6.38: *SkewT-logP diagram, 27 May 2014 at 12:00 UTC*

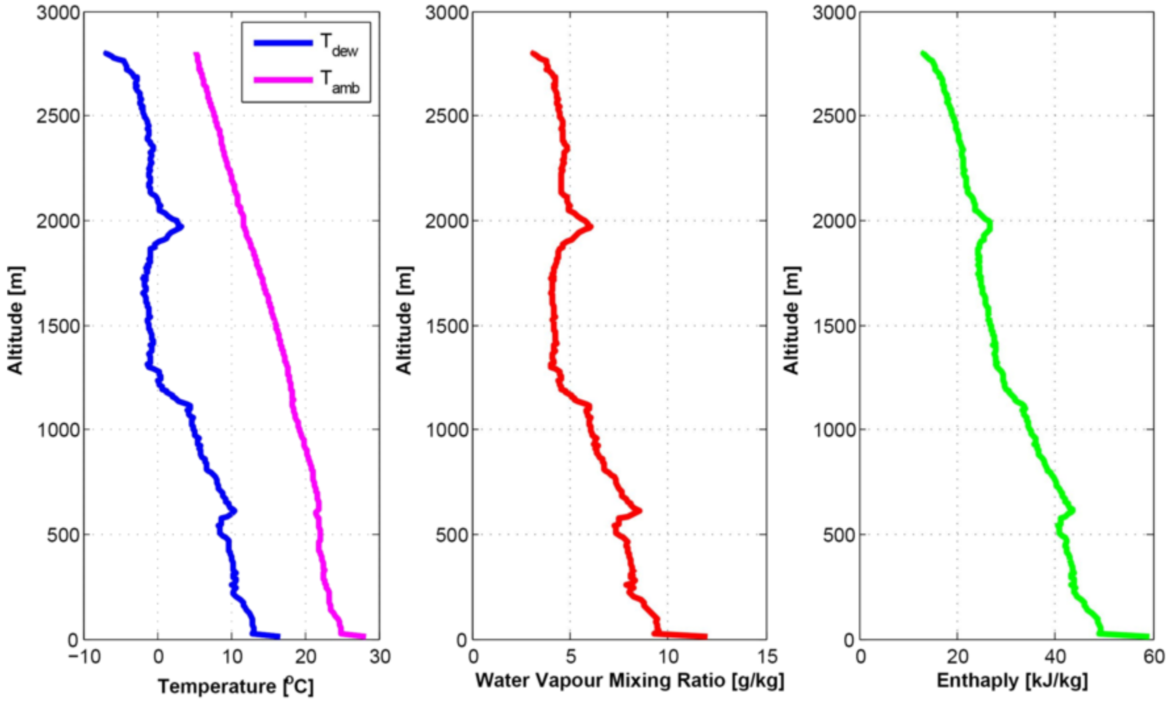

Σχήμα 6.39: *Vertical profiles from radiosonde, 27 May 2014 at 12:00 UTC. Left graph shows temperature and due point temperature, middle graph shows water vapor mixing ratio and right graph shows the enthalphy of air parcel.*

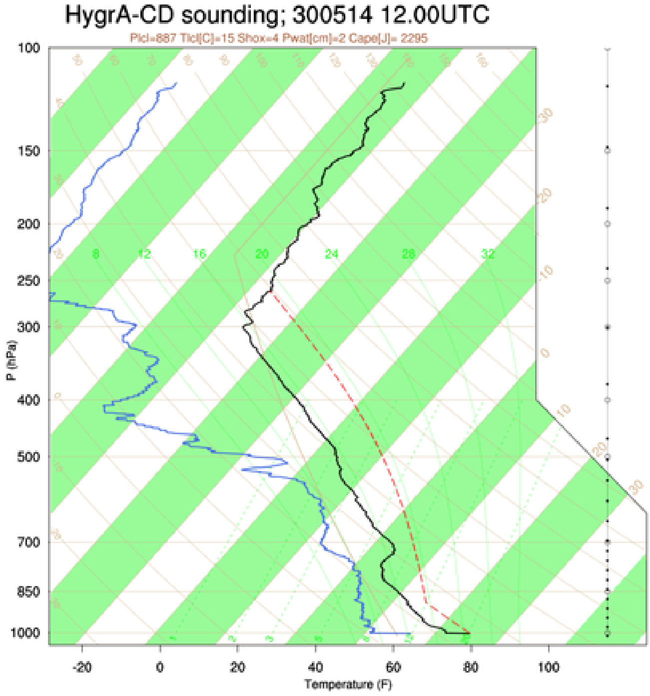

Σχήμα 6.40: *SkewT-logP diagram, 30 May 2014 at 12:00 UTC*

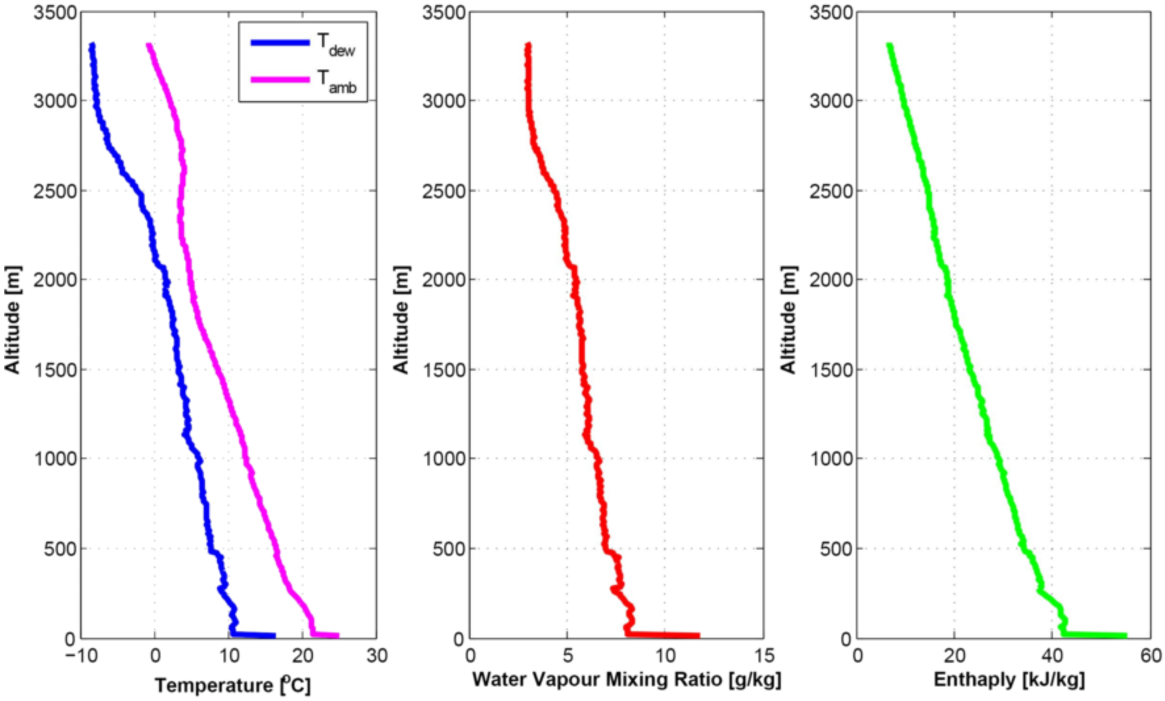

Σχήμα 6.41: *Vertical profiles from radiosonde, 30 May 2014 at 12:00 UTC. Left graph shows temperature and due point temperature, middle graph shows water vapor mixing ratio and right graph shows the enthalphy of air parcel.*

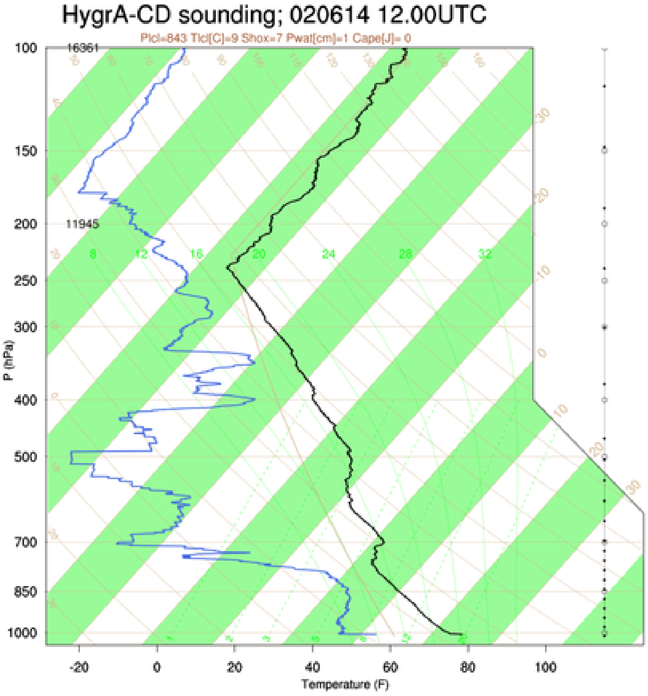

Σχήμα 6.42: *SkewT-logP diagram, 2 June 2014 at 12:00 UTC*

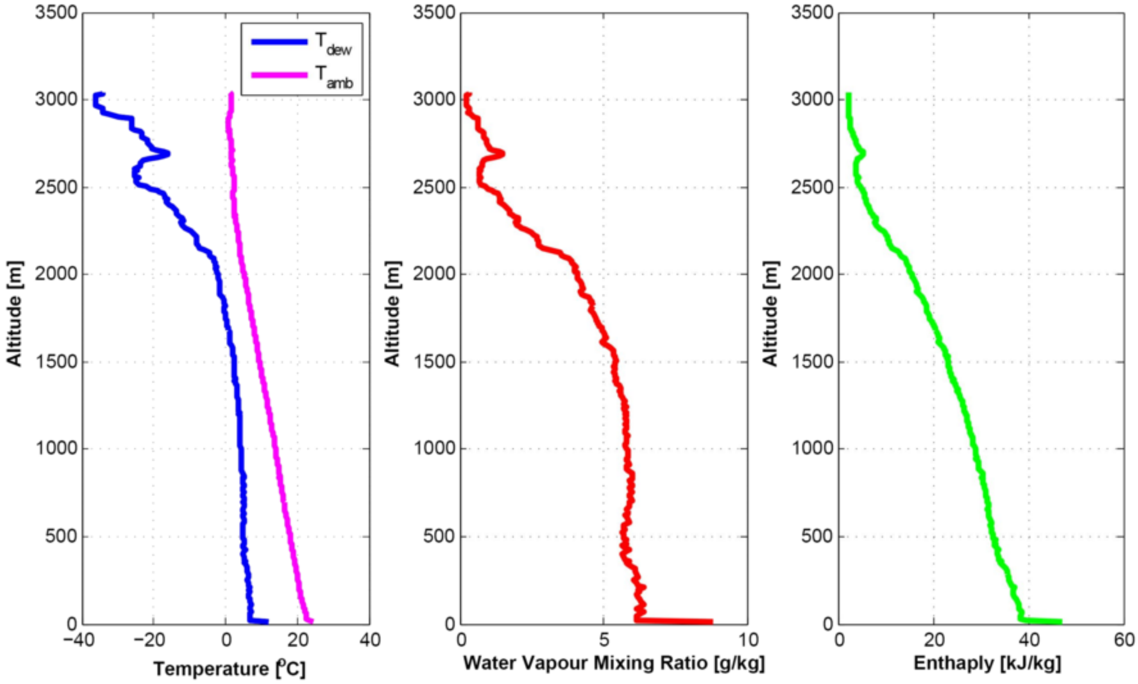

Σχήμα 6.43: *Vertical profiles from radiosonde, 2 June 2014 at 12:00 UTC. Left graph shows temperature and due point temperature, middle graph shows water vapor mixing ratio and right graph shows the enthalphy of air parcel.*

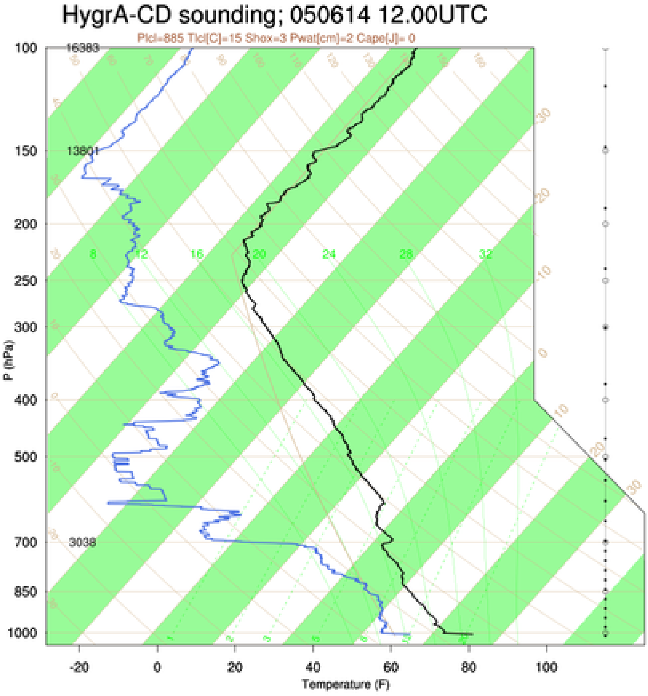

Σχήμα 6.44: *SkewT-logP diagram, 5 June 2014 at 12:00 UTC*

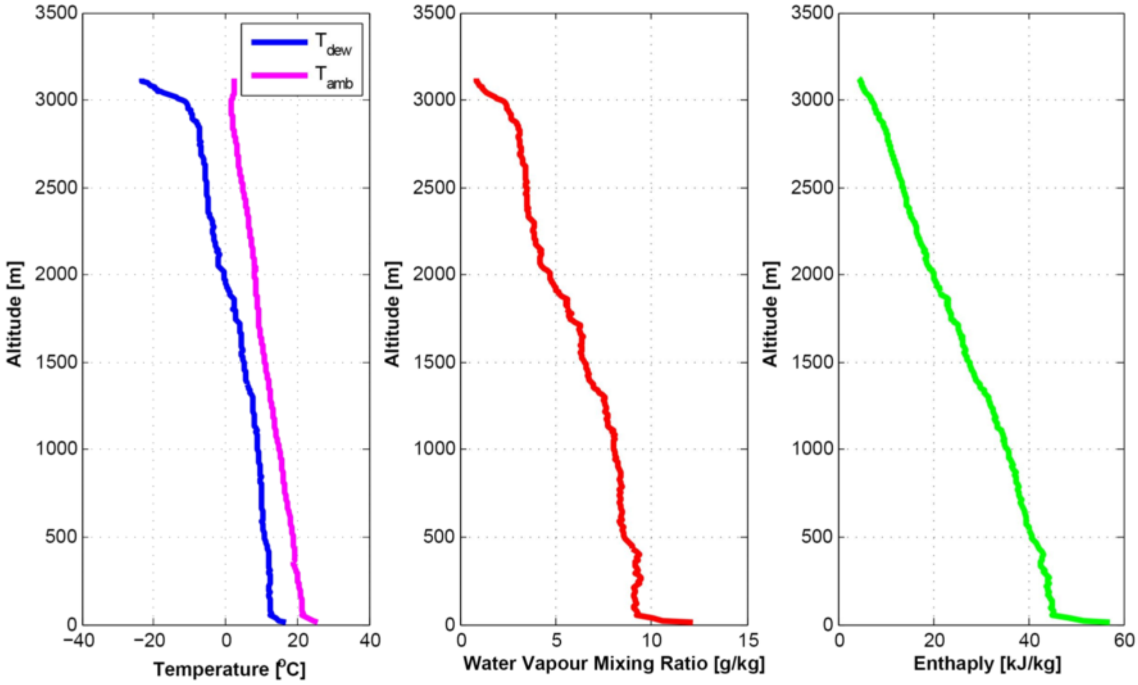

Σχήμα 6.45: *Vertical profiles from radiosonde, 5 June 2014 at 12:00 UTC. Left graph shows temperature and due point temperature, middle graph shows water vapor mixing ratio and right graph shows the enthalphy of air parcel.*

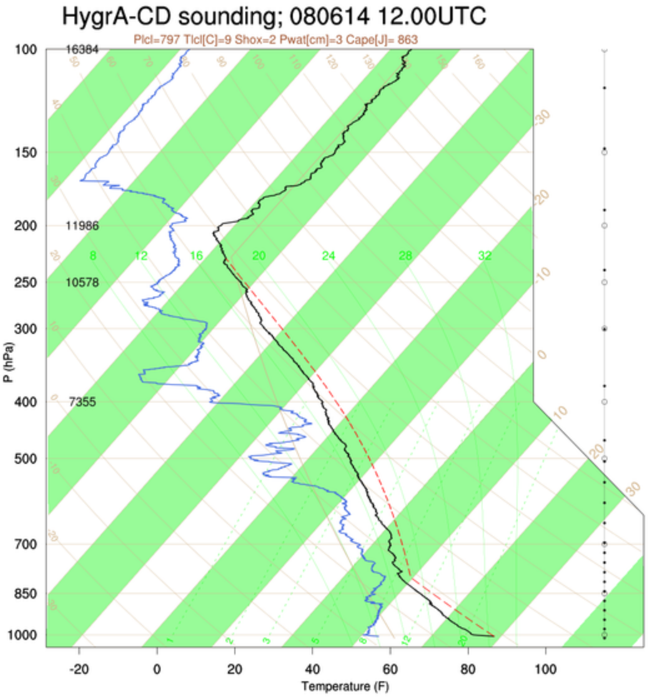

Σχήμα 6.46: *SkewT-logP diagram, 8 June 2014 at 12:00 UTC*

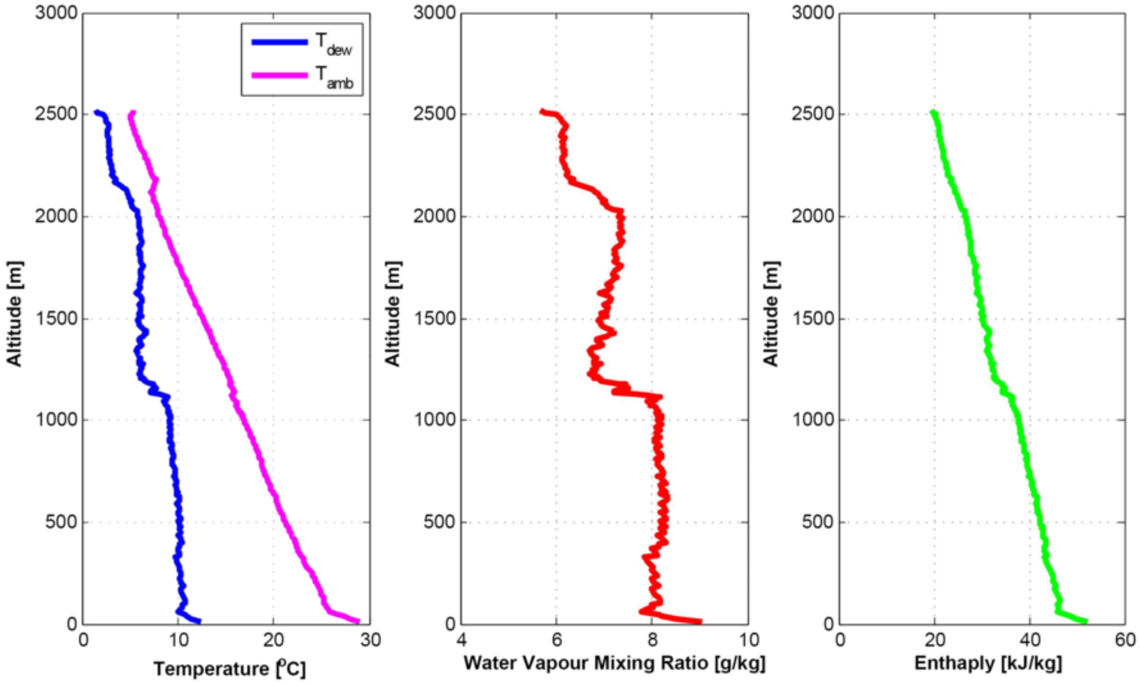

Σχήμα 6.47: *Vertical profiles from radiosonde, 8 June 2014 at 12:00 UTC. Left graph shows temperature and due point temperature, middle graph shows water vapor mixing ratio and right graph shows the enthalphy of air parcel.*

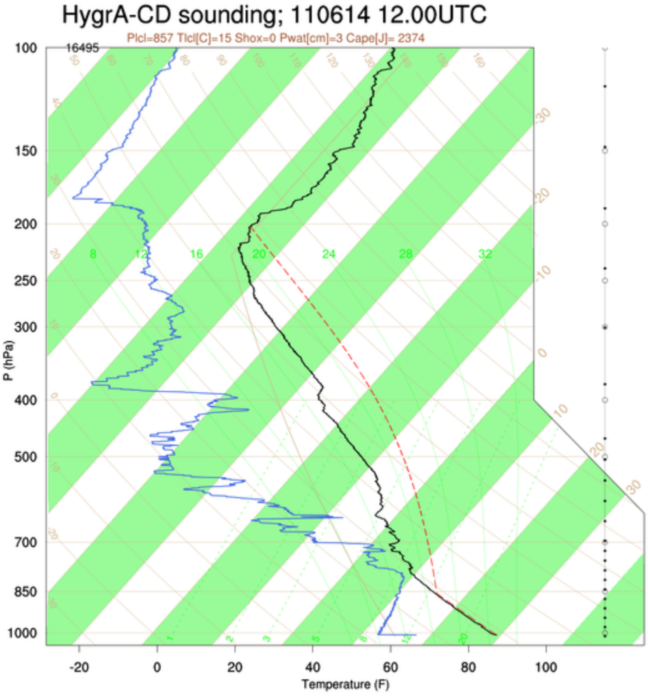

Σχήμα 6.48: *SkewT-logP diagram, 11 June 2014 at 12:00 UTC*

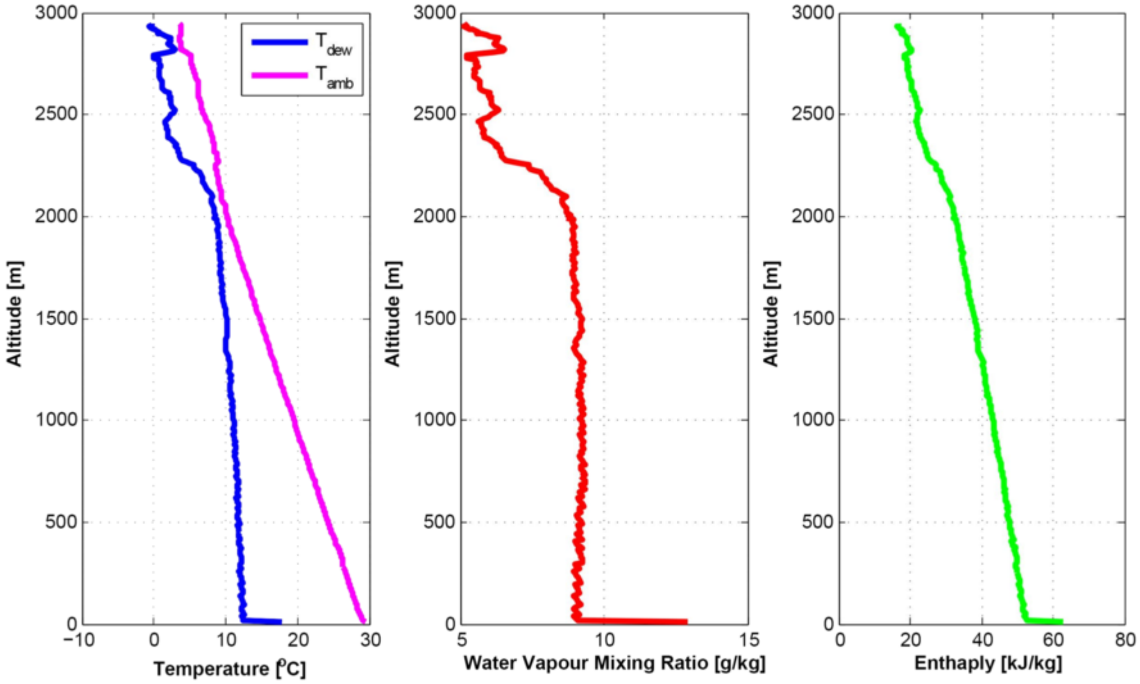

Σχήμα 6.49: *Vertical profiles from radiosonde, 11 June 2014 at 12:00 UTC. Left graph shows temperature and due point temperature, middle graph shows water vapor mixing ratio and right graph shows the enthalphy of air parcel.*

- the wind direction (and speed) determines the type of air masses which are advected above the study area. The origin and pathways of these masses are also very critical parameters, as they determine the aerosols' chemical composition and their physical properties. For instance, when masses are advected from S-SW directions, the most probable detected aerosol type over Athens is dust (in Appendix B we present the air mass back-trajectories arriving over the GAA for different dates and times during the HygrA-CD campaign, as provided using the HYSPLIT model. The arrival heights of these air masses are defined from the location of the aerosol layers detected by AIAS and EOLE lidars). Moreover, the wind direction plays a crucial role in the determination of air masses temperature and water vapor content. Irrespectively to the efficiency of the dust particles to form cloud droplets, when the amount of water vapor in the atmosphere is quite low, CCN activation cannot occur because the thermodynamic state of the atmosphere does not facilitate high supersaturation and hence, cloud formation.

- the wind speed is also an important modulation factor of the aerosol load within the PBL: e.g. low wind speeds lead to air mass stagnation, which facilitates the accumulation of air pollutants within the PBL in the vicinity of air pollution sources.

During HygrA-CD, the wind vector (speed and direction) has been retrieved using the scanning routines of the Halo Doppler lidar. In Figures 6.50 and 6.51, we present the mean wind speed and direction in a single colorplot for the whole campaign. This information is certainly useful for getting a quick overview of the wind characteristics in the PBL. Let' make a discrimination on the PBL wind speed by introducing three categories: (1) low intensity w<8 ms^{-1}, (2) moderate intensity 8<w<16 ms^{-1} and (3) high intensity w>16 ms^{-1}. In most of the cases, both strong and low wind speeds appeared when the wind direction was W-NW. Clouds appeared in the PBL when air masses arriving over Athens did not contain mineral dust and the wind was very strong like the cases of 15, 30 and 31 May (cf. Figure 6.50 and Table 6.5). When dust particles arrived over Athens from W-NW directions (e.g. cases of 24 and 25 May), the wind intensity was light and clouds did not form. Very frequently, moderate wind speed was measured from the Doppler lidar when the wind direction was N-NE (cf. Figures 6.50 and 6.51). For instance, in many cases (e.g. 21-22 May and 09-11 June) of cloud-topped PBL presence, air masses were arriving over Athens from N-NE directions and the measured wind intensity was moderate. The wind and turbulence characteristics of the PBL have proved to be very critical for the activation process of aerosols to cloud droplets even more critical that the aerosol number and chemical composition.

6.8 General conclusions from the HygrA-CD findings

Based on the summarized information shown in Table 6.5, we can conclude that clouds do not appear in the vicinity of the PBL when air masses arrive from S-SW directions and contain dust particles. The main reason for that is that the LCL appears at a very high altitude, well above the PBL top (e.g., >2-2.5 km), therefore, the ascending air masses within PBL never reach supersaturation.

On the contrary, cloud-topped PBLs frequently occur when air masses arrive from N-NE directions and carrying anthropogenic and biomass burning aerosols and very rarely dust. The contribution of local emissions to the total aerosol load can be considered negligible when N-NE wind directions dominate in GAA due to the high ventilation of the basin in the presence of such winds. It is easily observed in Table 6.5 that high AOD values (AOD>0.1 at 500 nm) do not correlate with PBL cloud formation. Hence, it is clear from the data obtained during HygrA-CD that cloud droplet activation, over a polluted site like Athens, cannot be directly linked to a single aerosol parameter, like the AOD as it has been shown in previous

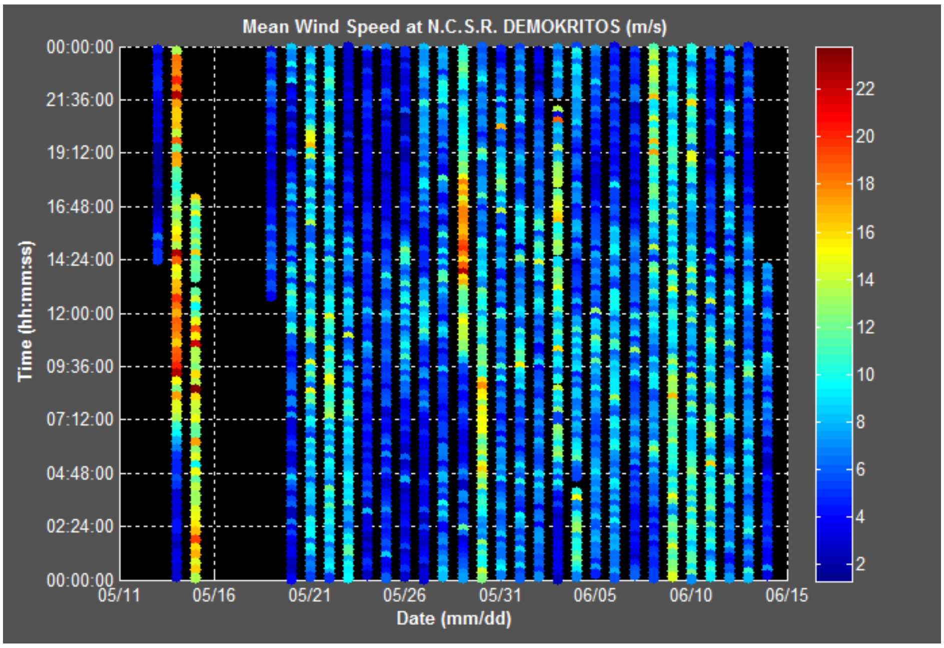

Σχήμα 6.50: *Mean wind speed in the PBL derived from the HALO wind lidar*

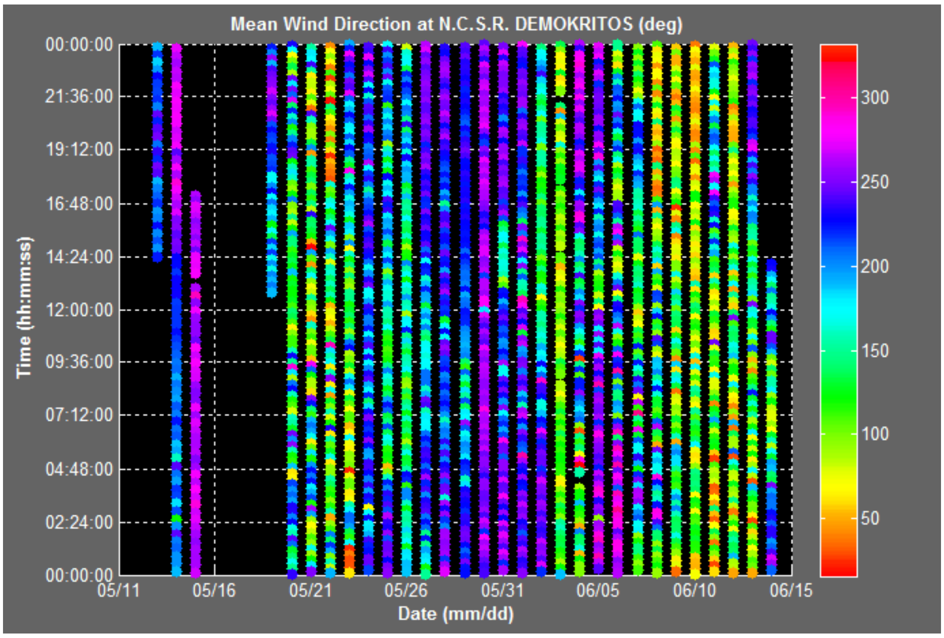

Σχήμα 6.51: *Mean wind direction in the PBL derived from the HALO wind lidar*

Πίνακας 6.5: *Aerosol and cloud presence in the PBL with respect to the wind field direction. AOD at 500 nm (third column) has been retrieved daytime from CIMEL sunphotometer as also shown in Figure 6.31.*

Date [dd/mm]	**Cloud formation**	**AOD** > 0.1	**W - NW**		**N - NE**		**S - SW**	**PBL height [m]**
			Dust	**Othe**	**Dust**	**Othe**	**Dust**	
15/05	x			x				0.85±0.15
16/05	x			x				1.68±0.07
17/05	x			x				1.13±0.07
18/05	x			x				1.69±0.20
19/05								N/A
20/05		x					x	2.01±0.10
21/05	x					x		1.71±0.10
22/05	x	x				x		2.52±0.20
23/05		x			x			2.59±0.20
24/05		x	x					0.79±0.15
25/05		x	x					1.82±0.10
26/05		x	x					1.57±0.07
27/05		x	x					1.94±0.15
28/05		x					x	0.79±0.10
29/05		x					x	N/A
30/05	x	x		x				1.52±0.20
31/05	x			x				1.71±0.25
01/06	x			x				2.31±0.15
02/06	x			x				2.32±0.15
03/06								N/A
04/06								N/A
05/06	x	x		x				0.68±0.10
06/06	x	x				x		0.65±0.05
07/06	x	x				x		0.72±0.05
08/06	x	x				x		1.88±0.16
09/06	x	N/A				x		2.23±0.25
10/06	x	N/A				x		1.45±0.18
11/06	x	x				x		2.47±0.20
12/06	x	x				x		2.31±0.20
13/06	x	N/A				x		2.57±0.07
14/06	x	N/A				x		2.13±0.18
15/06	x	N/A				x		2.33±0.20
16/06		x		x				1.86±0.30
17/06			x					0.86±0.15
18/06		N/A	x					N/A
19/06		N/A	x					2.11±0.20
20/06	x	N/A		x				1.98±0.15
21/06		N/A				x		1.18±0.16
22/06		N/A				x		1.88±0.15

studies [45], [132]. In practice the cloud formation occurs even in low AOD, when the positive buoyancy (measured by CAPE) is sufficiently high to vertically transport the aerosol layer at the LCL. From the HygrA-CD dataset, we can conclude that clouds form when the aerosols present have a critical size so as they become activated even at low supersaturation (e.g., $s<0.1$). Aerosols' hygroscopicity also plays a less essential role in cloud activation, since even less hygroscopic aerosols (like mineral dust) are activated when they reach their critical size during updrafts.

As a final conclusion, HygrA-CD showed the importance of the covariations of aerosol and dynamics in the formation of clouds in the vicinity of the PBL over a Mediterranean site with complex local topography, and that the highest contribution to the variance of the cloud droplet number is attributed to the updraft velocity variability and to a lesser extent to the variance in aerosol number concentration at ground level and their chemical composition and size distribution.

CHAPTER 7

Results from lidar remote sensing measurements

Making use of the HygrA-CD dataset, we focused on developing new methods to quantify 1) the CCN spectra and cloud droplet number concentration at a certain aerosol layer and 2) the vertical aerosol flux in the convective cloud-topped PBL. The first technique is presented in Section 7.1 and involves synergistic measurements from a multi-wavelength Raman lidar and a Doppler lidar. The second technique is presented in Section 7.2 and is based on collocated measurements from an elastic aerosol lidar and a Doppler lidar.

7.1 CCN spectra estimation using multi-wavelength Raman lidar

Aerosols play an important role in the terrestrial radiation balance by interacting with direct incoming sunlight and modifying the microphysical properties of clouds. In terms of low-level clouds, increased CCN concentrations tend to increase cloud droplet concentration [133] and increase shortwave cloud albedo. The enhanced droplet concentrations may also modify the efficiency of clouds to produce precipitation [134] with important impacts on vertical development and the hydrological cycle [135], [136], [40]. The so-called aerosols indirect effects lead the climate change prediction to highly uncertain results [40].

The lack of continuous collocated measurements of aerosol, cloud and thermodynamic variables throughout the atmosphere increases the uncertainty of aerosol-cloud processes in climate models. On a global scale, using means of satellite remote sensing, several attempts have been made to constrain aerosol-cloud-precipitation-climate interactions [137]. In this section, we describe a methodology for making use of ground-based lidar measurements to retrieve the number of CCN as a function of the supersaturation using data from the multi-wavelength Raman lidar EOLE. The information about the CCN number combined with the vertical wind component as retrieved from Doppler lidar enabled us to estimate the cloud droplet concentration as well.

7.1.1 Analysis & algorithmic description

Multi-wavelength Raman lidars are widely used to provide information about the vertical distribution of aerosols in the sampled atmospheric volume. The multi-wavelength Raman lidar EOLE allowed us to retrieve aerosol optical properties such as $\alpha(\lambda)$, $\beta(\lambda)$ coefficients. The basic idea and structure of our approach is illustrated in the flow chart of Figure 7.1. Primarily, the detected aerosol layers above the lidar are optically characterized (cf. Figure 6.24). Then, aerosol micro-physical properties are derived within the homogeneous atmospheric layer. In particular, the aerosol size distribution is retrieved from the optical properties through inversion technique (as described in Chapter 4). Provided that the detected aerosols have a known chemical composition and hence hygroscopic behavior, the CCN spectra are derived from the dry size distributions. Finally, with use of parameterization and known vertical wind component, the algorithm permits the calculation of droplet number concentration and attributions.

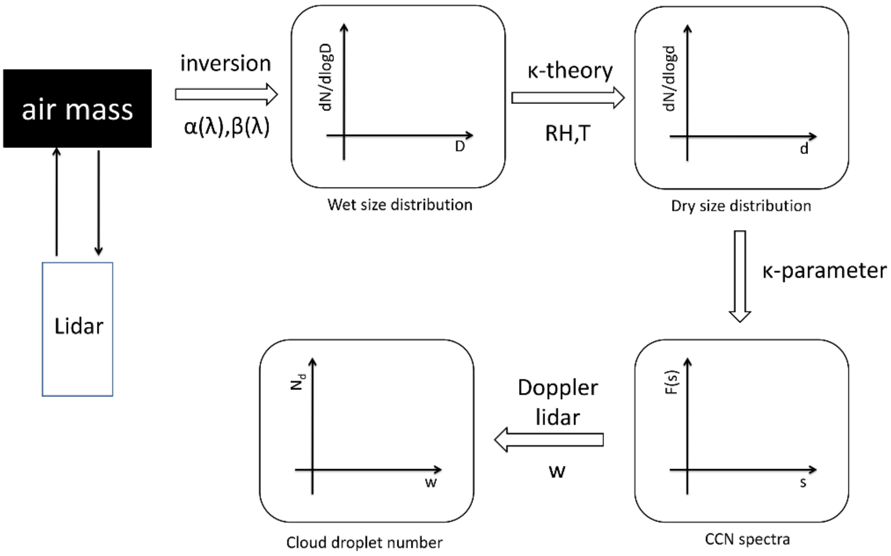

Σχήμα 7.1: *Presentation of the algorithm: retrievals and analysis*

In this study, we focus on the lower part of the atmosphere for altitudes <2000 m at the residual layer of the PBL. In particular, we work on the aerosol layers that satisfy the following criteria: (a) the detected aerosols are approximately spherical so as Mie theory is applicable (b) aerosol is internally mixed and (c) the air mass is uniform. The validity of aerosol sphericity is ensured by the retrieved linear particle depolarization ratio (δ_p) as measured from AIAS (c.f. Figure 6.25). Aerosols with a δ_p <5% are approximated to spherical particles [138]. Thus, the methodology is applied to case studies with detected aerosols layers characterized by a δ_p <5% [139]. The inversion of lidar data is restricted to the diameter range [0.1 μm, 20 μm] because light in the spectrum of 355 nm–1 μm interacts with particles of such sizes. The common origin of these air masses is confirmed from the backward trajectories implemented by HYSPLIT model [119]. The uniformity of air masses is not totally ensured, nevertheless, the chemical composition of the aerosols from these remote sources is comparable regarding water uptake.

Aerosol size distribution retrieved in ambient RH

The CCN activity spectra expressing the number of activated CCN as a function of ambient supersaturation are derived from the dry aerosol size distribution. Here, we retrieve the size spectrum of wet[1] aerosol $f(D)$ from lidar optical data. The obtained aerosol size distribution should be a lognormal distribution:

---

[1] We refer to wet aerosol because the detected aerosol is measured in ambient relative humidity.

$$f(D)=\frac{N}{\sqrt{2\pi}D\ln\sigma}\exp\left[-\frac{\left(\ln D-\ln\overline{D}\right)^2}{2\ln^2\sigma}\right], \tag{7.1}$$

where $\overline{D}$ is the mean wet diameter, σ the dispersion of the distribution and N the total aerosol number concentration. Lognormal parameterizations of aerosol size distribution and supersaturation activity spectra are broadly used in aerosol-cloud physics and climate studies.

In order to be consistent with the theoretical aerosol size distributions and mitigate the effect of ill-posedness in the lidar inversion retrieval, an ODE has been applied to the retrieved aerosol distributions prior to the CCN spectra estimation. The criterion for the selected optimal log-normal distribution is: *the corrected* f_{cor} *and initial* f *distribution have a maximum common likelihood for the size range* $[\overline{D}-\sigma,\ \overline{D}+\sigma]$. Mathematically, this is expressed as the minimization of the following expression

$$\left\|\sum_{D=D^{min}}^{D^{max}}(f-f_{cor})\,\mathrm{d}D\right\|\rightarrow\min \tag{7.2}$$

where $D^{min}=\overline{D}-\sigma$ and $D^{max}=\overline{D}+\sigma$.

CCN calculation

The ability of particles to act as CCN depends on their affinity to water vapor. When the ambient relative humidity exceeds a critical value, the wet aerosol particle undergoes a continuous hygroscopic growth in its diameter [63], [140]. Köhler theory is applied to dry aerosol spectra and, thus, a transformation from wet to dry diameter should be implemented. This is only possible if the soluble fraction of the aerosol is known. The so-called hygroscopicity κ-parameter for n-component particles can be predicted from the linear mixing rule:

$$\kappa=\sum_{i=1}^{n}\epsilon_i\kappa_i \tag{7.3}$$

where ϵ_i and κ_i are the dry volume fraction and hygroscopic parameter of the ith species respectively.

In theory, κ takes values from 0, when the aerosol has contributions of only insoluble species, up to 1.4, when it consists of only sodium chloride which is the most hygroscopic species [141]. However, in practice, it has been found that continental aerosols usually consist of chemical species which result into a κ value below 0.6 (i.e., a κ value of approximately 0.6 occurs when the dominant species is ammonium sulphate). The most uncertain components are the organic species, due to their high diversity, but in most atmospheric studies their hygroscopic parameter ranged from 0 to 0.3. A κ value of 0.1 characterizes an aerosol as less hygroscopic but still able to act as CCN while aerosols with a κ value of 0.3 are considered as effective CCN [141]. For this reason, in this study, we have considered two scenarios for the hygroscopic behavior of detected aerosols: (i) less hygroscopic, κ=0.1 or (ii) more hygroscopic κ=0.3. From previous studies on the hygroscopicity values of continental aerosols, a κ value of 0.3 has been found as the most characteristic for European continental aerosols [142].

Under the assumption that aerosols of the i$^{\text{th}}$ diameter range $[D_i, D_i+dD]$ have the same hygroscopic growth with aerosols of the (i+1)$^{\text{th}}$ diameter range, the i$^{\text{th}}$ dry diameter d_i is related to the wet diameter D_i with the following expression [143]:

$$d_i = D_i\left(\frac{\kappa RH}{1-RH}+1\right)^{-1/3} \tag{7.4}$$

Therefore, the dry aerosol size distribution will be a lognormal distribution with σ dispersion and mean dry geometric radius to be given by Equation (7.4). The spectrum comes as a result from the exploration of critical supersaturation for each aerosol's dry diameter with known hygroscopicity parameter. All possible pairs of dry diameter and critical supersaturation $[d, s_c]$ lie on the Köhler curves for $\kappa = 0.1$ and $\kappa = 0.3$ as depicted in Figure 7.2. The critical supersaturation is calculated from the following equation [144]:

$$s_c = \exp\left(\frac{4A^3}{27\kappa d^3}\right)^{\frac{1}{2}}, A = \frac{4\sigma_{s/a}M_w}{RT\rho_w} \tag{7.5}$$

where $\sigma_{s/a}$ is the surface tension of the solution/air interface, ρ_w the density of water, M_w the molecular weight of water, R the universal gas constant and T the temperature.

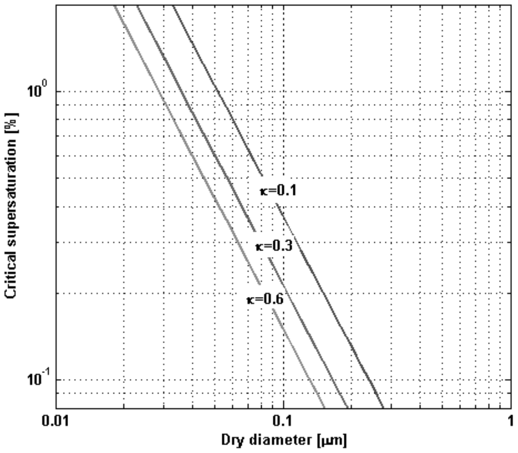

Σχήμα 7.2: *The critical supersaturation versus aerosol dry diameter. The κ hygroscopicity parameter has been determined equal to 0.1 (i.e., for less hygroscopic aerosols) and $\kappa = 0.3$ (i.e., for more hygroscopic aerosols) with respect to the reference $\kappa = 0.6$ of ammonium sulphate*

In mathematical formulation, the critical supersaturation s_c necessary for the CCN activation of an aerosol with dry diameter d defines the CCN differential supersaturation activity spectrum $\phi(s)$ which obey to the conservation law for the number concentration

$$f(d)\mathrm{d}d = -\phi(s)\mathrm{d}s \tag{7.6}$$

and can be reformulated as the following

$$\phi(s) = -f(d)\frac{\mathrm{d}d}{\mathrm{d}s} = \frac{2N}{3s\sqrt{2\pi}\ln\sigma}\exp\left(-\frac{\ln^2\left(\frac{s_c}{s}\right)^{2/3}}{2\ln^2\sigma}\right) \tag{7.7}$$

Then, CCN number concentration at any supersaturation expressed as $F(s)$ can be derived by the integration of $\phi(s)$ over the supersaturation range $[0, s_c]$

$$F(s_c) = \int_0^{s_c}\phi(s)\mathrm{d}s = \frac{N}{2}\left(1 - erf\left(-\frac{\sqrt{2}\ln\left(\frac{s_c}{s}\right)}{3\ln\sigma}\right)\right) \tag{7.8}$$

Let us introduce the initial and the corrected CCN differential supersaturation activity spectrum as $\phi_{in}(s)$ and $\phi_{cor}(s)$, respectively. Then, the discrepancy caused by the positive skewness of the initial aerosol size distribution can be quantifying by $\Delta\phi(s)$. Mathematically this variable is expressed as

$$\Delta\phi(s) = \frac{\phi_{in}(s) - \phi_{cor}(s)}{N}. \tag{7.9}$$

Calculation of droplet number and sensitivity to BL dynamics

The population-splitting concept has been used for the calculation of cloud droplets [145]. This concept has been applied to general circulation models as an attempt to include aerosol-cloud interactions. From the CCN size spectra, it is possible to calculate the number of expected cloud droplets by computing the maximum supersaturation of an ascending air parcel. The latter is computed from the partial derivative of cloud parcel's supersaturation:

$$\frac{\mathrm{d}s}{\mathrm{d}t} = \alpha v - \gamma\frac{\mathrm{d}W}{\mathrm{d}t} \tag{7.10}$$

$$\alpha = \frac{gM_w\Delta H_v}{c_pRT^2} - \frac{gM_\alpha}{RT}, \gamma = \frac{pM_\alpha}{p^sMw} - \frac{Mw\Delta H_v^2}{c_pRT^2} \tag{7.11}$$

where v: the vertical velocity of the ascending parcel, ΔH_v: latent heat of condensation of water, T: the parcel temperature, M_w: molecular weight of water, M_a: molecular weight of air, g: acceleration of gravity, c_p: heat capacity of air, p^s: water saturation vapor pressure, p: ambient pressure, $\frac{\mathrm{d}W}{\mathrm{d}t}$: condensation rate from liquid water to cloud droplets, R: universal gas constant. The maximum supersaturation s_{max} is achieved when Equation 7.10 becomes zero:

$$\frac{\mathrm{d}s}{\mathrm{d}t} = 0 \tag{7.12}$$

With known CCN spectrum $F(s)$ and the maximum supersaturation of the cloud parcel, the total number of activated cloud droplets can be expressed as:

$$N_d = F(s_{max}) = \int_0^{s_{max}} \phi(s)\mathrm{d}s \tag{7.13}$$

The vertical velocity of the ascending cloud parcel w is a critical parameter for the accurate determination of maximum supersaturation, and the cloud droplet number N_d. The vertical wind component w is a physical parameter we can retrieve with height from a Doppler lidar with high temporal resolution of 24 seconds [4]. However, the mean vertical wind has been proven not to be the characteristic quantity we need to retrieve [146]. Instead, the characteristic updraft velocity $w^\star = 0.79\sigma_w$ is proposed if $w \sim \mathcal{N}(\mu, \sigma_w^2)$ with a low mean value $\mu \approx 0$. From time series of vertical wind component the pdf of w, $g(w)$, has been constructed and checked for its validity on the requirement to follow a Gaussian distribution. Given the fact that the continuous variable w which takes any value in the set [-2,2] has an associate error δw which is range dependent [28], the discretization step should be carefully selected. Here, it has been selected equal to 0.3 such as the p.d.f of δw conforms to a Heaviside function:

$$g(\delta w) = \begin{cases} 1, & 0 < \delta w < 0.3 \\ 0, & \delta w > 0.3 \end{cases}$$

The Gaussian shape of g(w) is ensured from the Doppler lidar data within the diurnal PBL (c.f. Figure 7.3). In the cloud-topped PBL, updraft air flow becomes dominant. Several scenarios have been tried for the better determination of a representative $w^\star$: (1) whole time series (24h) have been considered; (2) only hours with dominant updrafts were used; (3) only one hour data were used so as $w^\star$ is time collocated with Raman lidar data.

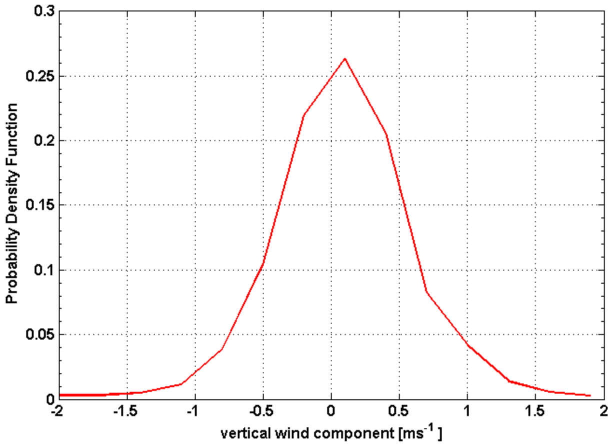

Σχήμα 7.3: *pdf for the vertical wind component from Doppler lidar data. Here is an example pdf which follows a Gaussian distribution with a positive but close to zero mean value.*

7.1.2 Case studies examined: results

The algorithm has been applied to four aerosol layers detected during the HygrA-CD campaign: 21 May, 22 May, 10 June and 11 June. The optical signature of the detected aerosols is demonstrated in Table 7.1. The cases of 21 May, 10 June and 11 June look very similar and they have been classified as common type of mixed BB (cf. Figure 6.24). The case of 22 May is of a more complicated BB type including some contribution of Asian dust. The dust contribution is apparent in aerosol intensive optical properties resulting to lower mean values of lidar ratio S_λ and AE.

Πίνακας 7.1: *Intensive aerosol optical properties at the inverted aerosol layers*

Date	**Layer boundaries** $[m]$	S_λ $[sr]$		**AE**
		355nm	**532nm**	
21 May	1200-1700	56 (5)	60 (8)	1.3 (0.3)
22 May	1200-1600	40 (8)	46 (3)	0.8 (0.6)
10 June	1200-1600	59 (4)	58 (8)	1.3 (0.4)
11 June	1200-1800	59 (4)	55 (9)	1.2 (0.4)

Aerosol size distribution from lidar inversion

For the layers of Table 7.1, the size distribution $f(D)$ have been retrieved and presented in Figure 7.4. The mode diameter for all cases is the same at $0.22\mu m$. However, provided that the wet aerosol spectra is a positively skewed distribution the long tail of the distribution points to the large diameters and the mean diameter is always larger than the mode diameter. The mean aerosol diameter of the wet size distribution is estimated as:

$$\overline{D} = \frac{1}{N}\int_{D_{min}}^{D_{max}} Df\left(D\right)\mathrm{d}D. \tag{7.14}$$

By considering that the n$^{\text{th}}$ central moment of the aerosol distribution about the mean is expressed as:

$$\mu_n = \frac{1}{N}\int_{D_{min}}^{D_{max}} \left(D - \overline{D}\right)^n f\left(D\right) \mathrm{d}D. \tag{7.15}$$

the statistical measures of the distribution (dispersion, skewness) can be calculated:

$$\sigma = \sqrt{\mu_2}, \gamma = \frac{\mu_3}{\mu_2^{3/2}} \tag{7.16}$$

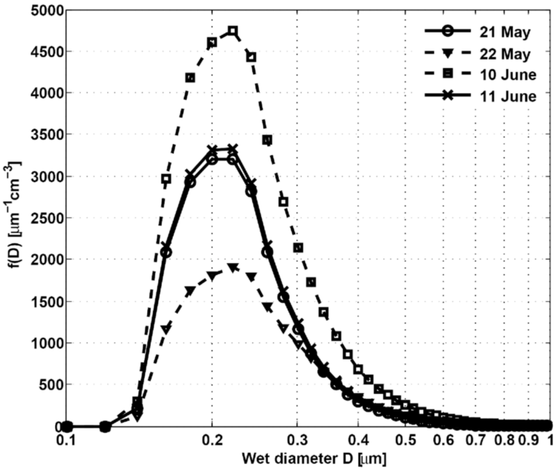

Σχήμα 7.4: *Wet size distribution as retrieved from lidar optical data in four cases.*

Πίνακας 7.2: *Lidar inversion in the 4 cases of Table 7.1. The retrieved positive-skewed lognormal size distribution with the following properties.*

Date	**Total Number** N $[cm^{-3}]$	**Mean Diameter** $\overline{D}$ $[\mu m]$	**Dispersion** σ	**Skewness** γ
21 May	460	0.25	1.25	20.3
22 May	330	0.29	1.46	20.9
10 June	770	0.27	1.30	19.9
11 June	480	0.26	1.27	19.6

The retrieved aerosol size distributions have been treated as log-normal. However, by reproducing the size distribution functions with the metrics of Table 7.2 it becomes evident that the cut-off diameter in the solution space of the distribution slightly changes the statistical nature of the distribution from a lognormal to a positively-skewed lognormal. In Figure 7.5, the initial positive skewed distributions of Figure 7.4 are compared to the lognormal distributions with the same statistics (i.e., total number N, mean diameter $\overline{D}$ and dispersion σ). For the corrected distributions, the respective mode and mean diameter are identical. The observed differences between the initial and corrected wet aerosol spectra imply that the ill-posedness of the lidar inverse problems will introduce some instability in the calculated CCN spectra and consequently in the total cloud droplet number.

Retrievals from wet to dry distribution

From a previous field campaign conducted at the same site and during the same year period (summer 2012) exhibiting same synoptic air flows, the aerosol hygroscopicity parameter at

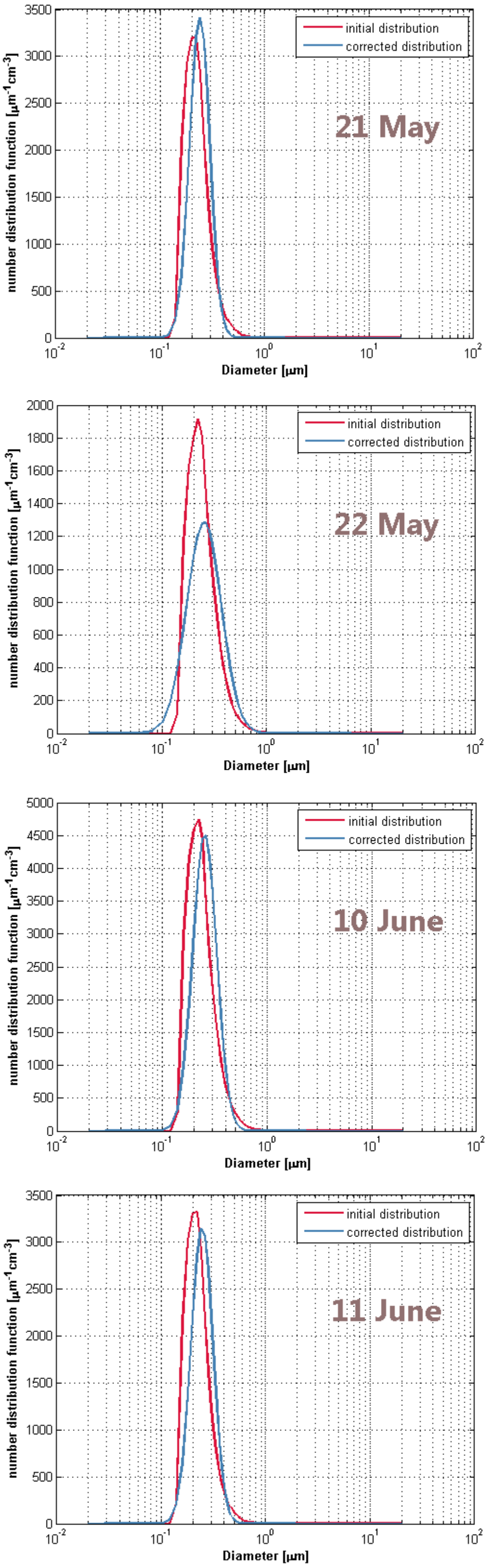

Σχήμα 7.5: *Aerosol size distribution positively-skewed log-normal (initial) versus log-normal (corrected) for all case studies. The corrected distributions have been produced from Eq.* (7.1) *with the statistical moments referred to Table 7.2.*

ground level was derived using multiple instrumentation, including a Hygroscopic Tandem Differential Mobility Analyzer (HTDMA), a High-Resolution Time-of-flight Aerosol Mass Spectrometer (HR-Tof-AMS) and filter samples. From the measurements it was derived that the majority of particles resided in the more hygroscopic mode (i.e., $\kappa > 0.1$) and were often externally mixed. The median κ value of particles having dry mobility diameters of 120 nm, regardless their mixing state (i.e., a value which was representative of the whole aerosol population, κ_{HTDMA}), was 0.27, ranging from 0.08 to 0.5. The measured κ values were compared with the hygroscopicity values derived from the aerosol chemical composition (κ_{CHEM}) which were estimated by employing the κ-Köhler theory over the measurements of an HR-Tof-AMS [147] and filter samples. κ_{CHEM} was found with the same median of 0.27 and all measurements were ranging from 0.12 to 0.46. Finally, estimates of the hygroscopic parameter based on the chemical composition from filter samples had a median κ value of 0.3. Comparative plots between the retrieved κ from HTDMA and filters and HTDMA and AMS are shown in the Figure 7.6(a) and 7.6(b) respectively. Keeping in mind the fact that a recent study in the area revealed that at higher altitudes the organic aerosol fraction is higher [148] and consequently the hygroscopicity parameter may decrease with height, it is believed that the two selected scenarios for the hygroscopic behavior of the detected aerosols are realistic and representative for the area.

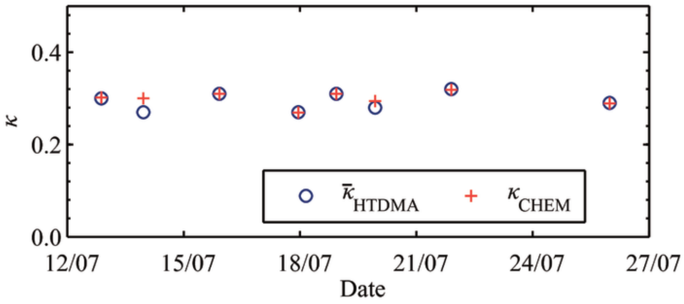

(a) Aerosol hygroscopic parameter (κ) obtained from 24-h average HTDMA measurements in comparison with the chemical composition derived particle hygroscopicity, obtained from filter samples.

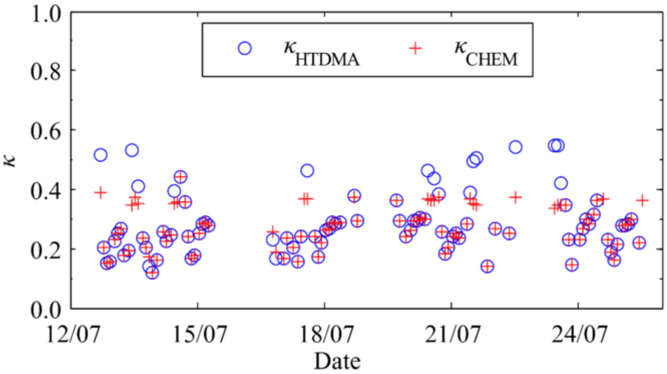

(b) Aerosol hygroscopic parameter (κ) obtained from 2-h average HTDMA measurements in comparison with the chemical composition derived particle hygroscopicity, obtained from the HR-Tof-AMS.

Σχήμα 7.6: *κ values for the area of study during Campaign of summer 2012*

The determination of the ambient RH in the studied layers of Table 7.1 have been done from Microwave Radiometer data [149] and radio soundings. The uncertainty on RH vertical

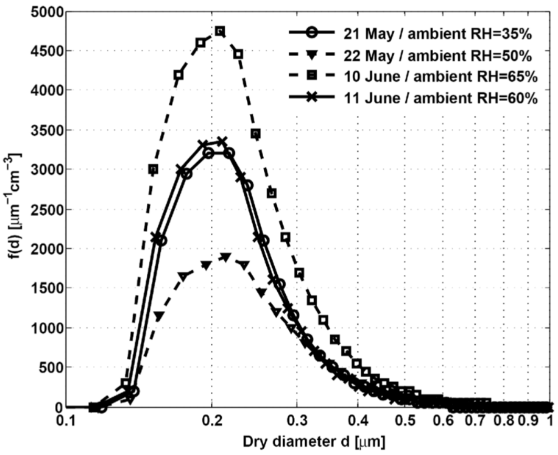

(a) $\kappa = 0.1$

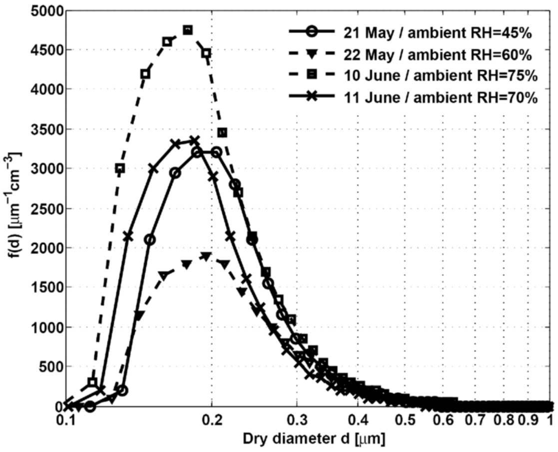

(b) $\kappa = 0.3$

Σχήμα 7.7: *Dry size spectra corrected with respect to the ambient RH*

profile is about 10% and should have a negligible impact on the CCN spectra calculations. Dry size distributions have been calculated with known RH and two possible hygroscopicity κ values and they are illustrated in Figure 7.7(a), 7.7(b).

Calculation of CCN spectra

The CCN spectrum[2] $F(s)$ for aerosol distributions of Figure 7.7 is shown for all cases separately in Figure 7.8. All available atmospheric particles turn to CCN above a certain supersaturation limit. The less hygroscopic particles ($\kappa = 0.1$) become all CCN active at supersaturation of approximately 0.2%. For the hygroscopic aerosols of $\kappa = 0.3$, the critical supersaturation drops to 0.1%. Comparing between the different case studies, we observe that the higher number of CCN appears for the case of 10 June since it is the case with the highest aerosol load. The maximum number of CCN is 770 per cm^{-3}. This is in good accordance with the AOD at 355 nm of the detected layer which was found equal to 0.069. On the contrary, the less polluted day seems to be the 22^{nd} of May with a total CCN number of 330 cm^{-3} in an aerosol layer

---

[2] The CCN spectra in all cases follow the power law approximation Cs^k for an index k and coefficient C. This is in accordance to [150] which presents a closure between the power law concept (with differential activity spectrum $\phi(s) = Cks^{k-1}$) and the lognormal parametrization of Equation 7.7.

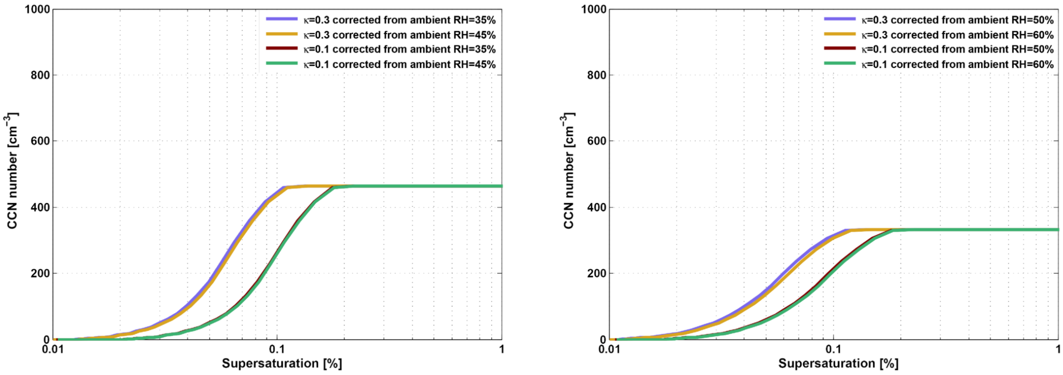

(a) **21 May:** $CCN_{max} = 460cm^{-3}$ (b) **22 May:** $CCN_{max} = 330cm^{-3}$

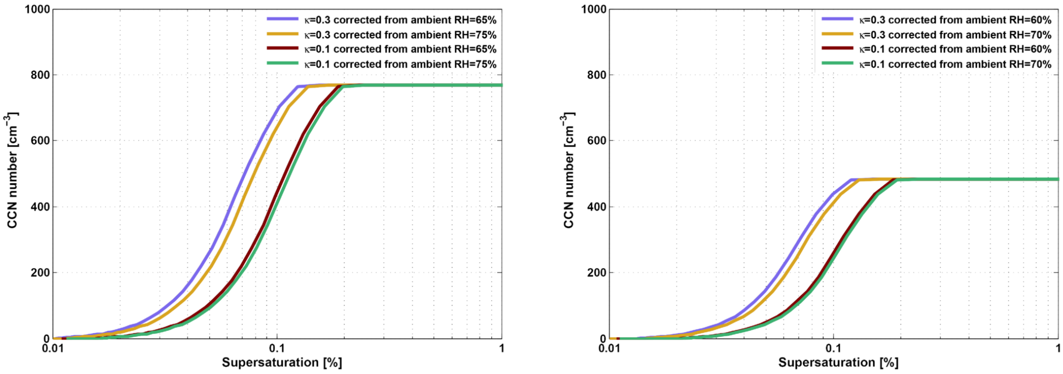

(c) **10 June:** $CCN_{max} = 770cm^{-3}$ (d) **11 June:** $CCN_{max} = 480cm^{-3}$

Σχήμα 7.8: *CCN spectra for the four case studies. The total activated CCN number as a function of the supersaturation is illustrated. In all cases, the detected aerosols are activated as CCN irrespectively to their physicochemical properties at supersaturations* $s > 0.2\%$

with AOD at 355 *nm* equal to 0.037. At higher supersaturations all aerosols become CCN, nevertheless CCN activation may happen at lower supersaturations. The obtained spectrum favors the classification of the aerosol layers with respect to their efficiency to act as CCN. Figure 7.9 shows the ability of aerosols to become CCN active for the several cases. The most efficient aerosol is that of 22 May. For an ambient supersaturation of 0.05%, the activation fraction in the case of 22 May is higher than 40% whereas in the case of 11 June less than 30% of the total aerosol is CCN activate. The former observation explains why the whole CCN spectra is a significant property which must be retrieved from lidar data and not only the total CCN number.

The response of the retrieval algorithm to the instability of inverted wet aerosol size distribution is clearly illustrated in Figure 7.10. The impact of ill-posed solutions is stronger for supersaturations lower than 0.1%. A maximum discrepancy of 30-35% appears for the cases of 10 and 11 June at 0.06% supersaturation. This means that an underestimation of approximately 30% will be introduced to the CCN number retrieval if the initial distribution provided to the algorithm deviates from the theoretical lognormal (see Figure 7.5). When the aerosol size distribution is wider (like in the case of 22 May), the discrepancy propagates towards the low supersaturation range.

The corrected aerosol size distribution after the ODE implementation is illustrated for the test case of 11 June in Figure 7.11. An apparent improvement is observed at the size range where the higher aerosol concentrations are lying. However, the corrected ODE distributions

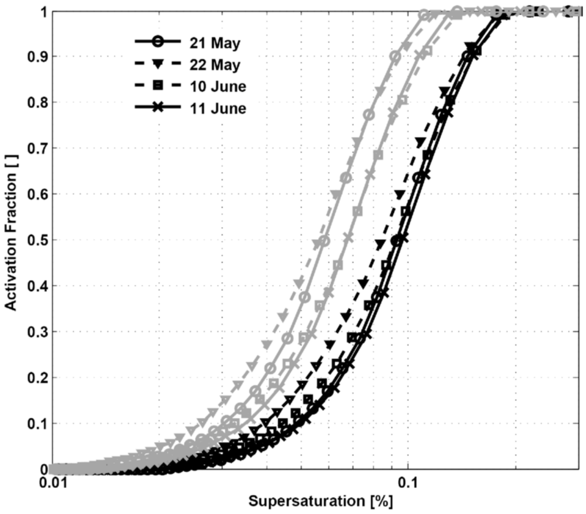

Σχήμα 7.9: *Activation fractions derived from CCN number over total aerosol number. Activation fractions are noted with grey color when* $\kappa = 0.3$ *and black color when* $\kappa = 0.1$*.*

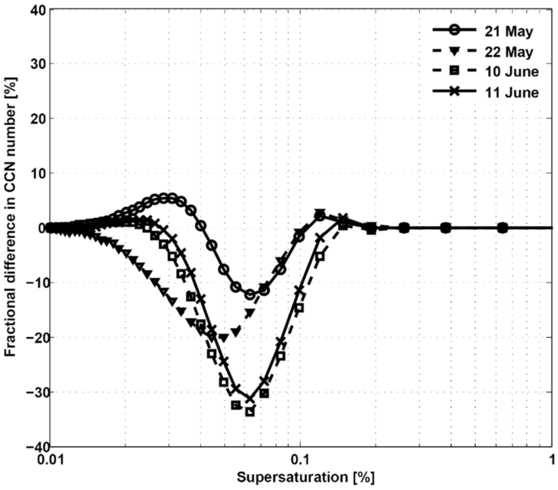

Σχήμα 7.10: *Fractional differences* $\Delta\phi(s)$ *along the supersaturation spectrum for all case studies.*

do not have a good overlap with the initial distributions at the tails of the distribution. In fact, this discrepancy should be less significant than in the case without ODE. A direct comparison on the CCN spectra retrieved from initial, corrected and corrected with ODE aerosol distributions verifies the improvement on the stability of the lidar CCN retrievals. In Figure 7.12, the initial CCN spectra seems better re-obtained by the corrected lognormal when ODE is applied. More precisely, the fractional difference in the CCN defined by Eq. (7.9) is significantly eliminated throughout the whole supersaturation spectrum. In Figure 7.13, for an ambient supersaturation of 0.06% we observe a mitigation in the underestimation of CCN number from 30% to about 10%.

Cloud droplet number calculations and sensitivity

Figure 7.14 shows the statistics for the vertical wind component from Doppler lidar time series. We observe that both updrafts and downdrafts dominate the PBL at different periods of the day. The diurnal mean characteristic velocity for all cases has been found equal to 0.6 ms^{-1} which is typical for a convective boundary layer [151]. Nevertheless, for the maximum

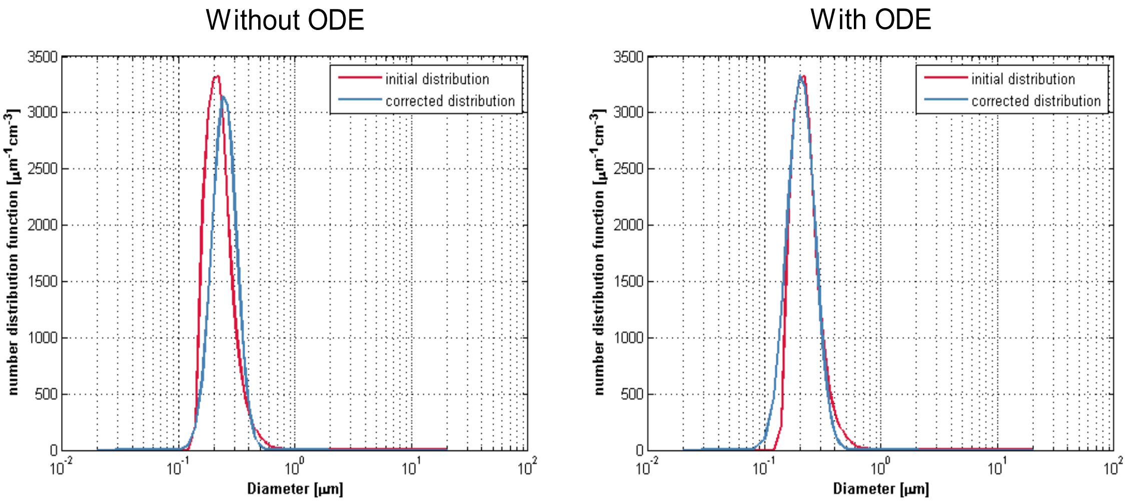

Σχήμα 7.11: *Comparison between the lidar retrieved aerosol size spectra with a lognormal distribution with and without ODE: application on the case study of 11 June.*

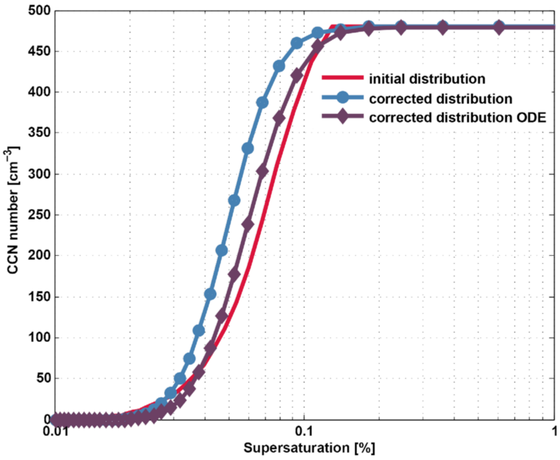

Σχήμα 7.12: *The retrieved CCN spectra for the aerosol size distributions of Figure 7.11.*

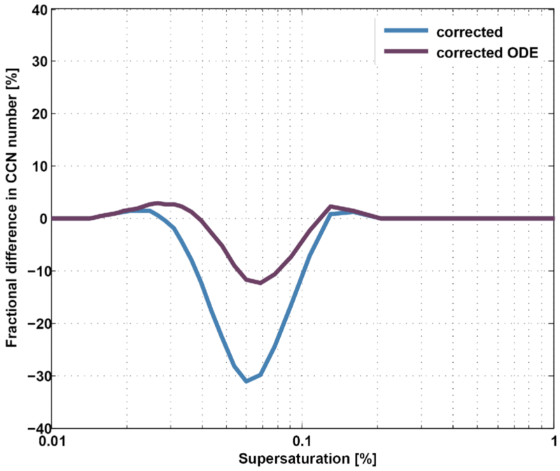

Σχήμα 7.13: *Fractional difference in CCN number before and after ODE application extracted from CCN spectra of Figure 7.12.*

supersaturation and cloud droplet calculations, all possible values of $w^\star$ summarized in Table 7.3 are considered. A range for cloud retrieved quantities is given in Table 7.4. The maximum s_{max} occurs for the case of 22 May. This leads to high cloud droplet activation fraction of 82% even at the lower bound of maximum supersaturation. Such a result, verifies the initial characterization for the aerosols of 22 May as the most efficient CCN among the studied cases. This is in good agreement with the statistical moments of aerosol size distribution summarized for all cases in Table 7.2. The absolute total aerosol number is the lowest of all days but mean diameter $\overline{D}$, dispersion σ and skewness γ are the highest among these cases.

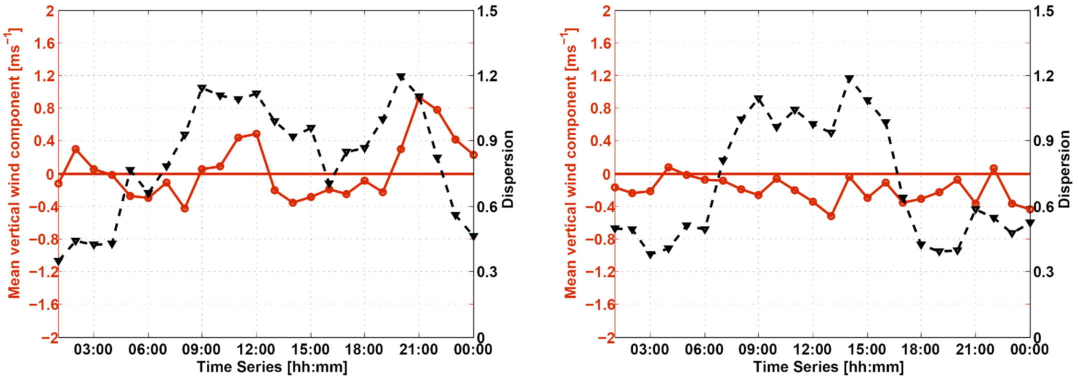

(a) **21 May** (b) **22 May**

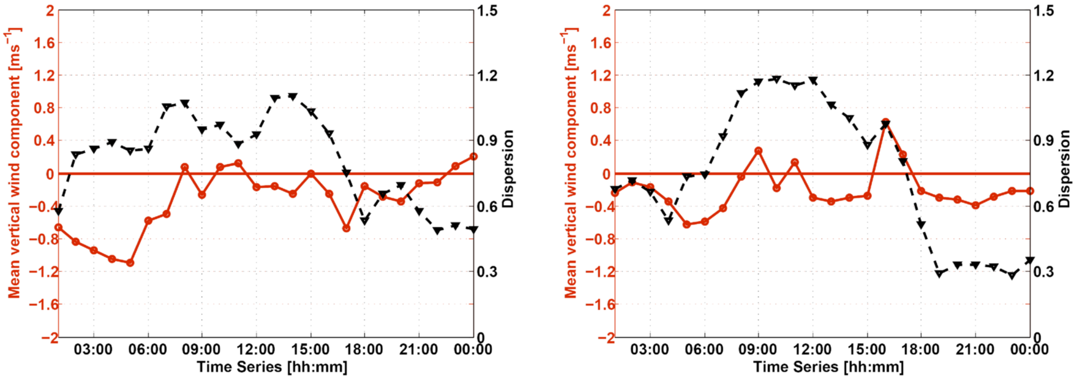

(c) **10 June** (d) **11 June**

Σχήμα 7.14: *Vertical velocity statistics from the retrieved pdf. The line with red color is the mean velocity while the black color line shows the dispersion about the mean. Both statistical moments have been estimated for hourly time series of Doppler lidar data.*

The predicted cloud droplet number is only slightly affected by the ill-posedness of the lidar inversion problem. As stated in Table 7.4, the cloud droplet number is estimated in all cases for a maximum supersaturation in the range $[0.13, 0.31]$. For a maximum supersaturation of 0.13% and above, the mean $\Delta\phi(s)$ tends to zero. Thus, the predicted total cloud droplet concentrations from lidar inverted data should be considered a stable retrieval with a small uncertainty.

As previously mentioned, the impact of unstable aerosol size distribution solutions on cloud droplet number is not so important. In Table 7.5, we compare the cloud droplet activation fraction for the initial aerosol spectra before correction of the positive skewness and after correction with and without ODE. For all case studies, the difference in the cloud droplet activation fraction between the initial and corrected spectra is less than 10% and it becomes less than 5% when ODE is applied.

Πίνακας 7.3: *Statistics from the pdf of the vertical wind component.*

	Diurnal (updrafts & downdrafts)			**Only updrafts**			**At the inversion time**
Mean value μ	*mean*	*min*	*max*	*mean*	*min*	*max*	
21 May	0.0	-0.1	0.3	0.4	0.0	0.3	0.9
22 May	-0.2	-0.2	0.0	0.1	0.1	0.1	-0.2
10 June	-0.3	-0.1	-0.3	0.1	0.2	0.1	-0.3
11 June	-0.2	-0.3	-0.2	0.3	0.2	0.3	-0.3
Dispersion σ	*mean*	*min*	*max*	*mean*	*min*	*max*	
21 May	0.8	0.3	1.2	0.9	0.4	1.2	1.1
22 May	0.7	0.4	1.2	0.5	0.4	0.5	0.6
10 June	0.8	0.5	1.1	0.8	0.5	1.1	0.7
11 June	0.7	0.3	1.2	1.0	0.8	1.2	0.3
Characteristic velocity $w^\star$	*mean*	*min*	*max*	*mean*	*min*	*max*	
21 May	0.6	0.2	1.0	0.7	0.3	1.0	0.9
22 May	0.6	0.3	1.0	0.4	0.3	0.4	0.5
10 June	0.6	0.4	0.9	0.6	0.4	0.9	0.6
11 June	0.6	0.2	1.0	0.8	0.6	1.0	0.2

Πίνακας 7.4: *Cloud droplet activation parameters*

	21 May	**22 May**	**10 June**	**11 June**
Maximum Supersaturation (%)	[0.13,0.26]	[0.15,0.31]	[0.14,0.19]	[0.13,0.26]
Cloud Droplet number (m^{-3})	[285,453]	[270,324]	[539,655]	[281,476]
Activation Fraction (%)	[62,98]	[82,98]	[70,90]	[58,98]

7.1.3 Summary and conclusions

This study provides a methodology to retrieve CCN spectra and total cloud droplet number with the use of synergistic ground-based optical remote sensing instruments. Aerosol Raman lidars are widely used for the vertical characterization of aerosol optical and microphysical properties. However, lidar retrievals were never used in the past for the classification of aerosols based on their efficiency to act as CCN. Here, for the first time lidar optical data can be linked to CCN number in an atmospheric layer. The Köhler theory has been applied to the inverted aerosol size spectra after being corrected from relative humidity effects. The ambient relative humidity in the detected aerosol layer is vertically resolved by combined information from radiosonde data and microwave radiometer. Then, the retrieved quantity is the CCN number along the supersaturation spectrum.

The proposed methodology has been applied to four case studies of HygrA-CD campaign. The origin of the detected air masses is from the industrial zone of Black Sea and the type of detected aerosol is mixed BB. The most polluted case is that of 10 June with a high aerosol load leading to cloud droplets concentration in the order of 539 to 655 cm^{-3}. The less polluted day if that of 22 May leading to cloud droplets in the range 270-324 cm^{-3}. However, when aerosols are characterized with respect to their efficiency to produce cloud droplets, aerosols of that day are proven as the most efficient CCN. This is a characteristic example explaining

Πίνακας 7.5: *Cloud droplet activation fraction [%] for initial, corrected and corrected with ODE size spectra*

	21 May	22 May	10 June	11 June
Initial	87	89	86	85
Corrected	93	91	91	94
Corrected with ODE	84	91	88	87

the importance of retrieving the whole CCN spectra.

The total number of activated cloud droplets is calculated from the maximum supersaturation (s_{max}) that reaches an ascending air parcel. For the determination of s_{max}, the characteristic vertical wind is a parameter which is obtained from a Doppler lidar. Such an instrument provides vertical profiles of Doppler velocity and other dynamic characteristics of PBL turbulence. First, the pdf of vertical wind has been constructed and, then, the characteristic velocity $w^{\star}$ has been calculated from the variance of the Doppler velocity distribution.

Finally, due to the ill-posedness of the lidar inverse problem, several tests has been done on the stability of the retrieved aerosol size spectra. Lognormal distributions have been generated with the same statistical properties of the initial distributions. These distributions have been used for the CCN spectra estimation and a maximum fractional difference of around 30% has been found. Specifically, the retrieval is more unstable for supersaturations below 0.1% and in particular the largest discrepancy has been observed around $s = 0.06\%$. This impact was significantly improved by 20% when an optimal maximum likelihood estimator has been applied on the initial retrieved aerosol spectra. The cloud droplet number does not appear very sensitive to aerosol retrieval uncertainties. In fact, cloud droplet number appears more sensitive to the BL dynamics which determine the air parcel maximum supersaturation.

7.2 Vertical aerosol flux estimation in the cloud-topped PBL

Vertical transport of aerosols within the PBL is a complex physical process and it has not been systematically studied with means of active remote sensing so far. Lately, there is a considerable need within Aerosols, Clouds, and Trace gases Research InfraStructure (ACTRIS)/EARLINET community to provide flux profile observations throughout the PBL. Collocated measurements from an elastic aerosol lidar and a Doppler lidar can be used synergistically in order to capture vertical aerosol fluxes in the PBL. A method has been implemented by [152] for dry atmospheric conditions in cloud-free conditions. Here, we extend this technique for the case of cloud-topped PBL where hygroscopic aerosol growth due to water uptake occurs. Aerosol vertical transport technique has been applied to a case study of a convective deep PBL ($\simeq$2 km) in an humid atmosphere (i.e., water vapor mixing ratio r=9 $g\ kg^{-1}$) with high Relative Humidity gradient within the PBL in the order of 25% per km.

Only quantification of aerosol number concentration fluxes near the surface [153] and near the ocean [154] have been achieved with in-situ instrumentation (i.e., combined ultrasonic anemometer with high resolution particle counter). Using remote sensing instruments, turbulent water vapor fluxes measurements have been achieved from ground-based vertically pointed water vapor differential absorption and Doppler lidars [155].

7.2.1 Measurements & methodology

Collocated measurements from a Doppler lidar and an aerosol elastic lidar have been performed at DEM during the HygrA-CD campaign. The quantification of aerosol vertical transport implies that the aerosol and Doppler lidar share the same illumination volume. The aerosol backscatter lidar is AIAS with an operational wavelength of 532 nm and a full overlap of about 300 m above ground level. The elastically backscattered light is collected with a sampling rate of 20 MHz resulting to vertical resolution of 7.5 m. The temporal resolution of the lidar has been set to 100 s in order to achieve a sufficiently good SNR per vertical profile. The latter allowed us to capture the fluctuations in the aerosol backscatter coefficient β with an accuracy of ∼15% [1]. The aerosol backscatter coefficients has been estimated from the Klett method [73], [120] by making an assumption on the lidar ratio S_λ. We selected a value of S_{532}=45 sr because this was the most frequently observed value within the campaign (cf. Figure 6.27). The wind lidar is a commercial coherent heterodyne pulsed Doppler scanning lidar system manufactured by HALO Photonics, the performance of which has been evaluated in [4]. This lidar is able to work in a combined mode of operation: vertical azimuth display (VAD) mode and a three-beam Doppler beam swinging (DBS) mode. When the instrument is operated in VAD mode, vertical wind component w can be measured with an accuracy of better than 0.1 ms^{-1} [156]. The range resolution of the vertical wind component measurement is 30 m and the temporal resolution is 14 s. The vertical profiles have been averaged so as the temporal resolution of wind measurements becomes similar to AIAS lidar (i.e., ∼ 100 s). The maximum range of measurement depends strongly on the atmospheric aerosol load and very rarely reaches a range of 2-3 km. This is a barrier for the application of the proposed methodology within the whole PBL depth.

Eddy correlation technique is the most direct turbulent flux measurement. This technique makes possible the measurement of the flux on the same time and spatial scales as the variability of various processes that influence the aerosol flux between the PBL and the ground beneath it. The methodology demands the calculation of the covariance of the vertical wind component fluctuation w' and the aerosol backscatter coefficient fluctuation β'. As any other statistical independent random variable, $w = w(z,t)$ and $\beta = \beta(z,t)$ expressed by Eq. 7.17 and 7.18 have a laminar component $\overline{w}$, $\overline{\beta}$ which is expressed as the ensemble average and a turbulent component w', β' which is the fluctuation about the mean:

$$w(z,t) = \overline{w}(z) + w'(z,t) \tag{7.17}$$

$$\beta(z,t) = \overline{\beta}(z) + \beta'(z,t) \tag{7.18}$$

Provided that lidars point vertically and illuminate the same atmospheric volume, in stationary flows, the laminar components are given from the temporal average

$$\overline{w}(z) = \frac{1}{\tau}\int_t^{t+\tau} w(z,t)\,\mathrm{d}t \tag{7.19}$$

$$\overline{\beta}(z) = \frac{1}{\tau}\int_t^{t+\tau} \beta(z,t)\,\mathrm{d}t \tag{7.20}$$

The application of eddy correlation technique for measuring the turbulent fluxes requires rapid data acquisition systems [157]. Therefore, AIAS temporal resolution (100 s) is indeed in the limits of the acceptable sampling rate for turbulent flux measurements. Another requirement is that of stationary turbulence in the averaging time window and can be met from the Taylor's hypothesis. In practice, when we study any meteorological parameter, the temporal fluctuations in a medium are expressed as a simple transfer of the spatial fluctuations with a velocity equal to the wind speed. This allows us to link the time and frequency scale of this parameter to its spatial scale of wavelength or wavenumber [158].

From the HygrA-CD dataset, we have selected the case of 11 June to apply our methodology. The reason is that in that day we observed cloud formation (see due point temperature and

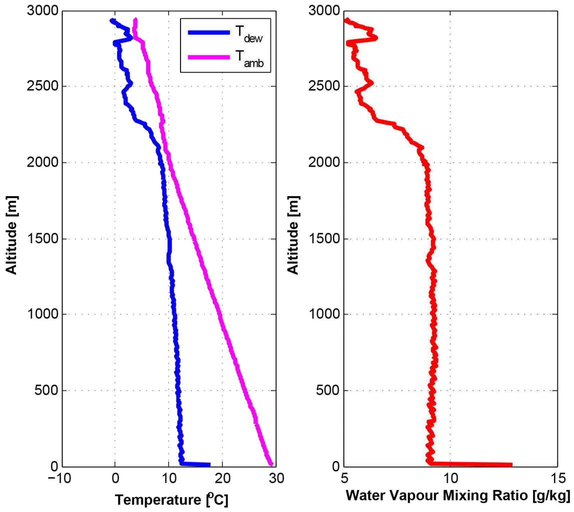

Σχήμα 7.15: *Vertical profiles from radiosonde data at 12:00 UTC at 11 June 2014. Left graph shows vertical profiles of ambient and due point temperature and right graph shows water vapor mixing ratio profile*

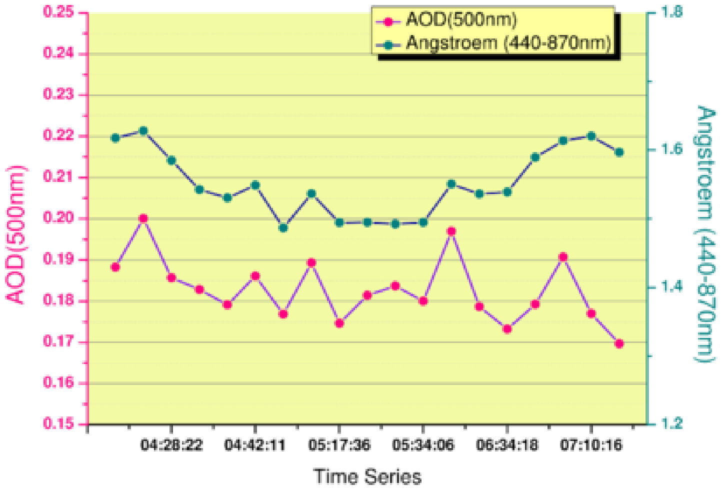

Σχήμα 7.16: *AOD and AE from sunphotometer data. The measurements stop at around 07.30 when the first clouds started forming (11 June 2014)*

temperature profiles in Figure 7.15) and a very good mixing in the lower atmosphere. The mixing state of the atmosphere is characterized from the vertical profile of the water vapor mixing ratio. In Figure 7.15, the mixing ratio r is almost constant and equal to 9 $g\ kg^{-1}$ from ground level up to 2000 m height. This is a good indication of a well-mixed PBL because of the earlier turbulent flux activity in the PBL. At the time of the radiosonde launch (12:00 UTC), the lapse rate has been estimated of about 9 Kkm^{-1} which is slightly higher than the adiabatic lapse rate. With respect to aerosol properties, this day was characterized by a relatively high AOD(500 nm)>0.17 and an AE(440/870 nm) of approximately 1.5-1.6 (cf. Figure 7.16). The time series of measurements stop at around 07:30 UTC because the first clouds started forming in the sky and contaminated the sun photometer data. AIAS lidar allowed us to derive the spatio-temporal evolution of range-corrected lidar signals which is illustrated in Figure 7.17. The first clouds were detected by AIAS at an altitude of approximately 1900

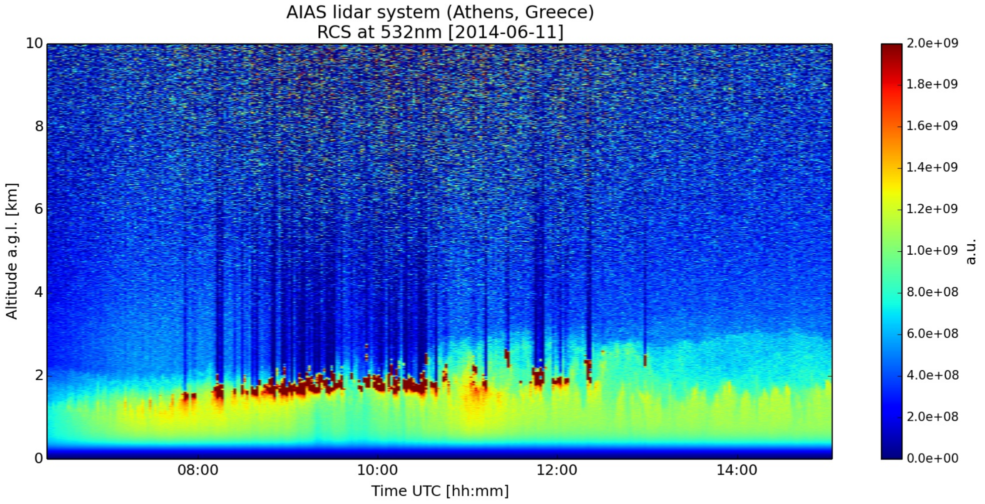

Σχήμα 7.17: *Spatio-temporal evolution of the range-corrected lidar signals on 11 June 2014 provided by AIAS.*

m just before 08:00 UTC. Therefore, a useful time integration window for investigating the aerosol turbulent flux is 06:40-07:45. The choice of this integral scale should be made with attention because is certainly important in turbulence studies [155], [159]. Exactly the same integral scale is consider for the wind measurements.

The vertical aerosol flux measurements are possible under the following assumption: *aerosol concentration is homogeneous in the horizontal x,y-directions above the lidars.* The validity of this assumption comes from the WRF model. The aerosol mass fluctuations above the lidars are primarily due to vertical transport of aerosol (in the atmospheric column) whilst horizontal advection from remote sources can be neglected. The emissivity intensity of the aerosol sources in the area of study seems to be approximately constant for the period 06:00 and 12:00 in Figure 7.18(a) and 7.18(b). Moreover, there are not observed significant differences in the emission sensitivity between the atmospheric layers 0-1 km and 1-2 km, meaning that we can consider the atmospheric layer from ground up to 2 km as horizontally homogeneous and isotropic.

7.2.2 Turbulent aerosol flux calculations within the PBL

The vertical aerosol mass fluxes are primarily carried by large eddies with length scale comparable to the boundary layer depth. However, provided that turbulence exists within a range of eddy lengths, it is convenient to construct the energy spectrum which simply expresses how much kinetic energy is contained in eddies with wavenumber k. The contribution to the spectra at the whole frequency range for the wind vertical component has been reported by [28]. Here, we explore the energy containing part of the spectrum which is covered by the aerosol backscatter lidar measurements. Therefore, we need to estimate the power spectral density of aerosol backscatter coefficient as

$$S_{\beta}(z,f) = |\tilde{\beta}(z,f)|^2, \tag{7.21}$$

where $\tilde{\beta}(z,f)$ is the Fourier transform of $\beta'(z,t)$ given as

$$\tilde{\beta}(z,f) = \int_0^{\mathcal{T}} \beta'(z,t)\exp(-2\pi i f t)\,\mathrm{d}t. \tag{7.22}$$

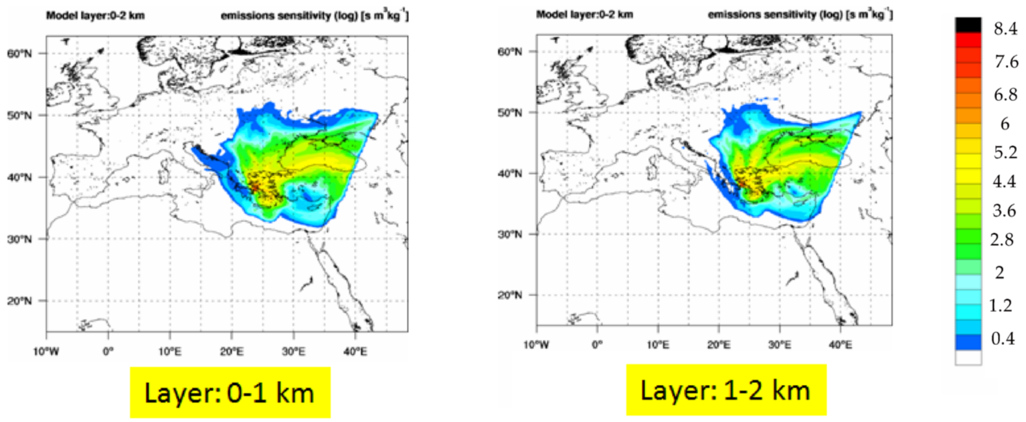

(a) 06:00 UTC

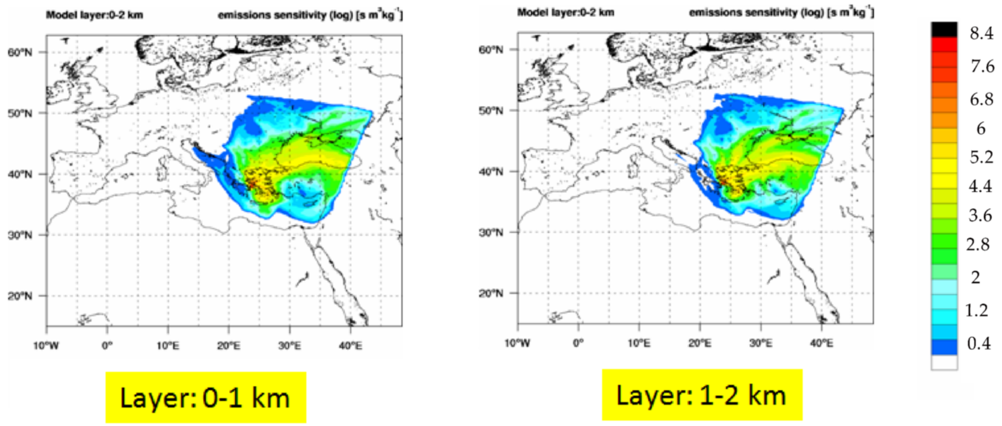

(b) 12:00 UTC

Σχήμα 7.18: *Emission sensitivity from WRF at 06:00 and 12:00 UTC for the atmospheric layers 0-1 km and 1-2 km (air masses ending over Athens on 11 June 2014)*

The backscatter power spectra are presented in Figure 7.19 for two heights in the time window 06:40-07:45. The spectra seem to cover most of the inertial subrange which follows the Kolmogorov hypothesis [160] about homogeneous and isotropic turbulence. A $-5/3$ power law is fitted to the data for the frequency spectrum $8\times10^{-3}-2\times10^{-2}$ Hz. At higher frequencies it flattens [161] because noise dominates in this part of the spectrum. In fact, we are restricted by the sampling frequency of 100 Hz and we cannot study smaller sizes of turbulent structures.

The partitioning of turbulent fluxes across the eddy lengths can be quantified through the co-spectrum of w' and β' which is the real part of the conjugate product of their Fourier transforms (see Eq. (7.22)) $\tilde{w}^*(z,f)\tilde{\beta}(z,f)$ [21]. In our case main frequencies contributing to the vertical flux range from 1×10^{-3} to 2×10^{-2} Hz (c.f. Figure 7.20). Under Taylor's hypothesis of frozen turbulence, we find that these frequencies correspond to eddy lengths in the 450-8000 m. Eddy wavelength λ was calculated from $\lambda=\frac{V}{f}$ considering a mean wind speed of $V=8ms^{-1}$. We need to notice that the dominant upward vertical transport appears where the co-spectra are positive; for eddy lengths in the range 450-1500 m which is comparable to the PBL depth of about 1800 m. Such a finding is typically seen in the convective PBL [162]. The fact that eddy length of few hundred of meters is comparable to the boundary

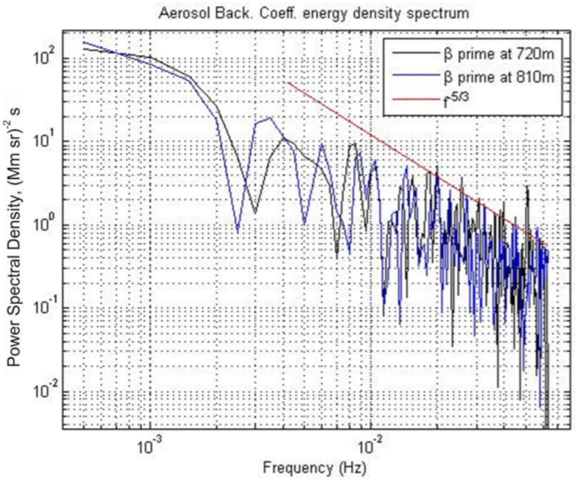

Σχήμα 7.19: *Power spectral density function of the backscatter coefficient at heights 720 and 810 m for the time period 06:40-07:45 UTC (11 June 2014)*

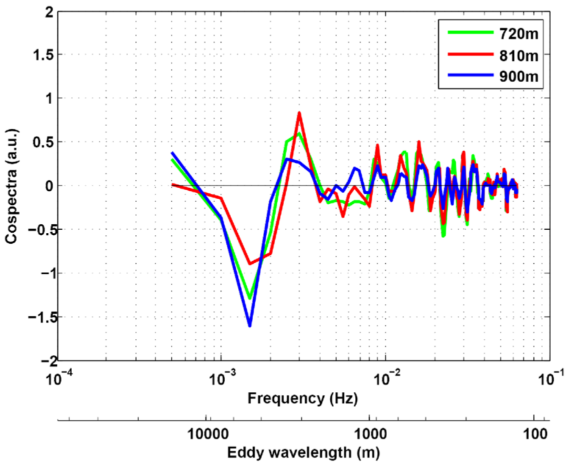

Σχήμα 7.20: *Cospectrum of aerosol backscatter coefficient and vertical wind fluctuations for the height levels 720, 810 and 900 m. Eddy wavelengths have been derived from frequency with mean wind speed of* $V = 8ms^{-1}$ *under Taylor's hypothesis (11 June 2014)*

layer depth justifies the vertical mixing. These eddies are responsible for the transport of aerosols from ground (i.e., close to their sources) upward. In order to quantify the flux, the covariance of the fluctuations w' and β' is estimated.

$$C_{w,\beta}(z) = \overline{w'(z,t)\,\beta'(z,t)} \tag{7.23}$$

The aerosol backscatter coefficient is a proxy for aerosol mass concentration in dry conditions (low RH). However, in atmospheric conditions with high RH we expect an enhancement in the aerosol backscatter coefficient due to aerosols' water uptake [163], [164], [165]. The mean aerosol backscatter coefficient $\overline{\beta}$ in the time window 06:40-07:45 is depicted in Figure 7.21. It is obvious that at around 1800 m there is an enhancement in aerosol backscattering. By looking to the vertical profile of RH (c.f. Figure 7.22) from the radiosonde launch at 12:00

UTC, we observe a sharp increase in the RH profile from ground level up to an altitude of about 2000 m. In particular, the RH gradient is around 2.5% every 100 m and RH exceeds 80% above 1800 m in height. In the same graph, again from the radiosonde data the vertical profile of potential temperature θ is plotted. Above 2000 m, the gradient $\frac{d\theta}{dz}$ gets a clearly positive value meaning that vertical motions are suppressed above that height.

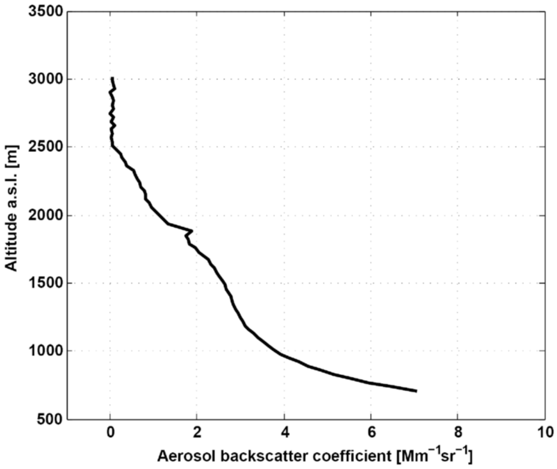

Σχήμα 7.21: *Mean aerosol backscatter coefficient $\overline{\beta}(z)$ in the time frame 06:40-07:45 UTC (11 June 2014)*

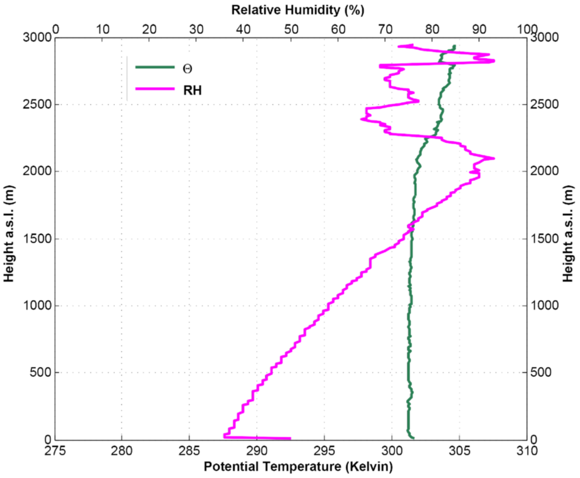

Σχήμα 7.22: *Vertical profiles of potential temperature and RH from radiosonde data at 12:00 UTC (11 June 2014)*

Relative humidity correction

Prior to the calculation of vertical aerosol flux, it is necessary to relieve the β profile from the humidity effect. The enhancement in aerosol backscattering coefficient f_β due to increase of ambient RH in the vertical profile is defined as

$$f_\beta(RH) = \frac{\beta(RH)}{\beta(RH_{ref})}, \tag{7.24}$$

where the reference RH_{ref} is determined according to the β vertical profile. The enhancement in scattering due to humidity effects is well parameterized by Hänel formula [166]

$$f\left(RH\right)=\left(\frac{1-RH}{100}\right)^{-\gamma} \tag{7.25}$$

In the particular case study of 11 June, we have retrieved the humidogram for $f_{\beta}\left(RH\right)$ by considering β and RH values for the height range 2100-2500 m. We assume that at this range (above the PBL) most of the differences in aerosol backscatter coefficient are observed due to variations in RH. Our assumption is confirmed by the positive gradient of potential temperature (cf. Figure 7.22). The resulting humidogram is presented in Figure 7.23. The selected RH_{ref} is 65% because it is the lower value measured at 2500 m height. By applying the Hänel parametrization for γ=0.85 we achieve a very good fit with the data at the RH range 65-70% and 80-90%. For the range of 70-80%, the enhancement factor estimated from the lidar data is larger than the parametrized one. This is probably seen because aerosol mass concentration is transported at these heights from below or above. The obtained γ value of 0.85 is almost an average of the found values 0.47-1.35 for urban aerosols in the city of Paris [167].

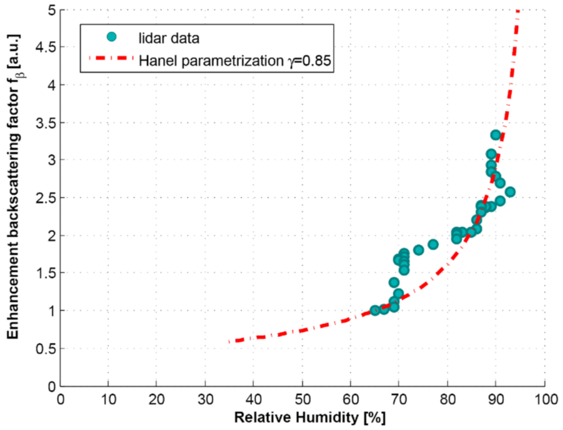

Σχήμα 7.23: *Backscattering enhancement factor* $f_{\beta}\left(RH\right)$ *normalized at* $RH_{ref}=65\%$ *with* γ *exponent equal to* 0.85 *(11 June 2014)*

In the case of dry atmospheric condition where the RH stays relatively constant with respect to height and well below 40%, the fluctuation in the aerosol backscatter coefficient is exclusively seen when there is a change in the aerosol concentration. However, in a humid atmosphere, an increase in aerosol backscatter coefficient does not necessarily imply an increase in the aerosol concentration due to vertical aerosol transport. Before retrieving aerosol concentration from the backscatter coefficient we need to correct the latter for humidity effects.

Aiming to reproduce an enhancement factor function which should be applied to the aerosol backscatter coefficient and corrected the β profiles from the RH effect, we need to normalize the parametrized data of Figure 7.23 at $RH_{ref}=40\%$. The reason is that aerosol mass at $RH<40\%$ can be considered dry and the impact of RH in the measured backscatter coefficient is almost negligible.

Finally, the mean aerosol backscatter coefficient profile corrected according to Eq. (7.23) with the backscattering enhancement function of Figure 7.24 is presented in Figure 7.25. The differences from the initial backscatter coefficient are significant. At around 1200 m height, the derived backscatter coefficient after the correction is about 2 times lower than the initial retrieved value. Therefore, without considering the effect of RH in the aerosol mass flux calculations, we would have gotten an overestimation on the flux. In the following section, we have tried to quantify this overestimation.

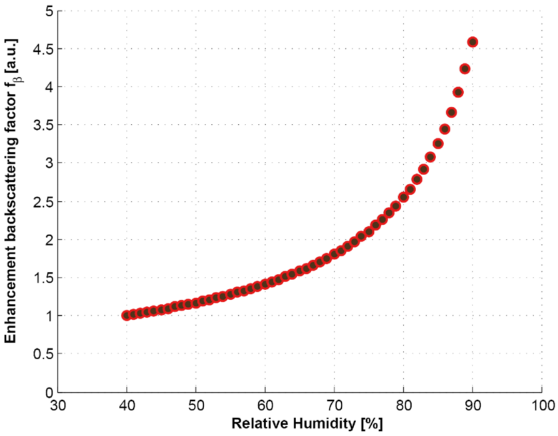

Σχήμα 7.24: *Parametrized backscattering enhancement factor* $f_\beta(RH)$ *normalized at* $RH_{ref} = 40\%$ *(11 June 2014)*

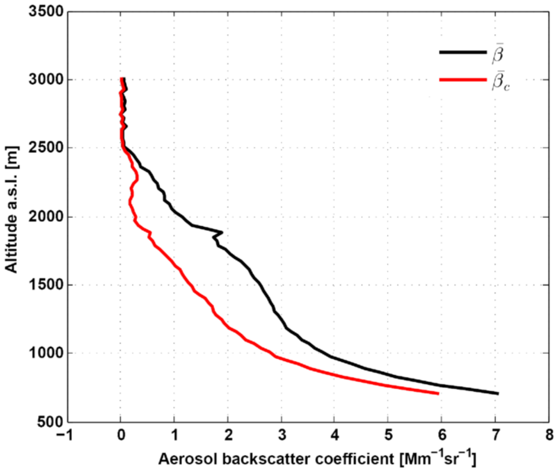

Σχήμα 7.25: *Mean aerosol backscatter coefficient in the time frame 06:40-07:45 UTC before (black line) and after (red line) the correction of RH effect (11 June 2014)*

Aerosol vertical flux

The aerosol vertical flux is calculated from the covariance $C_{w,\beta}$ and it is defined as upward flux when the covariance is positive and as downward flux when the covariance is negative. Let's reformulate the β' component into two terms

$$\beta' = \beta'_{RH} + \beta'_c \tag{7.26}$$

where the first term β'_{RH} denotes a change in the backscatter coefficient due to differences in the RH levels and the second term β'_c refers to the fluctuation in the backscatter coefficient due to aerosol concentration change. Therefore, what we need for the aerosol flux calculation is the second component β'_c which can be expressed by substituting Eq. (7.23) and (7.18) to Eq. (7.26)

$$\beta'_c = \left(\beta - \overline{\beta}\right)\left(1 - \frac{1}{f_\beta(RH)}\right) \tag{7.27}$$

The resulting aerosol flux for the height range 700-1300 m is illustrated in Figure 7.26. The restrictions on the range come from instrumental limitations; the lower bound is due to

AIAS full overlap and the upper bound is due to significant noise levels in the Doppler lidar data. The impact of RH becomes significant above 800 m.

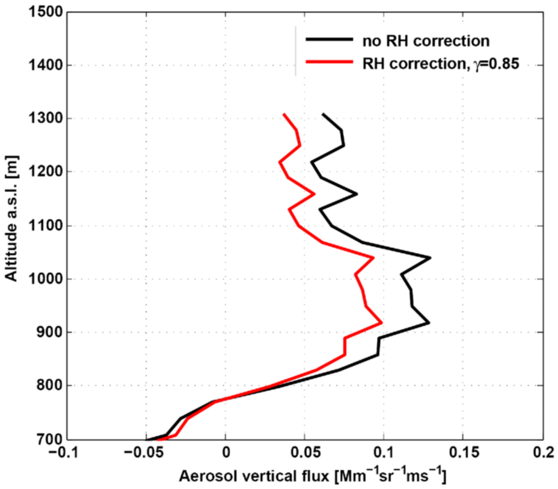

Σχήμα 7.26: *Aerosol vertical flux calculation for the time frame 06:40-07:45 UTC (11 June 2014)*

Conversion from aerosol backscatter coefficient to aerosol mass concentration

As analytically presented in Chapter 5, LIRIC has been proven a useful tool to derive vertical profiles of the volume concentration for fine- and coarse-mode particles. The case of 11 June is characterized by aerosols of both fine- and coarse-mode as depicted in Figure 7.27. The fine mode at the latest timeslot of 05:50 UTC becomes dominant. By combining three-wavelength elastic lidar signals from EOLE and the latest sun-photometer data, we retrieve the vertical profiles of aerosol volume concentration as illustrated in Figure 7.28. The fine mode aerosol concentration increases vertically at higher altitudes whereas coarse-mode aerosol concentration decreases with height. The total volume concentration decreases with height up to a certain level (∼ 1100 m) while at altitudes from 1300 m and up to 1600 m an increasing trend is observed.

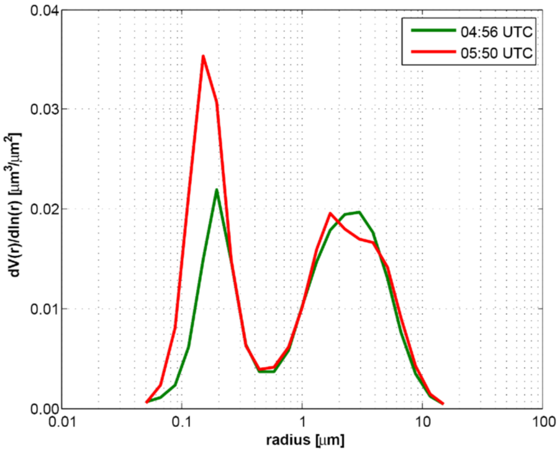

Σχήμα 7.27: *Aerosol size distribution measured from sun-photometer (11 June 2014)*

Provided that apart from the aerosol backscatter coefficient, volume concentration is also affected by the vertical increase in RH levels, we cannot confidently answer how much of the increase in volume concentration is due to aerosols' water uptake without having

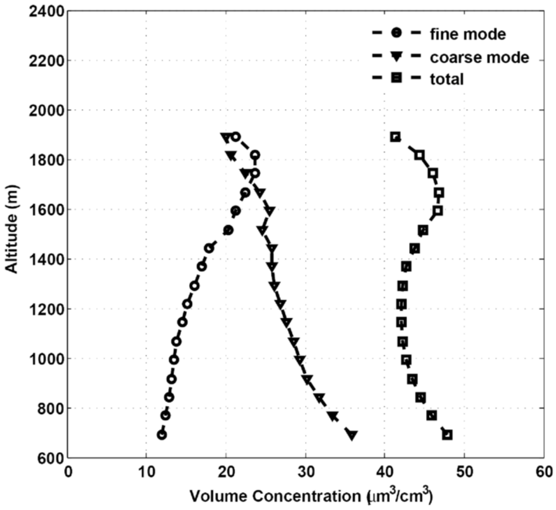

Σχήμα 7.28: *Vertical profiles of aerosol volume concentration using LIRIC algorithm (11 June 2014)*

Πίνακας 7.6: *Fine and coarse-mode aerosol volume concentration and their partial contributions to the total concentration V_t at specific altitudes*

Altitude $[m]$	$\mathbf{V}_f$ $[\mu m^3 cm^{-3}]$	$\mathbf{V}_c$ $[\mu m^3 cm^{-3}]$	$\mathbf{V}_t$ $[\mu m^3 cm^{-3}]$	$\mathbf{V_f}/\mathbf{V_t}$ [%]	$\mathbf{V_c}/\mathbf{V_t}$ [%]
700	12	35	47	26	74
1000	13	29	42	31	69
1300	16	26	42	38	62

any knowledge on the aerosol chemical composition. From Figure 7.28, it seems that only the fine-mode volume concentration is enhanced by the increased RH up to the altitude of 1700-1800 m. Similar findings for the fine-mode volume concentration profile are reported in [168].

The conversion factor C from aerosol backscatter to aerosol mass can be derived from

$$C(z) = \frac{m(z)}{\beta(z)} = \frac{\rho(z)V(z)}{\beta(z)} \tag{7.28}$$

where ρ is the aerosol density, V is the aerosol volume concentration and m the aerosol mass concentration. The aerosol density for the transformation of volume concentration to mass concentration stems from the typical fine- and coarse-mode aerosol density as

$$\rho(z) = \frac{V_f(z)}{V_t(z)}\rho_f(z) + \frac{V_c(z)}{V_t(z)}\rho_c(z) \tag{7.29}$$

In particular, we used for the calculations a density of ρ_f=1.6 gcm^{-3} [169], [170] and ρ_c=2.6 gcm^{-3} [171], [172] for fine- and coarse-mode aerosols, respectively. From the contribution of fine- and coarse-mode aerosol volume concentration to the total concentration (Table 7.6) the derived conversion factors are $C(z = 700\ m)$ =16 $\mu g\ m^{-3} Mmsr$, $C(z = 1000\ m)$ =24 $\mu g\ m^{-3} Mmsr$ and $C(z = 1300\ m)$ =30 $\mu g\ m^{-3} Mmsr$. Since the impact of RH on the enhancement of volume concentration is essentially strong for RH>60-65%, the aerosol mass flux has been estimated using the mean conversion factor $\overline{C}$=23.5 $\mu g\ m^{-3} Mmsr$.

The resulting vertical profile is presented in Figure 7.29. The derived values of 0.5-2.4 $\mu g\ m^{-2} s^{-1}$ in the upper active PBL (800-1300 m) seem very reasonable for a convective PBL. The mean mass flux of 1 $\mu g\ m^{-2} s^{-1}$ corresponds to an entrainment rate of 100 $m\ h^{-1}$ which

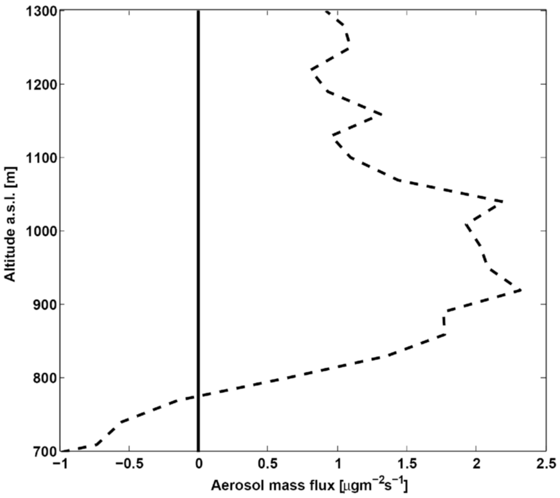

Σχήμα 7.29: *Aerosol mass flux estimation using a conversion factor of* $\overline{C}$=23.5 $\mu g\ m^{-3} Mmsr$ *(11 June 2014)*

was the mean PBL growth rate observed in Athens during summer-time in the late morning (07:00-07:30 UTC).

7.2.3 Summary and conclusions

In this study, we explored the possibility to quantify aerosol mass flux in the cloud-topped PBL by means of lidar remote sensing. The technique was first introduced by [152] using combined aerosol backscatter coefficient and vertical wind measurements in the dry convective PBL. We tried to extend the methodology to the cloud-topped PBL when there is high RH gradient. In the studied case, we found an RH gradient of approximately 25% per km.

The turbulent aerosol flux has been measured from the eddy correlation technique by calculating the co-spectra of vertical wind component and aerosol backscatter coefficient. The dominant upward vertical transport appeared for eddy lengths in the range 450-1500 m, comparable to the PBL depth.

In atmospheric conditions with high RH, the aerosol backscatter coefficient is not an absolute measure of aerosol mass. The reason is that aerosol backscatter is enhanced by the increased water vapor content. The backscattering enhancement function has been determined from β profile and the Hänel parametrization for γ=0.85. Then, aerosol backscatter coefficient was corrected from RH effects according to the retrieved backscattering enhancement function. Making use of the LIRIC algorithm for the retrieval of volume concentration, the conversion from aerosol backscatter to aerosol mass concentration has been achieved. Finally, the derived values of aerosol mass flux were in the range of 0.5-2.4 $\mu g\ m^{-2} s^{-1}$ in the altitudes 800-1300 m. Similar values were found by [152] for the dry convective PBL.

Chapter 8

Conclusions and Perspectives

The aim of this Ph.D. Thesis was to study the impact of aerosols on cloud properties under the effect of turbulence in the PBL. The major findings related to the cloud development in the vicinity of the PBL stemmed from the dataset of the HygrA-CD field campaign, which took place over Athens.

Cloud development above the PBL was observed for the days of a deep PBL (∼2-2.5 km). In Athens, this happens often during the Etesians, when moderate to strong winds from N-NW directions are blowing over the Athens basin. During the Etesians, the air masses arriving over the GAA generally come from the city of Istanbul (Turkey) and the industrial zones around the Black Sea, so they carry various pollutants aloft. Although, high concentrations of anthropogenic fine-mode aerosols enrich the PBL, and this may lead to low CCN numbers, under conditions of a deep PBL. A possible explanation is that aerosols compete for the same supersaturation and, finally, aerosols rich in inorganic species are activated because they are more hygroscopic.

As a future step, we propose to further study and characterize these long-range transported aerosols with respect to their hygroscopicity. Then, a correlation study between the growth rate in aerosol diameter and the enhancement in aerosol backscatter coefficient would provide a large number of tests cases for validation of the aerosol mass flux technique.

For the days characterized by a shallow PBL (<1-1.5 km under S-SW wind flow), supersaturation was prohibited at any height within the PBL. All cases in which the air flow was from S-SW directions were characterized as dry and the LCL appeared at a height level well above the PBL top. Investigating the water vapor content in the lower part of the atmosphere would provide a measure of how dry the atmosphere becomes when the dominant aerosol is mineral dust originating from the Saharan desert. Provided that dust particles are large in diameter, they should become CCN active at low supersaturation levels. Therefore, the study of atmosphere's water vapor content (e.g. from the vertical profiles of water vapor mixing ratio and RH) in conjunction to PBL dynamics would provide valuable information on how often supersaturation is not achieved and under which conditions.

The PBL depth seems to be inversely proportional to the wind speed when the observed air flow was from SW-W-NW directions. In days with moderate wind speed, the PBL top exceeds 2 km, whereas in cases with strong prevailing winds of SW-W-NW directions, the PBL height would be higher than 1.2 km. The effect of turbulence on PBL depth should be explored more for these cases. The complex topography of Athens might play a critical role on cloud formation when air masses arrive from these directions. Finally, any link between sea breeze and PBL turbulence in GAA should be further investigated for this cluster.

As a general conclusion, HygrA-CD highlighted the importance of the time-collocated measurements of aerosol and BL dynamics in understanding the formation of clouds in the vicinity of the PBL. Cloud droplet number is primarily determined by the updraft velocity, secondly by aerosol number concentration and finally by the aerosol's chemical composition. In future, similar campaigns would enable us to study aerosol-cloud interactions leading to cloud and rain formation, as some scientific issues still remain open including: optical and microphysical properties of mixed-phase and ice clouds; cloud life cycle (formation/development and dissipation); direct and indirect radiative effects of aerosols and clouds.

Aiming to retrieve the number of activated aerosols and cloud droplets in the detected by the lidar aerosol layers, a new methodology within this Ph.D. Thesis was developed for the estimation of the CCN spectra. This methodology combining data from a multi-wavelength Raman lidar and a Doppler lidar to retrieve the cloud droplet number aloft, was applied to four test cases from the HygrA-CD dataset. The activated particles were found to range between 330-770 cm^{-3}, while the obtained cloud droplet number varied in the range of 270-650 cm^{-3}. Since the inversion of the lidar optical data produce non-unique solutions for the aerosol number concentration, the retrieved CCN spectra had an associated uncertainty which was not exclusively related to the measurement uncertainty. In particular, we observed that the retrieved CCN spectra had high uncertainties (up to $\sim$30%) for supersaturations lower than 0.1%. The retrieved cloud droplet number was not significantly affected by the uncertainty in the CCN spectrum, but it appeared more sensitive to the uncertainty of the measured vertical wind component. The application of this newly developed approach to the HygrA-CD test cases is very encouraging and gives the potential to extend our knowledge of aerosol to cloud droplet population by means of synergistic lidar remote sensing.

As an attempt to quantify aerosol vertical transport in the PBL, the eddy correlation technique was applied to collocated data from an elastic aerosol lidar and a Doppler lidar. This technique had been applied to the dry atmosphere where there was absence of hygroscopic growth during vertical transport. The challenge of extending this methodology to conditions with high RH in the cloud-topped PBL originates from the non-linear relation between aerosol backscatter coefficient to aerosol mass concentration. The main reason is that the aerosol backscatter coefficient is enhanced significantly under high RH conditions and this enhancement is not related to aerosol mass fluctuation. We achieved to correct the aerosol backscatter coefficient by the effect of RH by constructing the corresponding backscattering enhancement function. Afterwards, by making use of the LIRIC algorithm, we retrieved the vertical profiles of volume concentration and converted the aerosol backscatter coefficient to aerosol mass concentration through typical aerosol mass densities. The results obtained seemed reasonable with a mean mass flux of 1 $\mu g\ m^{-2} s^{-1}$ which refer to an entrainment rate of 100 $m\ h^{-1}$.

As a future goal, the estimation of the vertical aerosol flux should be applied to more cases and the vertical profiles should be compared to models. Such a comparison would demonstrate whether our proposed approach is successful. Moreover, a closure study between simultaneous aerosol measurements at ground level and aloft within the upper active PBL is considered necessary to validate our proposed methodology.

Publication List

Journal Papers

1. Binietoglou, I., S. Basart, L. Alados-Arboledas, V. Amiridis, **A. Argyrouli**, H. Baars, J.M. Baldasano, D. Balis, L. Belegante, J.A. Bravo-Aranda, P. Burlizzi, V. Carrasco, A. Chaikovsky, A. Comerón, G. D'Amico, M. Filioglou, M.J. Granados-Muñoz, J.L. Guerrero-Rascado, L. Ilic, P. Kokkalis, A. Maurizi, L. Mona, F. Monti, C. Muñoz-Porcar, D. Nicolae, A. Papayannis, G. Pappalardo, G. Pejanovic, S.N. Pereira, M.R. Perrone, A. Pietruczuk, M. Posyniak, F. Rocadenbosch, A. Rodríguez-Gómez, M. Sicard, N. Siomos, A. Szkop, E. Terradellas, A. Tsekeri, A. Vukovic, U. Wandinger, and J. Wagner, A methodology for investigating dust model performance using synergistic EARLINET/AERONET dust concentration retrievals, *Atmos. Meas. Tech. 8(9)*, 3577-3600, 2015

2. Papayannis A., **A. Argyrouli**, A. Bougiatioti, E. Remoundaki, S. Vratolis, A. Nenes, J. Hey, M. Komppula, S. Solomos, S. Kazadzis, R. Banks, L. Labzovsky, J. Kalogiros, K. Eleftheriadis, I. Mantas, C. Tzanis, I. Binietoglou, E. Giannakaki, E. Diapouli and C. S. Zerefos, From hygroscopic aerosols to cloud droplets: the HygrA-CD Campaign in the Athens basin - An overview, *Science Total Environ.*, (in press, 2016)

3. **A. Argyrouli**, A. Bougiatioti, D. Müller, S. Bezantakos, A. Papayannis and A. Nenes, Cloud Condensation Nuclei spectra from a multi-wavelength Raman lidar and impacts on droplet number, *Atmos. Chem. Phys.*, (in preparation, 2016)

4. **A. Argyrouli**, S. Solomos, M. Komppula, A. Papayannis, I. Binietoglou, A. Chaikovsky et al., Upward aerosol flux within the cloud-topped Planetary Boundary Layer with the use of ground-based remote sensing, *Atmos. Meas. Techn.*, (in preparation, 2016)

5. Bougiatioti, A., **A. Argyrouli**, S. Solomos, S. Vratolis, K. Eleftheriadis, A. Papayannis and A. Nenes, CCN activity, variability and influence on droplet formation during the HygrA-CD campaign in Athens, *Atmos. Meas. Techn.*, (in preparation, 2016)

6. Kalogiros, J., **A. Argyrouli**, A. Papayannis and L. Labzovskii, Low level cloud observations using radar, lidar and microwave radiometer data during HygrA-CD experimental campaign, *Atmos. Res.*, (in preparation, 2016)

7. Papayannis, A., E. Giannakaki, D. Mueller, **A. Argyrouli**, S. Solomos, A. Nenes, P. Kokkalis, E. Remoundaki, S. Vratolis, K. Eleftheriadis, G. Tsaknakis, S. Kazadzis, P. Raptis, S. Basart, M. Komppula, I. Binietoglou, F. Rocadenbosch, M. Mylonaki, D. Alexiou, Vertical profiles of aerosol optical-microphysical, mass and chemical properties in the frame of the HygA-CD: a rare case of long-range transport of mixed biomass burning-polluted dust aerosols from the Russian Federation-Kazakhstan to Athens, Greece, *Atmos. Environ.*, (in preparation, 2016a)

8. Papayannis, A., **A. Argyrouli**, E. Remoundaki, S. Vratolis, S. Nenes, J. VandeHey, M. Komppula, S. Solomos, S. Kazadzis, R.F. Banks, L. Labzovsky, J. Kalogiros, K. Eleftheriadis, E. Mantas, C. Tzanis, I. Binietoglou, E. Giannakaki, Aerosol-cloud interactions over Athens, Greece: Case studies analysis during the HygrA-CD Campaign under typical meteorological conditions, *Science Total Environ.*, (in preparation, 2016b)

9. Fetfatzis, P., **A. Argyrouli**, J. Vande Hey, M. Komppula, S. Vratolis, A. Papayannis and K. Eleftheriadis, Conditions for closure between in situ optical-microphysical measurements and remote sensing techniques during the HygrA-CD campaign at DEM station, Athens, Greece, (in preparation, 2016)

10. Vratolis, S., P. Fetfatzis, K. Eleftheriadis, **A. Argyrouli**, A. Papayannis, Equivalent refractive index of the urban background aerosol in Athens, Greece, (in preparation, 2016)

Conference papers with proceedings

1. Papayannis, A., **A. Argyrouli**, P. Kokkalis, G. Tsaknakis, I. Binietoglou, S. Solomos, S. Kazadzis, S. Samaras, C. Böckmann, P. Raptis, and V. Amiridis, Vertical profiles of aerosol optical and microphysical properties during a rare case of long-range transport of mixed biomass burning-polluted dust aerosols from the Russian federation-Kazakhstan to Athens, Greece, *Proc.* 27*th* *International Laser Radar Conference*, 05-10/07/2015, New York, USA

2. Papayannis, A., **A. Argyrouli**, D. Müller, G. Tsaknakis, P. Kokkalis, I. Binietoglou, S. Kazadzis, S. Solomos and V. Amiridis, Tropospheric Vertical Profiles of aerosol optical, microphysical and concentration properties in the frame of the HygrA-CD campaign (Athens, Greece 2014): A case study of long-range transport of mixed aerosols, *Proc.* 27*th* *International Laser Radar Conference*, 05-10/07/2015, New York, USA

3. Bougiatioti A., A. Papayannis, S. Vratolis, **A. Argyrouli**, N. Mihalopoulos, M. Tsagkaraki, A. Nenes, and K. Eleftheriadis, Aerosol activity and hygroscopicity combined with lidar data in the urban atmosphere of Athens, Greece in the frame of the HygrA-CD campaign, *Proc.* 27*th* *International Laser Radar Conference*, 05-10/07/2015, New York, USA

4. **A. Argyrouli**, A. Papayannis, I. Binietoglou, P. Kokkalis, P. Fetfatzis, A. Bougiatioti, V. Amiridis, D. Müller and A. Nenes, Aerosol properties within the convective cloud-topped Planetary Boundary Layer above the megacity of Athens, Greece, *Proc.* 21*st* *European Aerosol Conference*, 06-11/09/2015, Milan, Italy

5. Fetfatzis P., **A. Argyrouli**, J. Vande Hey, M. Komppula, S. Vratolis, A. Papayannis and K. Eleftheriadis, Conditions for closure between in situ optical-microphysical measurements and remote sensing techniques during the HygrA-CD campaign at DEM station, Athens, *Proc.* 21*st* *European Aerosol Conference*, 06-11/09/2015, Milan, Italy

6. Vratolis S., P. Fetfatzis, A. Papayannis, **A. Argyrouli**, K. Eleftheriadis, Equivalent aerosol refractive index at an urban background station in Athens, *Proc.* 22*nd* *European Aerosol Conference*, 04-09/09/2016, Tours, France

7. Papayannis A., **A. Argyrouli**, A. Bougiatioti, A. Nenes, J. Van de Hey, M. Komppula, P. Kokkalis, S. Solomos, R. Banks, L. Labzovsky, J. Kalogiros, E. Giannakaki, From hygrospcopic aerosols to cloud droplets: the HygrA-CD Campaign in the Athens basin-An overview, *Proc.* 13*th* *International Conference on Meteorology, Climatology and Atmospheric Physics (COMECAP) 2016*, 19-21/9/2016, Thessaloniki, Greece

Conference and Seminars

1. **A. Argyrouli**, Study of cloud development above the Planetary Boundary Layer over Athens, Greece, 1st *ITaRS Summer School*, 23/9-04/10/2013, Bucharest, Romania

2. **A. Argyrouli**, and A. Papayannis, Sensitivity analysis for aerosol concentration profile retrieved from NTUA lidar data & future perspectives, *ITaRS Mid-term Review Meeting*, 19-21/02/2014, Potsdam, Germany

3. **A. Argyrouli**, A. Papayannis, S. Solomos, I. Christodoulakis, and C. Tzanis, Towards quantification of aerosol vertical fluxes in the cloud-topped PBL over Athens, Greece during the HygrA-CD, 2nd *ITaRS Summer School*, 08-17/09/2014, Julich, Germany

4. **A. Argyrouli**, M. Komppula, K. Bougiatioti, S. Solomos, A. Papayannis, P. Kokkalis, and G. Tsaknakis, Aerosol fluxes in the cloudy PBL from synergetic measurements of an aerosol lidar and a Doppler lidar, *ACTRIS-EARLINET Meeting*, 28-31/10/2014, Lille, France

5. Papayannis A., P. Kokkalis, **A. Argyrouli**, G. Tsaknakis, S. Solomos, L. Ilic, S. Nickovic, S. Kazantzis, E. Remoundaki, and V. Amiridis, Vertical profiles of aerosol optical and mass properties in the frame of the HygrA-CD campaign: A case study, *ACTRIS-EARLINET Meeting*, 28-31/10/2014, Lille, France

6. **A. Argyrouli**, Cloud-topped PBL, Meteorological Technology World Expo 2015, *ITaRS Special Session*, 13/10/2015, Brussels, Belgium

7. Tsakiri M., **A. Argyrouli**, A. Papayannis, G. Tsaknakis, Evaluation of tropospheric error in Global Navigation Satellite Systems (GNSS) measurements with the use of Water Vapor Raman lidar, 6th *National Conference of Metrology 2016*, 14/05/2016, Athens, Greece

8. **A. Argyrouli**, A. Nenes, K. Bougiatioti, S.Bezantakos and A. Papayannis, Cloud Condensation Nuclei (CCN) spectra estimation from a multi-wavelength Raman lidar durring HygrA-CD Campaign, Hellenic Association for Aerosol Research (HAAR), *Annual Meeting 2016*, Navarino Environmental Observatory, 16/05/2016, Pylos, Greece

9. **A. Argyrouli**, Instrumentation synergies for Planetary Boundary Layer studies, *Environmental Monitoring Day Seminar*, 31/05/2016, Athens, Greece

Bibliography

[1] A. Papayannis, D. Balis, P. Kokkalis, R. Mamouri, G. Tsaknakis, E. Giannakaki, N. Siomos, and V. Amiridis, “ARIADNE: the Greek lidar network,” in *Proceedings, 26th International Laser Radar Conference, Porto Heli, Greece*, pp. 25–29, 2012.

[2] P. Kokkalis, A. Papayannis, R. Mamouri, G. Tsaknakis, and V. Amiridis, “The EOLE lidar system of the National Technical University of Athens,” in *Reviewed and revised papers presented at the 26th International Laser Radar Conference*, pp. 25–29, 2012.

[3] A. Smirnov, B. Holben, T. Eck, O. Dubovik, and I. Slutsker, “Cloud-screening and quality control algorithms for the AERONET database,” *Remote Sensing of Environment*, vol. 73, no. 3, pp. 337–349, 2000.

[4] G. Pearson, F. Davies, and C. Collier, “An analysis of the performance of the UFAM pulsed Doppler lidar for observing the boundary layer,” *Journal of Atmospheric and Oceanic Technology*, vol. 26, no. 2, pp. 240–250, 2009.

[5] S. Crewell, H. Czekala, U. Löhnert, C. Simmer, T. Rose, R. Zimmermann, and R. Zimmermann, “Microwave Radiometer for Cloud Carthography: A 22-channel ground-based microwave radiometer for atmospheric research,” *Radio Science*, vol. 36, no. 4, pp. 621–638, 2001.

[6] U. Löhnert and S. Crewell, “Accuracy of cloud liquid water path from ground-based microwave radiometry 1. Dependency on cloud model statistics,” *Radio Science*, vol. 38, no. 3, 2003.

[7] J. C. Liljegren, S. Boukabara, K. Cady-Pereira, and S. A. Clough, “The effect of the half-width of the 22-GHz water vapor line on retrievals of temperature and water vapor profiles with a 12-channel microwave radiometer,” *IEEE Transactions on Geoscience and Remote Sensing*, vol. 43, no. 5, pp. 1102–1108, 2005.

[8] J. D. Vande Hey, *A Novel Lidar Ceilometer*. Springer International Publishing, 2015.

[9] J. Wurman, J. Straka, E. Rasmussen, M. Randall, and A. Zahrai, “Design and deployment of a portable, pencil-beam, pulsed, 3-cm Doppler radar,” *Journal of Atmospheric and Oceanic Technology*, vol. 14, no. 6, pp. 1502–1512, 1997.

[10] J. Kalogiros, M. N. Anagnostou, E. N. Anagnostou, M. Montopoli, E. Picciotti, and F. S. Marzano, “Optimum estimation of rain microphysical parameters from X-band dual-polarization radar observables,” *IEEE Transactions on Geoscience and Remote Sensing*, vol. 51, no. 5, pp. 3063–3076, 2013.

[11] J. Nash, T. Oakley, H. Vömel, and W. LI, “WMO Intercomparison of high Quality Radiosonde Systems Yangjiang, China, 12 July–3 August 2010; WMO report reference number IOM 107 (TD 1580),” 2010.

[12] M. Heim, B. J. Mullins, H. Umhauer, and G. Kasper, “Performance evaluation of three optical particle counters with an efficient “multimodal” calibration method,” *Journal of Aerosol Science*, vol. 39, no. 12, pp. 1019–1031, 2008.

[13] A. Wiedensohler, W. Birmili, A. Nowak, A. Sonntag, K. Weinhold, M. Merkel, B. Wehner, T. Tuch, S. Pfeifer, M. Fiebig, *et al.*, “Mobility particle size spectrometers: harmonization of technical standards and data structure to facilitate high quality long-term observations of atmospheric particle number size distributions,” *Atmospheric Measurement Techniques*, vol. 5, pp. 657–685, 2012.

[14] A. Bougiatioti, C. Fountoukis, N. Kalivitis, S. N. Pandis, A. Nenes, and N. Mihalopoulos, “Cloud condensation nuclei measurements in the marine boundary layer of the Eastern Mediterranean: CCN closure and droplet growth kinetics,” *Atmospheric Chemistry and Physics*, vol. 9, p. 7053, 2009.

[15] P. Fetfatzis, A. Argyrouli, J. Vande Hey, M. Komppula, S. Vratolis, A. Papayannis, and K. Eleftheriadis, “Conditions for closure between in situ optical-microphysical measurements and remote sensing techniques during the HygrA-CD campaign at DEM station, Athens, Greece,” in *European Aerosol Conference, 6-11 September 2015, Milan, Italy.*

[16] K. Eleftheriadis, S. Vratolis, and S. Nyeki, “Aerosol black carbon in the European Arctic: Measurements at Zeppelin station, Ny-Ålesund, Svalbard from 1998–2007,” *Geophysical Research Letters*, vol. 36, no. 2, 2009.

[17] V. Amiridis, C. Zerefos, S. Kazadzis, E. Gerasopoulos, K. Eleftheratos, M. Vrekoussis, A. Stohl, R. E. Mamouri, P. Kokkalis, A. Papayannis, *et al.*, “Impact of the 2009 Attica wild fires on the air quality in urban Athens,” *Atmospheric environment*, vol. 46, pp. 536–544, 2012.

[18] E. Diapouli, O. Popovicheva, M. Kistler, S. Vratolis, N. Persiantseva, M. Timofeev, A. Kasper-Giebl, and K. Eleftheriadis, “Physicochemical characterization of aged biomass burning aerosol after long-range transport to Greece from large scale wildfires in Russia and surrounding regions, Summer 2010,” *Atmospheric Environment*, vol. 96, pp. 393–404, 2014.

[19] E. Remoundaki, P. Kassomenos, E. Mantas, N. Mihalopoulos, and M. Tsezos, “Composition and mass closure of PM2. 5 in urban environment (Athens, Greece),” *Aerosol Air Qual. Res*, vol. 13, pp. 72–82, 2013.

[20] R. B. Stull, *An Introduction to Boundary Layer Meteorology.* Kluwer Academic Publishers, 1st ed., 1988.

[21] G. R. Garratt, *The atmospheric boundary layer.* Cambridge University Press, 1st ed., 1992.

[22] Y. Noh, W. Cheon, S. Hong, and S. Raasch, “Improvement of the K-profile model for the planetary boundary layer based on large eddy simulation data,” *Boundary-layer meteorology*, vol. 107, no. 2, pp. 401–427, 2003.

[23] J. W. Deardorff, “Numerical investigation of neutral and unstable planetary boundary layers,” *Journal of the Atmospheric Sciences*, vol. 29, no. 1, pp. 91–115, 1972.

[24] G. K. Batchelor, *The theory of homogeneous turbulence.* Cambridge University Press, 1953.

[25] R. B. Stull, *Meteorology for Scientists and Engineers.* Gary Garlson, 2nd ed., 2000.

[26] J. R. Holton and G. J. Hakim, *An introduction to dynamic meteorology*, vol. 88. Academic press, 2012.

[27] G. I. Taylor, "Statistical theory of turbulence," in *Proceedings of the Royal Society of London: A Mathematical, Physical and Engineering Sciences*, vol. 151, pp. 421–444, The Royal Society, 1935.

[28] E. J. O'Connor, A. J. Illingworth, I. M. Brooks, C. D. Westbrook, R. J. Hogan, F. Davies, and B. J. Brooks, "A method for estimating the turbulent kinetic energy dissipation rate from a vertically pointing Doppler lidar, and independent evaluation from balloon-borne in situ measurements," *Journal of atmospheric and oceanic technology*, vol. 27, no. 10, pp. 1652–1664, 2010.

[29] C. Senff, J. Bösenberg, G. Peters, and T. Schaberl, "Remote sensing of turbulent ozone fluxes and the ozone budget in the convective boundary layer with DIAL and radar-RASS: a case study," *Contributions to atmospheric physics*, vol. 69, no. 1, pp. 161–176, 1996.

[30] L. Menut, C. Flamant, J. Pelon, and P. H. Flamant, "Urban boundary-layer height determination from lidar measurements over the Paris area," *Applied Optics*, vol. 38, no. 6, pp. 945–954, 1999.

[31] I. M. Brooks, "Finding boundary layer top: Application of a wavelet covariance transform to lidar backscatter profiles," *Journal of Atmospheric and Oceanic Technology*, vol. 20, no. 8, pp. 1092–1105, 2003.

[32] R. G. Brown and P. Y. Hwang, "Introduction to random signals and applied Kalman filtering: with MATLAB exercises and solutions," *Introduction to random signals and applied Kalman filtering: with MATLAB exercises and solutions, by Brown, Robert Grover.; Hwang, Patrick YC New York: Wiley, c1997.*, vol. 1, 1997.

[33] R. F. Banks, J. Tiana-Alsina, J. M. Baldasano, F. Rocadenbosch, A. Papayannis, S. Solomos, and C. G. Tzanis, "Sensitivity of boundary-layer variables to PBL schemes in the WRF model based on surface meteorological observations, lidar, and radiosondes during the HygrA-CD campaign," *Atmospheric Research*, vol. 176, pp. 185–201, 2016.

[34] A. Holtslag and B. Boville, "Local versus nonlocal boundary-layer diffusion in a global climate model," *Journal of Climate*, vol. 6, no. 10, pp. 1825–1842, 1993.

[35] A. Jeričević and B. Grisogono, "The critical bulk Richardson number in urban areas: verification and application in a numerical weather prediction model," *Tellus A*, vol. 58, no. 1, pp. 19–27, 2006.

[36] H. Richardson, S. Basu, and A. Holtslag, "Improving stable boundary-layer height estimation using a stability-dependent critical bulk Richardson number," *Boundary-layer meteorology*, vol. 148, no. 1, pp. 93–109, 2013.

[37] S. R. Hanna, "The thickness of the planetary boundary layer," *Atmospheric Environment*, vol. 3, no. 5, pp. 519–536, 1969.

[38] J. A. Zhang, R. F. Rogers, D. S. Nolan, and F. D. Marks Jr, "On the characteristic height scales of the hurricane boundary layer," *Monthly Weather Review*, vol. 139, no. 8, pp. 2523–2535, 2011.

[39] Y. Zhang, Z. Gao, D. Li, Y. Li, N. Zhang, X. Zhao, and J. Chen, "On the computation of planetary boundary-layer height using the bulk Richardson number method," *Geoscientific Model Development*, vol. 7, no. 6, pp. 2599–2611, 2014.

[40] J. H. Seinfeld, C. Bretherton, K. S. Carslaw, H. Coe, P. J. DeMott, E. J. Dunlea, G. Feingold, S. Ghan, A. B. Guenther, R. Kahn, *et al.*, "Improving our fundamental understanding of the role of aerosol- cloud interactions in the climate system," *Proceedings of the National Academy of Sciences*, vol. 113, no. 21, pp. 5781–5790, 2016.

[41] G. Feingold, W. L. Eberhard, D. E. Veron, and M. Previdi, "First measurements of the Twomey indirect effect using ground-based remote sensors," *Geophysical Research Letters*, vol. 30, no. 6, 2003.

[42] J. Schmidt, A. Ansmann, J. Bühl, H. Baars, U. Wandinger, D. Müller, and A. V. Malinka, "Dual-FOV Raman and Doppler lidar studies of aerosol-cloud interactions: Simultaneous profiling of aerosols, warm-cloud properties, and vertical wind," *Journal of Geophysical Research: Atmospheres*, vol. 119, no. 9, pp. 5512–5527, 2014.

[43] K. Sarna and H. W. J. Russchenberg, "Ground-based remote sensing scheme for monitoring aerosol–cloud interactions," *Atmospheric Measurement Techniques*, vol. 9, no. 3, pp. 1039–1050, 2016.

[44] M. Pahlow, G. Feingold, A. Jefferson, E. Andrews, J. Ogren, J. Wang, Y. Lee, R. Ferrare, and D. Turner, "Comparison between lidar and nephelometer measurements of aerosol hygroscopicity at the Southern Great Plains Atmospheric Radiation Measurement site," *Journal of Geophysical Research: Atmospheres*, vol. 111, no. D5, 2006.

[45] M. O. Andreae, "Correlation between cloud condensation nuclei concentration and aerosol optical thickness in remote and polluted regions," *Atmospheric Chemistry and Physics*, vol. 9, no. 2, pp. 543–556, 2009.

[46] V. Kapustin, A. Clarke, Y. Shinozuka, S. Howell, V. Brekhovskikh, T. Nakajima, and A. Higurashi, "On the determination of a cloud condensation nuclei from satellite: Challenges and possibilities," *Journal of Geophysical Research: Atmospheres*, vol. 111, no. D4, 2006.

[47] I. Koren, L. Oreopoulos, G. Feingold, L. Remer, and O. Altaratz, "How small is a small cloud?," *Atmospheric Chemistry and Physics*, vol. 8, no. 14, pp. 3855–3864, 2008.

[48] Y. Zhu, D. Rosenfeld, X. Yu, and Z. Li, "Separating aerosol microphysical effects and satellite measurement artifacts of the relationships between warm rain onset height and aerosol optical depth," *Journal of Geophysical Research: Atmospheres*, vol. 120, no. 15, pp. 7726–7736, 2015.

[49] I. Lagzi, R. Mészáros, G. Gelybó, and A. Leelőssy, *Atmospheric Chemistry.* Eötvös Loránd University, 2013.

[50] P. Stier, J. Feichter, S. Kinne, S. Kloster, E. Vignati, J. Wilson, L. Ganzeveld, I. Tegen, M. Werner, Y. Balkanski, *et al.*, "The aerosol-climate model ECHAM5-HAM," *Atmospheric Chemistry and Physics*, vol. 5, no. 4, pp. 1125–1156, 2005.

[51] F. Dentener, S. Kinne, T. Bond, O. Boucher, J. Cofala, S. Generoso, P. Ginoux, S. Gong, J. Hoelzemann, A. Ito, *et al.*, "Emissions of primary aerosol and precursor gases in the years 2000 and 1750 prescribed data-sets for AeroCom," *Atmospheric Chemistry and Physics*, vol. 6, no. 12, pp. 4321–4344, 2006.

[52] G. Myhre, C. Myhre, B. Samset, and T. Storelvmo, "Aerosols and their relation to global climate and climate sensitivity," *Nature Education Knowledge*, vol. 4, no. 7, 2013.

[53] L. A. Remer, R. G. Kleidman, R. C. Levy, Y. J. Kaufman, D. Tanré, S. Mattoo, J. V. Martins, C. Ichoku, I. Koren, H. Yu, *et al.*, "Global aerosol climatology from the MODIS satellite sensors," *Journal of Geophysical Research: Atmospheres*, vol. 113, no. D14, 2008.

[54] G. Myhre, T. Berglen, M. Johnsrud, C. Hoyle, T. Berntsen, S. Christopher, D. Fahey, I. S. Isaksen, T. Jones, R. Kahn, *et al.*, "Modelled radiative forcing of the direct aerosol effect with multi-observation evaluation," *Atmos. Chem. Phys*, vol. 9, no. 4, pp. 1365–1392, 2009.

[55] D. Jacob, *Introduction to atmospheric chemistry.* Princeton University Press, 1999.

[56] P. Warneck, *Chemistry of the natural atmosphere*, vol. 71. Academic Press, 1999.

[57] J. Wallace and P. Hobbs, *Atmospheric Science: An Introductory Survey.* Elsevier Academic Press, Amsterdam, 2nd ed., 2006.

[58] M. L. Salby, *Fundamentals of atmospheric physics*, vol. 61. Academic Press, 1996.

[59] H. R. Pruppacher and J. D. Klett, "Microstructure of atmospheric clouds and precipitation," in *Microphysics of Clouds and Precipitation*, pp. 9–55, Springer, 1978.

[60] J. C. Moreno-Piraján, *Thermodynamics: Interaction Studies-Solids, Liquids and Gases.* InTech, 2011.

[61] P. Wang, *Physics and dynamics of clouds and precipitation.* Cambridge University Press, 2013.

[62] R. McIlveen, *Fundamentals of weather and climate.* Psychology Press, 1991.

[63] H. Köhler, "The nucleus in and the growth of hygroscopic droplets," *Transactions of the Faraday Society*, vol. 32, pp. 1152–1161, 1936.

[64] G. McFiggans, P. Artaxo, U. Baltensperger, H. Coe, M. C. Facchini, G. Feingold, S. Fuzzi, M. Gysel, A. Laaksonen, U. Lohmann, *et al.*, "The effect of physical and chemical aerosol properties on warm cloud droplet activation," *Atmospheric Chemistry and Physics*, vol. 6, no. 9, pp. 2593–2649, 2006.

[65] M. K. Yau and R. Rogers, *A short course in cloud physics.* Elsevier, 1996.

[66] N. Kapany, "Fiber optics. Principles and applications," *New York: Academic Press, 1967*, 1967.

[67] G. Simeonov, V.and Larcheveque, P. Quaglia, H. Van Den Bergh, and B. Calpini, "Influence of the photomultiplier tube spatial uniformity on lidar signals," *Applied optics*, vol. 38, no. 24, pp. 5186–5190, 1999.

[68] V. Freudenthaler, "Effects of spatially inhomogeneous photomultiplier sensitivity on lidar signals and remedies," in *22nd Internation Laser Radar Conference (ILRC 2004)*, vol. 561, p. 37, 2004.

[69] B. Liu and Z. Wang, "Improved calibration method for depolarization lidar measurement," *Optics Express*, vol. 21, no. 12, pp. 14583–14590, 2013.

[70] A. Behrendt and T. Nakamura, “Calculation of the calibration constant of polarization lidar and its dependency on atmospheric temperature,” *Optics Express*, vol. 10, no. 16, pp. 805–817, 2002.

[71] V. Freudenthaler, M. Esselborn, M. Wiegner, B. Heese, M. Tesche, A. Ansmann, D. Müller, D. Althausen, M. Wirth, A. Fix, *et al.*, “Depolarization ratio profiling at several wavelengths in pure Saharan dust during SAMUM 2006,” *Tellus B*, vol. 61, no. 1, pp. 165–179, 2009.

[72] F. G. Fernald, “Analysis of atmospheric lidar observations,” *Applied Optics*, vol. 23, no. 5, pp. 652–653, 1984.

[73] J. D. Klett, “Stable analytical inversion solution for processing lidar returns,” *Applied Optics*, vol. 20, no. 2, pp. 211–220, 1981.

[74] C. Weitkamp, *Lidar Range-Resolved Optical Remote Sensing of the Atmosphere*. Springer, 2005.

[75] A. Ansmann, M. Riebesell, and C. Weitkamp, “Measurement of atmospheric aerosol extinction profiles with a Raman lidar,” *Optics Letters*, vol. 15, no. 13, pp. 746–748, 1990.

[76] C. V. Raman and K. S. Krishnan, “A new type of secondary radiation,” *Nature*, vol. 121, pp. 501–502, 1928.

[77] U. Wandinger, “Raman lidar,” in *Lidar*, pp. 241–271, Springer, 2005.

[78] D. A. Long, “Raman spectroscopy,” *New York*, pp. 1–12, 1977.

[79] G. Avila, J. Fernandez, B. Maté, G. Tejeda, and S. Montero, “Ro-vibrational Raman cross sections of water vapor in the OH stretching region,” *Journal of molecular spectroscopy*, vol. 196, no. 1, pp. 77–92, 1999.

[80] G. D’Amico, A. Amodeo, I. Mattis, V. Freudenthaler, and G. Pappalardo, “Earlinet single calculus chain – technical – part 1: Pre-processing of raw lidar data,” *Atmospheric Measurement Techniques*, vol. 9, no. 2, pp. 491–507, 2016.

[81] V. A. Kovalev and W. E. Eichinger, *Elastic lidar: theory, practice, and analysis methods*. John Wiley & Sons, 2004.

[82] U. Wandinger and A. Ansmann, “Experimental determination of the lidar overlap profile with Raman lidar,” *Applied Optics*, vol. 41, no. 3, pp. 511–514, 2002.

[83] C. F. Bohren and D. R. Huffman, *Absorption and scattering of light by small particles*. John Wiley & Sons, 1983.

[84] J. J. David, *Classical electrodynamics*. Wiley Eastern Limited, 1975.

[85] G. Mie, “Beiträge zur Optik trüber Medien, speziell kolloidaler Metallösungen,” *Annalen der physik*, vol. 330, no. 3, pp. 377–445, 1908.

[86] A. Ishimaru, *Wave propagation and scattering in random media*, vol. 2. Academic press New York, 1978.

[87] H. C. Hulst and H. C. van de Hulst, *Light scattering by small particles*. Courier Corporation, 1957.

[88] M. I. Mishchenko, L. D. Travis, and A. A. Lacis, *Multiple scattering of light by particles: radiative transfer and coherent backscattering.* Cambridge University Press, 2006.

[89] J. Lenoble, L. Remer, and D. Tanré, *Aerosol remote sensing.* Springer Science & Business Media, 2013.

[90] D. Müller, U. Wandinger, and A. Ansmann, "Microphysical particle parameters from extinction and backscatter lidar data by inversion with regularization: theory," *Applied Optics*, vol. 38, no. 12, pp. 2346–2357, 1999.

[91] I. Veselovskii, A. Kolgotin, V. Griaznov, D. Müller, U. Wandinger, and D. N. Whiteman, "Inversion with regularization for the retrieval of tropospheric aerosol parameters from multiwavelength lidar sounding," *Applied Optics*, vol. 41, no. 18, pp. 3685–3699, 2002.

[92] S. Twomey, "Introduction to the Mathematics of Inversion in Remote Sensing and Indirect Measurements Elsevier," *New York*, vol. 19772, 1977.

[93] A. N. Tikhonov, A. Goncharsky, V. Stepanov, and A. G. Yagola, *Numerical methods for the solution of ill-posed problems*, vol. 328. Springer Science & Business Media, 2013.

[94] G. H. Golub, M. Heath, and G. Wahba, "Generalized cross-validation as a method for choosing a good ridge parameter," *Technometrics*, vol. 21, no. 2, pp. 215–223, 1979.

[95] F. O'Sullivan, "A statistical perspective on ill-posed inverse problems," *Statistical science*, pp. 502–518, 1986.

[96] J. Idier, *Bayesian approach to inverse problems.* John Wiley & Sons, 2013.

[97] V. Turchin, V. Kozlov, and M. Malkevich, "The use of mathematical-statistics methods in the solution of incorrectly posed problems," *Physics-Uspekhi*, vol. 13, no. 6, pp. 681–703, 1971.

[98] A. N. Tikhonov and V. Y. Arsenin, *Solutions of ill-posed problems.* Vh Winston, 1977.

[99] A. Tarantola, *Inverse problem theory: Methods for data fitting and parameter estimation.* Elsevier, Amsterdam, 1987.

[100] C. D. Rodgers, *Inverse methods for atmospheric sounding: theory and practice*, vol. 2. World scientific, 2000.

[101] B. N. Holben, T. Eck, I. Slutsker, D. Tanre, J. Buis, A. Setzer, E. Vermote, J. A. Reagan, Y. Kaufman, T. Nakajima, *et al.*, "AERONET—A federated instrument network and data archive for aerosol characterization," *Remote sensing of environment*, vol. 66, no. 1, pp. 1–16, 1998.

[102] O. Dubovik, M. D. King, *et al.*, "A flexible inversion algorithm for retrieval of aerosol optical properties from Sun and sky radiance measurements," *Journal of Geophysical Research*, vol. 105, no. D16, pp. 20673–20696, 2000.

[103] O. Dubovik, A. Sinyuk, T. Lapyonok, B. N. Holben, M. Mishchenko, P. Yang, T. F. Eck, H. Volten, O. Munoz, B. Veihelmann, *et al.*, "Application of spheroid models to account for aerosol particle nonsphericity in remote sensing of desert dust," *Journal of Geophysical Research: Atmospheres*, vol. 111, no. D11, 2006.

[104] O. Dubovik, M. Herman, A. Holdak, T. Lapyonok, D. Taure, J. Deuzé, F. Ducos, and A. Sinyuk, “Statistically optimized inversion algorithm for enhanced retrieval of aerosol properties from spectral multi-angle polarimetric satellite observations,” *Atmospheric Measurement Techniques*, vol. 4, no. 5, pp. 975–1018, 2011.

[105] O. Dubovik, A. Smirnov, B. Holben, M. King, Y. Kaufman, T. Eck, and I. Slutsker, “Accuracy assessments of aerosol optical properties retrieved from Aerosol Robotic Network (AERONET) Sun and sky radiance measurements,” *Journal of Geophysical Research: Atmospheres*, vol. 105, no. D8, pp. 9791–9806, 2000.

[106] G. L. Schuster, O. Dubovik, and B. N. Holben, “Angstrom exponent and bimodal aerosol size distributions,” *Journal of Geophysical Research: Atmospheres*, vol. 111, no. D7, 2006.

[107] A. Chaikovsky, O. Dubovik, B. Holben, A. Bril, P. Goloub, D. Tanré, G. Pappalardo, U. Wandinger, L. Chaikovskaya, S. Denisov, J. Grudo, A. Lopatin, Y. Karol, T. Lapyonok, V. Amiridis, A. Ansmann, A. Apituley, L. Allados-Arboledas, I. Binietoglou, A. Boselli, G. D’Amico, V. Freudenthaler, D. Giles, M. J. Granados-Muñoz, P. Kokkalis, D. Nicolae, S. Oshchepkov, A. Papayannis, M. R. Perrone, A. Pietruczuk, F. Rocadenbosch, M. Sicard, I. Slutsker, C. Talianu, F. DeÂ Tomasi, A. Tsekeri, J. Wagner, and X. Wang, “Lidar-Radiometer Inversion Code (LIRIC) for the retrieval of vertical aerosol properties from combined lidar/radiometer data: development and distribution in EARLINET,” *Atmospheric Measurement Techniques*, vol. 9, no. 3, pp. 1181–1205, 2016.

[108] M. Granados-Muñoz, J. Guerrero-Rascado, J. Bravo-Aranda, F. Navas-Guzmán, A. Valenzuela, H. Lyamani, A. Chaikovsky, U. Wandinger, A. Ansmann, O. Dubovik, *et al.*, “Retrieving aerosol microphysical properties by Lidar-Radiometer Inversion Code (LIRIC) for different aerosol types,” *Journal of Geophysical Research: Atmospheres*, vol. 119, no. 8, pp. 4836–4858, 2014.

[109] J. Wagner, A. Ansmann, U. Wandinger, P. Seifert, A. Schwarz, M. Tesche, A. Chaikovsky, and O. Dubovik, “Evaluation of the Lidar/Radiometer Inversion Code (LIRIC) to determine microphysical properties of volcanic and desert dust,” *Atmospheric Measurement Techniques*, vol. 6, no. 7, pp. 1707–1724, 2013.

[110] P. Kokkalis, A. Papayannis, V. Amiridis, R. E. Mamouri, I. Veselovskii, A. Kolgotin, G. Tsaknakis, N. I. Kristiansen, A. Stohl, and L. Mona, “Optical, microphysical, mass and geometrical properties of aged volcanic particles observed over Athens, Greece, during the Eyjafjallajökull eruption in April 2010 through synergy of Raman lidar and sunphotometer measurements,” *Atmospheric Chemistry and Physics*, vol. 13, no. 18, pp. 9303–9320, 2013.

[111] I. Binietoglou, S. Basart, L. Alados-Arboledas, V. Amiridis, A. Argyrouli, H. Baars, J. M. Baldasano, D. Balis, L. Belegante, J. A. Bravo-Aranda, P. Burlizzi, V. Carrasco, A. Chaikovsky, A. Comerón, G. D’Amico, M. Filioglou, M. J. Granados-Muñoz, J. L. Guerrero-Rascado, L. Ilic, P. Kokkalis, A. Maurizi, L. Mona, F. Monti, C. Muñoz Porcar, D. Nicolae, A. Papayannis, G. Pappalardo, G. Pejanovic, S. N. Pereira, M. R. Perrone, A. Pietruczuk, M. Posyniak, F. Rocadenbosch, A. Rodríguez-Gómez, M. Sicard, N. Siomos, A. Szkop, E. Terradellas, A. Tsekeri, A. Vukovic, U. Wandinger, and J. Wagner, “A methodology for investigating dust model performance using synergistic EARLINET/AERONET dust concentration retrievals,” *Atmospheric Measurement Techniques*, vol. 8, no. 9, pp. 3577–3600, 2015.

[112] A. Papayannis, A. Argyrouli, A. Bougiatioti, E. Remoundaki, E. Eleftheriadis, A. Nenes, J. Van de Hey, M. Komppula, S. Solomos, S. Kazadzis, *et al.*, “From hygroscopic aerosols to cloud droplets: The hygra-cd campaign in the athens basin — an overview,” *Science of The Total Environment*, vol. 574, pp. 216 – 233, 2017.

[113] P. Zieger, E. Weingartner, J. Henzing, M. Moerman, G. de Leeuw, J. Mikkilä, M. Ehn, T. Petäjä, K. Clémer, M. van Roozendael, S. Yilmaz, U. Frieß, H. Irie, T. Wagner, R. Shaiganfar, S. Beirle, A. Apituley, K. Wilson, and U. Baltensperger, “Comparison of ambient aerosol extinction coefficients obtained from in-situ, MAX-DOAS and LIDAR measurements at Cabauw,” *Atmospheric Chemistry and Physics*, vol. 11, no. 6, pp. 2603–2624, 2011.

[114] R. Engelmann, U. Wandinger, A. Ansmann, D. Mueller, E. Zeromskis, D. Althausen, and B. Wehner, “Lidar Observations of the Vertical Aerosol Flux in the Planetary Boundary Layer,” *Journal of Atmospheric and Oceanic Technology*, vol. 25, no. 8, pp. 1296–1306.

[115] A. Ansmann, J. Fruntke, and R. Engelmann, “Updraft and downdraft characterization with Doppler lidar: cloud-free versus cumuli-topped mixed layer,” *Atmospheric Chemistry and Physics*, vol. 10, no. 16, pp. 7845–7858, 2010.

[116] H. Baars, A. Ansmann, R. Engelmann, and D. Althausen, “Continuous monitoring of the boundary-layer top with lidar,” *Atmospheric Chemistry and Physics*, vol. 8, no. 23, pp. 7281–7296, 2008.

[117] D. Melas, I. Ziomas, O. Klemm, and C. Zerefos, “Flow dynamics in Athens area under moderate large-scale winds,” *Atmospheric Environment*, vol. 32, no. 12, pp. 2209–2222, 1998.

[118] Z. Fleming, P. S. Monks, and A. J. Manning, “Review: Untangling the influence of air-mass history in interpreting observed atmospheric composition,” *Atmospheric Research*, vol. 104, pp. 1–39, 2012.

[119] A. Stein, R. Draxler, G. Rolph, B. Stunder, M. Cohen, and F. Ngan, “NOAA’s HYSPLIT atmospheric transport and dispersion modeling system,” *Bulletin of the American Meteorological Society*, vol. 96, no. 12, pp. 2059–2077, 2015.

[120] J. D. Klett, “Lidar inversion with variable backscatter/extinction ratios,” *Applied Optics*, vol. 24, no. 11, pp. 1638–1643, 1985.

[121] S. Groß, M. Tesche, V. Freudenthaler, C. Toledano, M. Wiegner, A. Ansmann, D. Althausen, and M. Seefeldner, “Characterization of saharan dust, marine aerosols and mixtures of biomass-burning aerosols and dust by means of multi-wavelength depolarization and raman lidar measurements during SAMUM 2,” *Tellus B*, vol. 63, no. 4, pp. 706–724, 2011.

[122] S. Groß, M. Esselborn, B. Weinzierl, M. Wirth, A. Fix, and A. Petzold, “Aerosol classification by airborne high spectral resolution lidar observations,” *Atmospheric chemistry and physics*, vol. 13, no. 5, pp. 2487–2505, 2013.

[123] E. Giannakaki, P. G. v. Zyl, D. Müller, D. Balis, and M. Komppula, “Optical and microphysical characterization of aerosol layers over south africa by means of multi-wavelength depolarization and raman lidar measurements,” *Atmospheric Chemistry and Physics*, vol. 16, no. 13, pp. 8109–8123, 2016.

[124] R. Mamouri and A. Ansmann, "Estimated desert-dust ice nuclei profiles from polarization lidar: methodology and case studies," *Atmospheric Chemistry and Physics*, vol. 15, no. 6, pp. 3463–3477, 2015.

[125] R. Mamouri, A. Ansmann, A. Nisantzi, P. Kokkalis, A. Schwarz, and D. Hadjimitsis, "Low arabian dust extinction-to-backscatter ratio," *Geophysical Research Letters*, vol. 40, no. 17, pp. 4762–4766, 2013.

[126] A. Papayannis, D. Nicolae, P. Kokkalis, I. Binietoglou, C. Talianu, L. Belegante, G. Tsaknakis, M. Cazacu, I. Vetres, and L. Ilic, "Optical, size and mass properties of mixed type aerosols in Greece and Romania as observed by synergy of lidar and sunphotometers in combination with model simulations: A case study," *Science of The Total Environment*, vol. 500, pp. 277–294, 2014.

[127] M. Wiegner, S. Groß, V. Freudenthaler, F. Schnell, and J. Gasteiger, "The may/june 2008 saharan dust event over munich: Intensive aerosol parameters from lidar measurements," *Journal of Geophysical Research: Atmospheres*, vol. 116, no. D23, 2011.

[128] L. Giglio, J. Randerson, G. Van der Werf, P. Kasibhatla, G. Collatz, D. Morton, and R. DeFries, "Assessing variability and long-term trends in burned area by merging multiple satellite fire products," *Biogeosciences*, vol. 7, no. 3, 2010.

[129] R. Zhang, J. J. Qu, Y. Liu, X. Hao, C. Huang, and X. Zhan, "Detection of burned areas from mega-fires using daily and historical MODIS surface reflectance," *International Journal of Remote Sensing*, vol. 36, no. 4, pp. 1167–1187, 2015.

[130] C. Pérez, K. Haustein, Z. Janjic, O. Jorba, N. Huneeus, J. Baldasano, T. Black, S. Basart, S. Nickovic, R. Miller, *et al.*, "Atmospheric dust modeling from meso to global scales with the online NMMB/BSC-Dust model–part 1: Model description, annual simulations and evaluation," *Atmospheric Chemistry and Physics*, vol. 11, no. 24, pp. 13001–13027, 2011.

[131] J. Güldner and D. Spänkuch, "Remote sensing of the thermodynamic state of the atmospheric boundary layer by ground-based microwave radiometry," *Journal of Atmospheric and Oceanic Technology*, vol. 18, no. 6, pp. 925–933, 2001.

[132] J. Liu and Z. Li, "Estimation of cloud condensation nuclei concentration from aerosol optical quantities: influential factors and uncertainties," *Atmospheric Chemistry and Physics*, vol. 14, no. 1, pp. 471–483, 2014.

[133] S. Twomey, "Pollution and the planetary albedo," *Atmospheric Environment (1967)*, vol. 8, no. 12, pp. 1251–1256, 1974.

[134] B. Albrecht, "Aerosols, cloud microphysics, and fractional cloudiness," *Science*, vol. 245, no. 4923, pp. 1227–1230, 1989.

[135] D. Rosenfeld, U. Lohmann, G. B. Raga, C. D. O'Dowd, M. Kulmala, S. Fuzzi, A. Reissell, and M. O. Andreae, "Flood or drought: how do aerosols affect precipitation?," *Science*, vol. 321, no. 5894, pp. 1309–1313, 2008.

[136] B. Stevens and G. Feingold, "Untangling aerosol effects on clouds and precipitation in a buffered system," *Nature*, vol. 461, no. 7264, pp. 607–613, 2009.

[137] D. Rosenfeld, M. O. Andreae, A. Asmi, M. Chin, G. Leeuw, D. P. Donovan, R. Kahn, S. Kinne, N. Kivekäs, M. Kulmala, *et al.*, “Global observations of aerosol-cloud-precipitation-climate interactions,” *Reviews of Geophysics*, vol. 52, no. 4, pp. 750–808, 2014.

[138] A. Ansmann, P. Seifert, M. Tesche, and U. Wandinger, “Profiling of fine and coarse particle mass: case studies of Saharan dust and Eyjafjallajökull/Grimsvötn volcanic plumes,” *Atmospheric Chemistry and Physics*, vol. 12, no. 20, pp. 9399–9415, 2012.

[139] D. Müller, C. A. Hostetler, R. Ferrare, S. Burton, E. Chemyakin, A. Kolgotin, J. Hair, A. Cook, D. Harper, R. Rogers, *et al.*, “Airborne Multiwavelength High Spectral Resolution Lidar (HSRL-2) observations during TCAP 2012: vertical profiles of optical and microphysical properties of a smoke/urban haze plume over the northeastern coast of the US,” *Atmospheric Measurement Techniques*, vol. 7, no. 10, pp. 3487–3496, 2014.

[140] J. H. Seinfeld and S. N. Pandis, *Atmospheric chemistry and physics: from air pollution to climate change.* John Wiley & Sons, 2016.

[141] J. H. Kim, S. S. Yum, S. Shim, S.-C. Yoon, J. G. Hudson, J. Park, and S.-J. Lee, “On aerosol hygroscopicity, cloud condensation nuclei (CCN) spectra and critical supersaturation measured at two remote islands of Korea between 2006 and 2009,” *Atmospheric Chemistry and Physics*, vol. 11, no. 24, pp. 12627–12645, 2011.

[142] A. Bougiatioti, A. Nenes, C. Fountoukis, N. Kalivitis, S. N. Pandis, and N. Mihalopoulos, “Size-resolved CCN distributions and activation kinetics of aged continental and marine aerosol,” *Atmospheric Chemistry and Physics*, vol. 11, no. 16, pp. 8791–8808, 2011.

[143] M. D. Petters and S. M. Kreidenweis, “A single parameter representation of hygroscopic growth and cloud condensation nucleus activity,” *Atmospheric Chemistry and Physics*, vol. 7, no. 8, pp. 1961–1971, 2007.

[144] K. M. Cerully, T. Raatikainen, S. Lance, D. Tkacik, P. Tiitta, T. Petäjä, M. Ehn, M. Kulmala, D. R. Worsnop, A. Laaksonen, J. N. Smith, and A. Nenes, “Aerosol hygroscopicity and CCN activation kinetics in a boreal forest environment during the 2007 EUCAARI campaign,” *Atmospheric Chemistry and Physics*, vol. 11, no. 23, pp. 12369–12386, 2011.

[145] A. Nenes and J. H. Seinfeld, “Parameterization of cloud droplet formation in global climate models,” *Journal of Geophysical Research: Atmospheres*, vol. 108, no. D14, 2003.

[146] R. Morales and A. Nenes, “Characteristic updrafts for computing distribution-averaged cloud droplet number and stratocumulus cloud properties,” *Journal of Geophysical Research: Atmospheres*, vol. 115, no. D18.

[147] E. Kostenidou, K. Florou, C. Kaltsonoudis, M. Tsiflikiotou, S. Vratolis, K. Eleftheriadis, and S. Pandis, “Sources and chemical characterization of organic aerosol during the summer in the eastern Mediterranean,” *Atmospheric Chemistry and Physics*, vol. 15, no. 19, pp. 11355–11371, 2015.

[148] S. Bezantakos, K. Barmpounis, M. Giamarelou, E. Bossioli, M. Tombrou, N. Mihalopoulos, K. Eleftheriadis, J. Kalogiros, J. D Allan, A. Bacak, *et al.*, “Chemical composition and hygroscopic properties of aerosol particles over the Aegean Sea,” *Atmospheric Chemistry and Physics*, vol. 13, no. 22, pp. 11595–11608, 2013.

[149] U. Löhnert, S. Crewell, and C. Simmer, “An integrated approach toward retrieving physically consistent profiles of temperature, humidity, and cloud liquid water,” *Journal of Applied Meteorology*, vol. 43, no. 9, pp. 1295–1307, 2004.

[150] V. I. Khvorostyanov and J. A. Curry, “Aerosol size spectra and CCN activity spectra: Reconciling the lognormal, algebraic, and power laws,” *Journal of Geophysical Research: Atmospheres*, vol. 111, no. D12, 2006.

[151] C. Fountoukis and A. Nenes, “Continued development of a cloud droplet formation parameterization for global climate models,” *Journal of Geophysical Research: Atmospheres*, vol. 110, no. D11, 2005.

[152] R. Engelmann, U. Wandinger, A. Ansmann, D. Müller, E. Žeromskis, D. Althausen, and B. Wehner, “Lidar observations of the vertical aerosol flux in the planetary boundary layer,” *Journal of Atmospheric and Oceanic Technology*, vol. 25, no. 8, pp. 1296–1306, 2008.

[153] G. Buzorius, Ü. Rannik, J. M. Mäkelä, T. Vesala, and M. Kulmala, “Vertical aerosol particle fluxes measured by eddy covariance technique using condensational particle counter,” *Journal of Aerosol Science*, vol. 29, no. 1, pp. 157–171, 1998.

[154] G. Buzorius, J. Kalogiros, and V. Varutbangkul, “Airborne aerosol flux measurements with eddy correlation above the ocean in a coastal environment,” *Journal of Aerosol Science*, vol. 37, no. 10, pp. 1267–1286, 2006.

[155] A. Giez, G. Ehret, R. L. Schwiesow, K. J. Davis, and D. H. Lenschow, “Water vapor flux measurements from ground-based vertically pointed water vapor differential absorption and doppler lidars,” *Journal of Atmospheric and Oceanic Technology*, vol. 16, no. 2, pp. 237–250, 1999.

[156] S. Henderson, P. Gatt, D. Rees, and R. Huffaker, “Laser remote sensing,” *Wind Lidar, Takashii Fujii and Tetsuo Fukuchi*, pp. 469–722, 2005.

[157] C. Fairall, A. White, J. Edson, and J. Hare, “Integrated shipboard measurements of the marine boundary layer,” *Journal of Atmospheric and Oceanic Technology*, vol. 14, no. 3, pp. 338–359, 1997.

[158] G. I. Taylor, “The spectrum of turbulence,” in *Proceedings of the Royal Society of London A: Mathematical, Physical and Engineering Sciences*, vol. 164, pp. 476–490, The Royal Society, 1938.

[159] D. Lenschow, J. Mann, and L. Kristensen, “How long is long enough when measuring fluxes and other turbulence statistics?,” *Journal of Atmospheric and Oceanic Technology*, vol. 11, no. 3, pp. 661–673, 1994.

[160] A. N. Kolmogorov, “The local structure of turbulence in incompressible viscous fluid for very large reynolds numbers,” in *Dokl. Akad. Nauk SSSR*, vol. 30, pp. 301–305, JSTOR, 1941.

[161] R. Frehlich and L. Cornman, “Estimating spatial velocity statistics with coherent Doppler lidar,” *Journal of Atmospheric and Oceanic Technology*, vol. 19, no. 3, pp. 355–366, 2002.

[162] S. Caughey and M. Kitchen, “Simultaneous measurements of the turbulent and microphysical structure of nocturnal stratocumulus cloud,” *Quarterly Journal of the Royal Meteorological Society*, vol. 110, no. 463, pp. 13–34, 1984.

[163] S. Gassó, D. Hegg, D. Covert, D. Collins, K. Noone, E. Öström, B. Schmid, P. Russell, J. Livingston, P. Durkee, *et al.*, “Influence of humidity on the aerosol scattering coefficient and its effect on the upwelling radiance during ACE-2,” *Tellus B*, vol. 52, no. 2, pp. 546–567, 2000.

[164] R. A. Kotchenmther and P. V. Hobbs, “Humidification factors of aerosols from biomass burning,” *Journal of Geophysical Research*, vol. 103, no. D24, pp. 32–081, 1998.

[165] P. Zieger, R. Fierz-Schmidhauser, M. Gysel, J. Ström, S. Henne, K. E. Yttri, U. Baltensperger, and E. Weingartner, “Effects of relative humidity on aerosol light scattering in the Arctic,” *Atmospheric Chemistry and Physics*, vol. 10, no. 8, pp. 3875–3890, 2010.

[166] G. Hänel, “The properties of atmospheric aerosol particles as functions of the relative humidity at thermodynamic equilibrium with the surrounding moist air,” *Advances in Geophysics*, vol. 19, pp. 73–188, 1976.

[167] H. Randriamiarisoa, P. Chazette, P. Couvert, J. Sanak, and G. Mégie, “Relative humidity impact on aerosol parameters in a Paris suburban area,” *Atmospheric Chemistry and Physics*, vol. 6, no. 5, pp. 1389–1407, 2006.

[168] M. Granados-Muñoz, *Characterizing the atmospheric aerosol by active and passive remote sensing: microphysical properties and hygroscopic growth effects.* Universidad de Granada, 2014.

[169] J. Cozic, B. Verheggen, E. Weingartner, J. Crosier, K. Bower, M. Flynn, H. Coe, S. Henning, M. Steinbacher, S. Henne, *et al.*, “Chemical composition of free tropospheric aerosol for PM1 and coarse mode at the high alpine site Jungfraujoch,” *Atmospheric Chemistry and Physics*, vol. 8, no. 2, pp. 407–423, 2008.

[170] N. Bukowiecki, P. Zieger, E. Weingartner, Z. Jurányi, M. Gysel, B. Neininger, B. Schneider, C. Hueglin, A. Ulrich, A. Wichser, *et al.*, “Ground-based and airborne in-situ measurements of the Eyjafjallajökull volcanic aerosol plume in Switzerland in spring 2010,” *Atmospheric Chemistry and Physics*, vol. 11, no. 19, pp. 10011–10030, 2011.

[171] A. Ansmann, M. Tesche, P. Seifert, S. Gross, V. Freudenthaler, A. Apituley, K. Wilson, I. Serikov, H. Linné, B. Heinold, *et al.*, “Ash and fine-mode particle mass profiles from EARLINET-AERONET observations over central Europe after the eruptions of the Eyjafjallajökull volcano in 2010,” *Journal of Geophysical Research: Atmospheres*, vol. 116, no. D20, 2011.

[172] J. Gasteiger, S. Groß, V. Freudenthaler, and M. Wiegner, “Volcanic ash from iceland over munich: mass concentration retrieved from ground-based remote sensing measurements,” *Atmospheric Chemistry and Physics*, vol. 11, no. 5, pp. 2209–2223, 2011.

[173] W. E. Boyce, R. C. DiPrima, and C. W. Haines, *Elementary differential equations and boundary value problems*, vol. 9. Wiley New York, 1969.

Appendices

Appendix A

APPENDIX

Bernoulli differential equation of the form

$$\frac{\mathrm{d}y}{\mathrm{d}x}+P(x)\,y=Q(x)\,y^{n},n\neq 0,1. \tag{A.1}$$

The solution comes if we introduce the variable $u=y^{-n+1}$ and take the derivative of this with respect to x

$$\frac{\mathrm{d}u}{\mathrm{d}x}=(-n+1)\,y^{-n}\frac{\mathrm{d}y}{\mathrm{d}x}\Rightarrow y^{-n}\frac{\mathrm{d}y}{\mathrm{d}x}=\frac{1}{(-n+1)}\frac{\mathrm{d}u}{\mathrm{d}x}. \tag{A.2}$$

Then, Eq. (A.1) becomes

$$\frac{\mathrm{d}u}{\mathrm{d}x}+(-n+1)\,P(x)\,u=(-n+1)\,Q(x) \tag{A.3}$$

which is reformulated as

$$\frac{\mathrm{d}u}{\mathrm{d}x}=(-n+1)\left[-P(x)\,u+Q(x)\right]. \tag{A.4}$$

The d.e. above can be solved as a linear first-order d.e. of the form

$$\frac{\mathrm{d}u}{\mathrm{d}x}+up(x)=q(x), \tag{A.5}$$

where $p(x)=(-n+1)\,P(x)$ and $q(x)=(-n+1)\,Q(x)$. Eq. (A.5) can be solved with the use of an integrating factor

$$\begin{aligned} u &= \frac{\int \exp\left[\int p(x)\,dx\right] q(x)+c}{\exp\left[\int p(x)\,dx\right]} \\ &= \frac{(-n+1)\int \exp\left[(-n+1)\int P(x)\,dx\right] Q(x)+c}{\exp\left[(-n+1)\int P(x)\,dx\right]}. \end{aligned} \tag{A.6}$$

Therefore, the general solution for the initial d.e. (A.1) is [173]

$$y=\left[\frac{(-n+1)\int \exp\left[(-n+1)\int P(x)\,dx\right] Q(x)\,dx+c_1}{\exp\left[(-n+1)\int P(x)\,dx\right]}\right]^{\frac{1}{(-n+1)}} \tag{A.7}$$

For the case of $n=1$, the initial d.e. (A.1) becomes

$$\frac{\mathrm{d}y}{\mathrm{d}x} = [Q(x) - P(x)]\,y \Rightarrow \frac{dy}{y} = [Q(x) - P(x)]\,dx. \tag{A.8}$$

Then, the solution is $y = c_2 \exp\left[\int (Q(x) - P(x))\,dx\right]$.

Appendix B

APPENDIX

This Appendix includes the air mass backtrajectories derived from the HYSPLIT model together with the fire hotspots observed by the AQUA-TERRA satellites. The 9-days backtrajectories arrive over Athens at three heights. The lower altitude (red line) refers to the base of the aerosol layer, the middle altitude (blue line) refers to the centroid of the aerosol layer and the higher altitude (green line) refers to the layer top. In the following graphs, base and top of the layer are mentioned in the caption. The fires detected by MODIS have been included as brown circles in the same map using the Google Earth tool.

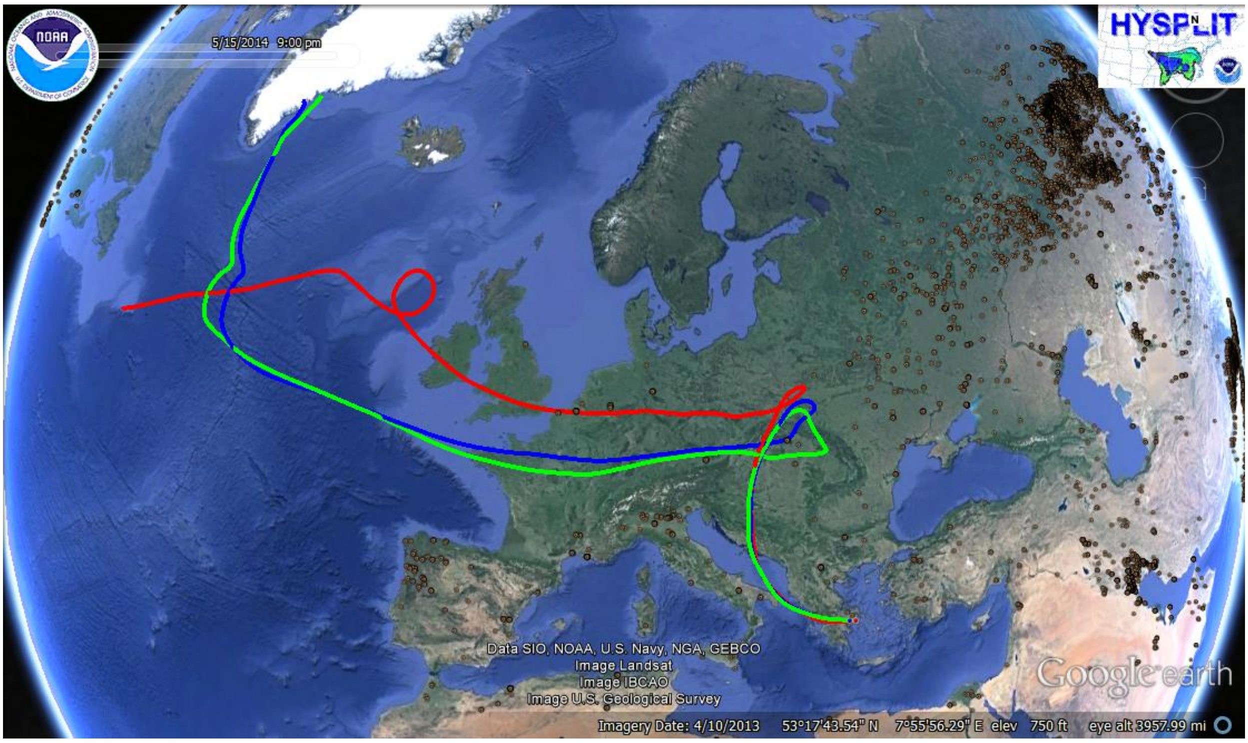

Σχήμα B.1: *Air mass backtrajectories arriving at 1.2-2.0 km on 15/05/2014, 18:30-19:30 UTC*

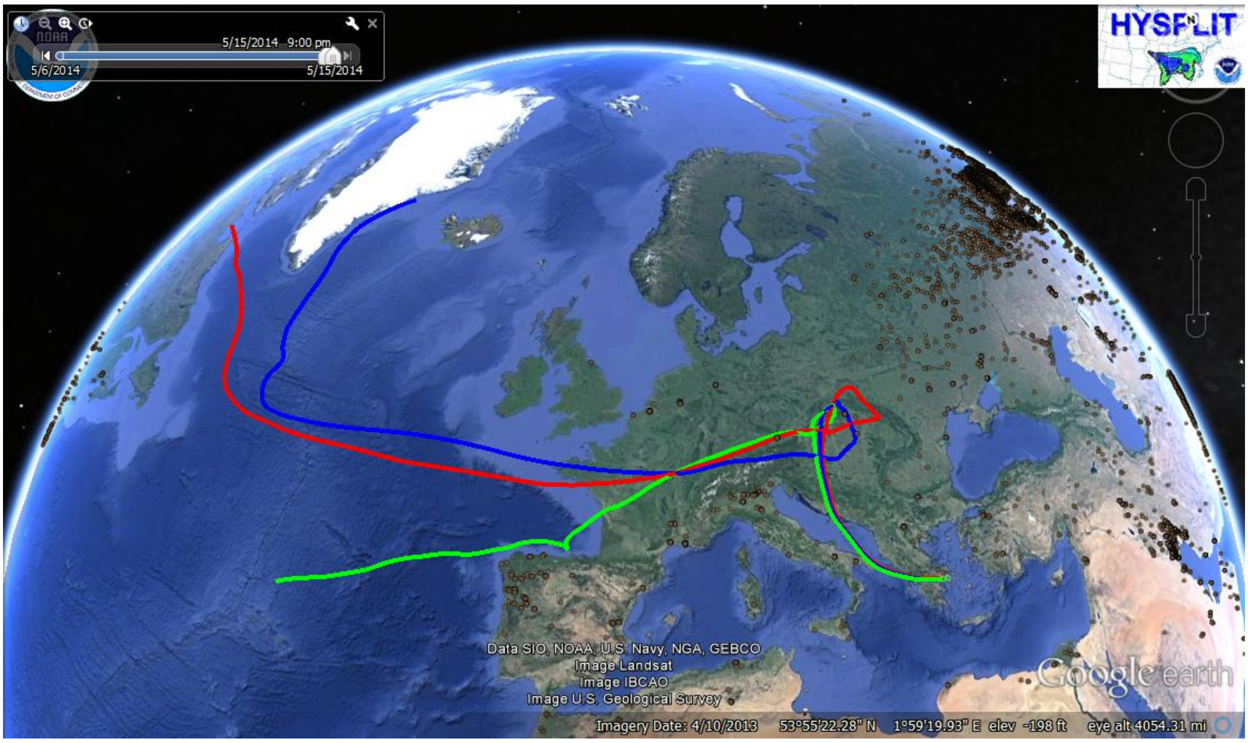

Σχήμα B.2: *Air mass backtrajectories arriving at 2.0-2.4 km on 15/05/2014, 18:30-19:30 UTC*

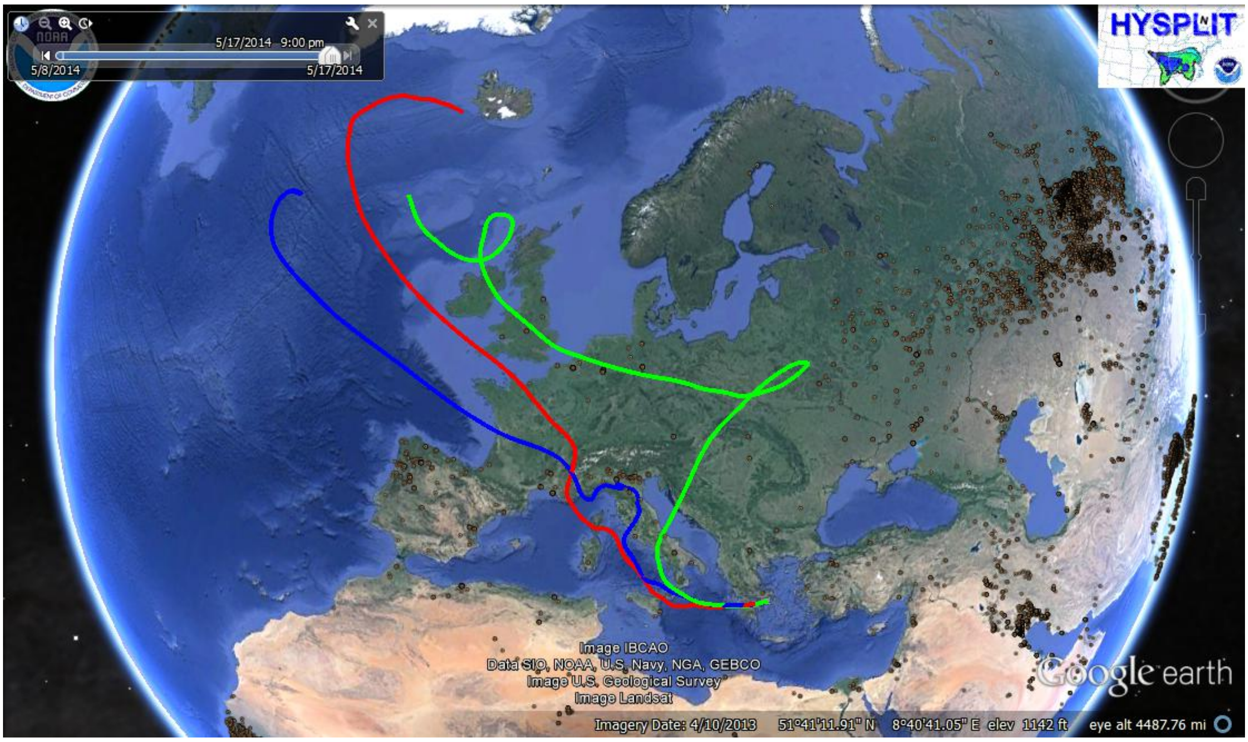

Σχήμα B.3: *Air mass backtrajectories arriving at 1.2-1.8 km on 17/05/2014, 18:30-19:30 UTC*

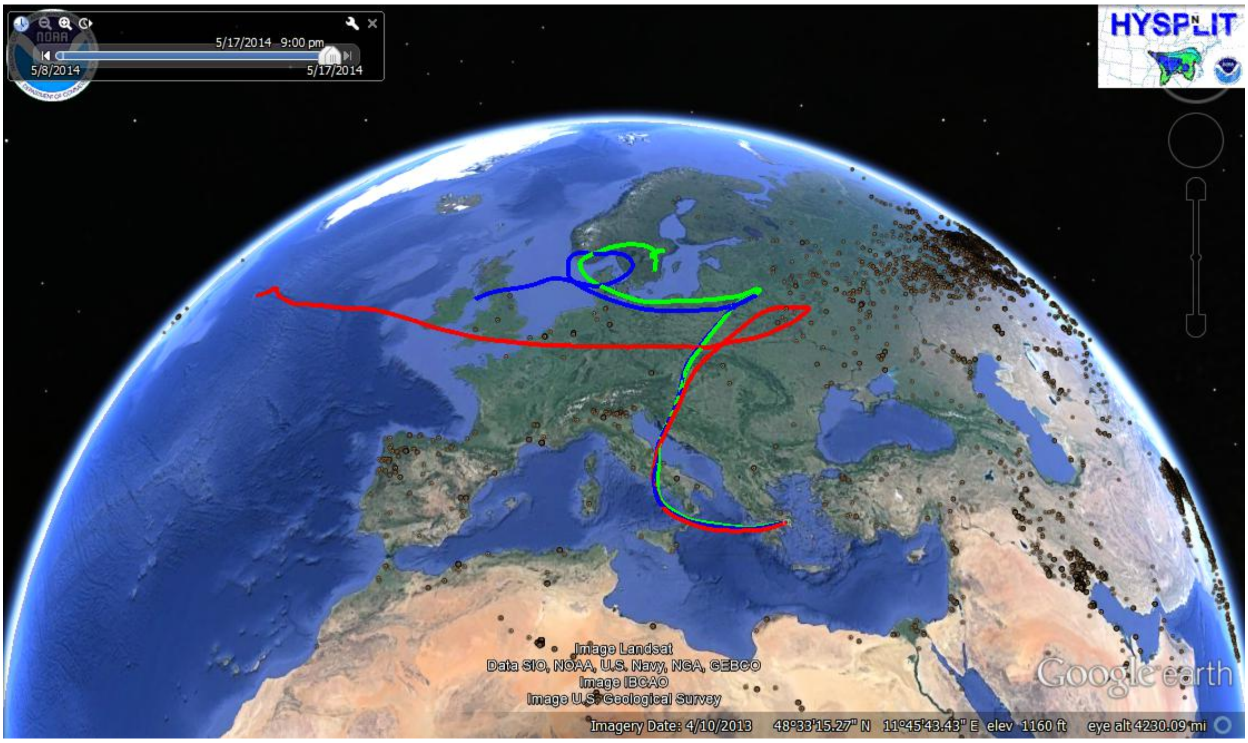

Σχήμα B.4: *Air mass backtrajectories arriving at 2.0-2.5 km on 17/05/2014, 18:30-19:30 UTC*

Σχήμα B.5: *Air mass backtrajectories arriving at 1.2-1.5 km on 18/05/2014, 19:00-20:00 UTC*

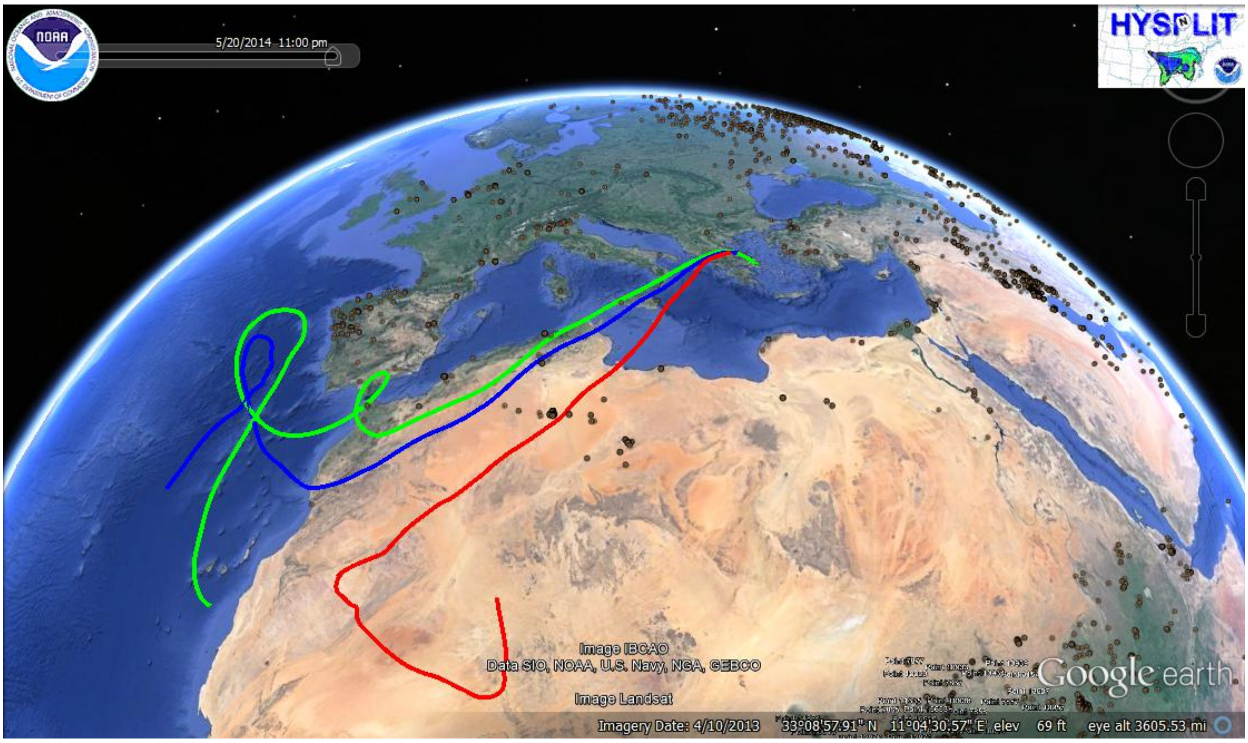

Σχήμα B.6: *Air mass backtrajectories arriving at 2.5-3.2 km on 20/05/2014, 21:00-22:00 UTC*

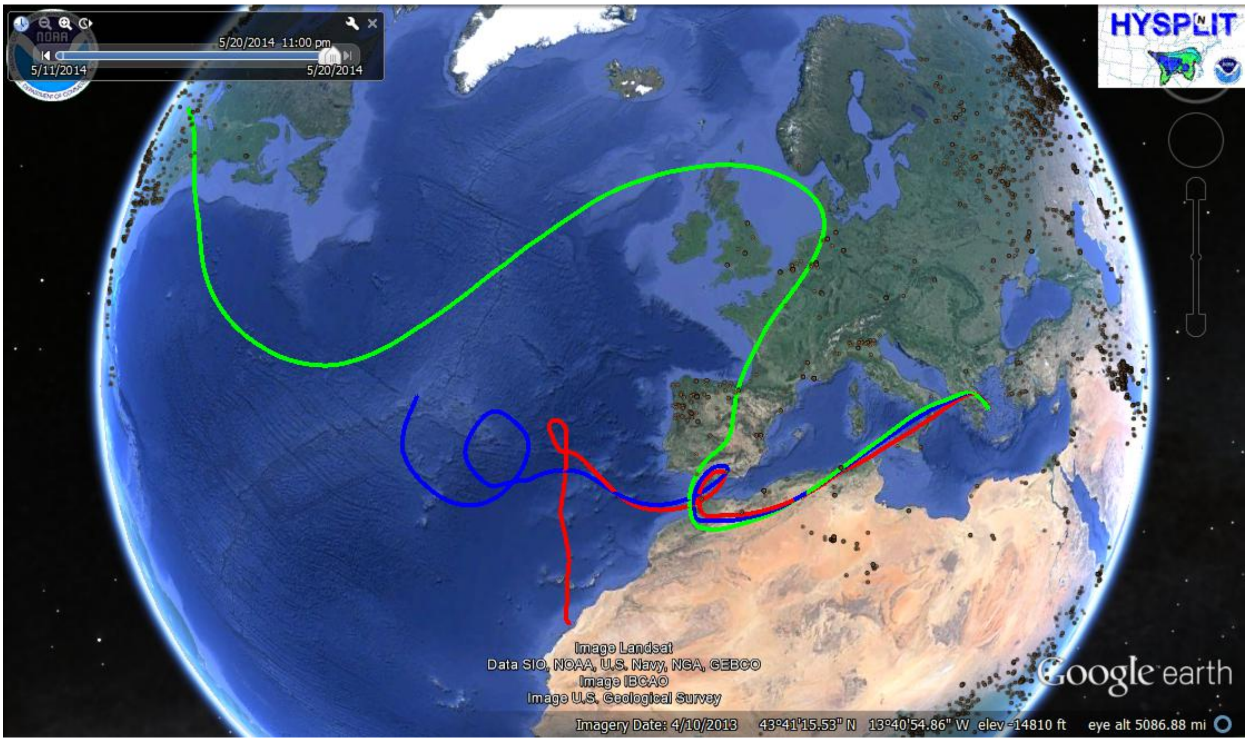

Σχήμα B.7: *Air mass backtrajectories arriving at 3.4-4.0 km on 20/05/2014, 21:00-22:00 UTC*

Σχήμα B.8: *Air mass backtrajectories arriving at 1.2-1.7 km on 21/05/2014, 20:00-21:00 UTC*

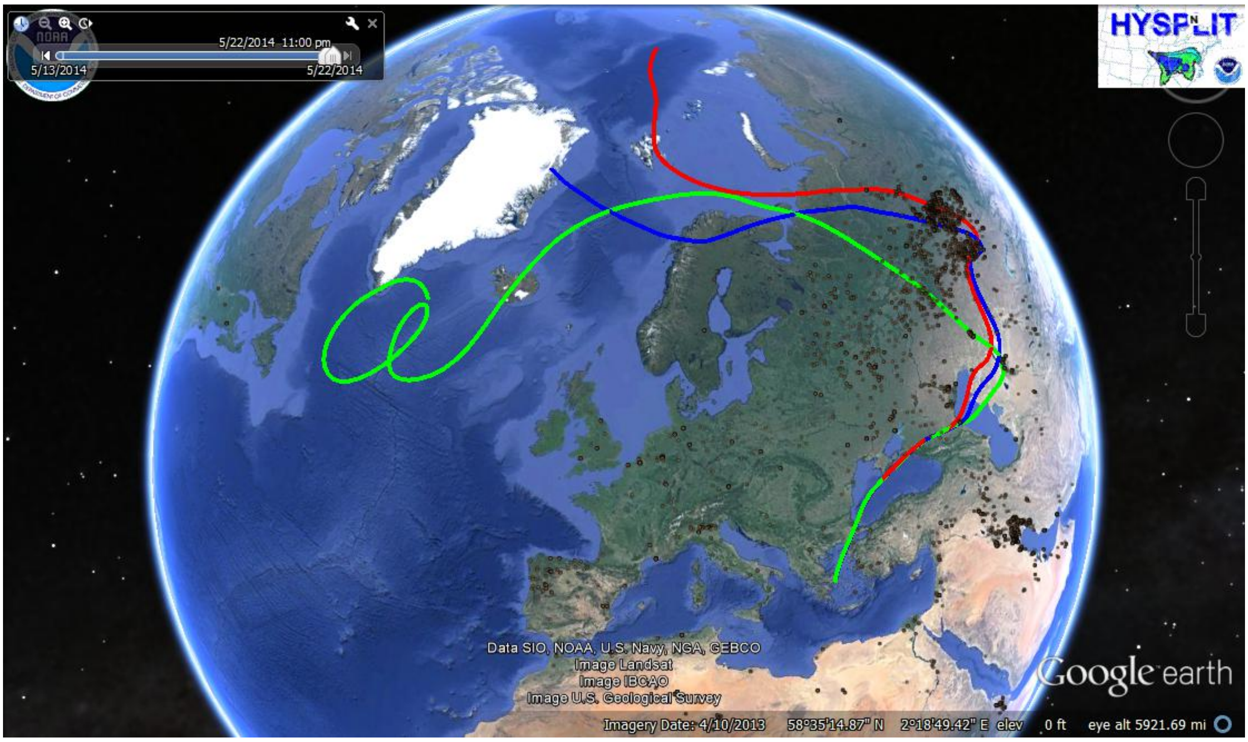

Σχήμα B.9: *Air mass backtrajectories arriving at 1.2-1.5 km on 22/05/2014, 20:30-21:30 UTC*

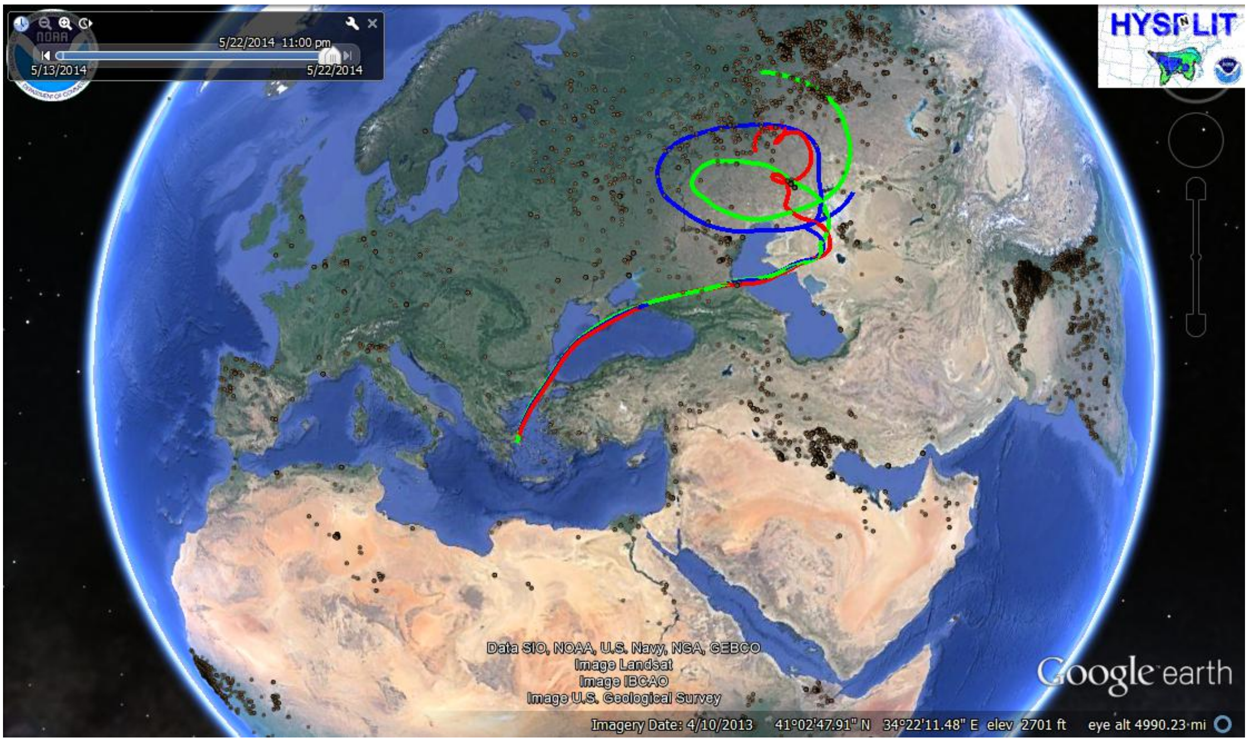

Σχήμα B.10: *Air mass backtrajectories arriving at 1.6-2.0 km on 22/05/2014, 20:30-21:30 UTC*

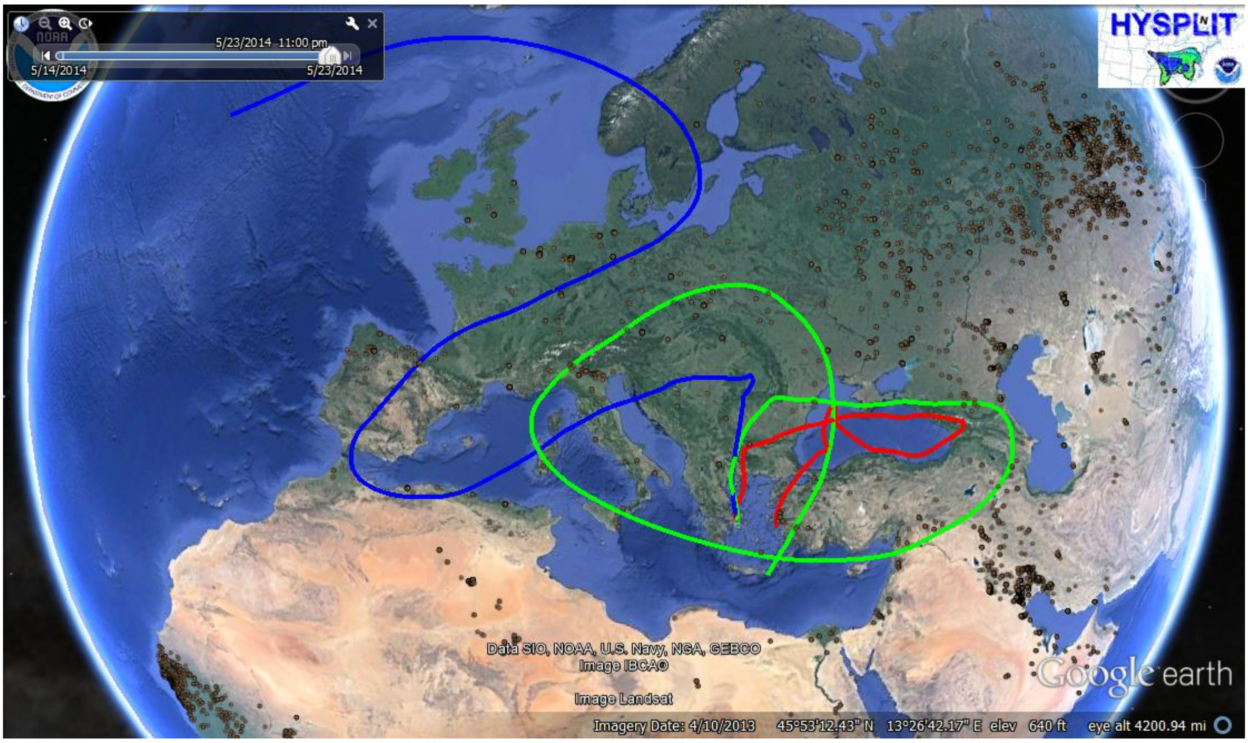

Σχήμα B.11: *Air mass backtrajectories arriving at 1.3-2.8 km on 23/05/2014, 20:30-21:30 UTC*

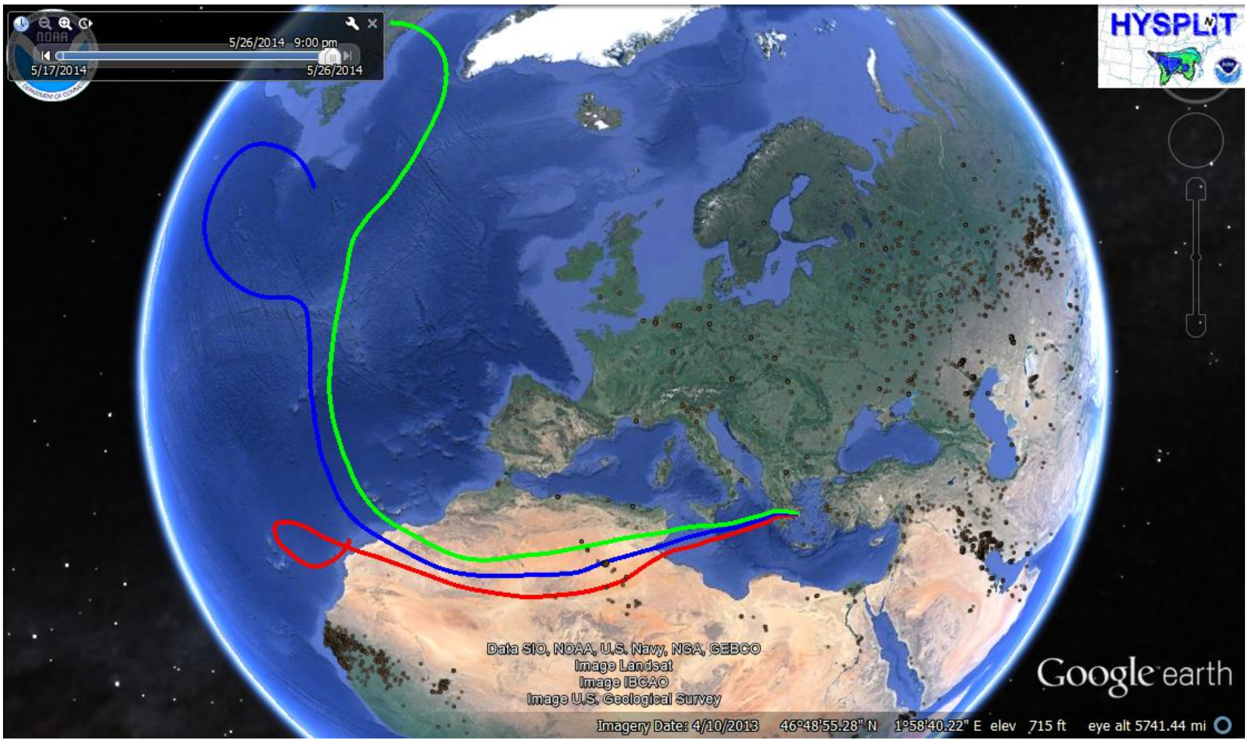

Σχήμα B.12: *Air mass backtrajectories arriving at 3.0-4.0 km on 26/05/2014, 19:00-20:00 UTC*

Σχήμα B.13: *Air mass backtrajectories arriving at 1.2-2.0 km on 27/05/2014, 19:30-20:30 UTC*

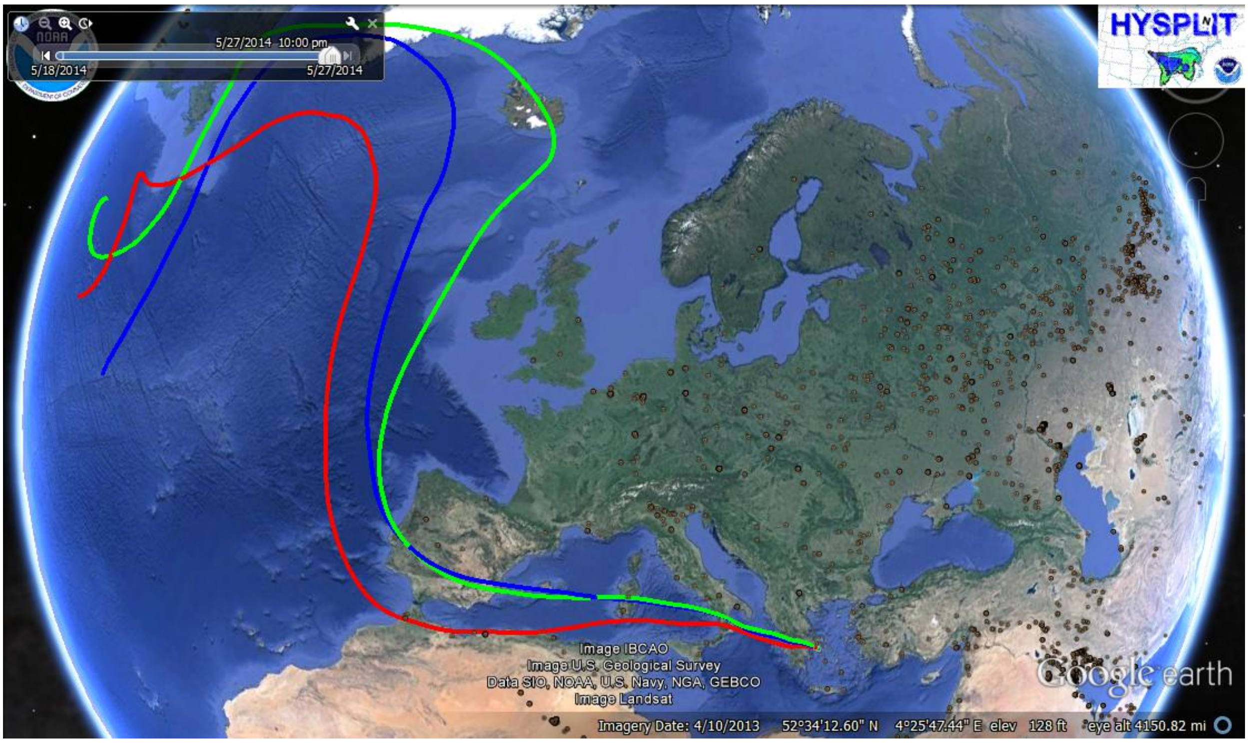

Σχήμα B.14: *Air mass backtrajectories arriving at 2.0-2.5 km on 27/05/2014, 19:30-20:30 UTC*

Σχήμα B.15: *Air mass backtrajectories arriving at 1.2-2.5 km on 01/06/2014, 20:30-21:30 UTC*

Σχήμα B.16: *Air mass backtrajectories arriving at 1.2-1.7 km on 07/06/2014, 22:00-23:00 UTC*

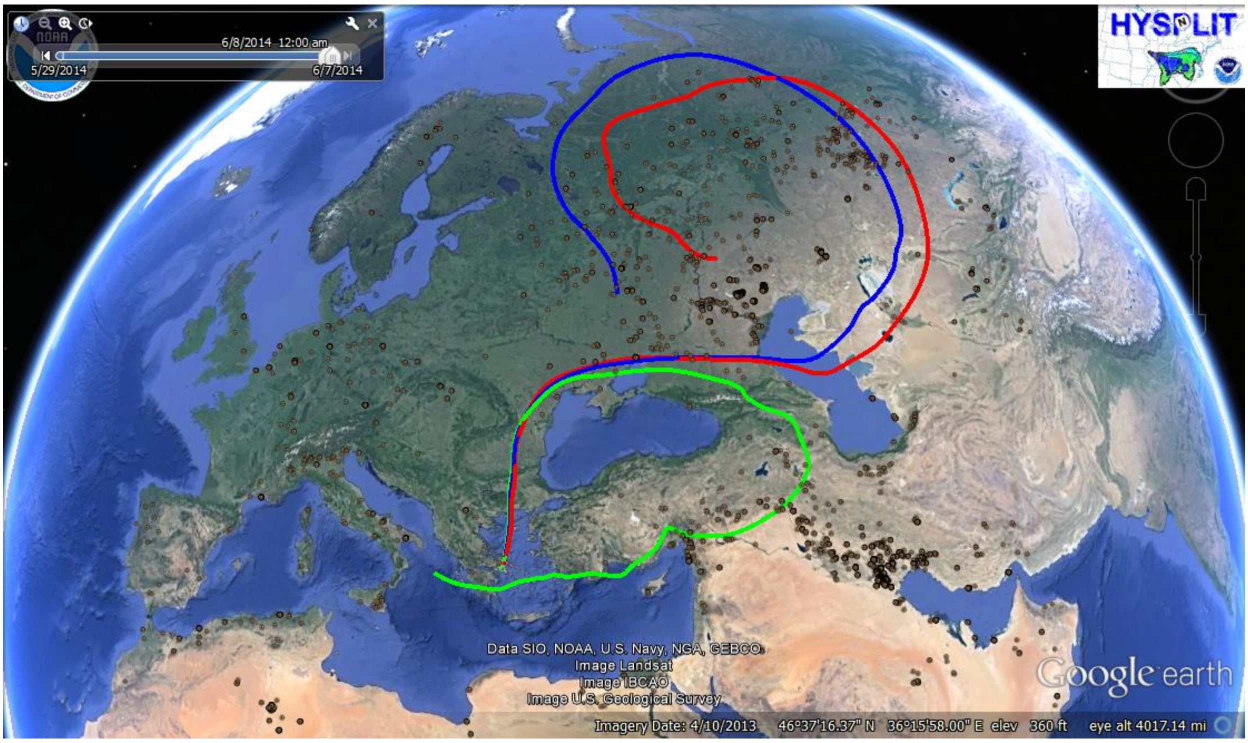

Σχήμα B.17: *Air mass backtrajectories arriving at 2.5-3.2 km on 07/06/2014, 22:00-23:00 UTC*

Σχήμα B.18: *Air mass backtrajectories arriving at 1.2-2.1 km on 10/06/2014, 19:00-20:00 UTC*

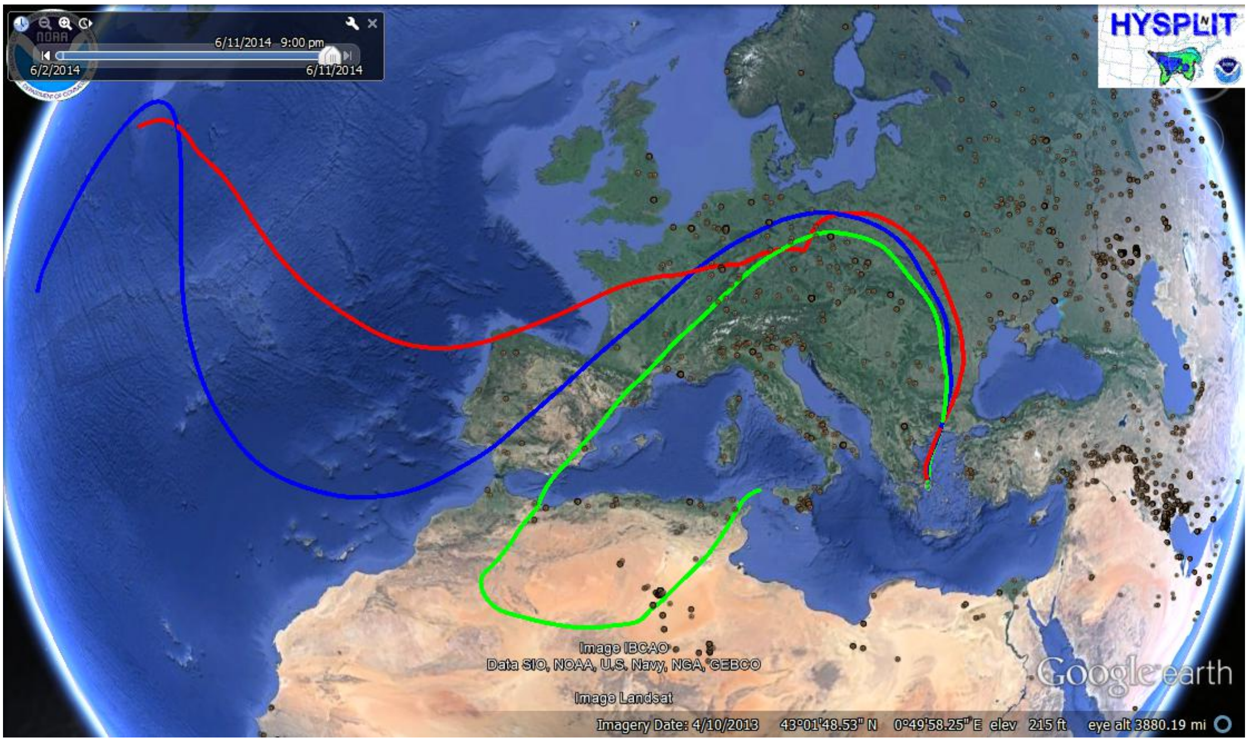

Σχήμα B.19: *Air mass backtrajectories arriving at 1.2-2.1 km on 11/06/2014, 19:00-20:00 UTC*

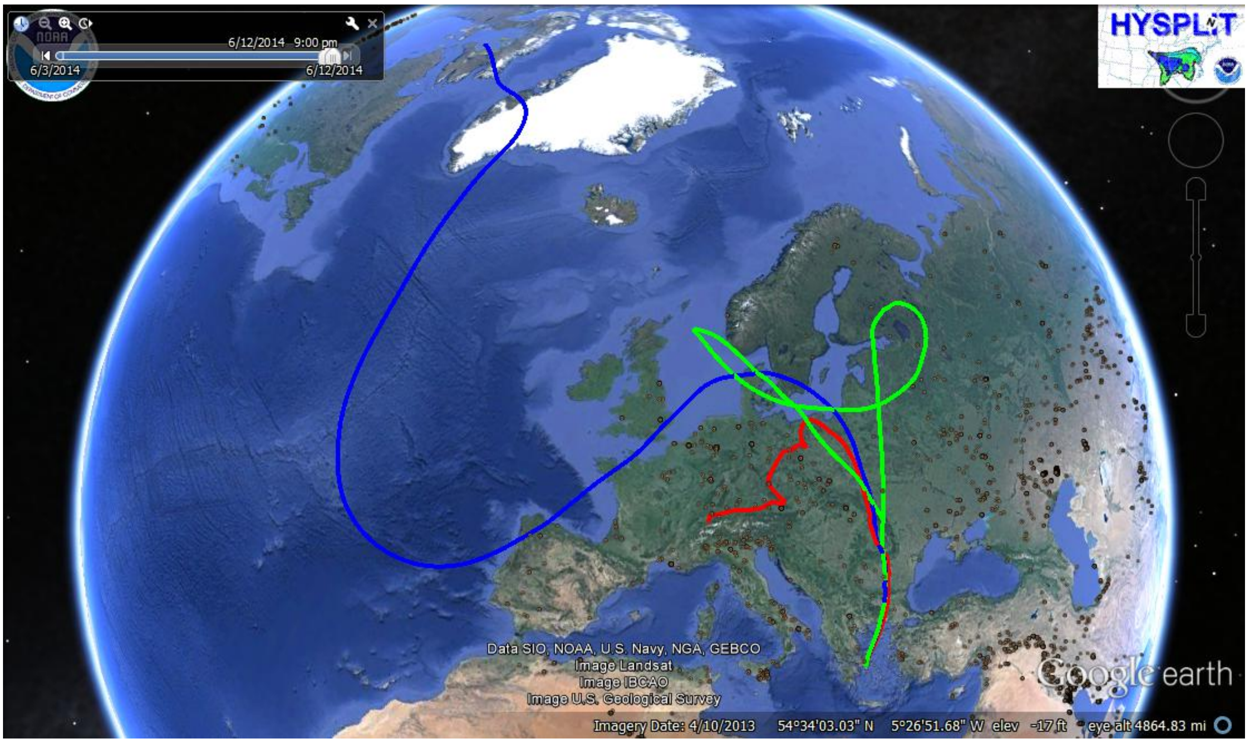

Σχήμα B.20: *Air mass backtrajectories arriving at 1.2-2.0 km on 12/06/2014, 19:00-20:00 UTC*

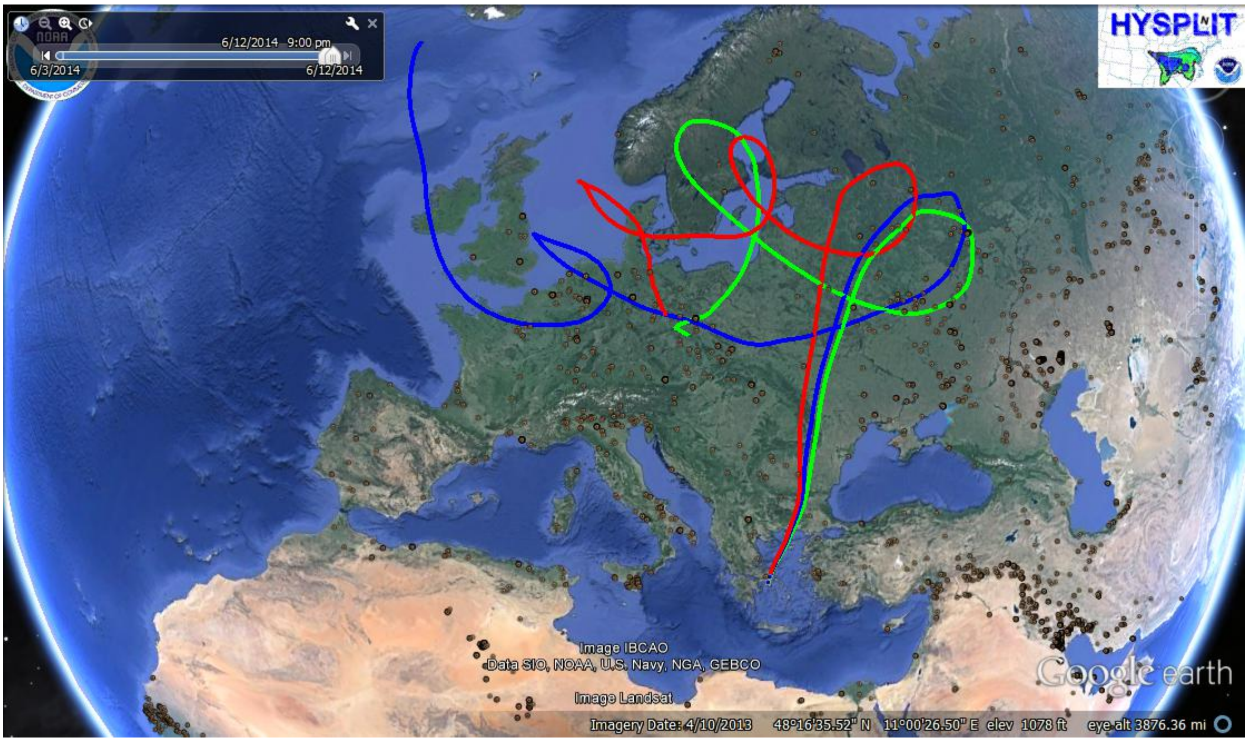

Σχήμα B.21: *Air mass backtrajectories arriving at 2.1-2.8 km on 12/06/2014, 19:00-20:00 UTC*

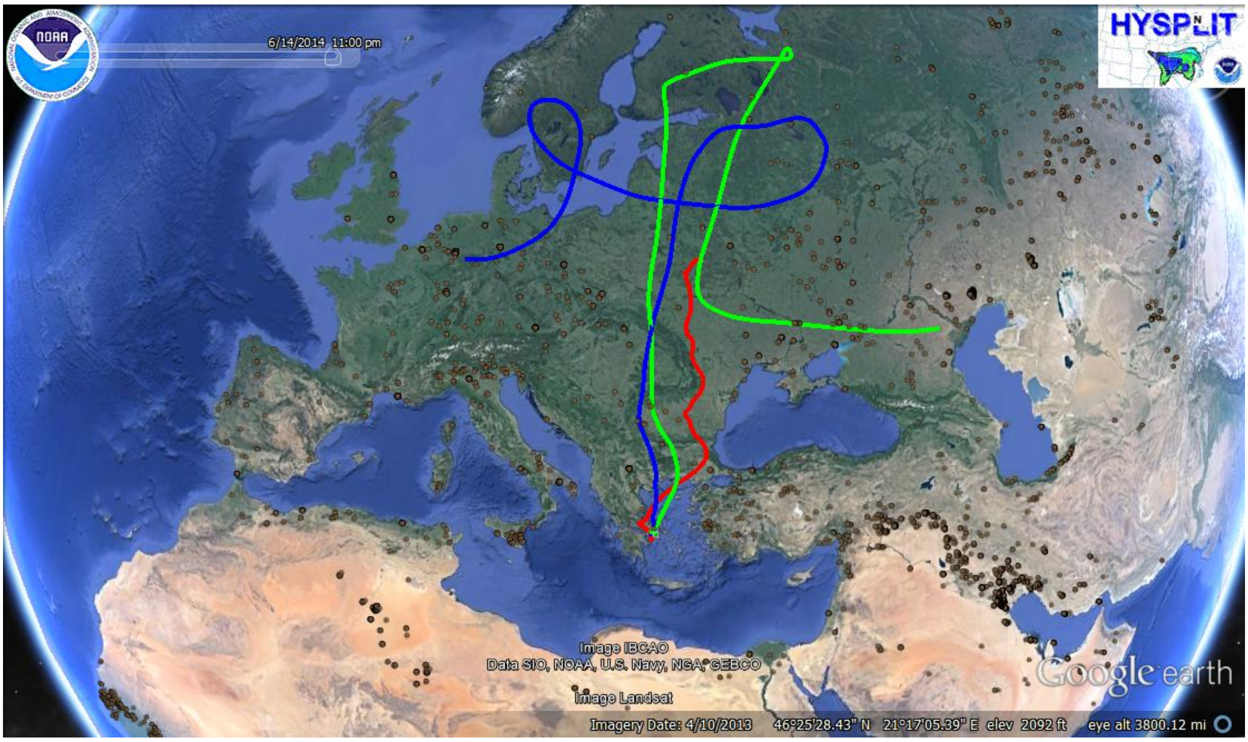

Σχήμα B.22: *Air mass backtrajectories arriving at 1.3-1.7 km on 14/06/2014, 20:30-21:30 UTC*

Σχήμα B.23: *Air mass backtrajectories arriving at 2.3-2.9 km on 14/06/2014, 20:30-21:30 UTC*

Σχήμα B.24: *Air mass backtrajectories arriving at 1.7-3.2 km on 15/06/2014, 20:30-31:30 UTC*

Σχήμα B.25: *Air mass backtrajectories arriving at 1.3-2.7 km on 16/06/2014, 19:00-20:00 UTC*

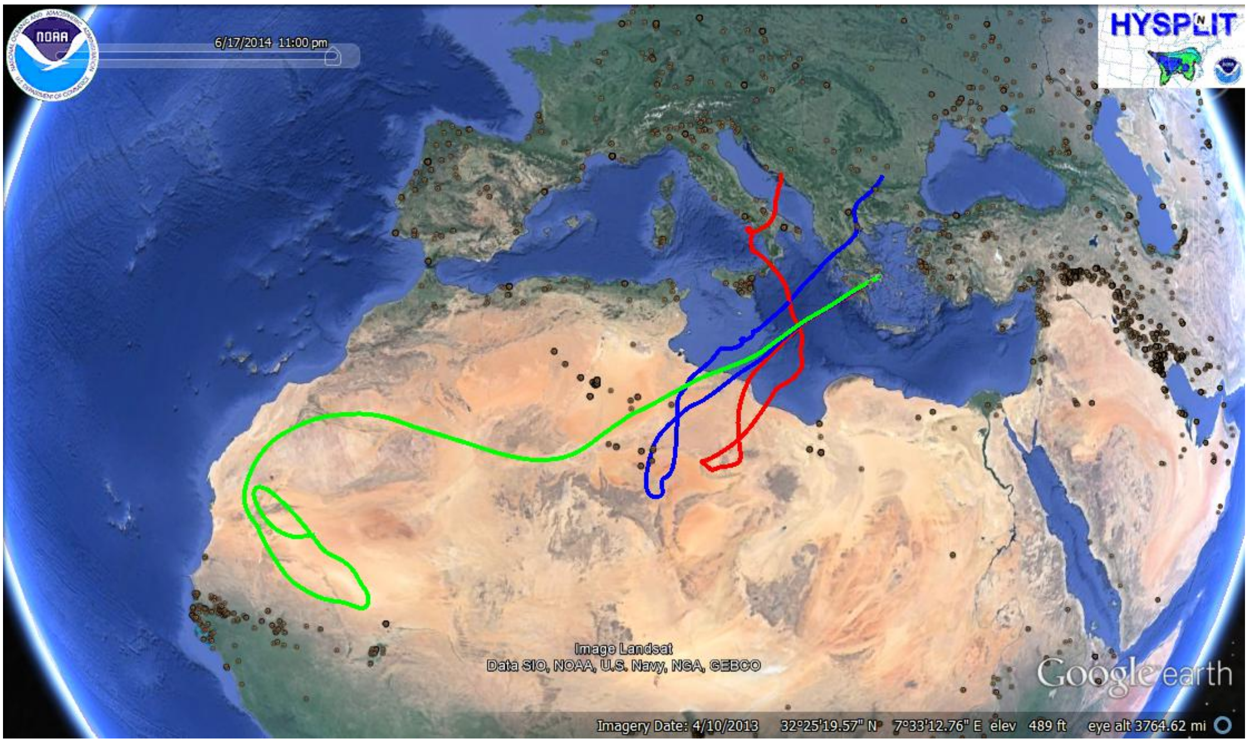

Σχήμα B.26: *Air mass backtrajectories arriving at 4.0-4.8 km on 17/06/2014, 21:00-22:00 UTC*

Σχήμα B.27: *Air mass backtrajectories arriving at 2.5-3.5 km on 18/06/2014, 19:00-20:00 UTC*

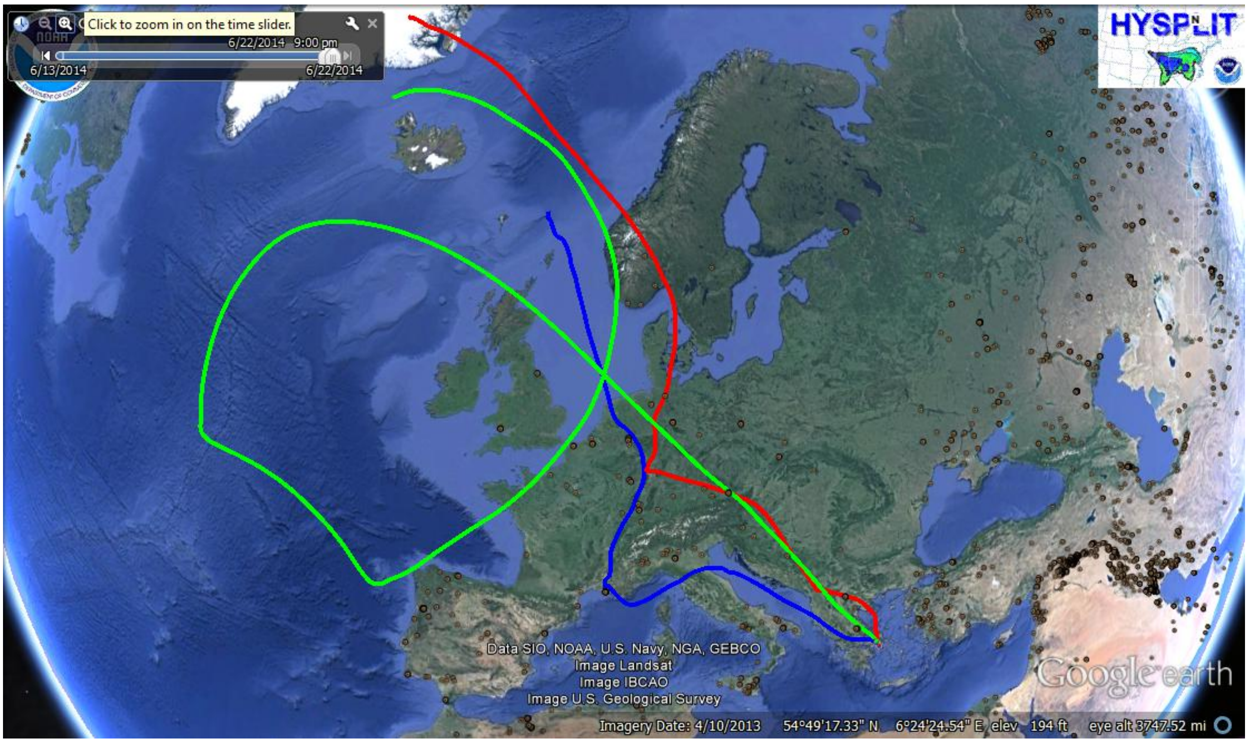

Σχήμα B.28: *Air mass backtrajectories arriving at 1.2-2.5 km on 22/06/2014, 19:00-20:00 UTC*